Model Predictive Control Applications to Spacecraft Rendezvous and Small Bodies Exploration

by

Julio César Sánchez Merino

A thesis submitted for the degree of Doctor of Philosophy
in Automation, Electronics and Telecommunications
Engineering

Universidad de Sevilla

Department of Aerospace Engineering and Fluid
Mechanics

Advisors

Rafael Vázquez Valenzuela
Francisco Gavilán Jiménez

September 2021

Dedicated to my parents and sister.

This page is intentionally left blank.

Acknowledgements

This work has been possible due to the continuous support and guidance of Prof. Rafael Vázquez and Prof. Francisco Gavilán. I would like to thank you Rafael for putting all the effort, patience and necessary means in order to make me grow as a researcher. Thank you Francisco for all your positiveness and by always showing me a valuable practical perspective on any issue. I will be always grateful to them for embarking me on the PhD journey.

A great amount of this research has been done during visits at LAAS-CNRS and Politecnico di Milano. In that line, I would like to express my deepest gratitude to Prof. Christophe Louembet. I really appreciate the long scientific discussions we had in order to produce high quality content and research. I am also indebted to Prof. Franco Bernelli-Zazzera and Prof. James D. Biggs for introducing me to a thrilling new research topic and keep providing effective directions of improvement.

Next, I want to thank all my colleagues at the Department of Aerospace Engineering and Fluid Mechanics. Especially, my office partners: Alonso, Eulalia, Irene, Paco and Sergio for all the nice moments we have shared inside and outside work (who can forget our long talks, lunches and board gaming sessions). I would also like to mention the members of the aerospace engineering research group: professors Alfonso Valenzuela, Antonio Franco, Damián Rivas and Sergio Esteban, for their help and kindness.

From applied mathematics, Prof. Jorge Galán-Vioque deserves an special acknowledgement for providing me access to high-performance computing devices. His intervention speeded up the obtention of results.

Along these years, I have enjoyed quality time with quality people. I want to acknowledge the friends I did during the aerospace degree: Carmen, Fernan, Herrerías, Lobit, Lolo, Loren, Rafa and Pablo. Each one careers have put distance between us but I hope that our paths will cross as they had often done during the last four years. I would also like to mention my friends from my home town: Duque, Hernández and Paquito, for that, for just being there which is important. Let's keep stonks and rocking on gaming.

Por último, me gustaría agradecer enormemente a mi padre, mi madre y mi hermana. Sin su apoyo, cariño y dedicación no hubiera llegado este momento. Esta tesis es por vosotros.

Julio.

This page is intentionally left blank.

Published Research

The research of this PhD thesis has been funded by a PIF (Research Personnel Training) grant by Universidad de Sevilla through its V research plan. This work has also been partially funded by project REACH (PGC2018-100680-B-C21) financed by the Spanish Ministry of Science. These studies have been awarded with the XI Manuel Gayan Buiza prize which recognizes the excellence of PhD students research related with engineering. The following research works are fully included in this dissertation:

Journal papers:

1. Julio C. Sanchez, Rafael Vazquez, James D. Biggs and Franco Bernelli-Zazzera. Orbit-attitude predictive control in the vicinity of asteroids with in-situ gravity estimation. *Journal of Guidance, Control and Dynamics* (accepted for publication), 2021.

2. Julio C. Sanchez, Christophe Louembet, Francisco Gavilan and Rafael Vazquez. Event-based Impulsive Control for Spacecraft Rendezvous Hovering Phases. *Journal of Guidance, Control and Dynamics*, 44(10):1794-1810, 2021. doi:10.2514/1.G005507

3. Julio C. Sanchez, Francisco Gavilan, and Rafael Vazquez. Chance constrained Model Predictive Control for Near Rectilinear Halo Orbit spacecraft rendezvous. *Aerospace Science and Technology*, 100:105827, 2020. doi:10.1016/j.ast.2020.105827

4. Julio C. Sanchez, Francisco Gavilan, Rafael Vazquez, and Christophe Louembet. A flatness-based predictive controller for six-degrees of freedom spacecraft rendezvous. *Acta Astronautica*, 167:391-403, 2020. doi:10.1016/j.actaastro.2019.11.026

Conference proceedings:

5. Julio C. Sanchez, Rafael Vazquez, James D. Biggs, and Franco Bernelli-Zazzera. Guidance, navigation and control for asteroid orbit station-keeping with in-situ gravity estimation. In *11th International ESA Conference on Guidance, Navigation and Control Systems*, held online, June 2021.

6. Julio C. Sanchez, Christophe Louembet, Francisco Gavilan, and Rafael Vazquez. An Event-Triggered Predictive Controller for Spacecraft Rendezvous Hovering Phases. In *21st IFAC Symposium on Automatic Control in Aerospace*, Cranfield, United Kingdom, August 2019. doi:10.1016/j.ifacol.2019.11.076.

7. Julio C. Sanchez, Francisco Gavilan, Rafael Vazquez, and Christophe Louembet. A Flatness-Based Trajectory Planning Algorithm for Rendezvous of Single-Thruster Spacecraft. In *Networked and Autonomous Air and Space Systems*, Santa Fe, United States of America, June 2018. doi:10.1016/j.ifacol.2018.07.098.

Other Research Merits

The following publications describe additional research work done during the thesis that is related to a certain degree. Nevertheless, their content is not included for the sake of compactness in this dissertation body of research.

Conference proceedings:

8. Rafael Vazquez, Julio C. Sanchez, Jose M. Montilla, Jorge Galan-Vioque, Francisco Gavilan, Fernando Soler-Lanagran, Javier Rey-Benayas, Francisco A. Rodriguez-Lopez, Jan Siminski, Cristina Perez-Hernandez. Manoeuvre detection for near-orbiting objects. In *8th European Conference on Space Debris*, Darmstad, Germany, April 2021.
URL https://conference.sdo.esoc.esa.int/proceedings/sdc8/paper/238

9. Julio C. Sanchez, Francisco Gavilan, and Rafael Vazquez. A Predictive Guidance Algorithm for Autonomous Asteroid Soft Landing. In *Networked and Autonomous Air and Space Systems*, Santa Fe, United States of America, June 2018. doi:10.1016/j.ifacol.2018.07.080

Abstract

Universidad de Sevilla
Department of Aerospace Engineering and Fluid Mechanics.

Model Predictive Control Applications to Spacecraft Rendezvous and Small Bodies Exploration

by Julio César Sánchez Merino

The overarching goal of this thesis is the design of model predictive control algorithms for spacecraft proximity operations. These include, but it is not limited to, spacecraft rendezvous, hovering phases or orbiting in the vicinity of small bodies. The main motivation behind this research is the increasing demand of autonomy, understood as the spacecraft capability to compute its own control plan, in current and future space operations. This push for autonomy is fostered by the recent introduction of disruptive technologies changing the traditional concept of space exploration and exploitation. The development of miniaturized satellite platforms and the drastic cost reduction in orbital access have boosted space activity to record levels. In the near future, it is envisioned that numerous artificial objects will simultaneously operate across the Solar System. In that context, human operators will be overwhelmed in the task of tracking and commanding each spacecraft in real time. As a consequence, developing intelligent and robust autonomous systems has been identified by several space agencies as a cornerstone technology.

Inspired by the previous facts, this work presents novel controllers to tackle several scenarios related to spacecraft proximity operations. Mastering proximity operations enables a wide variety of space missions such as active debris removal, astronauts transportation, flight-formation applications, space stations resupply and the in-situ exploration of small bodies. Future applications may also include satellite inspection and servicing. This thesis has focused on four scenarios: six-degrees of freedom spacecraft rendezvous; near-rectilinear halo orbits rendezvous; the hovering phase; orbit-attitude station-keeping in the vicinity of a small body. The first problem aims to demonstrate rendezvous capabilities for a lightweight satellite with few thrusters and a reaction wheels array. For near-rectilinear halo orbits rendezvous, the goal is to achieve higher levels of constraints satisfaction than with a state-of-the-art predictive controller. In the hovering phase, the objective is to augment the control accuracy and computational efficiency of a recent global stable controller. The small body exploration aims to demonstrate the positive impact of model-learning in the control accuracy.

Although based on model predictive control, the specific approach for each scenario differs. In six-degrees of freedom rendezvous, the attitude flatness property and the transition matrix for Keplerian-based relative are used to obtain a non-linear program. Then, the control loop is closed by linearizing the system around the previous solution. For near-rectilinear halo orbits rendezvous, the constraints are assured to be satisfied in the probabilistic sense by a chance-constrained approach. The disturbances statistical properties are estimated on-line. For the hovering phase problem, an aperiodic event-based predictive controller is designed. It uses a set of trigger rules, defined using reachability concepts, deciding when to execute a single-impulse control. In the small body exploration scenario, a novel learning-based model predictive controller is developed. This works by integrating unscented Kalman filtering and model predictive control. By doing so, the initially unknown small body inhomogeneous gravity field is estimated over time which augments the model predictive control accuracy.

Resumen

Universidad de Sevilla
Departmento de Ingeniería Aeroespacial y Mecánica de Fluidos.

Aplicaciones del Control Predictivo Basado en Modelo al Rendezvous de Vehículos Espaciales y la Exploración de Cuerpos Menores

por Julio César Sánchez Merino

El objeto de esta tesis es el diseño de algoritmos de control predictivo basado en modelo para operaciones de vehículos espaciales en proximidad. Esto incluye, pero no se limita, a la maniobra de rendezvous, las fases de *hovering* u orbitar alrededor de cuerpos menores. Esta tesis está motivada por la creciente demanda en la autonomía, entendida como la capacidad de un vehículo para calcular su propio plan de control, de las actuales y futuras misiones espaciales. Este interés en aumentar la autonomía está motivado por el cambio del concepto tradicional de exploración y explotación espacial debido al desarrollo de nuevas tecnologías disruptivas. Estas son las plataformas satelitales miniaturizadas y la drástica reducción de los costes de puesta en órbita. Dichas tecnologías han impulsado la actividad espacial a niveles de record. En un futuro próximo, se prevé que un gran número de objetos artificiales operen de manera simultánea a lo largo del Sistema Solar. En tal caso, el control terrestre quedará desbordado en la tarea de monitorizar y controlar cada satélite en tiempo real. Es por ello que el desarrollo de sistemas autónomos inteligentes y robustos es considerado una tecnología fundamental por diversas agencias espaciales.

Debido a lo anterior, este trabajo presenta nuevos resultados en el control de operaciones de vehículos espaciales en proximidad. Dominar dichas operaciones permite llevar a cabo una gran variedad de misiones espaciales como la retirada de basura espacial, transferir astronautas, aplicaciones de vuelo en formación, reabastecer estaciones espaciales y la exploración de cuerpos menores. Futuras aplicaciones podrían incluir operaciones de inspección y mantenimiento de satélites. Esta tesis se centra en cuatro escenarios: rendezvous de satélites con seis grados de libertad; rendezvous en órbitas halo cuasi-rectilíneas; la fase de *hovering*; el mantenimiento de órbita y actitud en las inmediaciones de un cuerpo menor. El primer caso trata de proveer capacidades de rendezvous para un satélite ligero con pocos propulsores y un conjunto de ruedas de reacción. Para el rendezvous en órbitas halo cuasi-rectilíneas, se intenta aumentar el grado de cumplimiento de restricciones con respecto a un controlador predictivo actual. Para la fase de *hovering*, se mejora la precisión y eficiencia computacional de un controlador globalmente estable. En la exploración de un cuerpo menor, se pretende demostrar el mayor grado de precisión en el control que se obtiene con el aprendizaje del modelo.

Siendo la base el control predictivo basado en modelo, el enfoque específico difiere en cada escenario. En el rendezvous con seis grados de libertad, se obtiene un programa no-lineal con el uso de la propiedad *flatness* de la actitud y la matriz de transición del movimiento relativo Kepleriano. El bucle de control se cierra linealizando en torno a la solución anterior. Para el rendezvous en órbitas halo cuasi-rectilíneas, el cumplimiento de restricciones se garantiza probabilísticamente mediante la técnica *chance-constrained.* Las propiedades estadísticas de las perturbaciones son estimadas on-line. En la fase de *hovering*, se usa el control predictivo basado en eventos. Ello consiste en unas reglas de activación, definidas con conceptos de alcanzabilidad, que deciden la ejecución de un incremento de velocidad. En la exploración de cuerpos menores, se desarrolla un controlador predictivo basado en el aprendizaje del modelo. Funciona integrando un filtro de Kalman con control predictivo basado en modelo. Con ello, se consigue estimar las inomogeneidades del campo gravitario, lo que repercute en un aumento de la precisión del controlador predictivo basado en modelo.

Contents

1 Introduction 1
1.1 Motivation and challenges . . . 2
1.1.1 The push for autonomy . . . 3
1.1.2 Spacecraft proximity operations . . . 5
1.1.3 The role of model predictive control . . . 18
1.2 Objectives of the Thesis . . . 23
1.3 Solution approach . . . 25
1.4 Contributions . . . 26
1.5 Outline of the document . . . 28

2 Spacecraft dynamics 31
2.1 Translational motion . . . 32
2.1.1 Absolute motion . . . 32
2.1.2 Relative motion . . . 39
2.1.3 Thrust models . . . 49
2.2 Angular motion . . . 51
2.2.1 Attitude representation . . . 51
2.2.2 Rotational dynamics . . . 55

3 A six-degrees of freedom model predictive controller for spacecraft rendezvous 59
3.1 Rendezvous planning problem . . . 61
3.1.1 Objective function . . . 62
3.1.2 Constraints . . . 63
3.2 State transition matrix and attitude flatness . . . 65
3.2.1 Translational state transition . . . 65
3.2.2 Attitude flatness . . . 66
3.2.3 Equivalent rendezvous planning problem . . . 66
3.3 Optimal control computation . . . 67
3.3.1 Non-linear programming description . . . 67
3.3.2 Initial guess (warm-start) . . . 71
3.4 Linearized MPC scheme . . . 74
3.4.1 Linearized prediction model . . . 74
3.4.2 Linearized control program . . . 76
3.4.3 MPC scheme . . . 78
3.5 Numerical results . . . 80
3.5.1 Simulation model and controller parameters . . . 80
3.5.2 Cargo spacecraft . . . 81

3.5.3 Lightweight spacecraft 86

4 **Robust model predictive control for near-rectilinear halo orbits spacecraft rendezvous** **93**
4.1 Rendezvous planning problem 95
4.1.1 Objective function 96
4.1.2 Constraints 96
4.2 Rendezvous problem robustification 97
4.2.1 State transition 97
4.2.2 Gaussian additive disturbances 98
4.2.3 Robust rendezvous planning problem 99
4.3 Robust control computation 99
4.3.1 Chance-constrained implementation 100
4.3.2 Quadratic programming description 102
4.4 Robust MPC scheme with disturbance estimation 107
4.4.1 Robust control program 107
4.4.2 On-line disturbance estimator 108
4.4.3 Robust MPC scheme 109
4.5 Numerical results 111
4.5.1 Simulation model and controller parameters 111
4.5.2 Impulsive thrusters scenario 114
4.5.3 Continuous thrusters scenario 119

5 **Event-based impulsive control for spacecraft rendezvous hovering phases** **125**
5.1 Hovering phase control problem 127
5.2 Constrained periodic relative orbits 128
5.3 Analysis of the admissible set reachability 129
5.3.1 Instantaneous reachable set 130
5.3.2 Admissible set reachability 132
5.3.3 Admissible set proximity 135
5.3.4 Region of attraction to the admissible set 139
5.4 Event-based predictive controller 140
5.4.1 Single-impulse control law 141
5.4.2 Trigger rules 144
5.5 Invariance of the single-impulse approach 146
5.5.1 Well-posedness for hybrid impulsive systems 146
5.5.2 Invariance of the hybrid impulsive system 149
5.5.3 Invariance under the presence of continuous disturbances 158
5.6 Numerical results 159
5.6.1 Simulation model and controller parameters 159
5.6.2 Impact of the leader eccentricity 160
5.6.3 Impact of the impulse thresholds 168

6 Learning-based model predictive control in the vicinity of a small body 173
6.1 Orbit-attitude station-keeping problem 175
6.1.1 Frames of reference 175
6.1.2 Station-keeping problem 178
6.2 Navigation with in-situ gravity estimation 179
6.2.1 Unscented Kalman filter 179
6.2.2 Orbit filter 182
6.2.3 Attitude filter 185
6.3 Model predictive guidance and control 186
6.3.1 Guidance 186
6.3.2 Control 188
6.4 Learning-based guidance, navigation and control 194
6.4.1 Integrated GNC scheme 194
6.4.2 Gravity estimation with a satellite constellation 195
6.5 Numerical results 196
6.5.1 Simulation model, GNC parameters and performance indexes 198
6.5.2 Efficiency of nullifying the out-of-plane control 201
6.5.3 Learning-based MPC vs non-learning MPC 202
6.5.4 Gravity estimation with constellations of satellites . . . 214

7 Conclusions and future work 223
7.1 Conclusions 224
7.2 Future work 226

Bibliography 229

A B-splines 253

B Periodic orbits in the CRTBP 257

C Implicitization of trigonometric functions 261

D Global stable impulsive control for spacecraft rendezvous hovering phases 265

This page is intentionally left blank.

List of Figures

1.1 Commercial launch market share from 2015 to 2020. Reusable launchers are sliced. 3
1.2 Cubesats proximity operations. Credits: ESA. 7
1.3 Teardrop (*left*) and constrained periodic relative (*right*) orbits. 11
1.4 Orion approaching the Lunar Orbital Platform. Credits: NASA. 14
1.5 Comet 67P/Churyumov-Gerasimenko predicted shape (*left*) and image from Rosetta (*right*). Credits: ESA, NASA and Philippe Lamy. 16
1.6 Model predictive control illustration. 19
1.7 Diagram of the generic solution approach. 26

2.1 Classical orbital elements. 33
2.2 Inertial and LVLH frame for Keplerian-based relative motion . 42
2.3 Inertial, synodic and LVLH frames for RTBP relative motion . 47
2.4 Euler angles for $\{zxy\}$ sequence. 52

3.1 Illustration of a six-degrees of freedom spacecraft rendezvous. . 63
3.2 Line-of-sight region. 64
3.3 Random realizations for the trajectories of the cargo spacecraft. 83
3.4 Random realizations for the trajectories projection on the target orbital plane of the cargo spacecraft. 83
3.5 Computed impulses for the first random realization of the cargo spacecraft. 84
3.6 Attitude and angular velocity for the first random realization of the cargo spacecraft. 84
3.7 Reaction wheels angular momentum and its variation for the first random realization of the cargo spacecraft. 85
3.8 Random realizations for the trajectories of the lightweight spacecraft. 88
3.9 Random realizations for the trajectories projection on the target orbital plane of the lightweight spacecraft. 88
3.10 Computed impulses for the first random realization of the lightweight spacecraft. 89
3.11 Attitude and angular velocity for the first random realization of the lightweight spacecraft. 89
3.12 Reaction wheels angular momentum and its variation for the first random realization of the lightweight spacecraft. 90

4.1 Robust satisfaction of constraints. 100

4.2 Probability density function of the chi-square distribution with six-degrees of freedom. 101
4.3 Projection of the chaser relative trajectories in the xz plane for different initial NRHO locations. 114
4.4 Total ΔV for different initial target locations around the NRHO. 115
4.5 Chaser relative trajectories of the robust MPC for the impulsive scenario. 116
4.6 Projection of the chaser relative trajectories in the xz plane of the robust MPC for the impulsive scenario. 116
4.7 Impulse sequence for the first random realization of the robust MPC for the impulsive scenario. 117
4.8 Disturbance estimation for the first random realization of the robust MPC for the impulsive scenario. 118
4.9 Projection of the chaser relative trajectories in the xz plane of the non-robust MPC for the impulsive scenario. 118
4.10 Total ΔV and constraints satisfaction of robust and non-robust MPC for the impulsive scenario. 119
4.11 Chaser relative trajectories of the robust MPC for the continuous thrusters scenario. 120
4.12 Projection of the chaser relative trajectories in the xz plane of the robust MPC for the continuous thrusters scenario. 121
4.13 Control acceleration evolution for the first random realization of the robust MPC for the continuous thrusters scenario. 121
4.14 Disturbance estimation for the first random realization of the robust MPC for the continuous thrusters scenario. 122
4.15 Projection of the chaser relative trajectories in the xz plane of the non-robust MPC for the continuous thrusters scenario. . . . 123
4.16 Control effort and constraints satisfaction of robust and non-robust MPC for the impulsive scenario. 124

5.1 Examples of constrained periodic relative orbits. 128
5.2 Sketch of the in-plane instantaneous reachability and proximity. 138
5.3 Sketch of the region of attraction to the admissible set. 140
5.4 Geometry of the out-of-plane admissible set reachability over one period: reachable (*left*) and unreachable (*right*). 154
5.5 Out-of-plane region of attraction, dead-zone and admissible sets: non-existent dead-zone set (*left*) and existing dead-zone set (*right*).155
5.6 Geometry of the in-plane admissible set reachability over one period: reachable (*left*) and unreachable (*right*). 156
5.7 In-plane region of attraction, dead-zone and admissible sets: non-existent dead-zone set (*left*) and existing dead-zone set (*right*).157
5.8 Hovering phase trajectory for $e_0 = 0$. 162
5.9 Hovering phase trajectory for $e_0 = 0.2$. 162
5.10 Hovering phase trajectory for $e_0 = 0.4$. 162

5.11 Hovering phase trajectory for $e_0 = 0.6$. 163
5.12 Admissible set proximity indicators and triggered impulses for $e_0 = 0$. 163
5.13 Admissible set proximity indicators and triggered impulses for $e_0 = 0.6$. 164
5.14 Triggers of the event-based predictive controller for different initial eccentricities of the leader. 164
5.15 Satisfaction of the hovering region constraints for different initial eccentricities of the leader. 166
5.16 Number of impulses for different initial eccentricities of the leader. 166
5.17 Fuel consumption for different initial eccentricities of the leader. 167
5.18 Satisfaction of the hovering region constraints and fuel consumption for several minimum impulse bits. 169
5.19 Triggers of the event-based predictive controller for several minimum impulse bits. 170
5.20 Satisfaction of the hovering region constraints and fuel consumption for several saturation thresholds. 171
5.21 Triggers of the event-based predictive controller for several saturation thresholds. 171

6.1 Escape trajectory due to 433 Eros inhomogeneous gravity field. 175
6.2 Collision trajectory due to 433 Eros inhomogeneous gravity field. 176
6.3 Asteroid, body, inertial and orbital reference frames. 177
6.4 Monte Carlo (black), EKF (pink) and UKF (yellow) approaches for uncertainty propagation. 180
6.5 GNC scheme for a single spacecraft orbiting around the asteroid. 195
6.6 Gravity estimation with a satellite constellation. 196
6.7 Orbital radius for different initial inclinations. Blue: learning-based MPC; red: non-learning MPC; black: reference. 203
6.8 Average tracking error per day (*left*) and fuel consumption per day (*right*). Dots: learning-based MPC; triangles: non-learning MPC. 204
6.9 Semi-major axis (*left*) and eccentricity (*right*) for $i_0 = 90°$. Blue: learning-based MPC; red: non-learning MPC. 204
6.10 Control acceleration for $i_0 = 90°$. Blue: learning-based MPC; red: non-learning MPC. 205
6.11 Pitch, roll and yaw for $i_0 = 90°$. Blue: learning-based MPC; red: non-learning MPC; black: reference. 206
6.12 Control torque for $i_0 = 90°$. Blue: learning-based MPC; red: non-learning MPC. 207
6.13 Orbital radius of the initial polar orbit in the sensitivity analysis. Blue: learning-based MPC; red: non-learning MPC; black: reference. 208

6.14 Navigation errors in radial, tangential and normal position coordinates. 210
6.15 Orbit filter residuals of pixels and range. 210
6.16 Navigation errors in pitch, roll and yaw angles. 211
6.17 Attitude filter residuals of star-tracker MRP and gyroscope angular velocity. 212
6.18 Trajectories in the asteroid centered inertial frame of the 9 sats constellation. Black dots: surface landmarks. 215
6.19 Trajectories in the asteroid centered fixed frame of the 9 sats constellation. Black dots: landmarks. 216
6.20 Orbital radius (*left*) and inclination (*right*) of 9 sats constellation. 216
6.21 Pitch, roll and yaw of 9 sats constellation. 217
6.22 Orbit reference tracking index, fuel consumption (*left*) and second-order gravity parameters (*right*) of 9 sats constellation. Dashed:truth; solid:estimation; dot-dashed:1-σ uncertainty. 217
6.23 Relevant third-order (*left*) and fourth-order gravity parameters (*right*) of 9 sats constellation. Dashed:truth; solid:estimation; dot-dashed:1-σ uncertainty 218

A.1 B-splines cubic basis functions. 254
A.2 Example of a cubic B-spline function and its derivatives. 255

B.1 Lagrange points of the Sun-Earth system. Credits: NASA/WMAP Science Team. 258
B.2 Southern halos of the Earth-Moon L2. 260
B.3 Stability indexes and orbital periods for the southern halos of the Earth-Moon L2. 260

C.1 Result of the implicitization. 263

D.1 Sketch of the global stable controller convergence. 269

List of Tables

1.1 Characteristics of MPC, LQR and PID. 20

3.1 Array of thrusters for the cargo spacecraft. 81
3.2 Initial and terminal conditions for the cargo spacecraft. 82
3.3 Statistical properties of impulses mishaps for the cargo spacecraft. 82
3.4 Control accuracy in the terminal conditions for the random realizations of the cargo spacecraft. 85
3.5 Total ΔV of the initial guess, open-loop and closed-loop solutions for the cargo spacecraft. 86
3.6 Computational time and its percentage over the sampling interval of the cargo spacecraft. 86
3.7 Array of thrusters for the lightweight spacecraft. 86
3.8 Initial and terminal conditions for the lightweight spacecraft. . 87
3.9 Statistical properties of impulses mishaps for the lightweight spacecraft. 87
3.10 Control accuracy in the terminal conditions for the random realizations of the lightweight spacecraft. 90
3.11 Total ΔV of the initial guess, open-loop and closed-loop solutions for the lightweight spacecraft. 90
3.12 Computational time and its percentage over the sampling interval of the lightweight spacecraft. 91

4.1 Parameters of the target NRHO. 112
4.2 Statistical properties of impulses mishaps. 113
4.3 Statistical properties of the continuous acceleration mishaps. . 113
4.4 Computational time and its percentage over the sampling interval for the impulsive scenario 119
4.5 Computational time and its percentage over the sampling interval for the continuous thrusters scenario. 123

5.1 Event-based predictive controller computation times. 167
5.2 Cumulated computation times for the hovering phase. 168

6.1 Mass distribution of the satellite. 198
6.2 Sensors datasheet. 199
6.3 Guidance and control algorithm parameters. 200
6.4 Orbit control performance with and without nullifying the out-of-plane control. 202
6.5 Orbit control performance of learning-based MPC and non-learning MPC. 204

6.6 Attitude control performance of learning-based MPC. 205
6.7 Attitude control performance of non-learning MPC. 206
6.8 Average orbit control performance of the learning-based MPC and non-learning MPC for the sensitivity analysis. 208
6.9 Absolute navigation errors in position of learning-based MPC for $i_0 = 90°$. 209
6.10 Orbit filter residuals statistics of learning-based MPC for $i_0 = 90°$.211
6.11 Absolute navigation errors in pitch, roll, yaw and gyroscope bias of learning-based MPC for $i_0 = 90°$. 212
6.12 Attitude filter residuals statistics of learning-based MPC for $i_0 = 90°$. 213
6.13 Computational times and its percentage over the sampling interval of the GNC modules for the learning-based MPC for $i_0 = 90°$.213
6.14 Relevant second order gravity parameters estimation. 219
6.15 Relevant third order gravity parameters estimation. 220
6.16 Relevant fourth order gravity parameters estimation. 221

A.1 Control points for cubic B-spline. 254

Nomenclature

A	Asteroid fixed frame
a	Semi-major axis
$\mathbf{a}$	Acceleration
B	Body frame
$\tilde{C}_{nm}$	Normalized spherical harmonics of degree n and order m
$\mathbf{d}$	Vector of relative parameters
e	Eccentricity
$\mathbf{F}$	Force
$\mathbf{H}$	Angular momentum
I	Inertial frame
I_{sp}	Specific impulse
$\mathbf{J}$	Inertia matrix
$\mathbf{L}$	Local-vertical/local-horizontal frame
m	Mass
O	Orbital frame
$\mathbf{R}$	Rotation matrix
r	Orbital radius
$\mathbf{r}$	Absolute position with respect to a central body
$\tilde{S}_{nm}$	Normalized spherical harmonics of degree n and order m
S	Synodic frame
T	Orbital period
$\mathbf{T}$	Torque
t	Time
$\mathbf{u}$	Control acceleration

$\mathbf{x}$	State
$\boldsymbol{\alpha}$	Classical orbital elements
$\tilde{\boldsymbol{\alpha}}$	Modified equinoctial elements
$\Delta\mathbf{V}$	Velocity increment
μ	Standard gravitational parameter
ν	True anomaly
$\boldsymbol{\rho}$	Cartesian relative position
$\boldsymbol{\sigma}$	Modified Rodrigues parameters
$\mathbf{\Phi}$	State transition matrix
$\boldsymbol{\omega}$	Angular velocity

Chapter 1

Introduction

Hemos descubierto e redondeado toda la redondeza del mundo, yendo por el occidente e veniendo por el oriente.

Juan Sebastián Elcano

The Earth is the cradle for humanity but one can not stay in the cradle forever.

Konstantin Tsiolkovskii

I would like to die on Mars. Just not on impact.

Elon Musk

Contents

1.1 Motivation and challenges 2
  1.1.1 The push for autonomy 3
  1.1.2 Spacecraft proximity operations 5
  1.1.3 The role of model predictive control 18
1.2 Objectives of the Thesis 23
1.3 Solution approach 25
1.4 Contributions 26
1.5 Outline of the document 28

1.1 Motivation and challenges

Space exploration and exploitation plays a key role in advancing mankind's knowledge and technological capabilities in several disciplines. Space applications range from Earth observation, human presence in space, planetary defence, satellite based navigation, scientific discoveries and telecommunications amongst others. In the past, space operations have been solely carried out by a few public organizations (e.g. NASA, ESA, Roscosmos) which were the only ones possessing the capability to access space. Nonetheless, a significant number of private initiatives, with the aim of reducing costs and finding unexplored economic revenues, have arisen over the past decade [Genta14]. These new actors have consolidated their presence in the space sector under two fundamental pillars. Firstly, they have allowed a more universal access to space, low-Earth orbit in particular, by drastically lowering launch costs. This low-cost orbit insertion has been achieved by SpaceX through the use of scalable and reusable launchers [Reddy18]. Secondly, satellite architectures have evolved towards lightweight miniaturized platforms [Shkolnik18]. This minimalist concept allows mass production (suitable for megaconstellations) and turnkey solutions for non-expert space businesses. Consequently, the space ecosystem is evolving more rapidly than ever as private companies are also looking forward to expand their activity to extra-terrestrial destinations such as the Moon and Mars [Musk17].

Space agencies have also set their own plans for the 2020 decade. These include a permanent sustainable human presence on the Moon (Artemis program) [v.Ehrenfried20], asteroid deflection [Cheng18], novel space telescopes [Sabelhaus07], rotorcraft-based extraterrestrial exploration [Lorenz18] and the first active space debris removal [Forshaw20]. Specifically, Artemis is an ambitious crewed lunar exploration program relying on international cooperation. As such, International Space Station partners will build, assembly and operate a space station in cislunar space, namely the Lunar Orbital Platform-Gateway (LOP-G) [Merri18]. To this end, NASA is finishing its new super-heavy lift vehicle, the Space Launch System, capable of sending between 26 to 45 tonnes on a trans-lunar injection. These plans are deemed critical in expanding human presence to the Moon, Mars and deeper in the Solar System.

Under the previous scenario, it is evident that reducing costs and resources allocation, without a loss of safety, is desirable to both maximize the taxpayers investments return and augment commercial applications competitiveness. In that sense, several disciplines such as autonomous systems, electric propulsion, materials science, observation devices and space farming, amongst others, are expected to provide breakthroughs, thus enabling novel mission concepts. In particular, this dissertation concerns autonomous systems for proximity operations. This topic is of special relevance to space exploration and exploitation needs as close distance operations enable a considerable number of the aforementioned missions (e.g. space station supplying, on-orbit assembly, small bodies exploration, etc.).

1.1.1 The push for autonomy

In the context of space operations, autonomy refers to the spacecraft capability to compute its own control sequence. The dawn of space exploration in 1950s-1960s focused on sending humans to Earth orbit and the Moon as a consequence of the space race between the Soviet Union and United States. At the same time, the use of cheaper and less risky robotic missions was necessary to understand the environment that manned missions will be facing as well as reaching further celestial bodies .

After completion of the Apollo program in the 1970s and the Soviet Union collapse in 1991, public interest and international competition in manned space exploration diminished over time. Nonetheless, human presence in space was maintained by building and operating low-Earth orbit space stations. In parallel, robotic missions achieved numerous successes with flybys to all Solar System planets, in-situ exploration of Mars and space station resupplying.

The cancellation of the Space Shuttle program in early 2010s left the United States superpower without the capability of putting astronauts into orbit from its own soil. However, this fact boosted private companies to search for new ways of reducing the cost of orbit insertion. In particular, SpaceX achieved a significant breakthrough by demonstrating the autonomous recovery of its launchers first stages. This technology achievement, in terms of autonomy, has allowed reusable launchers providers to dominate the commercial launch market from the past three years (a 57% of launches in 2020) as it can be seen in Fig. 1.1.

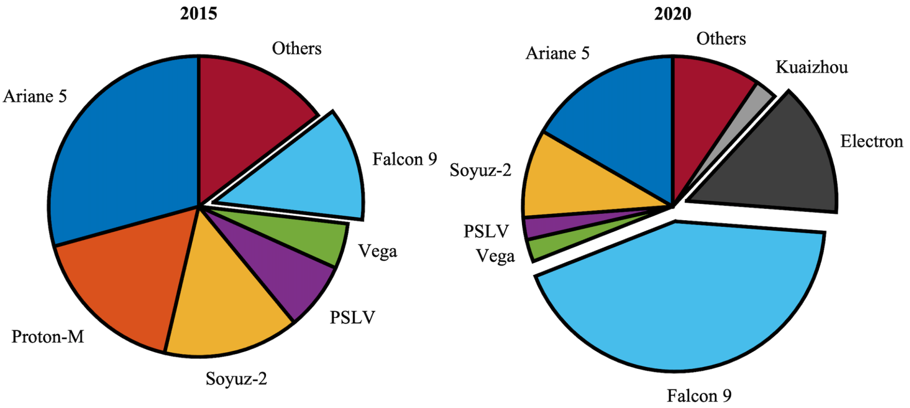

Figure 1.1: Commercial launch market share from 2015 to 2020. Reusable launchers are sliced.

In spite of an historical record with significant successes (e.g. Apollo guidance autopilot), autonomous space operations have also suffered several recent anomalies with a dramatic spacecraft loss in some cases. In 2005, the autonomous proximity operations demonstrator DART ran out of fuel and collided with its target telecommunications satellite [NASA07]. In 2009, the active satellite Iridium 33 and the defunct one Kosmos-2251 collided creating a huge cloud of debris. The automated collision assesment system failed to raise a high-risk impact alert because non-suitable orbital information was being used [Kelso09]. In 2016, the Schiaparelli module failed to autonomously land in Mars, thus crashing with the surface after a free fall from a 3 km altitude. Due to gyroscopes saturation coupled with on-board navigation data, an incorrect altitude prediction was made and the thrusters were fired prematurely [Tolker-Nielsen17]. The real possibility of failure during autonomous missions causes mission planners to frequently opt for ground-in-the-loop interventions for maneuvers executions.

Autonomous spacecraft maneuvering was considered a key enabling technology for most of NASA missions during the period 2013-2022, [NRC11]. Specifically, most of them are related with proximity operations around artificial bodies (e.g. satellites, space stations, debris, etc.) and Solar system bodies (e.g. asteroids, comets, etc.). In some cases, the need for autonomy arises due to the mission physical constraints. A good example is the Mars landing sequence where the 26 minutes lag due to two-way signal communication with Earth is greater than the seven minutes of atmospheric entry. This causes Mars entry, descent and landing operations to be fully autonomous. Similarly, close proximity operations around bodies, many of which are beyond Mars orbit, also require autonomous control due to the aforementioned transmission delay. In other cases, the demand for higher autonomy levels can be derived from the need to increase mission frequency, robustness and reliability. This mainly includes low Earth orbit missions such as autonomous rendezvous and docking and autonomous inspection and servicing. These needs are a direct consequence of the increasing commercialization of space that has been previously mentioned. The increasing mission frequency will made ground-in-the-loop guidance and control very prohibitive due a high number of conflicts and maintenance works. Moreover, the chances for human error will increase as well. In that sense, [Starek16] declares that spacecraft autonomy can overcome such drawbacks by enabling greater numbers and types of missions while augmenting robustness and reducing risks. In turn, this will increase future commercial and scientific return for space.

An autonomous guidance and control system is defined in [Starek16] as having the capability to compute its own control commands on-board. It is also convenient to distinguish between guidance and control. Guidance usually refers to the determination of an optimal open-loop plan to transfer a vehicle from an initial to a final destination. The control module closes the loop by counteracting the deviations to the guidance plan, thus assuring the final destination is reached. Consequently, because it has to be computed on-board while the plan is being executed, the control module is required to be fully autonomous in the majority of cases. This causes that the control algorithm has constraints on its execution times. On the other hand, the guidance plan admits the possibility of being computed by Earth operators and uploaded to the spacecraft before commencing the operation. In any case, to be autonomous, the full guidance and control system should fulfil the following requirements.

- **Efficient:** given that a feasible control solution exists, the optimal one is desired.
- **Real-time implementable:** control algorithms must be implemented and executed in on-board processors in a reasonable amount of time.
- **Verifiable:** there should exist design metrics accurately describing the performance and robustness under disturbances of guidance and control algorithms.

1.1.2 Spacecraft proximity operations

As stated before, guidance and control for relative motion is the most prominent example of autonomy needs. Mastering proximity operations enables several space activities such as active space debris removal [Sasaki19], asteroid mining [Hein20], collision avoidance maneuvers [Lee18], on-orbit assembly [Underwood15], satellite inspection [Bridges13] and space station resupplying [Souza07] amongst others. Due to its practical applications and its autonomy needs, spacecraft control in proximity operations is a topic with a vast and rapidly evolving literature.

The initial demands for proximity operations began due to the Apollo program. In order to reduce the payload mass, thus reducing launcher power needs, the idea of lunar orbital rendezvous was conceived [Neufeld08]. This concept was based on separating command and lunar modules when Moon's orbit is acquired. Then, the lunar module descends and lands on the Moon's surface while the command module remains on Moon's orbit. Once lunar surface operations are finished, the lunar module ascends to Moon's orbit where it rendezvouses and docks with the command module. Finally, the lunar module is discarded and left in Moon's orbit. Splitting the required hardware into a main spacecraft and a small lunar lander avoids to carry dead weights at several mission stages, thus saving payload mass.

However, at the time when the concept of lunar orbital rendezvous was proposed in the early 1960s, no other mission have achieved successful rendezvous and docking (not even in geocentric orbit). With the purpose of testing the feasibility of this solution, NASA conceived the Gemini project. One of the Gemini project goals was to demonstrate rendezvous and docking between two vehicles on Earth's orbit. Due to this sudden interest in proximity operations, the initial work of [Clohessy60] described the relative dynamics between two vehicles in orbit assuming Keplerian motion being one of them placed in a circular orbit. This led to the simplified Clohessy-Wiltshire equations. Afterwards, [Tschauner65] extended the previous model to two vehicles evolving in Keplerian elliptic orbits. Both [Clohessy60, Tschauner65] assumed the vehicles separation distance negligible with respect to the leader's semi-major axis, thus yielding linear relative models.

After the completion of the Apollo program, spacecraft proximity operations, such as rendezvous and docking, continued playing a vital role in low Earth orbit space activities. A good example of this is the International Space Station (ISS) which has rendezvoused a considerable number of times with the Automated Transfer Vehicle, the Dragon, the Progress, the Space Shuttle and the Soyuz amongst other spacecraft. Nonetheless, as mentioned before, proximity operations needs are expanding quickly to other activities and environments. In that sense, the following proximity operations of current interest (aligned with the previously mentioned space operational environment) are identified: automated rendezvous for cubesats, on-orbit inspection, cislunar space rendezvous and small bodies exploration. Each of these fields will be subsequently expanded with their own state-of-the-art analysis within the literature.

Cubesats revolution

Cubesats and, in a broader way, lightweight satellites (see Fig. 1.2) have emerged in the last decade as a low-cost alternative to traditional bulky satellites in some space activities (e.g. Earth observation [Foster17]). These miniaturized architectures are specially suitable for megaconstellation applications [delPortillo19], such as global satellite-based internet, as they can be mass produced and deployed in large numbers from a launcher. However, the hardware of their attitude and orbit control systems is usually minimalist due to its reduced and low-cost concept.

In the proximity operations domain, cubesats have the potential to provide affordable satellite servicing (inspection and refuelling), justified by the gain in extended mission lifetime of the serviced satellite. This presents a disruptive change in the space operational environment as the servicing concept is nowadays restricted to vital missions such as the ISS or the Hubble telescope. This restriction comes from the fact that only bulky and heavy cargo spacecraft possess rendezvous capabilities [Fehse03], thus precluding its use in a daily basis due to the high operational cost.

Nonetheless, cubesats-alike architectures do not possess autonomous rendezvous and docking capabilities. Efforts are being streamlined in that direction. Specifically, NASA is planning the Cubesat Proximity Operations Demonstration (CPOD) mission [Bowen15]. This mission will deploy two 3U cubesats of 5 kg equipped with high performance processors, imaging and GPS based navigation sensors, multi-thruster cold gas propulsion system and three-axis attitude determination and control. The on-orbit test proximity scenarios involve maintaining along-track formation, circumnavigation and docking as well as increasing and decreasing relative distance. For some scenarios, one of the cubesats will not cooperate thus validating this concept for on-orbit servicing scenarios.

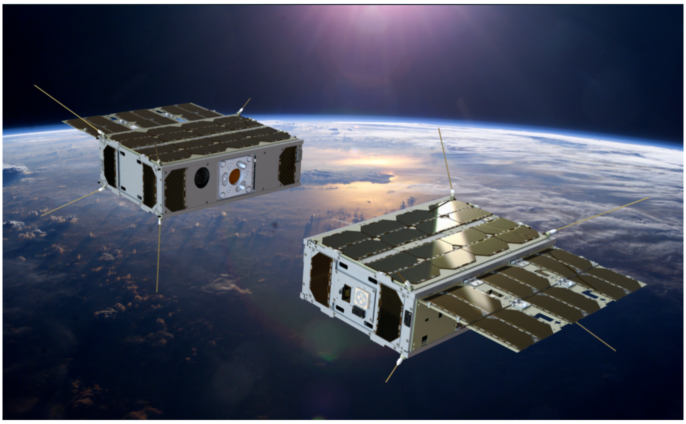

Figure 1.2: Cubesats proximity operations. Credits: ESA.

The spacecraft control literature has been aware of the previous facts. One of the major problems flagged, concerning cubesats automated rendezvous and docking, is a probable lack of thrusters to exert three-axis orbit control independently of their orientation. Attitude free orbit control can be ideally achieved considering an orthogonal array of three pair of thrusters (being the ones in the pair in opposite directions). This requires a minimum of six thrusters which could be prohibitive for small satellites configurations as most of them does not even have thrusters. The few cubesats with propulsive capabilities typically have one or two thrusters and adjust their orientation with reaction wheels or magnetorquers.

Consequently, for the majority of current small satellites with orbit control capabilities, autonomous spacecraft rendezvous has to be achieved by means of thrust-vectoring during the maneuver. That is, the attitude control system has to act perform reorientation maneuvers in order to point the thrusters at the commanded orbit control directions. As such, the attitude and orbit control subsystems will be mutually coupled. This is a considerable difference from traditional rendezvous maneuvering where the attitude control system just compensates gravity-gradient and orbit control parasitic torques.

The previous issue has raised a considerable number of works developing six-degrees of freedom (6-DOF) controllers for proximity operations. References [Filipe15] developed feedback-based adaptive tracking control for rendezvous while [Wang12] applied the same approach for flight-formation. Both works made use of dual quaternions as an orbit-attitude joint parameterization. Backstepping control has been by several authors [Kristiansen08, Zhang12, Yan16] as the attitude controller is mastered by orbit control needs. Reference [Zhang12] also proposed an unusual six-thrusters cuboid layout capable of providing simultaneous orbit-attitude control. Sliding mode control was considered by [Terui98] to capture a tumbling piece of debris. Alternatively, [Biggs18] employed quaternion-based covering maps to address 6-DOF motion planning using basis functions and closed-loop kinematic feedback.

As the attitude control requirements answer to orbit control needs, the works of [Naasz03, Wu09, Siva13, Moon16, Zhang20], concerning spacecraft rendezvous and flight-formation, divided the problem into two distinct stages. Firstly, they compute the required orbit control sequence which generates thrusters orientation requirements. This computation has been done via linear-quadratic regulators (LQR) [Wu09, Moon16], convex optimization [Siva13] or particle swarm optimization [Zhang20]. These works considered a number ranging from one to four thrusters combined with non-reactive attitude actuators such as control moment gyroscopes, magenetorquers and reaction wheels.

Still, the previous approaches have some drawbacks. Feedback-based and backstepping control are unable to guarantee path constraints satisfaction as usual for proximity operations (e.g. approach corridors, collision avoidance, safe zone). Sliding mode control is possibly an overconservative approach as the controller follows a predefined surface. The problem decomposition into two-stages seems a more natural solution, accounting for the different nature of orbit and attitude controllers. However, the orbit control demands may be unfeasible for attitude control capabilities, thus causing actuator saturation which can eventually degrade orbit performance as the right orientations are not achieved. This degradation can be avoided if both problems are again integrated, thus considering integrated orbit-attitude planning.

The problem of thrusters vectoring is an attitude reorientation planning problem. Reference [Leve15] defined two-dimensional reorientation profiles considering limitations up to the jerk (desirable for the case of flexible structures). Linearized model predictive control (MPC) was employed for attitude station-keeping purposes in [Hegrenæs05, Guiggiani15] though . The fact that attitude dynamics has the flatness property (see [Fliess95]) was exploited [Louembet09, Caubet15] to transform the non-linear continuous dynamics to algebraic relations. This way, states and control can be parameterized and embedded in an optimization problem to obtain optimal parameters values.

The conclusion is that achieving autonomous rendezvous and docking for small satellites requires six-degrees of freedom control. The literature review suggests an integrated orbit-attitude control framework could potentially improve state-of-the-art works in terms of safety and control performance. To this end, attitude reorientation works should be revisited. Six-degrees of freedom control is not only applicable for small satellites orbit operations as it has also received attention to geostationary satellites station-keeping [Weiss15b] and solar sailing [Gong09].

On-orbit inspection

The concept of spacecraft inspection was initially conceived, in the early phases of the space race, as a mean to survey potential space weapons from the other superpower (United States/Soviet Union). This urgent need was soon partly diffused as, in 1967, the Outer Space Treaty succeeded in compromising space nations to not place mass destruction weapons in orbit and make a peaceful use of space. In the last two decades, renew interest in achieving on-orbit inspection capabilities has been put for both civil and military reasons.

Nowadays, space powers posses large networks of observation stations capable of taking infrared, optical and radar surveillance data from a considerable number of objects and events [Butkus07]. However, ground-based sensors are limited by atmosphere conditions, distance and relative geometry with respect to the objects. Specifically, current imaging capabilities are very limited beyond low Earth orbit and can be disrupted by both weather and lighting conditions.

The previous ground-based imaging limitations and the increasing number of strategical space assets such as the ISS and global navigation satellite systems, motivates the need to verify the normal functioning of these (debris/micrometeroids impact assessment, materials oxidation). From a military point of view, recent 2020 reports[1] pointed out that a pair of Russian satellites were allegedly tailing a United States spy satellite. As such, on-orbit inspection capabilities are again appealing to the military as a way to inspect suspected unfriendly satellites.

Due to the military potential of on-orbit inspection, most of the demonstration missions and attempts have remained classified to the general public. One of the known demonstrations consisted of a nanosatellite equipped with a camera to inspect the ISS [Fredrickson03]. Furthermore, the United States Air Force Laboratory has possibly carried out similar technology demonstrations missions as well [Madison00].

The initial on-orbit inspection requirement was to maintain ranging distance and bearing with respect to the inspected satellite. However, this was highly stringent, as [Tschauner65] showed that relative Keplerian dynamics are generally unstable. Frequent counteraction maneuvering has a prohibitive cost in terms of fuel consumption. To relax the previous needs, the hovering operation concept was conceived. Spacecraft hovering refers to maintain the inspector within a position volume with respect to the inspected satellite[Hope03]. Due to this definition, hovering also applies to spacecraft rendezvous missions where there are hold-on phases awaiting mission control authorization to continue reducing the relative distance [Fehse03].

In the literature, the hovering problem was firstly studied in the context of small bodies exploration [Sawai02, Broschart05]. As such, maintaining an exploration probe flying over the same small body region allows to take high resolution images of its surface. In the 2000s decade, the United States Air

---

[1] https://www.space.com/russian-spacecraft-stalking-us-spy-satellite-space-force.html

Force translated the problem to geocentric missions under Keplerian-based relative dynamics [Tschauner65]. Its main focus was to derive fuel-efficient hovering control methods [Irvin07] as fuel is a non-renewable resource in space.

The hovering problem literature, under Keplerian assumptions, have used two distinctive approaches: teardrop orbits (also known as the pogo method) and constrained periodic relative orbits. The first method allows to intuitively design the orbit based on simple geometrical principles which is very appealing for Earth-based operators. However, an impulsive control has to be exerted periodically. The latter method exploits the Keplerian relative motion, by cancelling the unstable mode, which allows to maintain naturally (control free) the relative formation.

The initial works on fuel-efficient hovering control were based on the concept of teardrop orbits [Hope03, Irvin07, Irvin09]. A teardrop orbit is a natural relative trajectory portion within the hovering volume (see the left image of Fig. 1.3). This orbit has also the distinct property of intersecting itself at the volume frontier, thus being closed. A single-impulse has to be applied at this intersection to bounce back the satellite to the teardrop orbit. This method has also been named as pogo [Hope03].

The pogo method presents advantages and drawbacks. Its main advantage is that teardrop orbits can be constructed analytically and its design parameters have intuitive physical meaning (distance from leader, size, teardrop period). Nonetheless, two main drawbacks can be argued. Firstly, the teardrop orbits repetition pattern is only possible if the leader's orbit is circular, thus Clohessy-Wiltshire linear time invariant equations [Clohessy60] are used. Finally, a single-impulse control has to be periodically applied each time the spacecraft intersects with the volume frontier. This may impose an upper limit to the duration of the inspection.

Recent works have tried to diminish the previous concerns within the pogo formulation. Reference [Prince18] employed particle swarm optimization to find the minimum fuel consumption teardrops subject to time and geometrical bounds. The method was extended in [Bai20] to account for leader elliptical orbits, thus resulting in a time-varying pattern of teardrops envelope. Closed-loop control against J2 perturbation drift was considered in [Han20] under the combination of natural drift arcs and constant thrust arcs smoothing the bouncing instant.

The stability analysis of the Keplerian linear relative motion reveals the existence of periodic relative orbits around the leader spacecraft [Inhalan02]. Specifically, if the reference orbit is circular, a keep-out safe ellipsoid around the target can be established [Gaylor07]. In that spirit, [Deaconu12a] presented a semi-definite programming (SDP) method to compute relative periodic orbits within a fixed volume. As these constrained periodic orbits are natural (see the right image of Fig. 1.3) the fuel consumption is theoretically null. Then, when compared with teardrop orbits, the constrained periodic relative orbits always reduce fuel consumption needs by design.

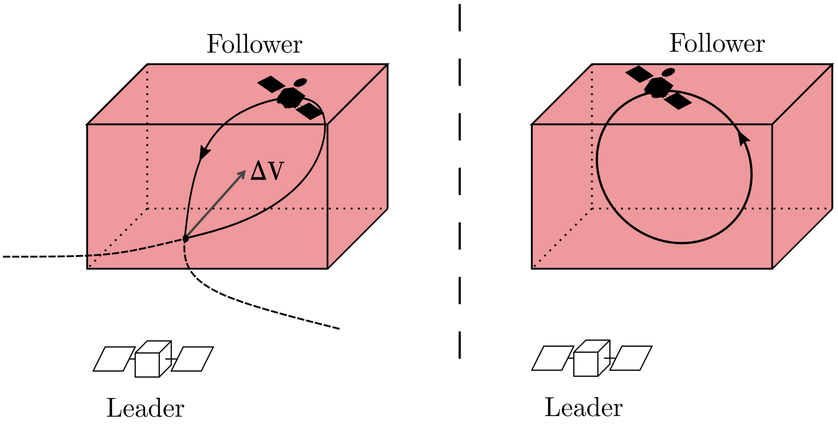

Figure 1.3: Teardrop (*left*) and constrained periodic relative (*right*) orbits.

Still, the constrained periodic relative orbits are more cumbersome to compute and less intuitive geometrically than teardrops. Constrained periodic orbits were further parameterized in [Deaconu13] through the vector of parameters. Parameterizing the relative periodic orbits was also considered in [Bennet16]. The vector of parameters substitutes the cartesian state establishing a periodicity state as well as providing insight into the orbit size, shape and offset distance from the leader. The previous work was extended in [Deaconu15] to solve the guidance problem towards a constrained periodic trajectory and orbital rendezvous under safety constraints. The latter one employed the concept of non-periodic constrained relative orbits. As mentioned before, the use of natural constrained periodic relative orbits does not require any control effort being an invariant set from the fuel consumption perspective.

Even under the vector of parameters it is not possible to directly check the membership of a relative state to the constrained periodic relative orbits set. An algebraic description of the previous set in terms of multivariate polynomials was provided by [Arantes-Gilz15]. Closed-loop controllers stabilizing the constrained periodic relative orbits set were designed by [Deaconu12b, Arantes-Gilz19]. Specifically, [Arantes-Gilz19] achieved global stabilization, under linear assumptions, through a three-impulsive sequence. Constrained relative orbits also admits non-periodical forms [Deaconu15], though these are only guaranteed to be within the hovering region for a finite period of time. As such, they are not appealing for hovering purposes as their periodic counterparts.

The previous vector of parameters approach has also some drawbacks. Specifically, just checking if a relative periodic orbit is within the hovering region was computationally cumbersome. Initially, a semi-definite programming problem has to be solved. By noticing that the hovering constraints were linear in the Cartesian space (if the hovering region is a cuboid) [Arantes-Gilz15] implicitized the previous linear constraints with respect to the true anomaly. The outcome is a formal description, purely state- dependent, of the hovering admissible set. The admissible set is composed of all the relative constrained periodic orbits. In a further work [Arantes-Gilz19], the formal description of the admissible set is exploited in order to design a global stable controller to the hovering region based on the periodical application of a three-impulses sequence.

Closed-loop control of periodic relative orbits has been addressed by means of global stabilization. This is suitable in order to perform an approach phase, in the proximity domain, to the constrained periodic orbits set. However, once the spacecraft is inserted in this set, it may not be accurate and efficient for station-keeping purposes. In the spirit of the pogo method, the constrained periodic relative orbits set could be bounced (note this is different with respect to volume frontier bouncing). To this end, event-based control [Aström08], which activates control based on a set of trigger rules, seems a promising technique for the hovering phase problem.

The previous literature focuses in hovering a leader object for inspection or a hold phase of a proximity maneuver (e.g. rendezvous). In that line, collision avoidance between the leader and follower is passively ensured by the design of the hovering region (e.g. by moving the cuboid along the in-track direction). For safety reasons, the hovering region should not include the origin if a physical object is hovered (it may be also the case where an artificial point in space is hovered, thus the origin can be included). The consideration of ultra-close proximity operations which requires an active control design for obstacle avoidance [Richards02] is out of the scope of this dissertation.

The expansion to cislunar space

In the 2020s decade, humans are expected to return to the Moon under the Artemis program [v.Ehrenfried20]. A vital part of these plans is the LOP-G which is an outpost around the Moon to support human and scientific exploration in deep space. Where to place the LOP-G requires an assessment of different criteria such as reachability from Earth (through the Space Launch System or the Falcon Heavy), lunar surface accessibility, station-keeping needs, communications with Earth and thermal environment. In [Whitley16], several LOP-G orbits were assessed according to previous figures of merit. The analyzed possibilities were lunar Keplerian orbits, lunar frozen orbits and Earth-Moon system periodic orbits.

Lunar Keplerian orbits provide the most faster and fuel efficient lunar surface access. However, due to its proximity with respect to the Moon's gravity dwell, low lunar orbits cannot be directly acquired by the Space Launch System (nor possibly the Falcon Heavy). This could be fixed by considering high apolune elliptic orbits but their station-keeping costs are very prohibitive

($>$ 300 m/s per year). Lunar frozen orbits, which maintain some motion parameters invariant in average, reduce the station-keeping demands to $\approx$ 0 m/s per year. In any case, Keplerian lunar orbits suffer frequent line-of-sight occultation with the Earth, thus making impossible continuous communication.

The Earth line-of-sight occultation can be totally avoided by some types of periodic orbits arising in the Earth-Moon restricted three-body problem (RTBP). These types are the halo and distant retrograde orbits, being both of them accessible by the Space Launch System and its embarked Orion capsule. Distant retrograde orbits appear to orbit the Moon in a retrograde manner with a slight inclination with respect to the Earth-Moon motion plane. Nonetheless, they are very far from the Moon, thus complicating lunar surface access in terms of time and cost. Most of the halo orbits (higher inclined) suffer the same drawbacks but amongst them, there is a small subset named near-rectilinear halo orbits (NRHOs) characterized by a resilience against the natural instability of halos [Zimovan17].

Near-rectilinear halo orbits visually appear to be nearly polar orbits with a close perilune passage ($\sim 3000 - 17000$ km), thus allowing lunar surface access travel in half a day. Combined with reasonable station-keeping costs ($\approx$ 10 m/s per year) they are deemed as the best option to place the LOP-G [Whitley16]. As a matter of fact, the final destination would be a southern L2 Earth-Moon NRHO with a 4:1 or 9:2 orbital period relation with respect to the Moon synodic period. These resonances prevent the occultation of the solar panels. The southern election would also allow large observation periods for the lunar south pole, where there are evidences of ice [Hayne15], when it is flew over at the orbit apolune.

In view of the previous plans, it is clear that a considerable number of space operations will take place in cislunar space where RTBP dynamics are dominant (see Fig. 1.4 for a practical application). This constitutes an unexplored operational scenario in terms of proximity operations where the vast majority of the applications has taken place in Keplerian geocentric or lunar orbits.

The RTBP, and more precisely the circular restricted three-body problem (CRTBP), has been a very active topic in spacecraft interplanetary optimization. The three-body problem periodic orbits are surrounded by stable and unstable invariant manifolds [Koon06] which naturally makes a spacecraft escape or approach them. In [Gomez04], the concept of connecting invariant manifolds, to freely travel between orbits, was proposed. As such, low energy interplanetary transit through invariant manifolds was exploited in the literature [Topputo05, Davis11, Chupin17].

Invariant manifolds connections were considered for rendezvous purposes by [Sato15]. However, it was evidenced that if the vehicles were too close, that is the case for proximity operations, relative-based guidance and control was more fuel-efficient. This suggests that RTBP proximity shall be treated in a similar way as Keplerian-based operations. The transition from Keplerian-based to RTBP relative motion is not straightforward. The main arising difficulty is

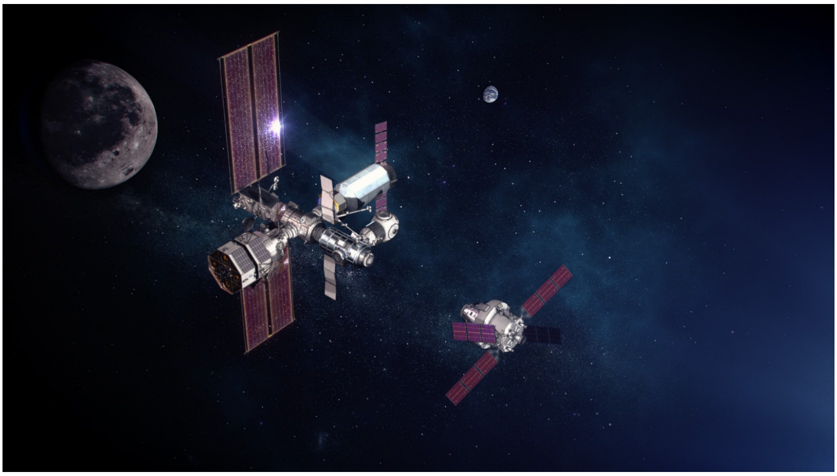

Figure 1.4: Orion approaching the Lunar Orbital Platform. Credits: NASA.

that RTBP periodic orbits are expressed numerically instead of having closed forms such as elliptical and circular Keplerian orbits.

Due to the numerical nature of the potential reference orbits, it was realized that achieving analytical solutions of the RTBP relative dynamics (in the same way as [Yamanaka02] provides a closed-form solution for Keplerian-based relative motion), even for the linear case, was not possible. Consequently, [Murakami15] realized solving RTBP linear relative motion would have to be done through the numerical integration of the state transition matrix (STM). A semi-analytical method based on an analytical approximation of the periodic orbit was developed in the PhD thesis [Conte19]. Still, numerical integration is required and the gain in computational time (~ 0.5 s) may not be worthy when compared to accuracy degradation which highly depends on the specific orbit.

In contrast to the Keplerian relative motion scenario, three-body problem close rendezvous strategies have not been extensively considered. The works of [Bucci18, Lizy-Destrez19] provided insight on how establishing hold-on points through the line-of-sight (LOS) corridor could allow passive safety trajectories (though they are not a-priori computed). It was also evidenced that expressing the relative motion in the RTBP synodic frame hampers the line-of-sight constraint. This issue was eased by [Franzini17, Franzini19a] works where the RTBP relative dynamics were expressed in a local-vertical/local-horizontal frame moving with the target orbit. Using the previous frame [Franzini19b] computed glideslope (V-bar, R-bar) and multi-impulsive rendezvous trajectories.

The applied control approaches to RTBP automated rendezvous are very simple in comparison to the employed in the Keplerian case. This literature gap is to be expected as its practical application of the LOP-G scenario was recently announced. Moreover, the numerical nature of RTBP orbits makes difficult to carry out rapid analyses. Fortunately, the extensive literature of Keplerian-based proximity operations can be of help. Unsurprisingly, passive safety trajectories [Breger08] and glideslope approaches [Ariba16] are inherited concepts of Keplerian-based rendezvous. In that spirit, robust control RTBP rendezvous seems a natural extension to the existing works. For that purpose, the works in robust control of [Gavilan12, Louembet15, Mammarella18] may be revisited.

The Artemis program has fostered calls for innovation in other spacecraft operations rather than the proximity domain. As such, NRHO station-keeping has been studied by [Bucci17, Guzzetti17, Newman18, Tos20, Muralidharan20]. Reference [Tselousova19] designed direct transfers from the Earth to NRHOs in cislunar space. Similarly, [Trofimov20, Lu21] built transfers from NRHOs to low lunar orbits and lunar surface. Moreover, NRHOs and lunar exploration is also a breeding ground for cubesats (LUMIO project [Speretta18]) which can be designed to carry out specific scientific activities.

Small bodies exploration

Small bodies such as asteroids, comets and dwarf planets are increasingly becoming a common destination for space missions. Studying these primitive bodies enable a deeper understanding of Solar System history and planetary processes. Additionally, asteroids can boost space travels as some concepts suggest their internal water could be extracted and converted into fuel [Zacny13].

The first mission to ever orbit and land an asteroid was the Near Earth Asteroid Rendezvous (NEAR) mission in 2001 [Holdridge02]. The NEAR Shoemaker visited 433 Eros which is the second-largest near-Earth object. This pioneering mission demonstrated the feasibility of small bodies exploration in proximity. This legacy continued with more missions in the 2010s decade. In 2010, JAXA's Hayabusa mission achieved sample-return from 25143 Itokawa [Yoshikawa15]. In 2014, ESA's Rosetta mission, composed of an orbiter and a small lander, rendezvoused and landed in comet 67P/Churyumov-Gerasimenko [Glassmeier07]. Some years later, NASA's Dawn mission visited and orbited two extra-terrestrial destinations [Russell11]: the asteroid 4 Vesta and the dwarf planet Ceres.

Since then, more missions have been recently executed while others are being planned. For example, JAXA's carried out a second sample-return mission (Hayabusa2) to asteroid 162173 Ryugu. The probe returned to Earth in late 2020. NASA OSIRIS-REx mission has also stowed samples of asteroid 101955 Bennu and will come back to Earth in 2021. In the 2020s decade there will be missions such as Lucy which will visit Jupiter's Trojan asteroids, Psyche which will visit the metallic asteroid with the same name and DART which will carry out an asteroid deflection test in 65803 Didymos [Cheng18]. To assess the effectiveness of the impact, a subsequent mission, named Hera, will survey the asteroid.

Operations in the vicinity of small bodies are challenging due to the dominance of their inhomogeneous gravity fields [Ceccaroni13]. Consequently, the dynamical response, in the asteroid proximity, could lead to collision and escape trajectories [Scheeres12]. Accordingly, active control has to be considered in order to station-keep a closed orbit, thus avoiding collisions and escapes. As in the lunar case, station-keeping fuel consumption can be reduced through frozen orbits [Lei19]. Similarly to RTBP orbits families, [Doedel03], periodic orbits can also be computed for inhomogeneous gravity fields [Yu12]. In both cases, an accurate knowledge of the small body gravity field is assumed. Nevertheless, little dynamical information is usually available prior to the spacecraft arrival. Earth sensors can only provide reliable estimations of orbit and spin. The asteroid mass and shape (to a certain extent) can be determined during the fly-by approach phase [Yoshikawa06, Jorda16]. However, the mass distribution remains unknown. Due to the previous fact, the gravity field inhomogeneities are unknown for preliminary mission design and the gravity parameters has to be characterized on the fly.

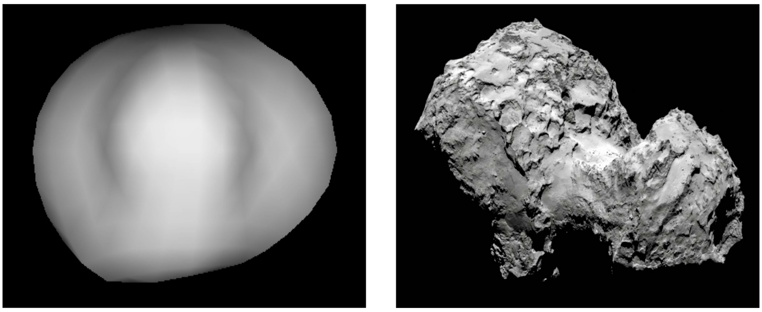

Figure 1.5: Comet 67P/Churyumov-Gerasimenko predicted shape (*left*) and image from Rosetta (*right*). Credits: ESA, NASA and Philippe Lamy.

The characterization of an inhomogeneous gravity field is also challenging. There are two distinct regions with different behaviours, the exterior and interior of Brillouin sphere. Let recall that the Brillouin sphere is the circumscribing sphere of the body. The external gravity field can be modelled by means of spherical harmonics expansions [Balmino94], polyhedral shapes [Werner96] or mass concentrations (namely mascons) [Chanut15]. Spherical harmonics are an indirect way to model both mass and shape inhomogeneities. The polyhedral models can model exact shapes but are based on an homogenous mass distribution assumption. The mascons models are based on multiple discrete mass points thus allowing to model arbitrary mass distributions by a suitable weight and placement. Regarding the interior gravity field (suitable for surface proximity operations), [Takahashi13] demonstrated that any exterior model can be transitioned to a transformed spherical harmonics expansion centered outside the Brillouin sphere.

In the NEAR Shoemaker mission, the gravity field (up to 15th degree) was determined by Earth's ground control through navigation and optical data [Miller02]. Achieving higher order gravity estimation requires on-orbit measurements for long periods of time. For example, the geocentric GRACE mission iterates its Earth's gravity model estimation after thirty days of collected measurements [Tapley08]. These procedures were repeated in recent gravity field estimations of Ceres (Dawm mission) [Konopliv18] and 101955 Bennu (OSIRIS-REX) [Scheeres19].

Based on Kalman filters, autonomous navigation techniques have been extensively studied and analyzed by [Vetrisano16, Dietrich17, Gil-Fernandez18, Pellacani18]. All of these works assume that the small body gravity field is a known input to the orbit determination process. However, the inhomogeneous gravity terms may not be available in the early mission phases. Fortunately, if sensors sampling rates suffice to match the frequencies of the gravity low order terms, the gravity parameters estimation could be added to the filters. Consequently, only some of the gravity parameters, but the most dominant ones, would be included within the filters computation. This may preclude oversizing the filter estimates which has a huge impact on computational burden. By estimating the dominant gravity field inhomogeneities, the preliminary design of frozen or periodic orbits is enabled. As a matter of fact, achieving a faster autonomous gravity estimation process could small bodies exploration and exploitation by enabling early proximity operations, reducing the residence time and allowing independent autonomous navigation.

Under the previous idea, the recent works of [Hesar15, Fujimoto16, Stacey18, Biggs19] proposed different autonomous gravity determination techniques. Reference [Hesar15] developed a filtering technique to determine gravity from relative measurements between probes. In that spirit, [Fujimoto16] proposed to eject and track (steoreoscopically) high albedo reflectors from two motherships, thus enabling in-situ determination from high orbits. Alternatively [Stacey18] employed an unscented Kalman filter (UKF) for simultaneous state and gravity estimation. Its mission concept is based on a satellites swarm maintaining close relative formation. Reference [Biggs19] employed an extended state observer to subsequently match the estimated disturbance with the small body gravity and sail degradation parameters through sequential batch least-squares. Its concept is based on solar-sailing station-keeping around an artificial equilibrium (which changes as the sail degradates).

Each of the previous approaches presents drawbacks in terms of their practical implementation. A relative-based sensing strategy can be dramatically endangered if one of the probes suffers from malfunctions. The reflectors ejection and tracking strategy is limited by the amount of carried particles which could be a bound the number of visited small bodies for a mission. However, the motherships guidance and control is eased as they can be maintained at higher orbits which are more stable. As it is designed, the swarming concept requires relative based control which is more challenging than absolute control. Finally, the solar sails concept could theoretically enable limitless asteroid exploration though this propulsion device is still under feasibility studies.

In view of the previous facts, there seems to be a literature gap in demonstrating absolute based guidance, navigation and control with gravity estimation. This will enables an independent probe to carry out autonomous asteroid exploration. As such, optical based landmark tracking measurements, which is a well proven technology, could be considered [Li05]. This has attitude control requirements as the optical devices shall point the asteroid surface [Wibben12, Gaudet20]. Regarding orbit guidance and control, the problem translates to station-keeping a closed orbit at the small body while undertaking the gravity determination.

This builds a scalable architecture where more satellites can be added and provide simultaneous estimation independently. The main drawback of the previous concept seems to be the required active control for station-keeping purposes. This also applies to orientation maintenance as asteroids gravity-gradient could differ from Earth's rules of thumb [Wang13]. Still, these concerns may be diminished as station-keeping typically requires a low control effort (at least in the short-term), allowing to use efficient devices such as electric thrusters and reaction wheels.

1.1.3 The role of model predictive control

The term model predictive control (MPC) does not designate a specific control strategy but rather an ample range of control methods which make explicit use of a model of the process to obtain the control signal by minimizing an objective function over a finite receding horizon [Camacho04]. In MPC, a model of the process is used to predict the future plant outputs, based on past and current values and on the proposed optimal future control actions. These actions are calculated by the optimizer taking into account the cost function (where the fuel or the energy consumption and the future tracking error are considered) as well as the constraints.

The implementation of an MPC scheme relies on an optimization problem which has to be solved on-line. Thus, at each sampling time, the optimizer obtains an optimal control sequence along the receding horizon, but only the first control action of the sequence is indeed applied. After that, the initial condition is updated with the measured state and the prediction horizon is usually slided forward in time to keep a constant prediction horizon [Mattingley10]. Under these new conditions, the optimization is solved and the control sequence is updated. This process could be infinitely repeated over time is equivalent to a closed-loop feedback controller. This imparts MPC the ability to tackle disturbances and mitigate, to a certain extent, the potential error growth. As a matter of fact [Mayne00] demonstrated, under certain assumptions, that MPC leads to close-loop stability and target convergence. An illustration of MPC for reference tracking can be seen in Fig. 1.6.

The model predictive control approach was firstly employed for chemical processes in industrial plants and oil refineries in the 1980s [Qin03]. Model predictive control enabled a reduction in the operational safety margins because its formulation explicitly accounts for process constraints. This allows to operate the process closer to its operational limits, with a high degree of accuracy, which augmented its efficiency. Due to the previous facts, [García89] concluded that MPC was the most suitable control technique for complex multivariate processes due to its flexible constraints-handling capabilities. Since then, it has been widely employed in aerospace [Gavilan15], automotive [Hrovat12], economics [Herzog07], electrical [Di Giorgio14] and robotics [Wilson16] applications amongst others.

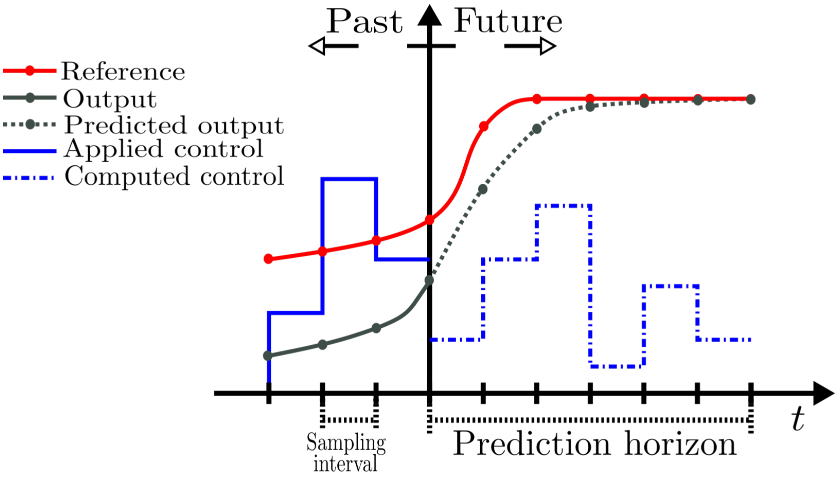

Figure 1.6: Model predictive control illustration.

Model predictive control presents some relevant differences with other state-of-the-art control approaches such as linear-quadratic-regulators (LQR) and proportional-integral-derivative (PID) state feedback. The LQR scheme uses the same control sequence attached to a fixed time window whereas MPC computes new control solutions due to its moving time horizon. As a consequence, MPC usually considers smaller time windows than LQR. This may lead to sub-optimal solutions. The LQR is also limited to linear systems while the generic form of MPC could support non-linear models. With respect to PID controllers, which only takes into account the current and past state, MPC has the benefit of anticipating future events by its predictive nature. Furthermore, the LQR and PID approaches do not consider constraints within their formulation while MPC is able to take into account both control and state constraints. However, MPC shall guarantee the optimization problem feasibility. From the computational perspective, PID is very efficient as only the current state has to be accounted in the control law. The LQR approach is more cumbersome, but not prohibitive, as its gain is adjusted through an algebraic expression (infinite-horizon) or the integration the continuous-time Ricatti differential equation (finite-horizon). Finally, due to its optimization approach MPC could present high computational burden if a continuous non-linear optimization problem is directly considered. Such issue could be partly mitigated via discretization and linearization methods in order to obtain a tractable static program. Table 1.1 summarizes these state-of-the-art control methods.

Method	Optimality	NL[2]	Horizon	Constraints	Comp. burden[3]
MPC	Sub-optimal[4]	Yes	Moving	Yes	High/medium
LQR	Optimal	No	Fixed	No	Medium
PID	No	Yes	Instant	No	Low

Table 1.1: Characteristics of MPC, LQR and PID.

Let analyze the details concerning the MPC optimization problem for a guidance and control application. In that application, the goal is to find an optimal control sequence steering the state from an initial point to a terminal set, in a finite period of time (namely the prediction horizon), while respecting the system dynamics, path constraints and control bounds. The underlying optimization problem of the associated MPC scheme can be mathematically expressed as problem (1.1)

$$\boxed{\begin{aligned} \underset{\mathbf{u}(t)}{\text{minimize}} \quad & J(\mathbf{u}(t)) = g_f(\mathbf{x}(t_f)) + \int_{t_0}^{t_f} g(\mathbf{x}(t), \mathbf{u}(t))dt, \\ \underset{\forall t \in [t_0, t_f]}{\text{subject to}} \quad & \dot{\mathbf{x}}(t) = \mathbf{f}(t, \mathbf{x}(t), \mathbf{u}(t), \mathbf{w}(t)), \\ & \mathbf{x}(t_0) = \mathbf{x}_0, \\ & \mathbf{x}(t_f) \in \mathcal{X}_f, \\ & \mathbf{x}(t) \in \mathcal{X}(t), \\ & \mathbf{u}(t) \in \mathcal{U}(t), \end{aligned}} \tag{1.1}$$

where $t \in \mathbb{R}$ is time, $\mathbf{x} \in \mathbb{R}^n$ is the state, $\mathbf{u} \in \mathbb{R}^m$ is the control, $\mathbf{w} \in \mathbb{R}^p$ is the disturbance and $\mathbf{f} : \mathbb{R}^{n+m+p+1} \to \mathbb{R}^n$ is the prediction model (which may differ from reality). The sets $\mathcal{X}_f$, $\mathcal{X}$ and $\mathcal{U}$ represents the terminal set, path constraints and control bounds respectively. The final time fulfils $t_f = t_0 + T$ where T is the prediction horizon. Many successful MPC implementations neglect the

---

[2] NL ≡ non-linear.

[3] Comp. burden ≡ computational burden.

[4] Optimal for the linear case.

effect of the disturbances though its consideration in the optimization problem could lead to explicit robust MPC formulations [Mayne05, Calafiore06].

An extensive survey of numerical methods to solve the optimal control problem (1.1) can be found in [Betts98]. In that publication, two distinct methodologies namely the direct and indirect optimization techniques were stated. Direct methods transform the continuous optimization problem (1.1) into a finite tractable static program by means of discretization [Hull97]. The outcome is a non-linear programming (NLP) optimization problem. On the contrary, indirect methods transforms the problem, in an equivalent way, to a two-point boundary value problem [Bryson75]. For autonomous operations, the direct method has been extensively preferred because there are available very efficient solvers, from the numerical perspective, for static programs. On the contrary, the indirect method two-point boundary value problem involves the addition of auxiliary variables (namely the adjoints) which are difficult to interpret. This fact complicates the construction of the initial guess which, if chosen wrongly, could endanger the convergence.

Unfortunately, even the direct technique is oftentimes difficult to implement in a practical MPC mainly for two reasons. First, the underlying optimization problem is frequently non-linear and therefore time-consuming; thus, real-time implementation becomes a challenge. This is sometimes referred to as the instantaneity problem. In addition, there might be no guarantee to find a feasible control solution (which could compromise the safety of the system). This is called the feasibility problem. As technology evolves, both the instantaneity and feasibility problems have become solvable when using certain techniques or if the models are adequately simplified [Siguerdidjane17]. Thus, MPC is considered a cornerstone control technique for spacecraft guidance and control [Starek16].

Overcoming the MPC instantaneity problem for an autonomous space system requires that the computational time of solving problem (1.1) has to be negligible when compared to the sampling rate. In that sense, it has to be noted that satellite on-board computers are limited by low power processors (to save energy) which are usually obsolete when compared with the most common personal computers available in the market (due to a long preflight certification process against radiation). The previous fact suggests that MPC optimization problem should be limited to convex forms such as linear, quadratic, second-order cone or semi-definite programs for which there exist efficient solvers, or what is better, to problems whose analytical solution can be found. Consequently, it is convenient to choose (or transform) the cost and constraints as linear or quadratic functions. This covers the minimization of fuel consumption which is directly related to control effort. If the control bounds, path constraints and terminal sets are non-linear but convex, these can be linearized by an approximation with hyperplanes. Moreover, some special cases of non-convex constraints can be convexified through relaxation techniques. This applies to non-convex obstacle avoidance [Jewison15] and precluding the thrusters shutdown [Açıkmeşe11].

The system dynamics is not on the hands of the mission designer. Spacecraft dynamics is subject to gravity which is non-linear due to its inverse relation with the squared distance to the massive body. Non-linear dynamics yields a non-linear optimization problem where both the state and control have to be simultaneously treated as decision variables (though an iterative scheme, by using the last state, could be considered [Lu13]). As a consequence, MPC has been extensively applied to autonomous spacecraft proximity operations or guidance tracking (e.g. station-keeping) where the dynamics is linear with a high degree of accuracy. In proximity operations, the close distance to a target allows to use linear relative dynamics [Tschauner65] around the target motion. Similarly, for guidance tracking, the dynamics can be linearized around the desired reference. This assumes that the control will be effective enough to maintain the state in the vicinity of the reference.

Under the previous motivation, there is a huge number of works using MPC for spacecraft rendezvous and station-keeping purposes. A thoughtful compendium of MPC-based spacecraft rendezvous, up to the year 2015, can be found in [Hartley15a]. A breakthrough happened in the year 2002 as [Yamanaka02] provided an analytical state transition matrix for the Tschauner-Hempel equations, [Tschauner65]. This allowed to propagate the Keplerian linear relative motion without the need numerical integration. The early work of [Richards03] demonstrated the feasibility and benefits of applying MPC to the rendezvous problem for operational scenarios such as the glideslope and line-of-sight corridor approaches. Reference [Breger08] demonstrated how passive safety abort trajectories can be considered within an MPC formulation. Reference [Cairano12] considered the rendezvous problem with a tumbling target. The previous results were fused in [Hartley12] to provide a full MPC-based rendezvous practical implementation which demonstrated to overcome, in terms of efficiency, the traditional preflight maneuvers libraries.

Practical implementations of MPC algorithms in on-board flight computers has been validated in [Hartley15b, Arantes-Gilz18]. The realistic consideration of controlling the thrusters valves opening times was done in [Vazquez17]. Other works aimed to provide robust MPC controllers against navigation uncertainties and impulses mishaps [Gavilan12, Louembet15, Mammarella18]. Reference [Gavilan12] employed the chance-constrained approach to assure probabilistic satisfaction of constraints. Reference [Louembet15] generated robust worst-case scenario plans to diminish the terminal spread due to the errors. Reference [Mammarella18] considered the tube-based approach where the set of uncertain trajectories is characterized and is kept within constraints bounds.

Orbit-attitude station-keeping is also a potential field for MPC forms. For example, MPC has been used for orbit-attitude station-keeping and momentum management of geostationary satellite [Weiss15a, TayyebTaher17]. Non-linear MPC forms have been recently applied to halo orbits station-keeping

[Kalabic15, Misra18, Subudhi20]. Due to atmospheric drag, low-Earth orbit satellites need frequent raising maneuvers that can be tackled through MPC [Tavakoli14]. Attitude control station-keeping, where a specific orientation has to be maintained, has also explored the use of MPC [Hegrenæs05, Vieira11, Leomanni13]. Furthermore, MPC schemes have been employed by a significant number of works [Manikonda99, Abdulrahman12, Breger08, Lim18, Xu19] for flight-formation purposes.

It can be concluded that model predictive control have been extensively analyzed in the context of space operations (even under explicit robust forms). Its main advantage is its flexibility when handling several types of constraints corresponding to different scenarios. Space operations may also benefit from novel concepts such as learning-based MPC [Hewing20]. The learning-based MPC estimates the model parameters on-line, thus updating the prediction model of the MPC optimization problem, which increases the control accuracy over time. This is specially appealing for systems where there is a large initial uncertainty in the model parameters.

1.2 Objectives of the Thesis

The overarching goal of this thesis is to produce innovative results in the field of spacecraft proximity operations. To this end, several forms of model predictive controllers have been developed for various scenarios of interest in proximity operations. The ultimate goal is to augment these operations autonomy by enhancing some control capabilities or figures of merit over other state-of-the-art controllers. This broader mission can be divided into the following requirements:

- **Objective 1:** to develop optimal closed-loop controllers. Closing the control loop guarantees that the controller is able to cope with disturbances at a certain extent. This guarantees that the mission phase will be fulfilled without human intervention which demonstrate the autonomy of the proposed solution. The control sequence shall also reduce the control effort as much as possible. Being fuel a limited resource in space, the previous consideration would result in higher reserves for the subsequent operations.

- **Objective 2:** to assess the control accuracy and efficiency of the developed algorithms. This refers to compare the designed controllers with other state-of-the-art methods whenever is possible. This allows to quantify the advantages and drawbacks of one methodology over another. The previous information is very useful because mission designers may use one controller or the other depending on their own preferences.

- **Objective 3:** to guarantee the problem feasibility and maintain a low or moderate computational burden. Being expected to be executed on-board, while the maneuver is ongoing, the control program should be always feasible from a mathematical perspective. For the same reason, the control program computational times should be low enough so that the delay between the need of a new control plan and its application is almost negligible.

- **Objective 4:** to consider scenarios of interest in proximity operations as per Section 1.1.2. Specifically:
  - Six-degrees of freedom spacecraft rendezvous: this refers to solve the integrated orbit-attitude control problem in order to achieve spacecraft rendezvous under Keplerian assumptions. When few thrusters are available, the spacecraft orientation has to be changed in order to apply translational control in the desired direction. Consequently, the orbital and attitude control systems have to be integrated in order to complete the rendezvous operation.
  - Near-rectilinear halo orbits rendezvous: proximity operations for periodic orbits in the restricted three-body problem is gaining momentum in the literature. In opposition to Keplerian orbits, the RTBP orbits are parameterized numerically. This fact precludes the obtention of a closed-form analytical expression of the transition matrix for the linearized motion. Currently, the practical application of RTBP operations is to rendezvous with a spacecraft in an Earth-Moon near-rectilinear halo orbit.
  - Spacecraft hovering phases: in-orbit inspection or rendezvous hold-on phases require to maintain the relative distance with the leader (hovering). Usually, the hovering phase lasts for several orbital periods which may have a very negative impact on fuel consumption. This can be partially mitigated by exploiting the periodic orbits of the linear Keplerian relative motion. Still, the orbital perturbations will make the spacecraft drift away from the previous orbits. Consequently, dealing with these perturbations requires a smart control strategy.
  - Orbit-attitude station-keeping around small bodies: the early phases of small bodies exploration are characterized by a high degree of dynamical uncertainty. The main unknown is the small body inhomogeneous gravity field which is the predominant perturbation in low orbits. As a consequence, orbit-attitude station-keeping has to be guaranteed while undertaking the small body gravity estimation in-situ. In the past, this process is carried out conservatively with a lengthy characterization phase prior to the descend into a low orbit. Currently, the combination of novel control and learning techniques may enable orbiting closer to the small body from the very beginning.

1.3 Solution approach

The solution approach consists in the algorithmic development of a specific model predictive controller for each scenario in Objective 4. The particularities and current state-of-the-art, of each scenario, cause the specific approach to vary between them (e.g. event-based predictive control is applied to the spacecraft hovering phases scenario).

The generic methodology, followed in this dissertation, is described in Fig. 1.7. Firstly, a detailed continuous optimization guidance and control problem is posed. As per Objective 1, the previous problem shall be recursively solved along the trajectory in order to close the control loop. There exist state-of-the-art techniques (e.g. collocation methods) able to solve non-linear continuous optimization problems. However, those techniques are characterized by a high computational burden which is in conflict with the low computational burden requirement of Objective 3. Moreover, equality constraints on the terminal state may be a source of infeasibility when the control horizon is slided forward in time (the equality constraint spans over a finite period of time). To overcome the previous issues, dynamics linearization, constraints relaxation (transforming constraints into penalty costs precluding potential infeasabilities) and time discretization techniques are simultaneously applied to reduce the continuous optimization problem. The result is a static control program.

It is desirable that the static program is expressed in terms of a linear programming (LP) or a quadratic programming (QP) form in the decision variables. Currently, there are very computationally-efficient state-of-the-art solvers (e.g. Gurobi [Gurobi14]) for linear or quadratic programming. To obtain these forms of the static control program, the dynamics, constraints and Objective function have to be posed linearly or quadratically. The constraints and Objective function can be designed as such which covers a wide variety of cases. Additionally, linearizing the system dynamics is adequate for the proximity operations scenarios of Objective 4. The previous step would result in a linear time-varying system which can be solved explicitly by using the state transition matrix and integrating the control [Kamen10]. Depending on the scenario, the dynamics is linearized with respect to the orbit of an orbiting object (assuming its orbit is known) or a guidance reference (that has to be tracked).

To summarize, the MPC updates its control sequence by solving a linear or quadratic program. The main motivation of closed-loop MPC is to cope with disturbances (to a certain extent) that will cause an open-loop trajectory to deviate from its initial plan. In order to do so, the developed controllers are numerically tested against the high-fidelity system dynamics. The high-fidelity dynamics includes control mishaps and unmodelled perturbations (partly caused by the linear dynamics assumption). The testing process ends by identifying relevant figures of merit[5] which also allow to compare the pro-

---

[5] The computational times of this thesis are measured using a i7-8700 3.2 GHz CPU.

posed approaches of this dissertation with other state-of-the-art controllers. This completes Objective 2.

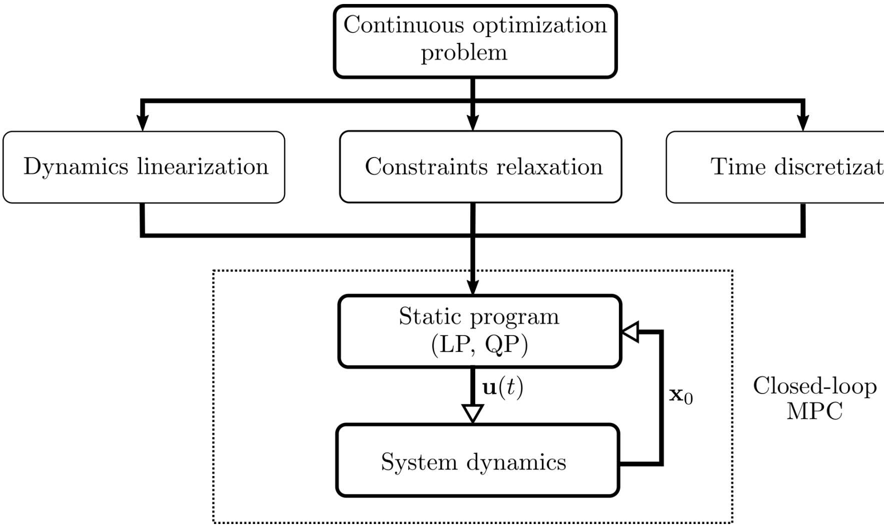

Figure 1.7: Diagram of the generic solution approach.

1.4 Contributions

The following summary comprises the original contributions of this thesis:

- **Contribution 1:** an integrated six-degrees of freedom model predictive controller for Keplerian-based rendezvous. The algorithm is valid for any chaser spacecraft equipped with impulsive thrusters and a reaction wheels array. It also allows to rendezvous with targets placed in elliptic orbits. The numerical approach is divided between the open-loop and closed-loop computations. The open-loop plan (can be viewed as guidance) is computed by solving a non-linear program. Linearizing the system over the previous solution, the loop is closed with a quadratic program in terms of incremental variables. The Keplerian linear relative motion transition matrix and the attitude flatness property are exploited in order to define the optimization programs. Results show the capability of the closed-loop control to complete the rendezvous maneuver in the presence of impulses mishaps. This contribution lead to the publication of the journal article [Sanchez20b] and the conference proceeding [Sanchez18].
- **Contribution 2:** a stochastic robust model predictive controller for near-rectilinear halo orbits rendezvous. The restricted-three body prob-

lem linear relative motion is used as the prediction model. The controller is robustified using the chance-constrained approach which ensures constraints (line-of-sight) satisfaction in a probabilistic sense. This is achieved by tightening the constraints so that a high percentage of random realizations fulfil the constraints. The disturbance statistical properties are inferred on-line via a disturbance estimator. The resulting optimization is a deterministic quadratic program that is recursively solved on-line with updated estimations of the disturbance, thus closing the loop. For a cislunar rendezvous scenario and under thrusters mishaps, the results show the superiority in terms of constraints satisfaction of the robust approach with respect to a non-robust model predictive controller. This contribution is published in the journal article [Sanchez20a].

- **Contribution 3:** an event-based predictive controller for the hovering phase of spacecraft rendezvous. The resulting algorithm allows to maintain relative formation between a leader in an eccentric orbit and a follower equipped with impulsive thrusters. At high level, the control strategy aims to maintain the follower within the set of constrained (in the hovering region) periodic relative orbits, namely the admissible set. In order to do so, predefined trigger rules decide when a single-impulse control has to be exerted. The triggering decision is based on membership and proximity indicators to the admissible set. The algorithm computational footprint is minimal since the most complex operation is the computation of the roots for an univariate polynomial. The results compare the event-based controller with the recent global stable controller of [Arantes-Gilz19]. The developed event-based strategy outperforms the global one in terms of control accuracy and computational burden. This contribution lead to the publication of the journal article [Sanchez21a] and the conference proceeding [Sanchez19].

- **Contribution 4:** a learning-based model predictive controller for orbit-attitude station-keeping in the vicinity of a small body. The control goal is to maintain a circular orbit with a stationary attitude, thus allowing for camera line-of-sight with the small body surface. The technical challenge is that the small body inhomogeneous gravity field is unknown. The learning-based approach combines unscented Kalman filtering with model predictive guidance and control. Using sensors measurements, the Kalman filter estimates the current state and the inhomogeneous gravity field parameters. The previous outputs feeds the model predictive guidance and control block. The guidance generates a reference to be subsequently tracked by a control program. For both orbit and attitude, the control works under a linearized model around the reference which yields a quadratic control program. The possibility of speeding up the gravity estimation with a satellite constellation concept is also explored. For the asteroid 433 Eros, the results shows the improvement in terms of orbital reference tracking accuracy and attitude control effort for the learning-based algorithm with respect to a non-learning one. The constellation concept also improves the gravity estimation process with respect to single satellite missions. This contribution lead to the submission of the journal article [Sanchez20c] and the publication of the conference proceeding [Sanchez21b].

1.5 Outline of the document

This dissertation is structured as follows:

- **Chapter 2** presents the orbit-attitude dynamics models used throughout this document. For the orbital dynamics, the linear relative dynamics are emphasized. The orbit and attitude actuators models are also described. This includes the possible addition of control mishaps.

- **Chapter 3** develops a six-degrees-of-freedom model predictive controller for spacecraft rendezvous. The solution approach exploits the transition matrix of Keplerian linear relative motion and the attitude flatness property. This leads to an open-loop non-linear program. The control loop is closed by linearizing the system around the initial open-loop solution which yields a quadratic program. The simulations test the controller performance, under the presence of impulses mishaps, for a cargo spacecraft and a lightweight satellite.

- **Chapter 4** develops a robust controller to rendezvous with a near-rectilinear halo orbit. The dynamics are modelled using the linear relative motion of the restricted three-body problem. The model predictive controller is robustified using the chance-constrained technique which assures constraints satisfaction in a probabilistic sense. Finally, an on-line disturbance estimator is developed so the disturbances statistical properties are inferred. The robust MPC is compared against a non-robust MPC for a rendezvous operation with a southern Earth-Moon L2 near-rectilinear halo orbit.

- **Chapter 5** presents an event-based predictive controller for spacecraft rendezvous hovering phases. The concept of natural constrained periodic relative orbits is employed in order to reduce fuel consumption needs. Combining a single-impulse control law and suitable trigger rules, the event-based controller aims to maintain the state within the previous set of constrained periodic orbits. The result is an aperiodic control algorithm with a low computational footprint. The invariance of the single-impulse is assessed using hybrid impulsive systems theory. The numerical results compare the event-based algorithm with a periodic global stable controller.

- **Chapter 6** introduces a learning-based model predictive control for orbit-attitude station-keeping in the vicinity of a small body. This method (learning-based MPC) is applied by combining an unscented Kalman filter with model predictive guidance and control. The filter is used to estimate the state and gravity parameters, thus updating the prediction model employed in the guidance and control block. The guidance generates a reference that is subsequently tracked by a quadratic control program. In order to speed up the gravity estimation process, a satellite constellation concept is also presented. The simulations show the superior performance, in terms of control accuracy, of the learning-based MPC with respect to a non-learning MPC. The constellation concept is also shown to achieve a faster gravity estimation convergence than just using a single satellite.

- **Chapter 7** ends this document with a resume and conclusions with respect to the presented research work. The technical contributions of the thesis are also highlighted. Finally, potential future research directions are pointed out.

- **Appendices** are devoted to present some of the auxiliary tools employed in this thesis (which are not original contributions per se). These include B-splines, periodic orbits in the circular restricted three-body problem, an implicitization method for trigonometric functions and the description of a global stable controller for the hovering phase.

This page is intentionally left blank.

Chapter 2

Spacecraft dynamics

> We can lick gravity, but sometimes the paperwork is overwhelming.
>
> Wernher von Braun

Contents

2.1 Translational motion 32
  2.1.1 Absolute motion 32
  2.1.2 Relative motion 39
  2.1.3 Thrust models 49
2.2 Angular motion 51
  2.2.1 Attitude representation 51
  2.2.2 Rotational dynamics 55

The spacecraft dynamics, under rigid body assumptions, can be divided into the translational and rotational motions. There exist several possible representations for each motion. This chapter will present some of them with special emphasis in relative motion models.

The dynamics is influenced by external forces and control actuators. As the presented dynamical systems will be employed for model prediction in the subsequent chapters, convenient simplifications, capturing the most relevant effects, are made.

2.1 Translational motion

In this section, the translational motion is presented for both the absolute and relative cases. The absolute motion is usually described with respect to an inertial frame and it is especially convenient for high-fidelity propagation. On the contrary, the relative motion is described with respect to a frame attached to a leader spacecraft. As such, the previous description is widely employed in proximity operations purposes. The motion is controlled by means of thrusters whose modelling is discussed.

2.1.1 Absolute motion

The spacecraft absolute motion can be described in terms of its Cartesian components, classical orbital elements or modified equinoctial elements (MEE). The Cartesian representation directly considers the spacecraft position and velocity. The orbital elements provide useful insight on the trajectory shape and orientation. The modified equinoctial elements prevents some singularities arising with classical orbital elements.

Cartesian coordinates

Let define an inertial frame $I:\{\mathbf{O}_I,\mathbf{i}_I,\mathbf{j}_I,\mathbf{k}_I\}$ where $\mathbf{O}$ is the center of mass of the main body (e.g. Sun, planet, small body), the directions $\mathbf{i}_I$ and $\mathbf{j}_I$ define the main body equatorial plane and $\mathbf{k}_I$ aligned with its rotation axis (assumed as constant). Let also define a generic orthogonal coordinate system $L:\{\mathbf{O}_L,\mathbf{i}_L,\mathbf{j}_L,\mathbf{k}_L\}$. The spacecraft motion can be characterized by means of its position $\mathbf{r}$ and velocity $\dot{\mathbf{r}}$ with respect to the main body (e.g. a Sun, a planet) in the frame L. Generally, the frame L will rotate with angular velocity $\boldsymbol{\omega}_{L/I}$ and acceleration $\dot{\boldsymbol{\omega}}_{L/I}$ with respect to the inertial frame . Using the previous definitions, the spacecraft equation of motion is

$$\ddot{\mathbf{r}}+\dot{\boldsymbol{\omega}}_{L/I}\times\mathbf{r}+2\boldsymbol{\omega}_{L/I}\times\dot{\mathbf{r}}+\boldsymbol{\omega}_{L/I}\times(\boldsymbol{\omega}_{L/I}\times\mathbf{r})=\frac{\mathbf{F}}{m}, \tag{2.1}$$

where the derivatives have been taken with respect to the frame L. The vector $\mathbf{F}$ is the external force and m is the spacecraft mass. In this dissertation, the spacecraft mass evolution is not studied as it is assumed the thrust force can be adjusted to provide the required control acceleration. The external force is composed of the main body Keplerian force, the orbital perturbations $\mathbf{F}_\mathrm{p}$ (which depends on the spacecraft state) and the exerted thrust $\mathbf{F}_u$ as

$$\mathbf{F} = -\frac{\mu m \mathbf{r}}{r^3} + \mathbf{F}_\mathrm{p}(\mathbf{r}, \dot{\mathbf{r}}) + \mathbf{F}_u, \tag{2.2}$$

where μ is the main body standard gravitational parameter.

In orbital mechanics, an usual choice is to attach the frame L to the satellite center of mass as

$$\mathbf{O}_L \equiv \mathbf{r}, \quad \mathbf{i}_L = \frac{\mathbf{r}}{\|\mathbf{r}\|_2}, \quad \mathbf{j}_L = \mathbf{k}_L \times \mathbf{i}_L, \quad \mathbf{k}_L = \frac{\mathbf{r} \times \dot{\mathbf{r}}}{\|\mathbf{r} \times \dot{\mathbf{r}}\|_2}, \tag{2.3}$$

where $\mathbf{i}_L$ is the radial direction, $\mathbf{j}_L$ is the tangential direction and $\mathbf{k}_L$ is the normal direction. The radial and in-track directions define the orbital plane while the normal direction is the out-of-plane component. The definition of the directions $\mathbf{i}_L$, $\mathbf{j}_L$ and $\mathbf{k}_L$ may be swapped amongst them depending on the specific application.

Classical orbital elements

The classical orbital elements are invariant quantities of the Keplerian motion. They are defined by $\boldsymbol{\alpha} = [a, e, i, \Omega, \omega, M]^T$ where a is the semi-major axis, e is the eccentricity, i is the inclination, Ω is the right ascension of the ascending node, ω is the argument of periapsis and M is the mean anomaly (it is also possible to use either the true anomaly ν or the eccentric anomaly E instead).

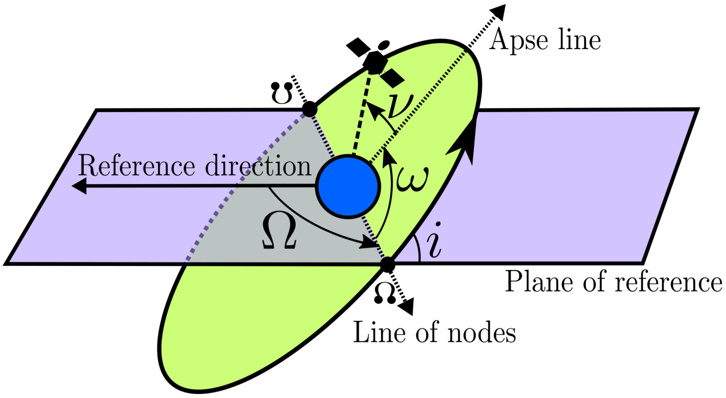

Figure 2.1: Classical orbital elements.

The classical orbital elements dynamics is stated in terms of the Gauss variational equations

$$\frac{d}{dt}\begin{bmatrix} a \\ e \\ i \\ \Omega \\ \omega \\ M \end{bmatrix} = \underbrace{\begin{bmatrix} 0 \\ 0 \\ 0 \\ 0 \\ 0 \\ \sqrt{\mu/a^3} \end{bmatrix}}_{\mathbf{c}(\boldsymbol{\alpha})} + \mathbf{A}(\boldsymbol{\alpha}) \begin{bmatrix} a_r \\ a_t \\ a_n \end{bmatrix}, \tag{2.4}$$

$$\mathbf{A}(\boldsymbol{\alpha}) = \begin{bmatrix} \frac{2a^2 e \sin\nu}{h} & \frac{2a^2 p}{rh} & 0 \\ \frac{p\sin\nu}{h} & \frac{(p+r)\cos\nu + re}{h} & 0 \\ 0 & 0 & \frac{r\cos(\omega+\nu)}{h} \\ 0 & 0 & \frac{r\cos(\omega+\nu)}{h\sin i} \\ -\frac{p\cos\nu}{he} & \frac{(p+r)\sin\nu}{he} & -\frac{r\sin(\omega+\nu)\cos i}{h\sin i} \\ \frac{b(p\cos f - 2re)}{ahe} & -\frac{b(p+r)\sin\nu}{ahe} & 0 \end{bmatrix},$$

where p is the semi-latus rectum, h is the modulus of the Keplerian orbit angular momentum and b the orbital semi-minor axis which are related to the classical orbital elements as

$$p = a(1-e^2), \quad h = \sqrt{p\mu}, \quad b = a\sqrt{1-e^2}. \tag{2.5}$$

The vector $\mathbf{a} = [a_r, a_t, a_n]^T$, is composed of the perturbing accelerations to the main body Keplerian motion. The subindexes $\{r, t, n\}$ represent the radial, tangential and normal directions which coincide with the frame defined in Eq. (2.3). Splitting the non-Keplerian perturbation into natural $\mathbf{a}_{\mathrm{p}}$ and control, $\mathbf{u}$, accelerations the Eq. (2.4) can be conveniently expressed as

$$\dot{\boldsymbol{\alpha}} = \mathbf{c}(\boldsymbol{\alpha}) + \mathbf{A}(\boldsymbol{\alpha})\mathbf{a}_{\mathrm{p}}(\boldsymbol{\alpha}) + \mathbf{A}(\boldsymbol{\alpha})\mathbf{u}. \tag{2.6}$$

However, the orbital elements dynamics is singular for circular $e = 0$ or equatorial orbits $i = 0, \pi$. Note that for a circular orbit, the argument of periapsis is not defined as there does not exist an apse line. For an equatorial orbit, there is no ascending node, therefore its right ascension cannot be defined.

Modified equinoctial elements

The modified equinoctial elements, $\tilde{\boldsymbol{\alpha}} = [p, f, g, h, k, L]^T$, were conceived in [Walker85] to avoid the singular cases of the classical orbital elements. The transformation from the classical orbital elements to modified equinoctial elements is

$$\begin{aligned} p &= a(1-e^2), \\ f &= e\cos(\omega+\Omega), \\ g &= e\sin(\omega+\Omega), \\ h &= \tan(i/2)\cos(\Omega), \\ k &= \tan(i/2)\sin(\Omega), \\ L &= \Omega+\omega+\nu. \end{aligned} \tag{2.7}$$

Accordingly, the Gauss variational equations for modified equinoctial elements are

$$\frac{d}{dt}\begin{bmatrix} p \\ f \\ g \\ h \\ k \\ L \end{bmatrix} = \underbrace{\begin{bmatrix} 0 \\ 0 \\ 0 \\ 0 \\ 0 \\ \sqrt{\mu p}(w/p)^2 \end{bmatrix}}_{\tilde{\mathbf{c}}(\tilde{\boldsymbol{\alpha}})} + \tilde{\mathbf{A}}(\tilde{\boldsymbol{\alpha}}) \begin{bmatrix} a_r \\ a_t \\ a_n \end{bmatrix}, \tag{2.8}$$

$$\tilde{\mathbf{A}}(\tilde{\boldsymbol{\alpha}}) = \sqrt{\frac{p}{\mu}} \begin{bmatrix} \frac{2p}{w} & 0 & 0 \\ \sin L & \frac{(1+w)\cos L + f}{w} & \frac{-g(h\sin L - k\cos L)}{w} \\ -\cos L & \frac{(1+w)\sin L + g}{w} & \frac{f(h\sin L - k\cos L)}{w} \\ 0 & 0 & \frac{s^2\cos L}{2w} \\ 0 & 0 & \frac{s^2\sin L}{2w} \\ 0 & 0 & \frac{h\sin L - k\cos L}{w} \end{bmatrix},$$

where

$$w = 1 + f\cos L + g\sin L, \quad s = \sqrt{1+h^2+k^2}. \tag{2.9}$$

The modified equinoctial elements dynamics can also be compactly expressed as

$$\dot{\tilde{\boldsymbol{\alpha}}} = \tilde{\mathbf{c}}(\tilde{\boldsymbol{\alpha}}) + \tilde{\mathbf{A}}(\boldsymbol{\alpha})\mathbf{a}_{\mathrm{p}}(\tilde{\boldsymbol{\alpha}}) + \tilde{\mathbf{A}}(\tilde{\boldsymbol{\alpha}})\mathbf{u}. \tag{2.10}$$

Note that the modified equinoctial elements have a singularity for retrograde equatorial orbits, $i = \pi$, due to the transformation defined in Eq. (2.7). However, this type of orbit is rarely used in practical applications.

The MEE can be transformed to the Cartesian inertial coordinates, $\mathbf{r}$ and

$\dot{\mathbf{r}}$, as

$$\begin{aligned}\mathbf{r} =& \frac{r}{s^2}\begin{bmatrix}(1+\alpha^2)\cos L + 2hk\sin L\\ (1-\alpha^2)\sin L + 2hk\cos L\\ 2h\sin L - 2k\cos L\end{bmatrix},\\ \dot{\mathbf{r}} =& \frac{\sqrt{\mu}}{\sqrt{p}s^2}\begin{bmatrix}-(g+\sin L)(1+\alpha^2)+2hk(f+\cos L)\\ (f+\cos L)(1-\alpha^2)-2hk(g+\sin L)\\ 2h\cos L + 2k\sin L + 2fh + 2gk\end{bmatrix},\end{aligned} \tag{2.11}$$

where

$$\alpha = \sqrt{h^2 - k^2}, \quad r = p/w. \tag{2.12}$$

Orbital perturbations

The natural non-Keplerian perturbation vector, $\mathbf{a}_{\mathrm{p}}$, is composed by the following terms

$$\mathbf{a}_{\mathrm{p}} = \mathbf{a}_{\mathrm{grav}} + \mathbf{a}_{\mathrm{bodies}} + \mathbf{a}_{\mathrm{drag}} + \mathbf{a}_{\mathrm{SRP}}. \tag{2.13}$$

where $\mathbf{a}_{\mathrm{grav}}$ is the acceleration due to the gravity inhomogeneities of the main body, $\mathbf{a}_{\mathrm{bodies}}$ is the Keplerian gravity due to third-bodies, $\mathbf{a}_{\mathrm{drag}}$ is the acceleration due to the atmospheric drag and $\mathbf{a}_{\mathrm{SRP}}$ is the perturbing acceleration due to the solar radiation pressure. Each one of these terms is further explained below.

Inhomogeneous gravity: the Keplerian motion assumes that the main body is a solid sphere with an homogeneous mass distribution. Nonetheless, this never happens in nature. Planets are oblate bodies due to their own rotation while small bodies (e.g. asteroids, comets) may present highly irregular shapes or considerable spatial density variations (contact binary asteroids). A classical model for the gravity field inhomogeneities acceleration is the spherical harmonics expansion

$$\begin{aligned}&\mathbf{a}_{\mathrm{grav}} =\\ &\sum_{n=2}^{n_{\max}}\sum_{m=0}^{n}\frac{\mu}{r^2}\left(\frac{R_e}{r}\right)^n\begin{bmatrix}-(n+1)\tilde{P}_n^{(m)}(\tilde{C}_{nm}\cos(m\lambda)+\tilde{S}_{nm}\sin(m\lambda))\\ \dfrac{m}{\cos\phi}\tilde{P}_n^{(m)}(-\tilde{C}_{nm}\sin(m\lambda)+\tilde{S}_{nm}\cos(m\lambda))\\ \cos\phi\tilde{P}_n^{(m)'}(\tilde{C}_{nm}\cos(m\lambda)+\tilde{S}_{nm}\sin(m\lambda))\end{bmatrix},\end{aligned} \tag{2.14}$$

where the satellite coordinates are expressed in terms of spherical coordinates $\{r, \lambda, \phi\}$ expressed in a fixed frame to the main body. The term r is the distance with respect to the main body center of mass, λ is the longitude (angle with respect to a fixed direction in the main body equatorial plane) and ϕ is the latitude (elevation with respect to the main body equatorial plane). The spherical harmonics coefficients have been expressed in terms of the normalized form as $\tilde{C}_{nm}$ and $\tilde{S}_{nm}$. The zonal coefficients correspond with $\tilde{C}_{n0}$ and are implicitly included in the summation (e.g. $J_2 = -\sqrt{5}\tilde{C}_{20}$). The scalar R_e is the normalization radius which usually is the maximum elongation of the body.

The term $\tilde{P}_n^{(m)}$ is the normalized Legendre function and $\tilde{P}_n^{(m)'}$ its derivative. The normalized Legendre function is defined as

$$\tilde{P}_n^{(m)}(\sin\phi) = \sqrt{(2-\delta_{m0})\frac{(n-m)!}{(n+m)!}}\cos^m\phi\frac{d^m\tilde{P}_n(\sin\phi)}{d(\sin\phi)^m}, \tag{2.15}$$

where $\tilde{P}_n(\sin\phi)$ is the normalized n^{th} degree Legendre polynomial of the first kind in $\sin\phi$. The term δ_{m0} is the Kronecker delta function which is unity for $m = 0$ and zero otherwise. The normalized Legendre functions are computed recursively as

$$\tilde{P}_n^{(m)} = \begin{cases} W_{nm}\left[\sqrt{2n-1}\sin\phi\tilde{P}_{n-1}^{(m)} - \sqrt{\dfrac{(n+m-1)(n-m-1)}{2n-3}}\right]\tilde{P}_{n-2}^{(m)}, & m < n, \\ \sqrt{\dfrac{2n+1}{2n}}\cos\phi\tilde{P}_{n-1}^{(m-1)}, & m = n, \\ 0, & m > n, \end{cases}$$

where $W_{nm} = \sqrt{(2n+1)/(n^2-m^2)}$. The sequence is initialized by

$$\tilde{P}_0^{(0)} = 1, \quad \tilde{P}_1^{(0)} = \sqrt{3}\sin\phi, \quad \tilde{P}_1^{(1)} = \sqrt{3}\cos\phi. \tag{2.16}$$

Similarly, the normalized Legendre derivative can also be computed as

$$\tilde{P}_n^{(m)'} = \frac{1}{\cos^2\phi}\left[-n\sin\phi\tilde{P}_n^{(m)} + \sqrt{\frac{(2n+1)(n+m)(n-m)}{2n-1}}\tilde{P}_{n-1}^{(m)}\right]. \tag{2.17}$$

Third bodies gravity: the Keplerian gravity perturbation of other bodies such as the Sun, planets or moons is considered as the following summation

$$\mathbf{a}_{\text{bodies}} = \sum_{i=2}^{n_{\text{bodies}}}\mu_i\left(\frac{\mathbf{r}_i - \mathbf{r}}{\|\mathbf{r}_i - \mathbf{r}\|_2^3} - \frac{\mathbf{r}_i}{\|\mathbf{r}_i\|_2^3}\right), \tag{2.18}$$

where $\mathbf{r}$ and $\mathbf{r}_i$ read as satellite and third-body positions with respect to a frame centered at the main body.

A well-known case arises when $n_{\text{bodies}} = 2$ and no other orbital perturbations are considered. If the satellite mass is neglected with respect to the two primaries masses, that is $M_1 \geq M_2 \gg m$, the primaries motion is independent of the satellite. This is referred as the restricted three-body problem. Under the previous conditions, its is more convenient to express the motion with respect to the synodic frame S. The synodic frame is defined as $S : \{\mathbf{O}_S, \mathbf{i}_S, \mathbf{j}_S, \mathbf{k}_S\}$ with the origin $\mathbf{O}_S$ placed at the barycenter of the primaries, $\mathbf{i}_S$ coincident with the line uniting the two primaries (main bodies) towards the second primary, $\mathbf{k}_S$ parallel to the system angular momentum and $\mathbf{j}_S$ completing a right-handed frame. The synodic frame rotates with angular velocity $\boldsymbol{\omega}_{S/I} = [0, 0, \omega(t)]^T$ and acceleration $\dot{\boldsymbol{\omega}}_{S/I} = [0, 0, \dot{\omega}(t)]^T$ with respect to an inertial frame placed at the system barycenter with $\mathbf{k}_I \equiv \mathbf{k}_S$. These quantities depend on the primaries motion which is a two-body problem. For this specific case, Eq. (2.1) yields

$$\begin{aligned}&\ddot{\mathbf{r}} + \dot{\boldsymbol{\omega}}_{S/I} \times \mathbf{r} + 2\boldsymbol{\omega}_{S/I} \times \dot{\mathbf{r}} + \boldsymbol{\omega}_{S/I} \times (\boldsymbol{\omega}_{S/I} \times \mathbf{r}) = \\ &- \frac{\mu_1(\mathbf{r} - \mathbf{r}_1)}{\|(\mathbf{r} - \mathbf{r}_1)\|_2^3} - \frac{\mu_2(\mathbf{r} - \mathbf{r}_2)}{\|(\mathbf{r} - \mathbf{r}_2)\|_2^3} + \mathbf{u},\end{aligned} \tag{2.19}$$

where $\mathbf{r} = [x, y, z]^T$ and $\dot{\mathbf{r}} = [\dot{x}, \dot{y}, \dot{z}]^T$ are the satellite position and velocity expressed in the synodic frame. The primaries positions correspond to $\mathbf{r}_1 = [x_1(t), 0, 0]^T$ and $\mathbf{r}_2 = [x_2(t), 0, 0]^T$ respectively. Note that the system (2.19) is time-varying as the angular velocity, acceleration and primaries positions vary due to the elliptic motion of the primaries.

A further simplification can be made by assuming the primaries motion is circular. This means that the distance D between them is constant which yields the case of the circular restricted three-body problem. In that case, $\omega = \sqrt{(\mu_1 + \mu_2)/D^3}$, thus $\dot{\omega} = 0$. Moreover, $x_1 = -\beta D$ and $x_2 = (1 - \beta)D$ being $\beta = \mu_2/(\mu_1 + \mu_2)$ the mass parameter. Expanding Eq. (2.19), one obtains the equation of motions for the circular restricted three-body problem

$$\begin{aligned}\ddot{x} &= \omega^2 x + 2\omega\dot{y} - \frac{\mu_1(x + \beta D)}{r_1^3} - \frac{\mu_2[x - (1 - \beta)D]}{r_2^3} + u_x, \\ \ddot{y} &= \omega^2 y - 2\omega\dot{x} - \frac{\mu_1 y}{r_1^3} - \frac{\mu_2 y}{r_2^3} + u_y, \\ \ddot{z} &= -\frac{\mu_1 z}{r_1^3} - \frac{\mu_2 z}{r_2^3} + u_z,\end{aligned} \tag{2.20}$$

where $r_1 = \sqrt{(x + \beta D)^2 + y^2 + z^2}$ and $r_2 = \sqrt{[x - (1 - \beta)D]^2 + y^2 + z^2}$ are the distances of the satellite with respect to each one of the primaries respectively. The CRTBP is an useful model for orbital mechanics as it models with adequate accuracy the intermediate region where none of the two bodies has a gravity predominance over the orbiting object. The system (2.20) has five libration points, namely the Lagrange points L_i $i = 1 \dots 5$. Around the Lagrange points, several families of periodic orbits can be computed numerically [Doedel07] (see also Appendix B for a specific case of them). The unstable or stable modes of these periodic orbits can also be exploited for the design of non-linear trajectories (invariant manifolds connection).

Atmospheric drag: if the main body has an atmosphere and the spacecraft is placed in a low enough orbit, the residual atmosphere may have a considerable effect opposing to the satellite velocity $\mathbf{v}$. The drag can be modelled as

$$\mathbf{a}_{\text{drag}} = -\frac{\rho_{\text{atm}}\|\mathbf{v} - \mathbf{v}_{\text{atm}}\|_2}{2B}(\mathbf{v} - \mathbf{v}_{\text{atm}}), \tag{2.21}$$

where ρ_{atm} is the atmospheric density, $\mathbf{v}_{\text{atm}}$ is the atmosphere velocity and B is the ballistic coefficient. The density is a highly uncertain parameter as it depends on the spatial region of the atmosphere and the solar activity. The atmosphere velocity can be assumed as the planet rotation velocity. The ballistic coefficient depends on the satellite as

$$B = \frac{m}{SC_D}, \tag{2.22}$$

where S is the frontal area and C_D is the drag coefficient. The exposed surface to the incident stream highly depends on the vehicle orientation. The drag coefficient can be roughly estimated. In view of the previous facts, it can be concluded that the atmospheric drag is hard to be modelled.

Solar radiation pressure: this is typically a minor effect (in comparison to the previous ones) but it is worth to mention as its long term impact could cause significant orbit drifting around small bodies. Moreover, solar sailing propulsion is based on this principle. Assuming the spacecraft can be approximated to l flat plates, the exerted acceleration is as follows

$$\mathbf{a}_{\text{SRP}} = \frac{1}{m}\sum_{i=1}^{l} C_{R,i}p_{1\text{AU}}A_i\cos\varphi_i\left(\frac{1\text{AU}}{r_\odot}\right)^2\frac{\mathbf{r}-\mathbf{r}_\odot}{\|\mathbf{r}-\mathbf{r}_\odot\|_2}, \tag{2.23}$$

where $C_{R,i}$ is the reflectivity coefficient, A_i is the exposed surface and φ is the light angle of incidence on each surface. The term $\mathbf{r}_\odot$ is the Sun position in a frame centered at the main body, thus $r_\odot$ is the distance between the Sun and the main body (e.g. Earth, Moon or an asteroid) in astronomical units. The variable $p_{1\text{AU}} = 4.5$ μPa is the magnitude of the solar radiation pressure, for an absorbing sheet, at a distance of 1 AU. The relative geometry between the satellite and other main bodies could eclipse the satellite-Sun line-of-sight which drastically reduces the SRP effect. The SRP perturbation is usually treated with an averaged formulation.

2.1.2 Relative motion

Proximity operations typically relies on relative models where the motion of a chaser vehicle is described with respect to a target. A relative motion model assumes the target orbit is known. Usually, the target (also named as leader or chief depending on the context) has a passive role while the chaser (also named as follower or deputy) has the control capability to change its orbit.

In the majority of cases, the relative motion between the chaser and target is studied under Keplerian assumptions. In proximity operations, the vehicles are considered to be close enough so that the relative dynamics can be linearized around the target orbit. Under the previous hypotheses, analytical solutions, providing useful insight about the relative trajectories, can be obtained. As in the absolute motion case, the relative state can be expressed using relative Cartesian coordinates [Tschauner65], classical relative orbital elements [Schaub02] or relative modified equinoctial elements [Gim05].

In this dissertation, the Cartesian representation of the relative state will be the one employed. Regarding dynamical effects, the Keplerian-based relative model will be predominantly employed. Additionally, a third-body gravity will be added for targets in periodic orbits of the restricted three-body problem. The differential inhomogeneous gravity, atmospheric drag and solar radiation pressure will not be considered in the subsequent relative motion models.

Generally, let define a frame of reference attached to the target, $\mathbf{r}_t$, as $L : \{\mathbf{r}_t, \mathbf{i}_L, \mathbf{j}_L, \mathbf{k}_L\}$. Define the relative position in the L frame as $\boldsymbol{\rho} = \mathbf{r} - \mathbf{r}_t = [x, y, z]^T$. In the frame L the relative dynamics yields

$$\begin{aligned}&\ddot{\boldsymbol{\rho}} + \dot{\boldsymbol{\omega}}_{L/I} \times \boldsymbol{\rho} + 2\boldsymbol{\omega}_{L/I} \times \dot{\boldsymbol{\rho}} + \boldsymbol{\omega}_{L/I} \times (\boldsymbol{\omega}_{L/I} \times \boldsymbol{\rho}) = \\ &-\frac{\mu(\mathbf{r}_t + \boldsymbol{\rho})}{\|\mathbf{r}_t + \boldsymbol{\rho}\|_2^3} + \frac{\mu \mathbf{r}_t}{\|\mathbf{r}_t\|_2^3} + \mathbf{a}_{\mathrm{p}} - \mathbf{a}_{\mathrm{p},t} + \mathbf{u} - \mathbf{u}_t,\end{aligned} \tag{2.24}$$

where the subindex t refers to the target. Note that $\boldsymbol{\omega}_{L/I}$ and $\dot{\boldsymbol{\omega}}_{L/I}$ are characterized by the target motion with respect to the inertial frame. Considering that the target spacecraft is passive, $\mathbf{u}_t = \mathbf{0}$, and including only third bodies gravities one obtains

$$\begin{aligned}&\ddot{\boldsymbol{\rho}} + \dot{\boldsymbol{\omega}}_{L/I} \times \boldsymbol{\rho} + 2\boldsymbol{\omega}_{L/I} \times \dot{\boldsymbol{\rho}} + \boldsymbol{\omega}_{L/I} \times (\boldsymbol{\omega}_{L/I} \times \boldsymbol{\rho}) = \\ &-\sum_{i=1}^{n_{\text{bodies}}} \mu_i \left(\frac{\mathbf{r}_{it} + \boldsymbol{\rho}}{\|\mathbf{r}_{it} + \boldsymbol{\rho}\|_2^3} - \frac{\mathbf{r}_{it}}{\|\mathbf{r}_{it}\|_2^3} \right) + \mathbf{u},\end{aligned} \tag{2.25}$$

where the main body gravity has been inserted within the summation for the sake of compactness. Note that $\mathbf{r}_{it}$ is the target position with respect to each body.

Under the proximity assumption, the relative distance is negligible against the chaser distance with respect to the main and third bodies, $\|\mathbf{r}_{it}\|_2 \gg \|\boldsymbol{\rho}\|_2$. Then, each one of the gravity terms in Eq. (2.25) can be linearized around the target position as

$$\frac{\mathbf{r}_{it} + \boldsymbol{\rho}}{\|\boldsymbol{\rho} + \mathbf{r}_{it}\|_2^3} \approx \frac{\mathbf{r}_{it}}{r_{it}^3} + \frac{1}{r_{it}^3} \left(\mathbf{I} - \frac{3\mathbf{r}_{it}\mathbf{r}_{it}^T}{r_{it}^2} \right) \boldsymbol{\rho}, \tag{2.26}$$

Introducing the linearized approximation of Eq. (2.26) into Eq. (2.25) yields

$$\begin{aligned}&\ddot{\boldsymbol{\rho}} + \dot{\boldsymbol{\omega}}_{L/I} \times \boldsymbol{\rho} + 2\boldsymbol{\omega}_{L/I} \times \dot{\boldsymbol{\rho}} + \boldsymbol{\omega}_{L/I} \times (\boldsymbol{\omega}_{L/I} \times \boldsymbol{\rho}) = \\ &-\sum_{i=1}^{n_{\text{bodies}}} \frac{\mu_i}{r_{it}^3} \left(\mathbf{I} - \frac{3\mathbf{r}_{it}\mathbf{r}_{it}^T}{r_{it}^2} \right) \boldsymbol{\rho} + \mathbf{u}.\end{aligned} \tag{2.27}$$

Equation (2.27) can be expressed algebraically as

$$\frac{d}{dt} \begin{bmatrix} \boldsymbol{\rho} \\ \dot{\boldsymbol{\rho}} \end{bmatrix} = \underbrace{\begin{bmatrix} \mathbf{0}_{3\times 3} & \mathbf{I} \\ -\dot{\boldsymbol{\Omega}}_{L/I} - \boldsymbol{\Omega}_{L/I}^2 + \mathbf{G}_{\text{grav}} & -2\boldsymbol{\Omega}_{L/I} \end{bmatrix}}_{\mathbf{A}(t)} \begin{bmatrix} \boldsymbol{\rho} \\ \dot{\boldsymbol{\rho}} \end{bmatrix} + \underbrace{\begin{bmatrix} \mathbf{0} \\ \mathbf{I} \end{bmatrix}}_{\mathbf{B}(t)} \mathbf{u}, \tag{2.28}$$

where $\boldsymbol{\Omega}_{L/I}$ and $\dot{\boldsymbol{\Omega}}_{L/I}$ express the cross product associated to $\boldsymbol{\omega}_{L/I}$ and $\dot{\boldsymbol{\omega}}_{L/I}$ algebraically

$$\boldsymbol{\Omega}_{L/I} = \begin{bmatrix} 0 & -\omega_{L/I,3} & \omega_{L/I,2} \\ \omega_{L/I,3} & 0 & -\omega_{L/I,1} \\ -\omega_{L/I,2} & \omega_{L/I,1} & 0 \end{bmatrix},$$
$$\dot{\boldsymbol{\Omega}}_{L/I} = \begin{bmatrix} 0 & -\dot{\omega}_{L/I,3} & \dot{\omega}_{L/I,2} \\ \dot{\omega}_{L/I,3} & 0 & -\dot{\omega}_{L/I,1} \\ -\dot{\omega}_{L/I,2} & \dot{\omega}_{L/I,1} & 0 \end{bmatrix}.$$

The matrix $\mathbf{G}_{\text{grav}}$ is the Jacobian of the gravity terms. The matrix $\mathbf{0}_{3\times3}$ is full of zeros. The relative motion model given by Eq. (2.28) is, in general, linear time-varying (LTV). This is a consequence of the state matrix dependence on the chaser motion. Let define the relative state as $\mathbf{x} = [\boldsymbol{\rho}^T, \dot{\boldsymbol{\rho}}^T]^T$. Then, Eq. (2.28) can be expressed as an LTV system

$$\dot{\mathbf{x}}(t) = \mathbf{A}(t)\mathbf{x}(t) + \mathbf{B}\mathbf{u}(t). \tag{2.29}$$

Keplerian-based linear relative motion

This model is largely employed for geocentric orbits. In this case, only a main body, $n_{\text{bodies}} = 1$, is considered (for the sake of clarity the subindex 1 is omitted in the sequel), thus both the target and chaser evolve in Keplerian orbits (as orbital perturbations are neglected). The relative position is expressed in a local-vertical/local-horizontal (LVLH) frame attached to the target as $L : \{\mathbf{r}_t, \mathbf{i}_L, \mathbf{j}_L, \mathbf{k}_L\}$. In the LVLH frame, $\mathbf{k}_L$ refers to the radial position (positive towards the main body centre), $\mathbf{j}_L$ to the cross-track position (opposite to the target orbit angular momentum) and $\mathbf{i}_L$ completes a right-handed system as

$$\mathbf{i}_L = \mathbf{j}_L \times \mathbf{k}_L, \quad \mathbf{j}_L = -\frac{\mathbf{r}_t \times \dot{\mathbf{r}}_t}{\|\mathbf{r}_t \times \dot{\mathbf{r}}_t\|_2}, \quad \mathbf{k}_L = -\frac{\mathbf{r}_t}{\|\mathbf{r}_t\|_2}. \tag{2.30}$$

The LVLH frame can be visually observed in Fig. 2.2. Since the target evolves in a Keplerian orbit, hence $\boldsymbol{\omega}_{L/I} = [0, -\dot{\nu}_t, 0]^T$, $\dot{\boldsymbol{\omega}}_{L/I} = [0, -\ddot{\nu}_t, 0]^T$ and $\mathbf{r}_t = [0, 0, -r_t]^T$. Let recall that ν_t is the target's true anomaly. For the sake of conciseness, the subindex t will be omitted from now on. Note that only the relative position, velocity and control correspond to the follower. Under the previous assumptions, Eq. (2.27) can be expanded as

$$\begin{aligned} \ddot{x} &= \ddot{\nu} z + 2\dot{\nu}\dot{z} + \dot{\nu}^2 x - \frac{\mu x}{r^3} + u_x, \\ \ddot{y} &= -\frac{\mu y}{r^3} + u_y, \\ \ddot{z} &= -\ddot{\nu} x - 2\dot{\nu}\dot{x} + \dot{\nu}^2 z + \frac{2\mu z}{r^3} + u_z. \end{aligned} \tag{2.31}$$

The previous set of equations is known as the Tschauner-Hempel relative motion model [Tschauner65]. Note that the in-plane (xz) motion is decoupled

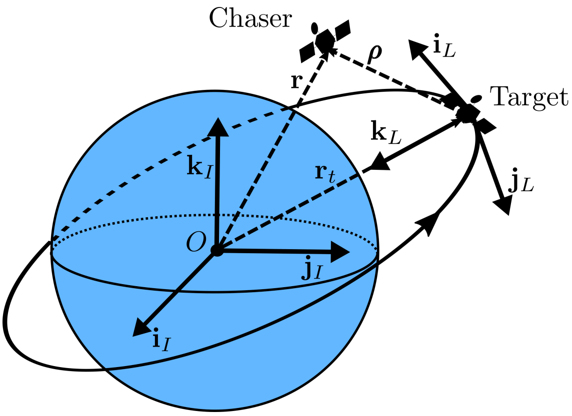

Figure 2.2: Inertial and LVLH frame for Keplerian-based relative motion

with respect to the out-of-plane (y) motion. It can be easily deduced that the solution to the out-of-plane motion is an harmonic function.

Yamanaka-Ankersen state transition matrix

The change of the independent variable from time, t, to the target true anomaly, ν, allows to obtain a more simple expression of the relative motion. The time derivatives are substituted as

$$\frac{d(\cdot)}{dt} = \frac{d(\cdot)}{d\nu}\frac{d\nu}{dt}, \quad \frac{d^2(\cdot)}{dt^2} = \frac{d^2(\cdot)}{d\nu^2}\left(\frac{d\nu}{dt}\right)^2 + \frac{d(\cdot)}{d\nu}\frac{d^2\nu}{dt^2}, \tag{2.32}$$

and the following change of variable is used

$$\tilde{\mathbf{x}}(\nu) = \mathbf{U}(\nu)\mathbf{x}(t) = \begin{bmatrix} (1+e\cos\nu)\mathbf{I} & \mathbf{0} \\ -e\sin\nu\mathbf{I} & \dfrac{1+e\cos\nu}{\dot{\nu}}\mathbf{I} \end{bmatrix}\mathbf{x}(t). \tag{2.33}$$

Applying the change of variable of Eq. (2.32)-(2.33) to the Tschauner-Hempel model, Eq. (2.31) leads to the following system

$$\tilde{\mathbf{x}}'(\nu) = \tilde{\mathbf{A}}(\nu)\tilde{\mathbf{x}}(\nu) + \mathbf{B}\tilde{\mathbf{u}}(\nu), \tag{2.34}$$

where the state matrix is now

$$\tilde{\mathbf{A}}(\nu) = \begin{bmatrix} 0 & 0 & 0 & 1 & 0 & 0 \\ 0 & 0 & 0 & 0 & 1 & 0 \\ 0 & 0 & 0 & 0 & 0 & 1 \\ 0 & 0 & 0 & 0 & 0 & 2 \\ 0 & -1 & 0 & 0 & 0 & 0 \\ 0 & 0 & \dfrac{3}{1+e\cos\nu} & -2 & 0 & 0 \end{bmatrix}. \tag{2.35}$$

An analytical state transition matrix, $\mathbf{\Phi}$, for the system given in Eq. (2.34), was deduced in [Yamanaka02]. This matrix is named as the Yamanaka-Ankersen state transition matrix. The transition from ν_0 to ν is defined in terms of the fundamental matrix $\mathbf{\Phi}_\nu$ as

$$\mathbf{\Phi}(\nu, \nu_0) = \mathbf{\Phi}_\nu \mathbf{\Phi}_{\nu_0}^{-1}, \tag{2.36}$$

$$\mathbf{\Phi}_\nu = \begin{bmatrix} 1 & 0 & -\mathrm{c}_\nu(1+\rho_\nu) & \mathrm{s}_\nu(1+\rho_\nu) & 0 & 3\rho_\nu^2 J \\ 0 & \mathrm{c}_\nu & 0 & 0 & \mathrm{s}_\nu & 0 \\ 0 & 0 & \mathrm{s}_\nu\rho_\nu & \mathrm{c}_\nu\rho_\nu & 0 & 2-3e\mathrm{s}_\nu\rho_\nu J \\ 0 & 0 & 2\mathrm{s}_\nu\rho_\nu & 2\mathrm{c}_\nu\rho_\nu - e & 0 & 3(1-2e\mathrm{s}_\nu\rho_\nu J) \\ 0 & -\mathrm{s}_\nu & 0 & 0 & \mathrm{c}_\nu & 0 \\ 0 & 0 & \mathrm{c}_\nu + e\mathrm{c}_{2\nu} & -\mathrm{s}_\nu - e\mathrm{s}_{2\nu} & 0 & -3e\left[(\mathrm{c}_\nu + e\mathrm{c}_{2\nu})J + \dfrac{\mathrm{s}_\nu}{\rho_\nu}\right] \end{bmatrix},$$

where $\mathrm{c}_\nu = \cos\nu$, $\mathrm{s}_\nu = \sin\nu$, $\mathrm{c}_{2\nu} = \cos 2\nu$, $\mathrm{s}_{2\nu} = \sin 2\nu$, $\rho_\nu = 1 + e\cos\nu$ and

$$J = \int_{\nu_0}^{\nu} \frac{1}{(1+e\cos\tau)^2} d\tau = \sqrt{\frac{\mu}{[a(1-e^2)]^3}}(t-t_0), \tag{2.37}$$

is the drift term. Note that $\det(\mathbf{\Phi}_\nu) = e^2 - 1$, thus the inverse of the fundamental matrix is always defined for elliptical orbits ($0 \leq e < 1$). Using the Yamanaka-Ankersen transition matrix, the relative state can be propagated as

$$\tilde{\mathbf{x}}(\nu) = \mathbf{\Phi}(\nu, \nu_0)\tilde{\mathbf{x}}(\nu_0) + \int_{\nu_0}^{\nu} \mathbf{\Phi}(\nu, \tau)\mathbf{B}\tilde{\mathbf{u}}(\tau) d\tau, \quad \nu \geq \nu_0. \tag{2.38}$$

Vector of relative parameters

In the spirit of the classical orbital elements, which are invariants of the absolute motion under a Keplerian model, the vector of relative parameters was conceived in [Deaconu13] to describe relative periodic orbits. By substituting the relative cartesian coordinates, the vector of relative parameters provides an alternate state description. This description is very convenient for flight formation purposes as it provides insight on the relative orbits center and size.

The transformation from Cartesian coordinates to the vector of relative parameters is subsequently derived. In [Deaconu13], it was noticed that the term $\mathbf{\Phi}_{\nu_0}^{-1}\tilde{\mathbf{x}}(\nu_0)$ arising in Eq. (2.38) is constant for a given initial time ν_0. Expanding Eq. (2.38) for the natural motion ($\mathbf{u}(t) = \mathbf{0}$) and factoring out the constant terms relative to $\mathbf{\Phi}_{\nu_0}^{-1}\tilde{\mathbf{x}}(\nu_0)$ gives

$$\begin{aligned}
\tilde{x} &= 3\rho_\nu^2 J d_0 + \mathrm{s}_\nu(1+\rho_\nu)d_1 - \mathrm{c}_\nu(1+\rho_\nu)d_2 + d_3,\\
\tilde{y} &= \mathrm{c}_\nu d_4 + \mathrm{s}_\nu d_5,\\
\tilde{z} &= (2 - 3e\mathrm{s}_\nu\rho_\nu J)d_0 + \mathrm{c}_\nu\rho_\nu d_1 + \mathrm{s}_\nu\rho_\nu d_2,\\
\tilde{v}_x &= 3(1 - 2e\mathrm{s}_\nu\rho_\nu J)d_0 + (2\mathrm{c}_\nu\rho_\nu - e)d_1 + 2\mathrm{s}_\nu\rho_\nu d_2,\\
\tilde{v}_y &= -\mathrm{s}_\nu d_4 + \mathrm{c}_\nu d_5,\\
\tilde{v}_z &= -3e\left[(\mathrm{c}_\nu + e\mathrm{c}_{2\nu})J + \frac{\mathrm{s}_\nu}{\rho_\nu}\right]d_0 - (\mathrm{s}_\nu + e\mathrm{s}_{2\nu})d_1 + (\mathrm{c}_\nu + e\mathrm{c}_{2\nu})d_2,
\end{aligned} \tag{2.39}$$

where the terms d_i are the components of $\mathbf{\Phi}_{\nu_0}^{-1}\tilde{\mathbf{x}}(\nu_0)$. Note that they are in a different order since $\{d_0, d_1, d_2, d_3\}$ have been associated to the xz coordinates while $\{d_4, d_5\}$ correspond to the y coordinate. Let define $\mathbf{d}$ as the vector of relative parameters, at time ν,

$$\mathbf{d}(\nu) = [d_0(\nu), d_1(\nu), d_2(\nu), d_3(\nu), d_4(\nu), d_5(\nu)]^T, \tag{2.40}$$

then the following relation between the relative state $\tilde{\mathbf{x}}$ and the vector of relative parameters $\mathbf{d}$ holds

$$\tilde{\mathbf{x}}(\nu) = \underbrace{\begin{bmatrix}
0 & \mathrm{s}_\nu(1+\rho_\nu) & -\mathrm{c}_\nu(1+\rho_\nu) & 1 & 0 & 0\\
0 & 0 & 0 & 0 & \mathrm{c}_\nu & \mathrm{s}_\nu\\
2 & \mathrm{c}_\nu\rho_\nu & \mathrm{s}_\nu\rho_\nu & 0 & 0 & 0\\
3 & 2\mathrm{c}_\nu\rho_\nu - e & 2\mathrm{s}_\nu\rho_\nu & 0 & 0 & 0\\
0 & 0 & 0 & 0 & -\mathrm{s}_\nu & \mathrm{c}_\nu\\
-\dfrac{3e\mathrm{s}_\nu}{\rho_\nu} & -(\mathrm{s}_\nu + e\mathrm{s}_{2\nu}) & \mathrm{c}_\nu + e\mathrm{c}_{2\nu} & 0 & 0 & 0
\end{bmatrix}}_{\mathbf{W}(\nu)} \mathbf{d}(\nu). \tag{2.41}$$

The transformation matrix $\mathbf{W}$ is composed of the fundamental matrix $\mathbf{\Phi}_\nu$ terms with the columns sorted as $\{1 \to 4, 2 \to 5, 4 \to 2, 5 \to 6, 6 \to 1\}$. This rearrangement is required because the in-plane terms $\{x, z, \dot{x}, \dot{z}\}$ have been associated to $\{d_0, d_1, d_2, d_3\}$ while the out-of-plane coordinates $\{y, \dot{y}\}$ are associated to $\{d_4, d_5\}$. Note that in the previous case the drift term is null, $J = 0$, because no drift arises during a single instant. Additionally the transformation matrix determinant is $\det(\mathbf{W}) = 1 - e^2$, thus being its inverse defined for closed orbits $(0 \le e < 1)$. Consequently, the inverse transformation exists as

$$\mathbf{d}(\nu) = \mathbf{W}^{-1}(\nu)\tilde{\mathbf{x}}(\nu) = \mathbf{C}(\nu)\tilde{\mathbf{x}}(\nu), \tag{2.42}$$

which represents a similarity transformation and $\mathbf{d}$ is a proper state vector with its own dynamics. Differentiating Eq. (2.42) with respect to the independent variable ν yields

$$\mathbf{d}'(\nu) = \mathbf{C}'(\nu)\tilde{\mathbf{x}}(\nu) + \mathbf{C}(\nu)\tilde{\mathbf{x}}'(\nu). \tag{2.43}$$

Then, introducing Eq. (2.34) and Eq. (2.41), into Eq. (2.43) provides the vector of relative parameters dynamics as

$$\begin{aligned}\mathbf{d}'(\nu) &= [\mathbf{C}'(\nu) + \mathbf{C}(\nu)\tilde{\mathbf{A}}(\nu)]\mathbf{W}(\nu)\mathbf{d}(\nu) + \mathbf{C}(\nu)\mathbf{B}\tilde{\mathbf{u}}(\nu) \\ &= \mathbf{A}_D(\nu)\mathbf{d}(\nu) + \mathbf{B}_D(\nu)\tilde{\mathbf{u}}(\nu).\end{aligned} \tag{2.44}$$

The vector of relative parameters state matrix $\mathbf{A}_D$ and control matrix $\mathbf{B}_D$ can be expanded as

$$\mathbf{A}_D(\nu) = \begin{bmatrix} 0 & 0 & 0 & 0 & 0 & 0 \\ 0 & 0 & 0 & 0 & 0 & 0 \\ -\dfrac{3e}{\rho_\nu^2} & 0 & 0 & 0 & 0 & 0 \\ \dfrac{3}{\rho_\nu^2} & 0 & 0 & 0 & 0 & 0 \\ 0 & 0 & 0 & 0 & 0 & 0 \\ 0 & 0 & 0 & 0 & 0 & 0 \end{bmatrix}, \tag{2.45}$$

$$\mathbf{B}_D(\nu) = \frac{1}{1-e^2}\begin{bmatrix} -\rho_\nu^2 & 0 & e\mathrm{s}_\nu\rho_\nu \\ 2\mathrm{c}_\nu + e\mathrm{c}_\nu^2 & 0 & -\mathrm{s}_\nu\rho_\nu \\ \mathrm{s}_\nu(2 + e\mathrm{c}_\nu) & 0 & \mathrm{c}_\nu + e\mathrm{c}_\nu^2 - 2e \\ -e\mathrm{s}_\nu(2 + e\mathrm{c}_\nu) & 0 & -(e^2\mathrm{c}_\nu^2 + e\mathrm{c}_\nu - 2) \\ 0 & -(1-e^2)s_\nu & 0 \\ 0 & (1-e^2)c_\nu & 0 \end{bmatrix}. \tag{2.46}$$

By examining the state matrix $\mathbf{A}_D$, it can be deduced that $d_0 = 0$ corresponds to a relative periodic orbit. The relative orbit periodicity has a 1:1 relation with the target orbital period. It is concluded that nullifying the term d_0 is the necessary and sufficient condition to obtain a relative periodic motion. This could have been also deduced by noting that in the explicit solution of Eq. (2.39) the only term associated with the drift J is d_0. For a periodic relative orbit, the parameters d_1 and d_2 master the relative orbit amplitudes in the orbital plane. The parameter d_3 is the center of the orbit which can only be varied along the in-track direction. Note that it is not possible to have the orbit center along the radial direction as this causes a drift due to the orbital periods difference. Similarly, the terms d_4 and d_5 master the out-of-plane coordinate amplitudes.

It should be noticed that the control action depends on the application time due to the control matrix $\mathbf{B}_D$ time dependency (see Eq. (2.46)).

The state transition matrix, for the vector of relative parameters, can be derived by inserting the similarity transformation of Eq. (2.41) into the Yamanaka-Ankersen transition matrix of Eq. (2.38)

$$\mathbf{d}(\nu) = \mathbf{W}^{-1}(\nu)\mathbf{\Phi}(\nu,\nu_0)\mathbf{W}(\nu_0)\mathbf{d}(\nu_0) = \mathbf{\Phi}_D(\nu,\nu_0)\mathbf{d}(\nu_0), \tag{2.47}$$

then $\mathbf{\Phi}_D$ states as

$$\mathbf{\Phi}_D(\nu,\nu_0)=\begin{bmatrix}1&0&0&0&0&0\\0&1&0&0&0&0\\-3eJ&0&1&0&0&0\\3J&0&0&1&0&0\\0&0&0&0&1&0\\0&0&0&0&0&1\end{bmatrix}. \tag{2.48}$$

The state propagation (see Eq. (2.38)) is projected in the vector of relative parameters space as

$$\mathbf{d}(\nu)=\mathbf{\Phi}_D(\nu,\nu_0)\mathbf{d}(\nu_0)+\int_{\nu_0}^{\nu}\mathbf{\Phi}_D(\nu,\tau)\mathbf{B}_D(\nu)\tilde{\mathbf{u}}(\tau)d\tau,\quad \nu\geq\nu_0. \tag{2.49}$$

Restricted three-body problem linear relative motion

Proximity operations around periodic orbits in the restricted three-body problem will be a reality in the near future. Consequently, there is a need to develop relative motion models under that scenario. Let start by projecting the linearized Eq. (2.27) of relative motion in the synodic frame S with two main bodies ($n_{\text{bodies}}=2$)

$$\begin{aligned}\ddot{\boldsymbol{\rho}}=&-\dot{\boldsymbol{\omega}}_{S/I}\times\boldsymbol{\rho}-2\boldsymbol{\omega}_{S/I}\times\dot{\boldsymbol{\rho}}-\boldsymbol{\omega}_{S/I}\times(\boldsymbol{\omega}_{S/I}\times\boldsymbol{\rho})\\&-\sum_{i=1}^{2}\mu_i\left(\frac{\mathbf{r}_{it}+\boldsymbol{\rho}}{\|\mathbf{r}_{it}+\boldsymbol{\rho}\|_2^3}-\frac{\mathbf{r}_{it}}{\|\mathbf{r}_{it}\|_2^3}\right)+\mathbf{u},\end{aligned} \tag{2.50}$$

which can be decomposed as

$$\begin{aligned}\ddot{x}&=\omega^2x+\dot{\omega}y+2\omega\dot{y}-\sum_{i=1}^{2}\frac{\mu_i}{r_{it}^3}\left[\left(1-\frac{3x_{it}^2}{r_{it}^2}\right)x-3\frac{x_{it}y_{it}}{r_{it}^2}y-3\frac{x_{it}z_{it}}{r_{it}^2}z\right]+u_x,\\ \ddot{y}&=\omega^2y-\dot{\omega}x-2\omega\dot{x}-\sum_{i=1}^{2}\frac{\mu_i}{r_{it}^3}\left[\left(1-\frac{3y_{it}^2}{r_{it}^2}\right)y-3\frac{x_{it}y_{it}}{r_{it}^2}x-3\frac{y_{it}z_{it}}{r_{it}^2}y\right]+u_y,\\ \ddot{z}&=-\sum_{i=1}^{2}\frac{\mu_i}{r_{it}^3}\left[\left(1-\frac{3z_{it}^2}{r_{it}^2}\right)z-3\frac{x_{it}z_{it}}{r_{it}^2}x-3\frac{y_{it}z_{it}}{r_{it}^2}y\right]+u_z.\end{aligned}$$

Unlike the Keplerian-based linear relative model, the motion in the plane of the primaries xy is mutually coupled with the out-of-plane motion z. An additional difficulty is that the restricted-three body problem periodic orbits are parameterized numerically. Assuming the target is placed in that orbit its position can not described analytically but $\mathbf{r}_t(t)=\mathbf{r}_t(t+kT)$ for $k\in\mathbb{N}$, where T is the orbital period, can be assured. Due to these facts, the system given by Eq. (2.50) is LTV with a periodicity of T. In any case, the state transition matrix has to be computed numerically by integrating the following system

$$\dot{\mathbf{\Phi}}(t,t_0)=\mathbf{A}(t)\mathbf{\Phi}(t,t_0),\quad t\geq t_0, \tag{2.51}$$

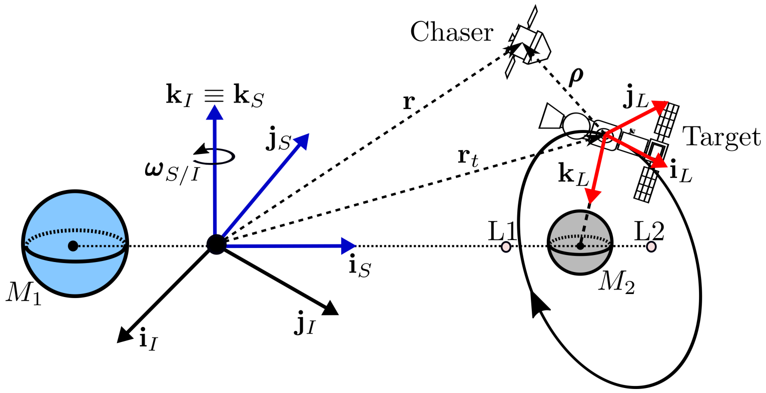

Figure 2.3: Inertial, synodic and LVLH frames for RTBP relative motion

which is composed of 36 linear ordinary differential equations. Due to the periodicity of the target orbit, the coefficient matrix is also periodic $\mathbf{A}(t) = \mathbf{A}(t+kT)$ as well as the state transition matrix $\mathbf{\Phi}(t) = \mathbf{\Phi}(t+kT)$. This fact suggests the possibility of pre-computing and storing the restricted-three body problem state transition matrices in order to diminish the computational load.

Local-vertical/local-horizontal frame

The use of a local frame attached to the target orbit provides a very intuitive idea of the relative position configuration. In order to mimic the Keplerian-based relative motion LVLH frame (see Fig. 2.2) [Franzini17] proposed its counterpart for relative motion in the RTBP. Moreover, it eases any kind of constraints referred to the target. To this end, the RTBP local-vertical local-horizontal frame is defined as $L : \{\mathbf{r}_t, \mathbf{i}_L, \mathbf{j}_L, \mathbf{k}_L\}$ (see Fig. 2.3) where the origin is attached to the position of the target center of mass $\mathbf{r}_t$, $\mathbf{k}_L$ points towards the second primary, $\mathbf{j}_L$ is parallel to the target kinetic momentum (as view from the S frame with respect to the second primary) and $\mathbf{i}_L$ closes the right-handed system such that

$$\mathbf{i}_L = \mathbf{j}_L \times \mathbf{k}_L, \quad \mathbf{j}_L = -\frac{\mathbf{r}_{2t} \times \dot{\mathbf{r}}_{2t}}{\|\mathbf{r}_{2t} \times \dot{\mathbf{r}}_{2t}\|_2}, \quad \mathbf{k}_L = -\frac{\mathbf{r}_{2t}}{\|\mathbf{r}_{2t}\|_2}. \tag{2.52}$$

Let recall that the previous frame assumed the second primary is the Moon, thus being specially convenient for systems with a mass parameter of $\beta \approx 0$. In that situation, the $L1$ and $L2$ libration points are close to the secondary, thus their associated families of periodic orbits are in the vicinity of the secondary. Projecting, the relative dynamics of Eq. (2.27) under RTBP assumptions, in the LVLH frame states

$$\begin{aligned}\ddot{\boldsymbol{\rho}} = & - \left[\dot{\boldsymbol{\Omega}}_{L/I} + \boldsymbol{\Omega}^2_{L/I} + \frac{\mu_1}{r^3_{1t}}\left(\mathbf{I} - 3\frac{\mathbf{r}_{1t}\mathbf{r}^T_{1t}}{r^2_{1t}}\right) + \frac{\mu_2}{r^3_{2t}}\left(\mathbf{I} - 3\frac{\mathbf{r}_{2t}\mathbf{r}^T_{2t}}{r^2_{2t}}\right)\right]\boldsymbol{\rho} \\ & - 2\boldsymbol{\Omega}_{L/I}\dot{\boldsymbol{\rho}} + \mathbf{u},\end{aligned} \tag{2.53}$$

which can be recast in the same compact form as Eq. (2.28)

$$\frac{d}{dt}\begin{bmatrix}\boldsymbol{\rho} \\ \dot{\boldsymbol{\rho}}\end{bmatrix} = \begin{bmatrix}\mathbf{0}_{3\times3} & \mathbf{I} \\ -\dot{\boldsymbol{\Omega}}_{L/I} - \boldsymbol{\Omega}^2_{L/I} + \mathbf{G}_{\text{grav}} & -2\boldsymbol{\Omega}_{L/I}\end{bmatrix}\begin{bmatrix}\boldsymbol{\rho} \\ \dot{\boldsymbol{\rho}}\end{bmatrix} + \begin{bmatrix}\mathbf{0} \\ \mathbf{I}\end{bmatrix}\mathbf{u}, \tag{2.54}$$

with the gravity Jacobian matrix as

$$\mathbf{G}_{\text{grav}} = -\frac{\mu_1}{r^3_{1t}}\left(\mathbf{I} - 3\frac{\mathbf{r}_{1t}\mathbf{r}^T_{1t}}{r^2_{1t}}\right) - \frac{\mu_2}{r^3_{2t}}\left(\mathbf{I} - 3\frac{\mathbf{r}_{2t}\mathbf{r}^T_{2t}}{r^2_{2t}}\right). \tag{2.55}$$

The rotation of the LVLH frame with respect to the inertial frame can be decomposed as

$$\boldsymbol{\omega}_{L/I} = \boldsymbol{\omega}_{L/S} + \boldsymbol{\omega}_{S/I}, \tag{2.56}$$

$$\dot{\boldsymbol{\omega}}_{L/I}\big|_L = \dot{\boldsymbol{\omega}}_{L/S}\big|_L + \dot{\boldsymbol{\omega}}_{S/I}\big|_S - \boldsymbol{\omega}_{L/S} \times \boldsymbol{\omega}_{S/I}, \tag{2.57}$$

where it should be noted that, when expressed in the synodic frame, $\boldsymbol{\omega}_{S/I}$ and $\dot{\boldsymbol{\omega}}_{S/I}$ only depend on the primaries motion which is a two-body problem (as mentioned in the *third bodies gravity* paragraph of Section 2.1.1). The terms $\boldsymbol{\omega}_{L/S}$ and $\dot{\boldsymbol{\omega}}_{L/S}$ depend on the target RTBP periodic orbit such that

$$\begin{aligned}\boldsymbol{\omega}_{L/S} = & - \left(\frac{\dot{\mathbf{r}}^T_{2t}\mathbf{i}_L}{r_{2t}}\right)\mathbf{j}_L + \left(\frac{r_{2t}}{h_{2t}}\ddot{\mathbf{r}}^T_{2t}\mathbf{j}_L\right)\mathbf{k}_L, \\ \dot{\boldsymbol{\omega}}_{L/S}\big|_L = & - \left(\frac{\ddot{\mathbf{r}}^T_{2t}\mathbf{i}_L + 2\dot{r}_{2t}\boldsymbol{\omega}^T_{L/S}\mathbf{j}_L}{r_{2t}}\right)\mathbf{j}_L \\ & + \left[\left(\frac{\dot{r}_{2t}}{h_{2t}}\ddot{\mathbf{r}}^T_{2t} + \frac{r_{2t}}{h_{2t}}\dddot{\mathbf{r}}^T_{2t}\right)\mathbf{j}_L - 2\frac{r^2_{2t}}{h^2_{2t}}(\ddot{\mathbf{r}}^T_{2t}\mathbf{i}_L)(\ddot{\mathbf{r}}^T_{2t}\mathbf{j}_L)\right]\mathbf{k}_L,\end{aligned}$$

where $h_{2t} = \|\mathbf{r}_{2t} \times \dot{\mathbf{r}}_{2t}\|_2$ is the module of the target orbit angular momentum (with respect to the secondary) in the synodic frame. Note that the angular velocity and acceleration of the LVLH frame with respect to the synodic frame exclusively depends on the target relative motion around the secondary, $\mathbf{r}_{2t} = \mathbf{r}_t - \mathbf{r}_2$. Let recall that, when expressed in the synodic frame, $\mathbf{r}_2 = [r_2(t), 0, 0]^T$ is time-varying if the primaries motion is eccentric ($r_2 \equiv$ constant if their motion is circular). The details of the relative equations of motion in the LVLH frame can be found in [Franzini17].

2.1.3 Thrust models

The orbit control model will depend on the employed thrusters. For instance, proximity operations largely rely on chemical or cold gas thrusters which can be modelled impulsively (jumps in the velocity). In a more sophisticated manner, pulse amplitude or width modulation models could be employed. Furthermore, the emergence of electric thrusters, able of providing low thrust during long periods of time, implies the necessity of continuous thrust models.

Impulsive model

The velocity jump provided by a chemical or cold gas array of thrusters, acted at time t_k, can be quantified as

$$\Delta\mathbf{V}(t) = \lim_{\Delta t_k \to 0} \int_{t_k}^{t_k+\Delta t_k} \mathbf{u}(\tau) d\tau \delta(t-t_k) = \Delta\mathbf{V}_k \delta(t-t_k), \tag{2.58}$$

where δ is the Kronecker delta function. It is assumed that the thrusters opening times, Δt_k, can be adjusted to produce the required impulse amplitude. In that line, the impulsive model changes the relative velocity instantaneously as

$$\dot{\boldsymbol{\rho}}^+(t) = \dot{\boldsymbol{\rho}}(t) + \Delta\mathbf{V}(t), \tag{2.59}$$

where the superscript $^+$ denotes the velocity after the impulse is applied.

For Keplerian-based relative motion, the vector of parameters is affected by an impulse in a very particular way such that

$$\mathbf{d}^+(\nu) = \mathbf{d}(\nu) + \mathbf{B}_D(\nu)\Delta\mathbf{V}(\nu), \tag{2.60}$$

where the impulse effect, on the state, depends on the application instant as

$$\mathbf{B}_D(\nu) = \mathbf{W}^{-1}(\nu)\mathbf{U}(\nu)\mathbf{B} = \sqrt{\frac{p^3}{\mu}} \frac{1}{(e^2-1)\rho_\nu} \begin{bmatrix} \rho_\nu^2 & 0 & -e\mathrm{s}_\nu\rho_\nu \\ -2\mathrm{c}_\nu - e(1+\mathrm{c}_\nu^2) & 0 & \mathrm{s}_\nu\rho_\nu \\ -\mathrm{s}_\nu(2+e\mathrm{c}_\nu) & 0 & 2e-\mathrm{c}_\nu\rho_\nu \\ e\mathrm{s}_\nu(2+e\mathrm{c}_\nu) & 0 & e\mathrm{c}_\nu\rho_\nu - 2 \\ 0 & -(e^2-1)\mathrm{s}_\nu & 0 \\ 0 & (e^2-1)\mathrm{c}_\nu & 0 \end{bmatrix}. \tag{2.61}$$

Let recall that p is the semi-latus rectum. The impulsive effect on orbital and modified equinoctial elements is not stated as it is not used through this dissertation.

Acceleration models

Three acceleration based control models are presented. The pulse amplitude modulation and continuous models are appropriate for electric thrusters. The pulse width modulation model expands the impulsive model providing a more realistic way of operating chemical or cold gas thrusters. Finally, a disturbance model is presented for both the applied impulse or acceleration.

Pulse amplitude modulation (PAM)

This model assumes a time discretization where the exerted acceleration is constant along each discretized interval. Assume N intervals over the control horizon, each one spanning from the instant t_{k-1} to the instant t_k, then

$$\mathbf{u}(t) := \{\mathbf{u}_k, \quad t \in [t_{k-1}, t_k), \quad k = 1 \ldots N\}. \tag{2.62}$$

It is assumed that instantaneous changes in the accelerations between intervals occur. A more realistic model could consider the thrusters rise time as

$$\mathbf{u}(t) := \{\mathbf{u}_k + e^{-\tau(t-t_{k-1})}(\mathbf{u}_{k-1} - \mathbf{u}_k), \quad t \in [t_{k-1}, t_k), \quad k = 1 \ldots N\}, \tag{2.63}$$

where the time constant τ determines how fast the thruster can change its exerted acceleration.

Pulse width modulation (PWM)

This model directly controls the thrusters valves opening and closing times. The thrusters operate in an ON/OFF regime with the same level of thrust. This way, the control variables are the thruster opening time, τ, and its duration κ. Assuming an array of n_T thrusters

$$\mathbf{u}(t) = \sum_{p=1}^{n_T} u_p(t)\mathbf{w}_p, \quad u_p(t) = \begin{cases} 0, & t < \tau_p, \\ \bar{u}_p, & t \in [\tau_p, \tau_p + \kappa_p], \\ 0, & t > \tau_p + \kappa_p, \end{cases} \tag{2.64}$$

where the subindex p refers to each thruster of the array, $\bar{u}_p$ the control acceleration level and $\mathbf{w}_p$ refers to each thruster control direction.

B-splines parameterization

Both the PAM and PWM models assume instantaneous jumps of the control signal when a control switch activates. However, the particular case of electric thrusters may require a continuous control acceleration profile. To this end, the control signal can be parameterized in terms of B-splines (see Appendix A for the details), to achieve continuity up to C^q

$$\mathbf{u}(t) = \sum_{j=1}^{n_c} B_{j,q}(t)\boldsymbol{\xi}_j, \tag{2.65}$$

where $B_{j,q}$ are q^{th} order B-splines, built on a predefined knots sequence $\mathbf{t}_{\text{knots}}$, while $\boldsymbol{\xi}_j$ are the control points.

Disturbances

Typically, the applied control, $\Delta\mathbf{V}^*$ or $\mathbf{u}^*$, will differ from the computed one. Assuming the application times are perfectly controlled, the discrepancy is caused by the thrusters imperfect alignment and mismatches on the thrust level. Generally, additive and multiplicative noises may be considered as

$$\Delta\mathbf{V}^* = \Delta\mathbf{R}(\boldsymbol{\delta\theta})[\Delta\mathbf{V}(1+\epsilon_{\Delta V}) + \boldsymbol{\delta}\mathbf{V}], \tag{2.66}$$

$$\mathbf{u}^* = \Delta\mathbf{R}(\boldsymbol{\delta\theta})[\mathbf{u}(1+\epsilon_u) + \boldsymbol{\delta}\mathbf{u}], \tag{2.67}$$

where $\Delta\mathbf{R}$ is the misalignment rotation matrix whose input are the small angles $\boldsymbol{\delta\theta}$. Regarding thrust level mismatch, $\epsilon_{\Delta V}$ and ϵ_u are multiplicative disturbances affecting the computed thrust level proportionally. The multiplicative disturbance could model, in a simplified way, thrust level losses due to the transient responses to thrust changes. On the other hand, $\boldsymbol{\delta}\mathbf{V}$ and $\boldsymbol{\delta}\mathbf{u}$ are additive disturbances independent of the commanded thrust level. The additive disturbance could account for inherent fabrication defects affecting all the thrusters in the same way.

In this dissertation, the disturbances are assumed to be Gaussian as

$$\boldsymbol{\delta\theta} \sim N_3(\widehat{\boldsymbol{\delta\theta}}, \boldsymbol{\Sigma}_{\boldsymbol{\delta\theta}}), \tag{2.68}$$

$$\epsilon_{\Delta V} \sim N(\hat{\epsilon}_{\Delta V}, \sigma^2_{\epsilon_{\Delta V}}), \qquad \boldsymbol{\delta}\mathbf{V} \sim N_3(\widehat{\boldsymbol{\delta}\mathbf{V}}, \boldsymbol{\Sigma}_{\boldsymbol{\delta}\mathbf{V}}), \tag{2.69}$$

$$\epsilon_u \sim N(\hat{\epsilon}_u, \sigma^2_{\epsilon_u}), \qquad \boldsymbol{\delta}\mathbf{u} \sim N_3(\widehat{\boldsymbol{\delta}\mathbf{u}}, \boldsymbol{\Sigma}_{\boldsymbol{\delta}\mathbf{u}}), \tag{2.70}$$

where N_n is a multivariate Gaussian distribution of dimension n. The hat symbol denotes the random variable bias, σ the standard deviation and $\boldsymbol{\Sigma}$ the covariance matrix.

2.2 Angular motion

The angular motion describes the spacecraft orientation (namely the attitude) evolution. In this dissertation, the Euler angles, quaternions and modified Rodrigues parameters representations will be presented. Then, the body frame is employed to express the attitude dynamics. A coupling with the translational motion arises if the gravity-gradient torque is considered. In this work, the considered mean of attitude control is reaction wheels for which two simplified models will be presented.

2.2.1 Attitude representation

This section presents several attitude representation options such as Euler angles, quaternions and modified Rodrigues parameters.

Euler angles

The Euler angles are three angles describing the orientation of a rigid body with respect to a coordinate system. Each angle defines an elemental rotation with respect to an axis. As a matter of fact, there exist twelve possible sequences of rotations:

- Proper Euler angles: $\{zxz\}$, $\{xyx\}$, $\{yzy\}$, $\{zyz\}$, $\{xzx\}$, $\{yxy\}$.
- Tait-Bryan angles: $\{xyz\}$, $\{yzx\}$, $\{zxy\}$, $\{xzy\}\}$, $\{zyx\}$, $\{yxz\}$.

A widely employed sequence in aerospace engineering is the $\{zxy\}$ which is properly defined as

$$I \xrightarrow[z_I]{\theta_3} S \xrightarrow[y_S]{\theta_2} S' \xrightarrow[x_{S'}]{\theta_1} B, \tag{2.71}$$

where $\theta_3 \equiv$ yaw, $\theta_2 \equiv$ pitch and $\theta_1 \equiv$ roll.

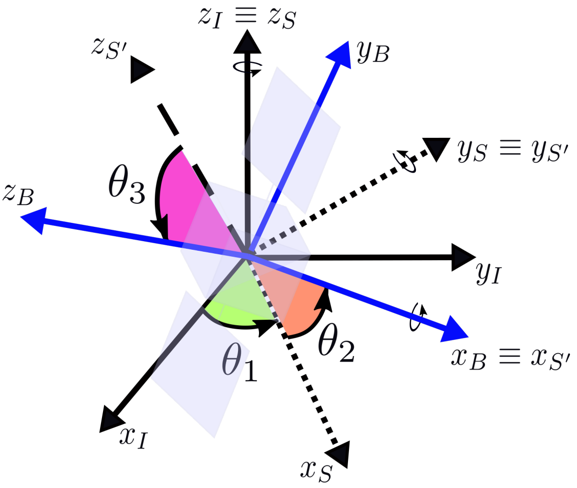

Figure 2.4: Euler angles for $\{zxy\}$ sequence.

The associated rotation matrix can be expressed as the composition of these elemental rotations. For the $\{zxy\}$ sequence

$$\begin{aligned}\mathbf{R}(\theta_1,\theta_2,\theta_3) &= \mathbf{R}_x(\theta_1)\mathbf{R}_y(\theta_2)\mathbf{R}_z(\theta_3)\\ &= \begin{bmatrix} c_{\theta_2}c_{\theta_3} & c_{\theta_2}s_{\theta_3} & -s_{\theta_2}\\ -c_{\theta_1}s_{\theta_3}+s_{\theta_1}s_{\theta_2}c_{\theta_3} & c_{\theta_1}c_{\theta_3}+s_{\theta_1}s_{\theta_2}s_{\theta_3} & s_{\theta_1}c_{\theta_2}\\ s_{\theta_1}s_{\theta_3}+c_{\theta_1}s_{\theta_2}c_{\theta_3} & -s_{\theta_1}c_{\theta_3}+c_{\theta_1}s_{\theta_2}s_{\theta_3} & c_{\theta_1}c_{\theta_2}\end{bmatrix},\end{aligned} \tag{2.72}$$

where $c_{(\cdot)} = \cos(\cdot)$ and $s_{(\cdot)} = \sin(\cdot)$. Note that, according to Eq. (2.72), $\{\theta_1+\pi, \pi-\theta_2, \theta_3+\pi\}$ represents the same orientation as $\{\theta_1,\theta_2,\theta_3\}$. To avoid this ambiguity, the pitch angle is usually restricted as $\theta_2 \in [-\pi/2, \pi/2]$. The Euler angles kinematics is derived taking into account that the angular velocity between frames is the composition of each elemental rotation angular velocity

$$\boldsymbol{\omega}^B_{B/I} = \boldsymbol{\omega}^B_{B/S'} + \boldsymbol{\omega}^B_{S'/S} + \boldsymbol{\omega}^B_{S/I}, \tag{2.73}$$

where taking into account that

$$\boldsymbol{\omega}^B_{B/S'} = [\dot{\theta}_1, 0, 0]^T, \quad \boldsymbol{\omega}^{S'}_{S'/S} = [0, \dot{\theta}_2, 0]^T, \quad \boldsymbol{\omega}^S_{S/I'} = [0, 0, \dot{\theta}_3]^T, \tag{2.74}$$

Eq. (2.73) can be rewritten as

$$\boldsymbol{\omega}^B_{B/I} = \boldsymbol{\omega}^B_{B/S'} + \mathbf{R}^B_{S'}\boldsymbol{\omega}^{S'}_{S'/S} + \mathbf{R}^B_S\boldsymbol{\omega}^S_{S/I}, \tag{2.75}$$

thus, developing this equation and clearing the Euler angles derivatives, one obtains the kinematics expression

$$\frac{d}{dt}\begin{bmatrix}\theta_1\\ \theta_2\\ \theta_3\end{bmatrix} = \frac{1}{\mathrm{c}_{\theta_2}}\begin{bmatrix}\mathrm{c}_{\theta_2} & \mathrm{s}_{\theta_1}\mathrm{s}_{\theta_2} & \mathrm{c}_{\theta_1}\mathrm{s}_{\theta_2}\\ 0 & \mathrm{c}_{\theta_1}\mathrm{c}_{\theta_2} & -\mathrm{s}_{\theta_1}\mathrm{c}_{\theta_2}\\ 0 & \mathrm{s}_{\theta_1} & \mathrm{c}_{\theta_1}\end{bmatrix}\begin{bmatrix}\omega_1\\ \omega_2\\ \omega_3\end{bmatrix}, \tag{2.76}$$

where $\boldsymbol{\omega}^B_{B/I} = [\omega_1, \omega_2, \omega_3]^T$. The kinematics can be expressed compactly as

$$\dot{\boldsymbol{\theta}}_{B/I} = \mathbf{C}(\boldsymbol{\theta}_{B/I})\boldsymbol{\omega}^B_{B/I}, \tag{2.77}$$

where $\boldsymbol{\theta}_{B/I} = [\theta_1, \theta_2, \theta_3]^T$ are the Euler angles representing the body orientation with respect to the inertial frame. Sometimes it could be advantageous to express the body orientation with respect to a non-inertial frame L. In such case, the kinematics can be modified as

$$\dot{\boldsymbol{\theta}}_{B/L} = \mathbf{C}(\boldsymbol{\theta}_{B/L})[\boldsymbol{\omega}^B_{B/I} - \mathbf{R}(\boldsymbol{\theta}_{B/L})\boldsymbol{\omega}^L_{L/I}], \tag{2.78}$$

where the non-inertial frame angular velocity with respect to the inertial frame has to be known. Note that $\mathbf{R}(\boldsymbol{\theta}_{B/L}) = \mathbf{R}^B_L$ is the rotation matrix from the L frame to the B frame.

The Euler angles kinematics (see Eq. (2.76)) suffers singularities for $\theta_2 = \pm\pi/2$. This highlights the major drawback of this representation even though it is very intuitive from a geometrical perspective as it can be seen in Fig. 2.4.

Quaternions

Quaternions are an extension to complex numbers as $q = q_0 + q_1 i + q_2 j + q_3 k$. Using a vector notation, $\mathbf{q} = [q_0, q_1, q_2, q_3]^T$. The quaternions addition follows a sum component by component. The quaternion product, denoted as $\mathbf{q}'' = \mathbf{q}' \star \mathbf{q}$, can be expressed algebraically as

$$\begin{bmatrix}q''_0\\ q''_1\\ q''_2\\ q''_3\end{bmatrix} = \begin{bmatrix}q'_0 & -q'_1 & -q'_2 & -q'_3\\ q'_1 & q'_0 & -q'_3 & q'_2\\ q'_2 & q'_3 & q'_0 & -q'_1\\ q'_3 & -q'_2 & q'_1 & q'_0\end{bmatrix}\begin{bmatrix}q_0\\ q_1\\ q_2\\ q_3\end{bmatrix}. \tag{2.79}$$

A unit norm quaternion ($\|\mathbf{q}\|_2 = 1$) is able to express the orientation between two frames. An attitude quaternion is directly related to the rotation axis, $\mathbf{e}_{\text{rot}}$, and angle, θ_{rot}, as

$$\mathbf{q} = \begin{bmatrix} \cos \dfrac{\theta_{\text{rot}}}{2} \\ \mathbf{e}_{\text{rot}} \sin \dfrac{\theta_{\text{rot}}}{2} \end{bmatrix}. \tag{2.80}$$

The rotation matrix associated to quaternions is given by

$$\mathbf{R}(\mathbf{q}) = \begin{bmatrix} q_0^2 + q_1^2 - q_2^2 - q_3^2 & 2(q_1 q_2 + q_0 q_3) & 2(q_1 q_3 - q_0 q_2) \\ 2(q_1 q_2 - q_0 q_3) & q_0^2 - q_1^2 + q_2^2 - q_3^2 & 2(q_2 q_3 + q_0 q_1) \\ 2(q_1 q_3 + q_0 q_2) & 2(q_2 q_3 - q_0 q_1) & q_0^2 - q_1^2 - q_2^2 + q_3^2 \end{bmatrix}. \tag{2.81}$$

Note that $\mathbf{R}(\mathbf{q}) = \mathbf{R}(-\mathbf{q})$, thus $\mathbf{q}$ and $-\mathbf{q}$ represent the same attitude. The attitude composition rule for quaternions is straightforward as it is given by means of the quaternion product

$$I \to S \to S' \to B, \quad \mathbf{q}_{B/I} = (\mathbf{q}_{S/I} \star \mathbf{q}_{S'/S}) \star \mathbf{q}_{B/S'}. \tag{2.82}$$

The attitude kinematics for quaternions is given as

$$\frac{d}{dt} \begin{bmatrix} q_0 \\ q_1 \\ q_2 \\ q_3 \end{bmatrix} = \frac{1}{2} \begin{bmatrix} -q_1 & -q_2 & -q_3 \\ q_0 & -q_3 & q_2 \\ q_3 & q_0 & -q_1 \\ -q_2 & q_1 & q_0 \end{bmatrix} \begin{bmatrix} \omega_1 \\ \omega_2 \\ \omega_3 \end{bmatrix}, \tag{2.83}$$

which can be algebraically presented as

$$\dot{\mathbf{q}}_{B/I} = \mathbf{C}(\mathbf{q}_{B/I}) \boldsymbol{\omega}^B_{B/I}. \tag{2.84}$$

Again, if the attitude quaternion express the orientation of the body frame with respect to a non-inertial frame L, the kinematics can be modified as

$$\dot{\mathbf{q}}_{B/L} = \mathbf{C}(\mathbf{q}_{B/L}) [\boldsymbol{\omega}^B_{B/I} - \mathbf{R}(\mathbf{q}_{B/L}) \boldsymbol{\omega}^L_{L/I}]. \tag{2.85}$$

The quaternion kinematics (see Eq. (2.83)) is a bilinear differential system without singularities. However, the quaternion representation has a tight numerical constraint as the unit-norm shall be guaranteed in order to properly define an orientation. This is a drawback when considering quaternions in optimization problems.

Modified Rodrigues parameters

Modified Rodrigues parameters (MRP), $\boldsymbol{\sigma}$, are an alternate attitude representation related to the rotation axis and angle as

$$\boldsymbol{\sigma} = \mathbf{e}_{\text{rot}} \tan(\theta_{\text{rot}}/4). \tag{2.86}$$

MRP singularities arise for $\theta_{\text{rot}} = \pm 2k\pi,\ k \in \mathbb{N}$. However, the rotation angle can be constrained as $\theta_{\text{rot}} \in [-\pi, \pi]$ since $\{\mathbf{e}_{\text{rot}}, \theta_{\text{rot}}\} \equiv \{-\mathbf{e}_{\text{rot}}, 2\pi - \theta_{\text{rot}}\}$ represent the same orientation. The rotation matrix can be expressed in terms of MRP as

$$\mathbf{R}(\boldsymbol{\sigma}) = \mathbf{I} + \frac{8\boldsymbol{\sigma}^{\times}\boldsymbol{\sigma}^{\times} - 4(1 - ||\boldsymbol{\sigma}||_2^2)\boldsymbol{\sigma}^{\times}}{(1 + ||\boldsymbol{\sigma}||_2^2)^2}, \tag{2.87}$$

where $\boldsymbol{\sigma}^{\times} \in \mathbb{R}^{3\times3}$ denote the cross product matrix associated to $\boldsymbol{\sigma}$. If the attitude composition between the following frames $I \to S \to B$ has to be made, the MRP composition rule is as follows

$$\boldsymbol{\sigma}_{B/I} = \frac{(1 - ||\boldsymbol{\sigma}_{B/S}||_2^2)\boldsymbol{\sigma}_{S/I} + (1 - ||\boldsymbol{\sigma}_{S/I}||_2^2)\boldsymbol{\sigma}_{B/S} + 2\boldsymbol{\sigma}_{S/I} \times \boldsymbol{\sigma}_{B/S}}{1 + (||\boldsymbol{\sigma}_{S/I}||_2||\boldsymbol{\sigma}_{B/S}||_2)^2 - 2\boldsymbol{\sigma}_{S/I}^T\boldsymbol{\sigma}_{B/S}}. \tag{2.88}$$

The attitude kinematics equation for MRP is

$$\begin{bmatrix}\dot{\sigma}_1\\ \dot{\sigma}_2\\ \dot{\sigma}_3\end{bmatrix} = \underbrace{\frac{1}{4}\begin{bmatrix}1 + \sigma_1^2 - \sigma_2^2 - \sigma_3^2 & 2(\sigma_1\sigma_2 - \sigma_3) & 2(\sigma_1\sigma_3 + \sigma_2)\\ 2(\sigma_1\sigma_2 + \sigma_3) & 1 - \sigma_1^2 + \sigma_2^2 - \sigma_3^2 & 2(\sigma_2\sigma_3 - \sigma_1)\\ 2(\sigma_1\sigma_3 - \sigma_2) & 2(\sigma_2\sigma_3 + \sigma_1) & 1 - \sigma_1^2 - \sigma_2^2 + \sigma_3^2\end{bmatrix}}_{\mathbf{C}(\boldsymbol{\sigma})}\begin{bmatrix}\omega_1\\ \omega_2\\ \omega_3\end{bmatrix},$$

which can be expressed as

$$\dot{\boldsymbol{\sigma}}_{B/I} = \mathbf{C}(\boldsymbol{\sigma}_{B/I})\boldsymbol{\omega}_{B/I}^B. \tag{2.89}$$

In the case that the attitude is represented with respect to a non-inertial frame L, the kinematics modifies as

$$\dot{\boldsymbol{\sigma}}_{B/L} = \mathbf{C}(\boldsymbol{\sigma}_{B/L})[\boldsymbol{\omega}_{B/I}^B - \mathbf{R}(\boldsymbol{\sigma}_{B/L})\boldsymbol{\omega}_{L/I}^L]. \tag{2.90}$$

The MRP kinematics Eq. (2.2.1) does not present singularities. Moreover, as they are a minimal representation (three parameters), no constraints are necessary. This fact makes MRP very convenient for optimization problems. References [Marandi87, Schaub96] provide a thorough description of MRP and its use for spacecraft attitude dynamics.

2.2.2 Rotational dynamics

The rotational dynamics is usually expressed in spacecraft body frame $B : \{\mathbf{r}, \mathbf{i}_B, \mathbf{j}_B, \mathbf{k}_B\}$ as the spacecraft inertia matrix $\mathbf{J} \in \mathbb{R}^{3\times3}$ is constant in that frame. Therefore, this section assumes every term is projected in the body frame. Assuming a rigid body, its rotational dynamics is given by

$$\mathbf{J}\dot{\boldsymbol{\omega}}_{B/I} + \boldsymbol{\omega}_{B/I} \times (\mathbf{J}\boldsymbol{\omega}_{B/I}) = \mathbf{T}_{\text{p}} + \mathbf{T}_u, \tag{2.91}$$

where $\mathbf{T}_{\text{p}}$ is the natural perturbing external torque and $\mathbf{T}_u$ is the control torque.

The perturbing torque arises due to the orbital forces (gravity, drag and solar radiation pressure) spatial differences in the vehicle. However, the most significant and persistent torque perturbation is the gravity-gradient one. Due to this fact, this dissertation only considers the gravity-gradient torque, thus neglecting drag or SRP torques, for the specific scenario of asteroid exploration. Additionally, parasitic torques coming from thrusters actuation are also neglected as it is assumed they are perfectly aligned with the center of gravity.

The control torque will be provided internally by means of reaction wheels. These devices are able to change their angular momentum (by speeding or slowing down their rotation), thus provoking an opposite angular reaction of the satellite. Subsequently, two simplified models for reaction wheels are presented.

Gravity-gradient torque

The gravity-gradient torque arises due to the spacecraft non-homogeneous mass distribution. This effect is properly accounted for by adding the individual torque contribution of each infinitesimal mass

$$\mathbf{T}_{\mathrm{grav}} = \int_m \Delta\mathbf{r} \times \left[-\frac{\mu(\mathbf{r}+\Delta\mathbf{r})}{\|\mathbf{r}+\Delta\mathbf{r}\|_2^3} + \mathbf{a}_{\mathrm{grav}}(\mathbf{r}+\Delta\mathbf{r}) \right] dm, \tag{2.92}$$

where $\Delta\mathbf{r}$ is the distance of each differential mass with respect to the spacecraft center of gravity $\mathbf{r}$. However, the direct integration of Eq. (2.92) could not be possible as the mass distribution function $m \equiv m(\Delta\mathbf{r})$ may not be available. Alternatively, if a simplified discrete mass distribution of the spacecraft is available, the integral computation boils down to a simple summation as

$$\mathbf{T}_{\mathrm{grav}} \approx \sum_{j=1}^{n} m_j \Delta\mathbf{r}_j \times \left[-\frac{\mu(\mathbf{r}+\Delta\mathbf{r}_j)}{\|\mathbf{r}+\Delta\mathbf{r}_j\|_2^3} + \mathbf{a}_{\mathrm{grav}}(\mathbf{r}+\Delta\mathbf{r}_j) \right], \tag{2.93}$$

where the spacecraft distribution is now considered by means of discrete masses m_j in positions $\Delta\mathbf{r}_j$ with respect to the center of gravity. Note that the gravity-gradient torque depends on the translational motion due to center of gravity position $\mathbf{r}$.

Reaction wheels

If a three-axis reaction wheels array is considered to exert torque on the spacecraft, then

$$\mathbf{T}_u = -\dot{\mathbf{H}}_{\mathrm{rw}} - \boldsymbol{\omega}_{B/I} \times \mathbf{H}_{\mathrm{rw}}, \tag{2.94}$$

where $\mathbf{H}_{\mathrm{rw}}$ and $\dot{\mathbf{H}}_{\mathrm{rw}}$ are the reaction wheels angular momentum and its variation. The reaction wheels angular momentum variation is a caused by the applied torque on the wheels array, $\mathbf{T}_{u,\mathrm{rw}}$, as

$$\dot{\mathbf{H}}_{\mathrm{rw}} + \mathbf{J}_{\mathrm{rw}}\dot{\boldsymbol{\omega}}_{B/I} = \mathbf{T}_{u,\mathrm{rw}}, \tag{2.95}$$

where $\mathbf{J}_{\text{rw}}$ is the reaction wheels array inertia matrix. It should be noted that this detailed model boils down to the consideration of the reaction wheels applied torque $\mathbf{T}_{u,\text{rw}}$. As such consideration complicates the attitude control process since the reaction wheels angular momentum is added as an attitude state, two simplified reaction wheels models will be presented.

External torque free model

Assuming no external torque is applied ($\mathbf{T}_{\text{p}} = \mathbf{0}$), which accurately approximates the case of a mass homogeneous satellite, the body total angular momentum is conserved over time as

$$\mathbf{H}_{\text{tot}} = \mathbf{J}\boldsymbol{\omega}_{B/I}(t) + \mathbf{H}_{\text{rw}}(t) \equiv \text{constant}. \tag{2.96}$$

Introducing Eq. (2.94) and (2.96) into Eq. (2.91) yields

$$\mathbf{J}\dot{\boldsymbol{\omega}}_{B/I}(t) + \dot{\mathbf{H}}_{\text{rw}}(t) + \boldsymbol{\omega}_{B/I}(t) \times \mathbf{H}_{\text{tot}} = \mathbf{0}, \tag{2.97}$$

where the control variable is directly the reactions wheels angular momentum variation, $\dot{\mathbf{H}}_{\text{rw}}$. This is a convenient simplified description as reaction wheels are limited by two factors. Firstly, the reaction wheel saturates at a maximum angular velocity. This causes $H_{\text{rw},i} = \overline{H}_{\text{rw},i} \equiv \text{constant} \longrightarrow \dot{H}_{\text{rw},i} = 0$ and the wheel has to desaturate in order to acquire control capability in that axis again. The control variable itself, angular momentum variation, is also limited by the reaction wheels own dynamics as well.

Pulse amplitude modulation

The previous model assumes that no external torque is exerted on the spacecraft, thus the total angular momentum remains constant. This may not be valid for long-term scenario where the external torque effect (gravity-gradient), though weak, accumulates over time. In such case, it would be valid to use a simplified PAM based model assuming the reaction wheels can provide a constant torque over an interval spanning from t_{k-1} to t_k

$$\mathbf{T}_u(t) := \{\mathbf{T}_{u_k}, \quad t \in [t_{k-1}, t_k), \quad k = 1 \ldots N\}. \tag{2.98}$$

This could be effectively achieved by further controlling, through Eq. (2.95), the reaction wheels angular momentum and its variation to continuosly make the torque constant as per Eq. (2.94). It should be noted that the torque PAM model does not explicitly take into account the reaction wheels saturation as only the torque amplitude can be limited.

This page is intentionally left blank.

Chapter 3

A six-degrees of freedom model predictive controller for spacecraft rendezvous

> Quaternions came from Hamilton after his really good work had been done, and though beautifully ingenious, have been an unmixed evil to those who have touched them in any way.
>
> Lord Kelvin

Contents

3.1 Rendezvous planning problem 61
  3.1.1 Objective function 62
  3.1.2 Constraints 63
3.2 State transition matrix and attitude flatness 65
  3.2.1 Translational state transition 65
  3.2.2 Attitude flatness 66
  3.2.3 Equivalent rendezvous planning problem 66
3.3 Optimal control computation 67
  3.3.1 Non-linear programming description 67
  3.3.2 Initial guess (warm-start) 71
3.4 Linearized MPC scheme 74
  3.4.1 Linearized prediction model 74
  3.4.2 Linearized control program 76
  3.4.3 MPC scheme 78
3.5 Numerical results 80
  3.5.1 Simulation model and controller parameters 80
  3.5.2 Cargo spacecraft 81
  3.5.3 Lightweight spacecraft 86

This chapter presents a closed-loop model predictive control algorithm for six-degrees of freedom spacecraft rendezvous. This refers to change the chaser orientation in order to align its thrusters with the required orbit control directions and possibly finish rendezvous with some required attitude. The previous procedure guarantees rendezvous capabilities for spacecraft with only a few number of available control thrusters. For the previous situation, the target is assumed to be placed in a Keplerian orbit and has a passive role. The chaser is in close proximity so that the relative distance is negligible with respect to the orbit semi-major axis $\|\boldsymbol{\rho}\|_2/a \ll 1$. The chaser is equipped with an arbitrary number of impulsive thrusters (e.g. chemical or cold gas) and a reaction wheels array. The thrusters control direction is always assumed to be aligned with the center of mass, hence no parasitic torques are induced when they are actuated. The main results of this problem has been presented in the journal article [Sanchez20b] and the conference proceeding [Sanchez18].

Under the previous considerations, the Keplerian-based linear relative dynamics as per Eq. (2.31) can be employed. The relative state is instantaneously changed according to Eq. (2.58) model. Considering a number of n_T thrusters providing orbit control along their respective $\mathbf{w}_p$ ($p = 1 \dots n_T$) directions yields the following total impulse in the local-vertical local-horizontal frame

$$\Delta\mathbf{V} = \sum_{p=1}^{n_T} (\mathbf{R}_L^B)^T \mathbf{w}_p^B \Delta V_p, \quad \Delta V_p \geq 0, \tag{3.1}$$

where ΔV_p is the p thruster impulse amplitude and $\mathbf{R}_L^B$ is the rotation matrix from LVLH to body frame. Then, the control directions can be changed through the rotation matrix which explicitly depends on the spacecraft orientation. In this chapter, it is considered that the spacecraft can be rotated with an array of reaction wheels according to the external torque free model of Eq. (2.97). The gravity-gradient torque perturbation is neglected since the close proximity rendezvous maneuver is usually completed in less than one orbital period.

The whole problem can be decomposed into two stages: 1) a spacecraft rendezvous controller computing the required total impulse; 2) an attitude controller to meet the required thrusters orientation at specified times. Using the previous decomposition [Wu09, Siva13, Moon16] developed a two-stages approach where the rendezvous plan is firstly computed (with LQR or convex optimization) and a subsequent feedback-based attitude controller tracks the demanded orientations. The previous research works assume the attitude control will always be able to rotate the spacecraft in order to meet the commanded orientations. However, it is not guaranteed that the reorientation maneuvers are doable due to the possibility of control saturation.

In order to overcome the previous drawback, an integrated six-degrees of freedom controller is proposed. This way, the required impulses directions are consistent with the attitude control maneuvering capabilities (e.g. dividing a large reorientation into a concatenation of small ones). To do so, the first step consists in stating the integrated 6-DOF rendezvous problem in a continuous optimization form. Then, the translational and angular dynamics are transcribed by exploiting the Yamanaka-Ankersen transition matrix and the attitude flatness property respectively. This transforms the orbit-attitude differential dynamics into algebraic expressions. Subsequently, by parameterizing the attitude with B-splines and discretizing the problem in the time domain, the initial problem is reduced to a finite tractable static non-linear program. Finally, the problem is linearized around the previous non-linear program solution so that a quadratic program, in terms of small increments of the decision variables, is obtained. The previous QP problem closes the loop.

The outcome is a computationally affordable (QP) closed-loop MPC controller able to cope with disturbances and unmodelled dynamics (to a certain extent). The initial open-loop solution has a high computational burden because it involves finding a solution of a NLP optimization problem. However, this initial step could be computed and uplinked by ground control. The algorithm is tested numerically, under the presence of impulses mishaps, for a heavy cargo and a lightweight spacecraft respectively.

3.1 Rendezvous planning problem

Generally, under linear Keplerian assumptions and neglecting the external torque, the 6-DOF rendezvous problem states as

$$\boxed{\begin{array}{ll}
\underset{\Delta V_p(t_j),\,\dot{\mathbf{H}}_{\mathrm{rw}}(t)}{\text{minimize}} & J(\Delta V_p(t_j),\, \dot{\mathbf{H}}_{\mathrm{rw}}(t)),\\
\text{subject to} & \ddot{\boldsymbol{\rho}}(t) = -2\boldsymbol{\omega}_{L/I} \times \dot{\boldsymbol{\rho}} - \dot{\boldsymbol{\omega}}_{L/I} \times \boldsymbol{\rho} - \boldsymbol{\omega}_{L/I} \times (\boldsymbol{\omega}_{L/I} \times \boldsymbol{\rho})\\
& \qquad - \left(\mu/r_t^3\right) \left[\mathbf{I} - 3\left(\mathbf{r}_t^T \mathbf{r}_t/r_t^2\right)\right] \boldsymbol{\rho},\\
& \dot{\boldsymbol{\rho}}^+(t_j) = \dot{\boldsymbol{\rho}}(t_j) + \displaystyle\sum_{j=0}^{N}\sum_{p=1}^{n_T} \mathbf{R}^T(\boldsymbol{\sigma}(t_j))\mathbf{w}_p \Delta V_p(t_j),\\
& \dot{\boldsymbol{\omega}}(t) = -\mathbf{J}^{-1}\left[\dot{\mathbf{H}}_{\mathrm{rw}}(t) + \boldsymbol{\omega}(t) \times \mathbf{H}_{\mathrm{tot}}\right],\\
& \dot{\boldsymbol{\sigma}}(t) = \mathbf{C}(\boldsymbol{\sigma}(t))[\boldsymbol{\omega}(t) - \mathbf{R}(\boldsymbol{\sigma}(t))\boldsymbol{\omega}_{L/I}(t)],\\
& 0 \leq \Delta V_p(t_j) \leq \overline{\Delta V}_p,\\
& -\overline{\mathbf{H}}_{\mathrm{rw}} \leq \mathbf{H}_{\mathrm{rw}}(t) \leq \overline{\mathbf{H}}_{\mathrm{rw}},\\
& -\dot{\overline{\mathbf{H}}}_{\mathrm{rw}} \leq \dot{\mathbf{H}}_{\mathrm{rw}}(t) \leq \dot{\overline{\mathbf{H}}}_{\mathrm{rw}},\\
& \boldsymbol{\rho}(t) \in \mathcal{X}_{\mathrm{LOS}},\\
& \boldsymbol{\rho}(t_0) = \boldsymbol{\rho}_0, \quad \dot{\boldsymbol{\rho}}(t_0) = \dot{\boldsymbol{\rho}}_0, \quad \boldsymbol{\sigma}(t_0) = \boldsymbol{\sigma}_0, \quad \dot{\boldsymbol{\sigma}}(t_0) = \dot{\boldsymbol{\sigma}}_0,\\
& \boldsymbol{\rho}(t_f) = \boldsymbol{\rho}_f, \quad \dot{\boldsymbol{\rho}}(t_f) = \mathbf{0}, \quad \boldsymbol{\sigma}(t_f) = \boldsymbol{\sigma}_f, \quad \dot{\boldsymbol{\sigma}}(t_f) = \mathbf{0}.
\end{array}} \tag{3.2}$$

The time dependencies have been omitted at the right hand side of the relative motion dynamics for the sake of clarity. The following notation is employed throughout the entire chapter. The body orientation with respect to the LVLH frame is simply denoted as $\boldsymbol{\sigma} \equiv \boldsymbol{\sigma}_{B/L}$. Nonetheless, the body angular velocity is referred to the inertial frame as $\boldsymbol{\omega} \equiv \boldsymbol{\omega}_{B/I}$. In general, to ease the notation, superscripts denoting the variables reference frames are omitted. The thrusters control direction $\mathbf{w}_p$ is always expressed in the body frame. The target orbital radius r_t, its orbit angular velocity $\boldsymbol{\omega}_{L/I}$ and its acceleration $\dot{\boldsymbol{\omega}}_{L/I}$ are a function of its true anomaly, semi-major axis and eccentricity.

The following considerations have been implicitly made in problem (3.2):

- The translational relative motion is parameterized using cartesian coordinates. The attitude is described using the modified Rodrigues parameters.
- At $N+1$ predefined instants t_j, each thruster could apply a control impulse. The amplitude of the control impulse is bounded.
- The attitude control variable is the variation of the reaction wheels angular momentum. The reaction wheels angular momentum and its variation are bounded below and above due to saturation.
- During the maneuver, the relative position has to be within the state subset $\mathcal{X}_{\text{LOS}}$. This subset refers to the line-of-sight (LOS) region which guarantees line-of-sight with the docking port and prevents collision with the target (see Fig. 3.1).
- The initial orbit-attitude state is given. The desired terminal state would leave the chaser motionless at a certain relative distance from the target with an adequate orientation.

In any case, the objective function and constraints are detailed down below.

3.1.1 Objective function

The chosen objective function seeks to directly minimize fuel consumption. According to the Tsiolkovski rocket equation the fuel consumption is related to a velocity increment as $m_F = m_0\left(1 - e^{-\Delta V/g_0 I_{\text{sp}}}\right)$. Note that $g_0 = 9.80665$ m/s^2 is the Earth's gravity at sea level and I_{sp} is the thruster specific impulse. Assuming all thrusters have the same specific impulse, the minimization of the total fuel consumption is equivalent to minimize the summation of all the applied impulses. Then, the objective function is

$$J = \sum_{j=0}^{N} \sum_{p=1}^{n_T} \Delta V_p(t_j). \tag{3.3}$$

Note that the impulse amplitude of each thruster is always positive or null $\Delta V_p \geq 0$.

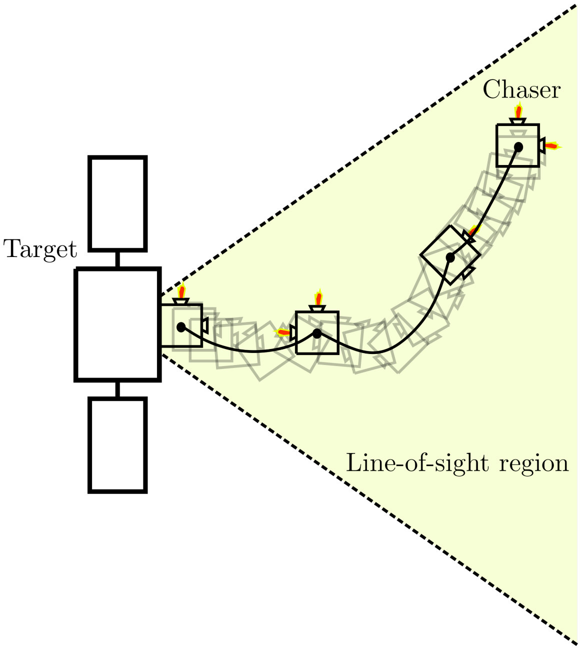

Figure 3.1: Illustration of a six-degrees of freedom spacecraft rendezvous.

3.1.2 Constraints

Three sets of constraints are considered in this problem. Firstly, path constraints on the relative position; secondly, both the thrusters and reaction wheels have control limits; and finally, the translational and rotational states are prescribed at the initial and final instants of the maneuver. In the sequel, the relative position and velocity are stacked in the state $\mathbf{x} = [\boldsymbol{\rho}^T, \dot{\boldsymbol{\rho}}^T]^T$.

Path constraints

During the close rendezvous operation, the chaser must remain within a line-of-sight area from the docking port while avoiding collision with the target [Breger08]. This guarantees that the docking port is visible from the sensors of the chaser. The LOS region is the half of a cone whose apex is the docking port. In order to have a simpler linear constraint, the cone can be approximated by five planes as $\{x \geq c_y(y - y_0),\ x \geq -c_y(y + y_0),\ x \geq c_z(z - z_0),\ x \geq -c_z(z + z_0),\ x \geq 0\}$ (see Fig. 3.2). Note that this represents a V-bar alike approach where the constraint $x \geq 0$ precludes collision with the target. The

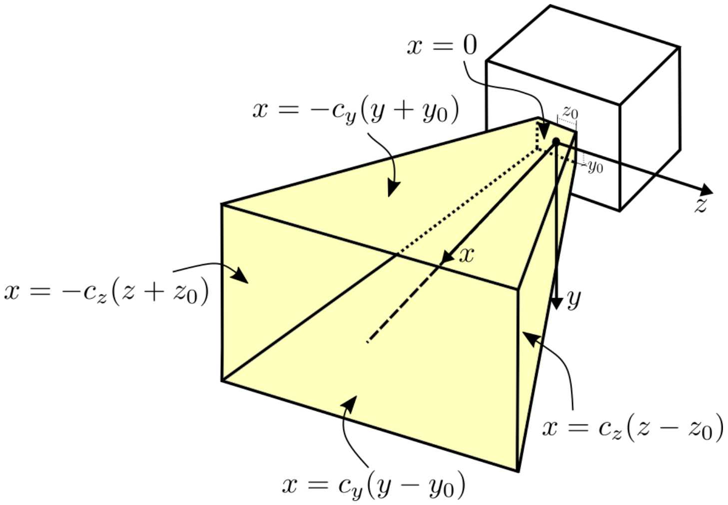

Figure 3.2: Line-of-sight region.

LOS constraint can be expressed algebraically as

$$\underbrace{\begin{bmatrix} -1 & c_y & 0 & 0 & 0 & 0 \\ -1 & -c_y & 0 & 0 & 0 & 0 \\ -1 & 0 & c_z & 0 & 0 & 0 \\ -1 & 0 & -c_z & 0 & 0 & 0 \\ -1 & 0 & 0 & 0 & 0 & 0 \end{bmatrix}}_{\mathbf{A}_{\mathrm{LOS}}} \mathbf{x}(t) \leq \underbrace{\begin{bmatrix} c_y y_0 \\ c_y y_0 \\ c_z z_0 \\ c_z z_0 \\ 0 \end{bmatrix}}_{\mathbf{b}_{\mathrm{LOS}}}, \tag{3.4}$$

where $\mathbf{A}_{\mathrm{LOS}}$ and $\mathbf{b}_{\mathrm{LOS}}$ are the line-of-sight inequality matrix and vector respectively.

Control bounds

Due to physical limitations, the amount of control that thrusters and reaction wheels can exert is limited.

Thrusters: the impulse amplitude is assumed to be bounded above (and below by zero)

$$0 \leq \Delta V_p(t_j) \leq \overline{\Delta V}_p, \quad p = 1 \ldots n_T, \tag{3.5}$$

where $\overline{\Delta V}_p$ is the maximum change of velocity that each thruster can provide. The variable ΔV_p can take any value in the allowed interval. It is assumed that the thruster valves opening times can be adjusted to produce the exact amount of impulse amplitude.

Reaction wheels: each wheel saturates when a certain amount of angular momentum is stored. Additionally, the reaction wheels variations are bounded due to physical limitations. The previous considerations yield

$$-\overline{\mathbf{H}}_{\mathrm{rw}} \leq \mathbf{H}_{\mathrm{rw}}(t) \leq \overline{\mathbf{H}}_{\mathrm{rw}}, \tag{3.6}$$

$$-\dot{\overline{\mathbf{H}}}_{\mathrm{rw}} \leq \dot{\mathbf{H}}_{\mathrm{rw}}(t) \leq \dot{\overline{\mathbf{H}}}_{\mathrm{rw}}, \tag{3.7}$$

where $\overline{\mathbf{H}}_{\mathrm{rw}}$ is the maximum amount of angular momentum the wheels can store on each axis whereas the term $\dot{\overline{\mathbf{H}}}_{\mathrm{rw}}$ is their maximum rate of variation. The reaction wheels array is considered to be symmetrical on its 3-axis, thus $\overline{\mathbf{H}}_{\mathrm{rw}} = [\overline{H}_{\mathrm{rw}}, \overline{H}_{\mathrm{rw}}, \overline{H}_{\mathrm{rw}}]^T$ and $\dot{\overline{\mathbf{H}}}_{\mathrm{rw}} = [\dot{\overline{H}}_{\mathrm{rw}}, \dot{\overline{H}}_{\mathrm{rw}}, \dot{\overline{H}}_{\mathrm{rw}}]^T$.

Boundary constraints

The chaser is assumed to depart from a given position and velocity with a specific orientation and angular velocity

$$\mathbf{x}(t_0) = \mathbf{x}_0, \quad \boldsymbol{\sigma}(t_0) = \boldsymbol{\sigma}_0, \quad \dot{\boldsymbol{\sigma}}(t_0) = \dot{\boldsymbol{\sigma}}_0. \tag{3.8}$$

The 6-DOF rendezvous operation finishes when a stationary relative position and orientation is achieved as

$$\mathbf{x}(t_f) = \mathbf{x}_f, \quad \boldsymbol{\sigma}(t_f) = \boldsymbol{\sigma}_f, \quad \dot{\boldsymbol{\sigma}}(t_f) = \mathbf{0}, \tag{3.9}$$

where $\mathbf{x}_f = [\boldsymbol{\rho}_f^T, \mathbf{0}^T]^T$. As Keplerian-based relative dynamics are unstable (see Eq. (2.39)), further station-keeping (which is out of the scope of this work) could be required to maintain this terminal condition.

3.2 State transition matrix and attitude flatness

Exploiting the state transition matrix and the attitude flatness property, the orbit-attitude differential dynamics of the problem (3.2) will be transcribed to algebraic relations.

3.2.1 Translational state transition

Using the Yamanaka-Ankersen transition matrix $\boldsymbol{\Phi}$ (see Eq. (2.36)) and the instantaneous velocity changes of Eq. (2.58), the relative state propagation of problem (3.2) is equivalent to

$$\begin{gathered} \mathbf{x}(t) = \boldsymbol{\Phi}(t, t_0)\mathbf{x}_0 + \sum_{i=0}^{j} \sum_{p=1}^{n_T} \boldsymbol{\Phi}(t, t_i)\mathbf{B}\mathbf{R}^T(\boldsymbol{\sigma}(t_i))\mathbf{w}_p \Delta V_p(t_i), \\ t_j \leq t < t_{j+1}, \end{gathered} \tag{3.10}$$

where the state is continuous within the interval $[t_j, t_{j+1})$ between impulses. The control direction of each thruster depends non-linearly on the vehicle orientation through the rotation matrix.

3.2.2 Attitude flatness

The angular dynamical system of the 6-DOF rendezvous problem 3.2 has the differential flatness property [Louembet09].

Remark 3.1: a differentially flat system has the special property that all its states and inputs can be explicitly expressed, using algebraic relations, as a function of a flat output and a finite number of its derivatives [Fliess95].

For the external torque free attitude dynamics, the flat output can be directly chosen as the attitude representation parameter [Louembet09]. Consequently, in this case, the attitude dynamics of problem (3.2) are expressed as a function of the MRP and its derivatives. Clearing the angular velocity in the MRP kinematics (see Eq. (2.90)) and deriving the obtained expression with respect to time one obtains

$$\boldsymbol{\omega}(t) = \mathbf{C}(\boldsymbol{\sigma})^{-1}\dot{\boldsymbol{\sigma}} + \mathbf{R}(\boldsymbol{\sigma})\boldsymbol{\omega}_{L/I}, \tag{3.11}$$

$$\dot{\boldsymbol{\omega}}(t) = \dot{\mathbf{C}}(\boldsymbol{\sigma})^{-1}\dot{\boldsymbol{\sigma}} + \mathbf{C}(\boldsymbol{\sigma})^{-1}\ddot{\boldsymbol{\sigma}} + \dot{\mathbf{R}}(\boldsymbol{\sigma})\boldsymbol{\omega}_{L/I} + \mathbf{R}(\boldsymbol{\sigma})\dot{\boldsymbol{\omega}}_{L/I}. \tag{3.12}$$

Then, Eq. (3.11)-(3.12) are introduced into the attitude dynamics of Eq. (2.97) and the reaction wheels angular momentum variation is cleared

$$\begin{aligned}\dot{\mathbf{H}}_{\mathrm{rw}}(t) = &- \mathbf{J}^{-1}\left[\mathbf{C}^{-1}(\boldsymbol{\sigma})\left(\ddot{\boldsymbol{\sigma}} - \dot{\mathbf{C}}(\boldsymbol{\sigma})\mathbf{C}^{-1}(\boldsymbol{\sigma})\dot{\boldsymbol{\sigma}}\right) + \dot{\mathbf{R}}(\boldsymbol{\sigma})\dot{\boldsymbol{\omega}}_{L/I}\right] \\ &- \left(\mathbf{C}^{-1}(\boldsymbol{\sigma})\dot{\boldsymbol{\sigma}} + \mathbf{R}(\boldsymbol{\sigma})\boldsymbol{\omega}_{L/I}\right) \times \mathbf{H}_{\mathrm{tot}}.\end{aligned} \tag{3.13}$$

This way, all the system variables have been expressed as algebraic functions of the flat output and its derivatives. The key idea behind applying the flatness property is to parameterize the flat output evolution, thus directly obtaining the associated control as per Eq. (3.13).

The reaction wheels angular momentum can be also expressed as a function of the flat output using the conservation of the total angular momentum (see Eq. (2.96))

$$\mathbf{H}_{\mathrm{rw}}(t) = \mathbf{H}_{\mathrm{tot}} - \mathbf{J}\left(\mathbf{C}^{-1}(\boldsymbol{\sigma})\dot{\boldsymbol{\sigma}} + \mathbf{R}(\boldsymbol{\sigma})\boldsymbol{\omega}_{L/I}\right). \tag{3.14}$$

Note that the dependencies with time have been omitted at the right-hand sides of Eq. (3.11)-(3.14) for the sake of clarity.

3.2.3 Equivalent rendezvous planning problem

Using Eq. (3.10) transition and the attitude flatness relations of Eq. (3.13)-(3.14), the differential dynamics of the 6-DOF rendezvous problem (3.2) are equivalently transcribed to algebraic relations as

$$
\begin{aligned}
\underset{\Delta V_p(t_j),\,\boldsymbol{\sigma}(t)}{\text{minimize}} \quad & \sum_{j=0}^{N}\sum_{p=1}^{n_T}\Delta V_p(t_j),\\
\text{subject to} \quad & \mathbf{x}(t) = \sum_{i=0}^{j}\sum_{p=1}^{n_T}\boldsymbol{\Phi}(t,t_i)\mathbf{B}\mathbf{R}^T(\boldsymbol{\sigma}(t_i))\mathbf{w}_p\Delta V_p(t_i)\\
& \qquad + \boldsymbol{\Phi}(t,t_0)\mathbf{x}(t_0), \quad t_j \leq t < t_{j+1},\\
& \mathbf{A}_{\mathrm{LOS}}\mathbf{x}(t) \leq \mathbf{b}_{\mathrm{LOS}},\\
& 0 \leq \Delta V_p(t) \leq \overline{\Delta V}_p, \quad p = 1\ldots n_T,\\
& -\overline{\mathbf{H}}_{\mathrm{rw}} \leq \mathbf{H}_{\mathrm{rw}}(\boldsymbol{\sigma}(t),\dot{\boldsymbol{\sigma}}(t)) \leq \overline{\mathbf{H}}_{\mathrm{rw}},\\
& -\dot{\overline{\mathbf{H}}}_{\mathrm{rw}} \leq \dot{\mathbf{H}}_{\mathrm{rw}}(\boldsymbol{\sigma}(t),\dot{\boldsymbol{\sigma}}(t),\ddot{\boldsymbol{\sigma}}(t)) \leq \dot{\overline{\mathbf{H}}}_{\mathrm{rw}},\\
& \mathbf{x}(t_0) = \mathbf{x}_0, \quad \boldsymbol{\sigma}(t_0) = \boldsymbol{\sigma}_0, \quad \dot{\boldsymbol{\sigma}}(t_0) = \dot{\boldsymbol{\sigma}}_0,\\
& \mathbf{x}(t_f) = \mathbf{x}_f, \quad \boldsymbol{\sigma}(t_f) = \boldsymbol{\sigma}_f, \quad \dot{\boldsymbol{\sigma}}(t_f) = \mathbf{0}.
\end{aligned}
\tag{3.15}
$$

This problem is still continuous with infinite degrees of freedom.

3.3 Optimal control computation

In this section, a method to solve the equivalent 6-DOF rendezvous problem (3.15) is presented. The solution approach is based on a B-spline parameterization of the flat output, $\boldsymbol{\sigma}$, and the discretization of continuous constraints (line-of-sight and reaction wheels control bounds). Finally, a warm-start initial guess for the resulting NLP problem is provided.

3.3.1 Non-linear programming description

In this section, the necessary steps towards transforming problem (3.15) into a finite tractable static program are described.

Impulses placement

The thrusters can be fired at $N+1$ predefined number times. These are considered to be equally spaced in time as $t_j = t_0 + j\Delta t$, $j = 0\ldots N$ with $\Delta t = (t_f - t_0)/N$. The firing times, t_j, are denoted as nodes. During the intervals between impulses, the attitude control system has to change the thrusters orientation.

B-splines parameterization of the flat output

The attitude differential flatness property allows any kind of MRP parameterization as long as the time derivatives are continuous. Following [Louembet09], B-splines (see Appendix A) for the details, are chosen to parameterize the flat output. This is due to their capability of describing flexible trajectories with a high degree of differentiability using a low number of parameters. Consequently,

$$\boldsymbol{\sigma}(t) = \sum_{i=1}^{n_c} B_{i,q}(t)\mathbf{c}_i, \tag{3.16}$$

where $B_{i,q}(t) \in \mathbb{R}$ are q^{th} order basis functions built on a sequence of knots $\mathbf{t}_{\text{knots}} \in \mathbb{R}^{n_{\text{knots}}}$ (which is defined below) and the coefficients $\mathbf{c}_i \in \mathbb{R}^3$ are control points. By using Eq. (3.16), the attitude decision variable is the set of control points $\mathbf{c}_i$. To have physical meaning, the attitude time evolution should be continuous up to its second derivative, hence $q \geq 2$. The number of control points is chosen as $n_c = N + 5$ where $N + 1$ correspond to each node and the remaining ones allow to enforce initial and terminal conditions on the MRP derivatives $\{\dot{\boldsymbol{\sigma}}(t_0), \ddot{\boldsymbol{\sigma}}(t_0)\}$ and $\{\dot{\boldsymbol{\sigma}}(t_f), \ddot{\boldsymbol{\sigma}}(t_f)\}$ respectively. Therefore, the number of knots must be $n_{\text{knots}} = N + q + 6$. The knots sequence is built by using the impulses nodes as a base. The $q + 5$ remaining knots are filled by repetition of the initial and final nodes to the left and right

$$\mathbf{t}_{\text{knots}} = [\underbrace{t_0, \ldots, t_0}_{q/2+3 \text{ times}}, t_1, \ldots, t_{N-1}, \underbrace{t_f, \ldots, t_f}_{q/2+3 \text{ times}}]^T. \tag{3.17}$$

By choosing to repeat the initial and final nodes, the B-splines q^{th} order continuity is maintained.

Discretization of continuous constraints

The continuous constraints of problem (3.15) are the line-of-sight region and the reaction wheels control bounds (angular momentum storage and variation). Each one of these constraints is discretized by enforcing them at some discrete times within each interval j between impulses.

Line-of-sight constraint: within each interval between impulses, the LOS constraint is enforced at n_{LOS} equally spaced times separated by $\Delta t_{\text{LOS}} = \Delta t / n_{\text{LOS}}$

$$\begin{aligned} \mathbf{A}_{\text{LOS}}\mathbf{x}(t_{j,l}) \leq \mathbf{b}_{\text{LOS}}, \quad & t_{j,l} = t_0 + (j-1)\Delta t + l\Delta t_{\text{LOS}}, \\ & j = 1 \ldots N, \quad l = 1 \ldots n_{\text{LOS}}. \end{aligned} \tag{3.18}$$

Reaction wheels constraints: in the same way, the reaction wheels constraints are enforced at n_{rw} instants between impulses. The instants are equally separated by $\Delta t_{\text{rw}} = \Delta t / n_{\text{rw}}$

$$-\overline{\mathbf{H}}_{\text{rw}} \leq \mathbf{H}_{\text{rw}}(t_{j,m}, \mathbf{c}_i) \leq \overline{\mathbf{H}}_{\text{rw}}, \tag{3.19}$$

$$-\dot{\overline{\mathbf{H}}}_{\text{rw}} \leq \dot{\mathbf{H}}_{\text{rw}}(t_{j,m}, \mathbf{c}_i) \leq \dot{\overline{\mathbf{H}}}_{\text{rw}}, \tag{3.20}$$

$$t_{j,m} = t_0 + (j-1)\Delta t + m\Delta t_{\text{rw}}, \quad j = 1 \ldots N, \quad m = 0 \ldots n_{\text{rw}}.$$

Compact formulation

Following [Gavilan12], to ease the notation, a compact formulation for the discretized problem is developed. Let define stack vectors, $\mathbf{x}_\mathbf{S} \in \mathbb{R}^{6n_{\mathrm{LOS}}N}$, $\Delta\mathbf{V}_{\mathbf{S}p} \in \mathbb{R}^{N+1}$, $\boldsymbol{\sigma}_\mathbf{S} \in \mathbb{R}^{3(N+1)}$ and $\mathbf{c}_\mathbf{S} \in \mathbb{R}^{3n_c}$, associated with the relative state, each thruster impulse amplitudes, attitude at the nodes and the MRP control points respectively

$$\mathbf{x}_\mathbf{S} = [\mathbf{x}_{1,1}^T, \ldots, \mathbf{x}_{1,n_{\mathrm{LOS}}}^T, \mathbf{x}_{2,1}^T, \ldots, \mathbf{x}_{2,n_{\mathrm{LOS}}}^T, \mathbf{x}_{3,1}^T, \ldots\ldots, \mathbf{x}_{N,n_{\mathrm{LOS}}}^T]^T,$$
$$\Delta\mathbf{V}_{\mathbf{S}p} = \begin{bmatrix} \Delta V_{p,0} \\ \Delta V_{p,1} \\ \vdots \\ \Delta V_{p,N} \end{bmatrix}, \quad \boldsymbol{\sigma}_\mathbf{S} = \begin{bmatrix} \boldsymbol{\sigma}_0 \\ \boldsymbol{\sigma}_1 \\ \vdots \\ \boldsymbol{\sigma}_N \end{bmatrix}, \quad \mathbf{c}_\mathbf{S} = \begin{bmatrix} \mathbf{c}_1 \\ \mathbf{c}_2 \\ \vdots \\ \mathbf{c}_{n_c} \end{bmatrix}, \tag{3.21}$$

and the stack matrices $\mathbf{F} \in \mathbb{R}^{6n_{\mathrm{LOS}}N\times 6}$, $\mathbf{G}_p \in \mathbb{R}^{6n_{\mathrm{LOS}}N\times(N+1)}$ and $\mathbf{K}_\sigma \in \mathbb{R}^{3(N+1)\times 3n_c}$

$$\mathbf{F} = \begin{bmatrix} \boldsymbol{\Phi}(t_{1,1}, t_0) \\ \vdots \\ \boldsymbol{\Phi}(t_{1,n_{\mathrm{LOS}}}, t_0) \\ \boldsymbol{\Phi}(t_{2,n_{\mathrm{LOS}}}, t_0) \\ \vdots \\ \\ \vdots \\ \boldsymbol{\Phi}(t_{N,n_{\mathrm{LOS}}}, t_0) \\ \\ \end{bmatrix}, \tag{3.22}$$

$$\mathbf{G}_p =$$
$$\begin{bmatrix} \boldsymbol{\Phi}(t_{1,1}, t_0)\mathbf{B}\mathbf{R}^T(\boldsymbol{\sigma}_0)\mathbf{w}_p & \mathbf{0}_{6\times1} & \ldots & \mathbf{0}_{6\times1} \\ \vdots & \vdots & \ddots & \vdots \\ \boldsymbol{\Phi}(t_{1,n_{\mathrm{LOS}}}, t_0)\mathbf{B}\mathbf{R}^T(\boldsymbol{\sigma}_0)\mathbf{w}_p & \mathbf{0}_{6\times1} & \ldots & \mathbf{0}_{6\times1} \\ \boldsymbol{\Phi}(t_{2,1}, t_0)\mathbf{B}\mathbf{R}^T(\boldsymbol{\sigma}_0)\mathbf{w}_p & \boldsymbol{\Phi}(t_{2,1}, t_1)\mathbf{B}\mathbf{R}^T(\boldsymbol{\sigma}_1)\mathbf{w}_p & \ldots & \mathbf{0}_{6\times1} \\ \vdots & \vdots & \ddots & \vdots \\ \boldsymbol{\Phi}(t_{2,n_{\mathrm{LOS}}}, t_0)\mathbf{B}\mathbf{R}^T(\boldsymbol{\sigma}_0)\mathbf{w}_p & \boldsymbol{\Phi}(t_{2,n_{\mathrm{LOS}}}, t_1)\mathbf{B}\mathbf{R}^T(\boldsymbol{\sigma}_1)\mathbf{w}_p & \ldots & \mathbf{0}_{6\times1} \\ \boldsymbol{\Phi}(t_{3,1}, t_0)\mathbf{B}\mathbf{R}^T(\boldsymbol{\sigma}_0)\mathbf{w}_p & \boldsymbol{\Phi}(t_{3,n_{\mathrm{LOS}}}, t_1)\mathbf{B}\mathbf{R}^T(\boldsymbol{\sigma}_1)\mathbf{w}_p & \ldots & \mathbf{0}_{6\times1} \\ \vdots & \vdots & \ddots & \vdots \\ \vdots & \vdots & \ddots & \vdots \\ \boldsymbol{\Phi}(t_{N,n_{\mathrm{LOS}}}, t_0)\mathbf{B}\mathbf{R}^T(\boldsymbol{\sigma}_0)\mathbf{w}_p & \boldsymbol{\Phi}(t_{N,n_{\mathrm{LOS}}}, t_1)\mathbf{B}\mathbf{R}^T(\boldsymbol{\sigma}_1)\mathbf{w}_p & \ldots & \mathbf{B}\mathbf{R}^T(\boldsymbol{\sigma}_N)\mathbf{w}_p \end{bmatrix},$$

$$\mathbf{K}_\sigma = \begin{bmatrix} B_{1,q}(t_0)\mathbf{I} & B_{2,q}(t_0)\mathbf{I} & \ldots & B_{n_c,q}(t_0)\mathbf{I} \\ B_{1,q}(t_1)\mathbf{I} & B_{2,q}(t_1)\mathbf{I} & \ldots & B_{n_c,q}(t_1)\mathbf{I} \\ \vdots & \vdots & \ddots & \vdots \\ B_{1,q}(t_N)\mathbf{I} & B_{2,q}(t_N)\mathbf{I} & \ldots & B_{n_c,q}(t_N)\mathbf{I} \end{bmatrix}, \tag{3.23}$$

The relation between the stack vectors (see Eq. (3.21)) and matrices (see Eq. (3.22)-(3.23)) is given by

$$\mathbf{x}_{\mathbf{S}} = \mathbf{F}\mathbf{x}_0 + \sum_{p=1}^{n_T} \mathbf{G}_p(\boldsymbol{\sigma}_{\mathbf{S}})\Delta\mathbf{V}_{\mathbf{S}p}, \quad \boldsymbol{\sigma}_{\mathbf{S}} = \mathbf{K}_{\sigma}\mathbf{c}_{\mathbf{S}}. \tag{3.24}$$

In the same way, the reaction wheels constraints enforcement instants (see Eq. (3.19)-(3.20)) can be compacted as

$$\boldsymbol{\sigma}_{\mathbf{S},\mathrm{rw}} = \mathbf{K}_{\sigma_{\mathrm{rw}}}\mathbf{c}_{\mathbf{S}}, \quad \dot{\boldsymbol{\sigma}}_{\mathbf{S},\mathrm{rw}} = \mathbf{K}_{\dot{\sigma}_{\mathrm{rw}}}\mathbf{c}_{\mathbf{S}}, \quad \ddot{\boldsymbol{\sigma}}_{\mathbf{S},\mathrm{rw}} = \mathbf{K}_{\ddot{\sigma}_{\mathrm{rw}}}\mathbf{c}_{\mathbf{S}}, \tag{3.25}$$

where the vectors $\boldsymbol{\sigma}_{\mathbf{S},\mathrm{rw}}, \dot{\boldsymbol{\sigma}}_{\mathbf{S},\mathrm{rw}}, \ddot{\boldsymbol{\sigma}}_{\mathbf{S},\mathrm{rw}} \in \mathbb{R}^{3n_{\mathrm{rw}}N}$ stack the MRP and its derivatives at the reaction wheels constraints enforcement instants. The stack matrices $\mathbf{K}_{\sigma_{\mathrm{rw}}}, \mathbf{K}_{\dot{\sigma}_{\mathrm{rw}}}, \mathbf{K}_{\ddot{\sigma}_{\mathrm{rw}}} \in \mathbb{R}^{3n_{\mathrm{rw}}N \times 3n_c}$ map the control points to the MRP and its derivatives with a similar structure as Eq. (3.23). Using the previous formulation, the stack vectors of the reaction wheels angular momentum and variation can be considered as

$$\mathbf{H}_{\mathbf{S},\mathrm{rw}} \equiv \mathbf{H}_{\mathbf{S},\mathrm{rw}}(\boldsymbol{\sigma}_{\mathbf{S},\mathrm{rw}}, \dot{\boldsymbol{\sigma}}_{\mathbf{S},\mathrm{rw}}), \quad \dot{\mathbf{H}}_{\mathbf{S},\mathrm{rw}} \equiv \dot{\mathbf{H}}_{\mathbf{S}\mathrm{rw}}(\boldsymbol{\sigma}_{\mathbf{S},\mathrm{rw}}, \dot{\boldsymbol{\sigma}}_{\mathbf{S},\mathrm{rw}}, \ddot{\boldsymbol{\sigma}}_{\mathbf{S},\mathrm{rw}}), \tag{3.26}$$

where $\mathbf{H}_{\mathbf{S},\mathrm{rw}}, \dot{\mathbf{H}}_{\mathbf{S},\mathrm{rw}} \in \mathbb{R}^{3n_{\mathrm{rw}}N}$. Let recall that the relation of the reaction wheels angular momentum and its variation with the MRP and its derivatives (thus, the same applies to the MRP control points) is non-linear according to Eq. (3.13)-(3.14).

Six-degrees of freedom rendezvous static program

Joining the discretization of continuous constraints with the compact formulation, the equivalent continuous planning problem (3.15) is reduced to a nonlinear program

$$\boxed{\begin{aligned}
\underset{\Delta\mathbf{V}_{\mathbf{S}p},\,\mathbf{c}_{\mathbf{S}}}{\text{minimize}} \quad & \sum_{p=1}^{n_T} \|\Delta\mathbf{V}_{\mathbf{S}p}\|_1, \\
\text{subject to} \quad & \mathbf{x}_{\mathbf{S}} = \mathbf{F}\mathbf{x}_0 + \sum_{p=1}^{n_T} \mathbf{G}_p(\boldsymbol{\sigma}_{\mathbf{S}})\Delta\mathbf{V}_{\mathbf{S}p}, \quad \boldsymbol{\sigma}_{\mathbf{S}} = \mathbf{K}_{\sigma}\mathbf{c}_{\mathbf{S}}, \\
& \mathbf{A}_{\mathbf{S},\mathrm{LOS}}\mathbf{x}_{\mathbf{S}} \leq \mathbf{b}_{\mathbf{S},\mathrm{LOS}}, \\
& \mathbf{0} \leq \Delta\mathbf{V}_{\mathbf{S}p} \leq \overline{\Delta\mathbf{V}}_{\mathbf{S}p}, \quad p = 1\ldots n_T, \\
& -\overline{\mathbf{H}}_{\mathbf{S},\mathrm{rw}} \leq \mathbf{H}_{\mathbf{S},\mathrm{rw}}(\boldsymbol{\sigma}_{\mathbf{S},\mathrm{rw}}, \dot{\boldsymbol{\sigma}}_{\mathbf{S},\mathrm{rw}}) \leq \overline{\mathbf{H}}_{\mathbf{S},\mathrm{rw}}, \\
& -\dot{\overline{\mathbf{H}}}_{\mathbf{S},\mathrm{rw}} \leq \dot{\mathbf{H}}_{\mathbf{S}\mathrm{rw}}(\boldsymbol{\sigma}_{\mathbf{S},\mathrm{rw}}, \dot{\boldsymbol{\sigma}}_{\mathbf{S},\mathrm{rw}}, \ddot{\boldsymbol{\sigma}}_{\mathbf{S},\mathrm{rw}}) \leq \dot{\overline{\mathbf{H}}}_{\mathbf{S},\mathrm{rw}}, \\
& \boldsymbol{\sigma}_{\mathbf{S},\mathrm{rw}} = \mathbf{K}_{\sigma_{\mathrm{rw}}}\mathbf{c}_{\mathbf{S}}, \quad \dot{\boldsymbol{\sigma}}_{\mathbf{S},\mathrm{rw}} = \mathbf{K}_{\dot{\sigma}_{\mathrm{rw}}}\mathbf{c}_{\mathbf{S}}, \quad \ddot{\boldsymbol{\sigma}}_{\mathbf{S},\mathrm{rw}} = \mathbf{K}_{\ddot{\sigma}_{\mathrm{rw}}}\mathbf{c}_{\mathbf{S}}, \\
& \mathbf{A}_{\mathbf{x}_f}\mathbf{x}_{\mathbf{S}} = \mathbf{x}_f, \\
& \boldsymbol{\sigma}(t_0,\, \mathbf{c}_{\mathbf{S}}) = \boldsymbol{\sigma}_0,\ \dot{\boldsymbol{\sigma}}(t_0,\, \mathbf{c}_{\mathbf{S}}) = \mathbf{0},\ \ddot{\boldsymbol{\sigma}}(t_0,\, \mathbf{c}_{\mathbf{S}}) = \mathbf{0}, \\
& \boldsymbol{\sigma}(t_f,\, \mathbf{c}_{\mathbf{S}}) = \boldsymbol{\sigma}_f,\ \dot{\boldsymbol{\sigma}}(t_f,\, \mathbf{c}_{\mathbf{S}}) = \mathbf{0},\ \ddot{\boldsymbol{\sigma}}(t_f,\, \mathbf{c}_{\mathbf{S}}) = \mathbf{0},
\end{aligned}} \tag{3.27}$$

where $\mathbf{A}_{\mathbf{S},\mathrm{LOS}} \in \mathbb{R}^{5n_{\mathrm{LOS}}N\times 6n_{\mathrm{LOS}}N}$ and $\mathbf{b}_{\mathbf{S},\mathrm{LOS}} \in \mathbb{R}^{5n_{\mathrm{LOS}}N}$ stack the LOS inequality matrix and vector (see Eq. (3.4)) as

$$\mathbf{A}_{\mathbf{S},\mathrm{LOS}} = \begin{bmatrix} \mathbf{A}_{\mathrm{LOS}} & \mathbf{0}_{5\times 6} & \dots & \mathbf{0}_{5\times 6} \\ \mathbf{0}_{5\times 6} & \mathbf{A}_{\mathrm{LOS}} & \dots & \mathbf{0}_{5\times 6} \\ \vdots & \vdots & \ddots & \vdots \\ \mathbf{0}_{5\times 6} & \mathbf{0}_{5\times 6} & \dots & \mathbf{A}_{\mathrm{LOS}} \end{bmatrix}, \quad \mathbf{b}_{\mathbf{S},\mathrm{LOS}} = \begin{bmatrix} \mathbf{b}_{\mathrm{LOS}} \\ \mathbf{b}_{\mathrm{LOS}} \\ \vdots \\ \mathbf{b}_{\mathrm{LOS}} \end{bmatrix}. \tag{3.28}$$

The terms $\overline{\Delta\mathbf{V}}_{\mathbf{S}p} \in \mathbb{R}^{N+1}$, $\overline{\mathbf{H}}_{\mathbf{S},\mathrm{rw}} \in \mathbb{R}^{3n_{\mathrm{rw}}N}$ and $\dot{\overline{\mathbf{H}}}_{\mathbf{S},\mathrm{rw}} \in \mathbb{R}^{3n_{\mathrm{rw}}N}$ stack the maximum amplitude impulse, reaction wheels angular momentum and its variation respectively

$$\overline{\Delta\mathbf{V}}_{\mathbf{S}p} = \begin{bmatrix} \overline{\Delta V}_p \\ \vdots \\ \overline{\Delta V}_p \end{bmatrix}, \quad \overline{\mathbf{H}}_{\mathbf{S},\mathrm{rw}} = \begin{bmatrix} \overline{\mathbf{H}}_{\mathrm{rw}} \\ \vdots \\ \overline{\mathbf{H}}_{\mathrm{rw}} \end{bmatrix}, \quad \dot{\overline{\mathbf{H}}}_{\mathbf{S},\mathrm{rw}} = \begin{bmatrix} \dot{\overline{\mathbf{H}}}_{\mathrm{rw}} \\ \vdots \\ \dot{\overline{\mathbf{H}}}_{\mathrm{rw}} \end{bmatrix}. \tag{3.29}$$

The matrix $\mathbf{A}_{\mathbf{x}_f} \in \mathbb{R}^{6\times 6n_{\mathrm{LOS}}N}$ extracts the final translational state (rendezvous condition)

$$\mathbf{A}_{\mathbf{x}_f} = \begin{bmatrix} \mathbf{0}_{6(n_{\mathrm{LOS}}N-1)\times 6(n_{\mathrm{LOS}}N-1)} & \mathbf{0}_{6(n_{\mathrm{LOS}}N-1)\times 6} \\ \mathbf{0}_{6\times 6(n_{\mathrm{LOS}}N-1)} & \mathbf{I}_{6\times 6} \end{bmatrix}. \tag{3.30}$$

Besides initial and terminal conditions on attitude and angular velocity, it has been considered that the reaction wheels kinetic momentum and its variation shall be null at the beginning and end of the maneuver. This is the reason why the MRP second derivative is nullified at the initial and final instants of the program (3.27).

3.3.2 Initial guess (warm-start)

Any non-linear programming solver requires an initial guess to compute an optimal solution for problem (3.27). Accordingly, the convergence process can be eased if the initial guess is close to the optimal value while respecting the constraints from the very beginning. For this purpose, the solution to a simplified problem is employed to initialize the NLP solver. This is named as a warm-start because the simplified problem may not fullfil all the constraints.

In this case, a simplified rendezvous problem which only considers translational control is expressed as a quadratically constrained linear program (QCLP). Then, the QCLP solution is converted to the NLP decision variables $\Delta\mathbf{V}_{\mathbf{S}p}$ and $\mathbf{c}_{\mathbf{S}}$.

Simplified rendezvous planning problem

The simplified rendezvous planning problem assumes full three-axis translational control. In the practice, this corresponds to have three pairs of opposite thrusters alligned with each LVLH direction. Under the previous consideration, the relative state propagation is

$$\mathbf{x}(t) = \boldsymbol{\Phi}(t, t_0)\mathbf{x}_0 + \sum_{i=0}^{j} \boldsymbol{\Phi}(t, t_i)\mathbf{B}\Delta\mathbf{V}_i, \quad t_j \leq t < t_{j+1}, \tag{3.31}$$

where $\Delta\mathbf{V} = [\Delta V_x, \Delta V_y, \Delta V_z]^T$. In this hypothetical case, as the number of control directions exactly matches the translational degrees of freedom, the attitude control should only guarantee the alignment of the body frame with respect to the LVLH frame. This causes translational and angular controls to be decoupled.

Under the previous consideration, the simplified rendezvous program is

$$\begin{aligned}
\underset{\Delta\mathbf{V}_j}{\text{minimize}} \quad & \sum_{k=0}^{N} \|\Delta\mathbf{V}_j\|_1, \\
\text{subject to} \quad & \mathbf{x}(t_{j,l}) = \boldsymbol{\Phi}(t_{j,l}, t_0)\mathbf{x}_0 + \sum_{i=0}^{j} \boldsymbol{\Phi}(t_{j,l}, t_i)\mathbf{B}\Delta\mathbf{V}_i, \\
& \qquad\qquad t_j \leq t_{j,l} < t_{j+1}, \\
& \mathbf{A}_{\text{LOS}}\mathbf{x}(t_{j,l}) \leq \mathbf{b}_{\text{LOS}}, \\
& -\max(\overline{\Delta V}_p)/\sqrt{3} \leq \Delta\mathbf{V}_j \leq \max(\overline{\Delta V}_p)/\sqrt{3}, \\
& \mathbf{x}(t_f) = \mathbf{x}_f, \\
& \Delta\mathbf{V}_0^T \mathbf{A}_{i,\boldsymbol{\sigma}_0} \Delta\mathbf{V}_0 = \mathbf{0}, \qquad i = 1, 2, 3, \\
& \Delta\mathbf{V}_N^T \mathbf{A}_{i,\boldsymbol{\sigma}_N} \Delta\mathbf{V}_N = \mathbf{0}, \quad i = 1, 2, 3,
\end{aligned} \tag{3.32}$$

where the continuous line-of-sight constraint has been introduced directly in the discrete form. The impulse amplitude on each translational direction is conservatively constrained to not violate the upper bound of the most reactive thruster in the array when all the simplified problem translational directions saturate simultaneously (thus the division by $\sqrt{3}$). The aim of the last quadratic constraint is to generate an initial solution compatible with the prescribed initial and terminal orientations in problem (3.27). To this end, the quadratic constraints matrices $\mathbf{A}_{i,\boldsymbol{\sigma}_0}$ and $\mathbf{A}_{i,\boldsymbol{\sigma}_N}$ are defined as

$$\mathbf{A}_{i,\boldsymbol{\sigma}_j} = \begin{bmatrix} \delta(i-1) - v_{1,j}^2 & 0 & 0 \\ 0 & \delta(i-2) - v_{2,j}^2 & 0 \\ 0 & 0 & \delta(i-3) - v_{3,j}^2 \end{bmatrix}, \tag{3.33}$$

where δ is the Dirac delta function (its value is the unity if the argument is zero and null otherwise) and $\mathbf{v}_j = [v_{1,j}, v_{2,j}, v_{3,j}]^T = \mathbf{R}(\boldsymbol{\sigma}_j)\mathbf{w}_1$ with the subscript 1 denoting the most reactive thruster of the array ($\overline{\Delta V}_1 \geq \overline{\Delta V}_{p\neq 1}$). This way, the initial guess impulse sequence is compatible with the spacecraft orientation at the start, $\boldsymbol{\sigma}_0$, and the end, $\boldsymbol{\sigma}_f$. Note that the only unaccounted constraints of the 6-DOF NLP problem (3.27) are the reaction wheels control bounds.

NLP initial solution computation from six-thrusters QCLP solution

Once a solution of the QCLP (3.32) is obtained, the three-axis impulse sequence is transferred to the array of thrusters as

$$\Delta V_{1,j} = \|\Delta \mathbf{V}_j\|_2, \quad \Delta V_{p\neq 1,j} = 0. \tag{3.34}$$

It is remarked that the thruster labelled with the subscript 1 has the highest impulse amplitude $\overline{\Delta V}_p$.

The initial guess of B-spline control points, $\mathbf{a_S}$, is computed by matching the three-axis translational control impulses to equivalent single-thruster orientations. These orientations are obtained by aid of the rotation axis and angle. Let denote by j_i^* the nodes where there is a non-null impulse amplitude ($\|\Delta \mathbf{V}_{j_i^*}\|_2 > 0$) or an attitude is prescribed (instants t_0, t_f). The subscript i is just an internal counter of these situations. For those nodes, compute the equivalent single-thruster pointing direction, $\mathbf{v}_{j_i^*}$,

$$\mathbf{v}_{j_i^*} = \frac{\Delta \mathbf{V}_j}{\|\Delta \mathbf{V}_j\|_2}, \quad j_i^* = j, \quad \text{if } (j = 0, N) \vee (\|\Delta \mathbf{V}_j\|_2 > 0). \tag{3.35}$$

Then, the rotation MRP, $\boldsymbol{\sigma}_{\text{rot}}$, associated to consecutive orientations can be computed. For the non-mandatory nodes where $(j \neq 0, N) \wedge (\|\mathbf{V}_{j_i^*}\|_2 = 0)$, the rotation MRP is interpolated. This yields

$$\boldsymbol{\sigma}_{\text{rot}_{j/j-1}} = \mathbf{e}_{j_i^*} \tan\left(\frac{s_j \theta_{j_i^*}}{4}\right), \quad s_j = \frac{j - j_{i-1}^*}{j_i^* - j_{i-1}^*}, \quad t_{j-1}, t_j \in [t_{j_i^*-1}, t_{j_i^*}], \tag{3.36}$$

where the rotation axis, $\mathbf{e}_{j_i^*}$, and angle, $\theta_{j_i^*}$ are obtained through Eq. (3.35) mandatory orientations

$$\mathbf{e}_{j_i^*} = \frac{\mathbf{v}_{j_i^*} \times \mathbf{v}_{j_{i-1}^*}}{\|\mathbf{v}_{j_i^*} \times \mathbf{v}_{j_{i-1}^*}\|_2}, \quad \theta_{j_i^*} = \arccos(\mathbf{v}_{j_i^*}^T \mathbf{v}_{j_{i-1}^*}). \tag{3.37}$$

This way, a well-defined and smooth attitude profile will be obtained. Since $\theta_{j_i^*} \in [-\pi, \pi]$, no singularities arise when computing $\boldsymbol{\sigma}_{\text{rot}}$ through Eq. (3.36). The attitude at the nodes, $\boldsymbol{\sigma}_j$, can be computed by applying the MRP attitude composition rule Eq. (2.88) between nodes

$$\begin{gathered}\boldsymbol{\sigma}_j = \\ \frac{(1 - \|\boldsymbol{\sigma}_{\text{rot}_{j/j-1}}\|_2^2)\boldsymbol{\sigma}_{j-1} + (1 - \|\boldsymbol{\sigma}_{j-1}\|_2^2)\boldsymbol{\sigma}_{\text{rot}_{j/j-1}} + 2\boldsymbol{\sigma}_{j-1} \times \boldsymbol{\sigma}_{\text{rot}_{j/j-1}}}{1 + (\|\boldsymbol{\sigma}_{\text{rot}_{j/j-1}}\|_2 \|\boldsymbol{\sigma}_{j-1}\|_2)^2 - 2\boldsymbol{\sigma}_{\text{rot}_{j/j-1}}^T \boldsymbol{\sigma}_{j-1}}, \\ \text{for } \; j = 1 \dots N, \quad \text{initialized with } \; \boldsymbol{\sigma}_0.\end{gathered} \tag{3.38}$$

The last step consists in obtaining the corresponding B-spline control points $\mathbf{a_S}$ matching the previous attitude sequence $\boldsymbol{\sigma}_j$. By imposing boundary conditions such as null first and second derivatives of the flat output at the initial and final instants ($\dot{\boldsymbol{\sigma}}_0 = \ddot{\boldsymbol{\sigma}}_0 = \mathbf{0}, \dot{\boldsymbol{\sigma}}_N = \ddot{\boldsymbol{\sigma}}_N = \mathbf{0}$), a linear system of $3n_c$ equations (remember that $n_c = N + 5$ was chosen) with the $3n_c$ unknown control points can be posed (see [Kress98])

$$\begin{bmatrix} B_{1,q}(t_0)\mathbf{I} & B_{2,q}(t_0)\mathbf{I} & \dots & B_{n_c,q}(t_0)\mathbf{I} \\ B_{1,q}(t_1)\mathbf{I} & B_{2,q}(t_1)\mathbf{I} & \dots & B_{n_c,q}(t_1)\mathbf{I} \\ \vdots & \vdots & \ddots & \vdots \\ B_{1,q}(t_N)\mathbf{I} & B_{2,q}(t_N)\mathbf{I} & \dots & B_{n_c,q}(t_N)\mathbf{I} \\ \dot{B}_{1,q}(t_0)\mathbf{I} & \dot{B}_{2,q}(t_0)\mathbf{I} & \dots & \dot{B}_{n_c,q}(t_0)\mathbf{I} \\ \dot{B}_{1,q}(t_N)\mathbf{I} & \dot{B}_{2,q}(t_N)\mathbf{I} & \dots & \dot{B}_{n_c,q}(t_N)\mathbf{I} \\ \ddot{B}_{1,q}(t_0)\mathbf{I} & \ddot{B}_{2,q}(t_0)\mathbf{I} & \dots & \ddot{B}_{n_c,q}(t_0)\mathbf{I} \\ \ddot{B}_{1,q}(t_N)\mathbf{I} & \ddot{B}_{2,q}(t_N)\mathbf{I} & \dots & \ddot{B}_{n_c,q}(t_N)\mathbf{I} \end{bmatrix} \begin{bmatrix} \mathbf{c}_1 \\ \mathbf{c}_2 \\ \vdots \\ \mathbf{c}_{n_c} \end{bmatrix} = \begin{bmatrix} \boldsymbol{\sigma}_0 \\ \boldsymbol{\sigma}_1 \\ \vdots \\ \boldsymbol{\sigma}_N \\ \mathbf{0} \\ \mathbf{0} \\ \mathbf{0} \\ \mathbf{0} \end{bmatrix}. \tag{3.39}$$

The solution can be obtained by inverting the matrix premultiplying the unknown control points. Note that $B_{i,q}(t) = 0$ if $t \notin [t_{\text{knots},i}, t_{\text{knots},i+q+1})$.

3.4 Linearized MPC scheme

By solving the NLP optimization problem (3.27), an open-loop control solution is obtained. In practice, control mishaps and unmodelled dynamics may perturb this solution deviating the chaser from the planned trajectory. One could directly update the control plan by obtaining new solutions of the NLP problem. However, this approach is not friendly from an autonomous system perspective. The computational time to obtain the NLP solution may overcome the interval between impulses, thus failing to recalculate the control sequence.

Alternatively, by assuming the trajectory deviations are weak enough, the linearization of the problem around the initial open-loop solution reduces the program to quadratic programming. The decision variables are small increments with respect to the last available control sequence. Using the previous linearized based approach, an MPC scheme is feasible. This consists in updating the decision variables on-line, sliding the control horizon forward in time, by solving a QP problem after each impulse is applied. As the sliding control horizon approach may cause infeasibilities because the terminal constraints are advanced in time, these are relaxed by transforming them into terminal costs.

3.4.1 Linearized prediction model

Let define increments of each thruster impulse amplitude as ξ_p and of the MRP control points as $\Delta\mathbf{c}_r$. Introducing these increments in the relative state transition, given by Eq. (3.10), and expanding the expression up to first-order one obtains

$$\begin{aligned}\mathbf{x}(t) \approx \boldsymbol{\Phi}(t, t_k)\mathbf{x}_k + \sum_{i=k}^{k+j}\sum_{p=1}^{n_T} \boldsymbol{\Phi}(t, t_i)\mathbf{B}\Bigg[\mathbf{R}^T(\mathbf{c}_{\mathbf{S}})\mathbf{w}_p(\Delta V_p(t_i) + \xi_p(t_i)) \\ + \sum_{r=k+1}^{k+n_c} \mathbf{R}_{\mathbf{w}_p,\mathbf{c}_r}(\boldsymbol{\sigma}_i)\Delta\mathbf{c}_r\Delta V_p(t_i)\Bigg], \quad t \in [t_{k+j}, t_{k+j+1}), \\ k = 1 \dots N,\end{aligned} \tag{3.40}$$

where k is the current MPC step (which increases as impulses are applied) and $\mathbf{R}_{\mathbf{w}_p,\mathbf{c}_r} \in \mathbb{R}^{3\times3}$ is the Jacobian matrix resulting of the projection of each thruster control direction in the LVLH frame, $\mathbf{R}^T(\boldsymbol{\sigma}_i)\mathbf{w}_p$, with respect to the MRP control point $\mathbf{c}_r$

$$\mathbf{R}_{\mathbf{w}_p,\mathbf{c}_r} = \frac{\partial(\mathbf{R}(\boldsymbol{\sigma})\mathbf{w}_p)}{\partial\boldsymbol{\sigma}}\frac{\partial\boldsymbol{\sigma}}{\partial\mathbf{c}_r}. \tag{3.41}$$

In accordance with Eq. (3.21)-(3.30) compact formulation, let define stack vectors of the incremental decision variables $\boldsymbol{\xi}_{\mathbf{S}p}(k) \in \mathbb{R}^{N+1}$ and $\Delta\mathbf{c}_{\mathbf{S}}(k) \in \mathbb{R}^{3n_c}$ as

$$\boldsymbol{\xi}_{\mathbf{S}p}(k) = \begin{bmatrix} \xi_{p,k} \\ \vdots \\ \xi_{p,k+N} \end{bmatrix}, \quad \Delta\mathbf{c}_{\mathbf{S}}(k) = \begin{bmatrix} \mathbf{c}_{k+1} \\ \vdots \\ \mathbf{c}_{k+n_c} \end{bmatrix}. \tag{3.42}$$

As well, let define the stack matrix $\mathbf{G}_{p,\mathbf{c}_{\mathbf{S}}}(k) \in \mathbb{R}^{6n_{\mathrm{LOS}N}\times3n_c}$

$$\mathbf{G}_{p,\mathbf{c}_{\mathbf{S}}}(k) =$$

$$\begin{bmatrix} \boldsymbol{\Phi}(t_{k+1,1}, t_k)\Delta\mathbf{x}_{p,k+1}(t_k) & \dots & \boldsymbol{\Phi}(t_{k+1,1}, t_k)\Delta\mathbf{x}_{p,k+n_c}(t_k) \\ \vdots & \ddots & \vdots \\ \boldsymbol{\Phi}(t_{k+1,n_{\mathrm{LOS}}}, t_k)\Delta\mathbf{x}_{p,k+1}(t_k) & \dots & \boldsymbol{\Phi}(t_{k+1,n_{\mathrm{LOS}}}, t_k)\Delta\mathbf{x}_{p,k+n_c}(t_k) \\ \vdots & \ddots & \vdots \\ \vdots & \ddots & \vdots \\ \sum\limits_{i=k}^{k+N} \boldsymbol{\Phi}(t_{k+N,n_{\mathrm{LOS}}}, t_i)\Delta\mathbf{x}_{p,k+1}(t_i) & \dots & \sum\limits_{i=k}^{k+N} \boldsymbol{\Phi}(t_{k+N,n_{\mathrm{LOS}}}, t_i)\Delta\mathbf{x}_{p,k+n_c}(t_i) \end{bmatrix},$$

where $\Delta\mathbf{x}_{p,k+r}(t_{k+j}) = \mathbf{B}\Delta\mathbf{R}_{\mathbf{w}_p,\mathbf{c}_{k+r}}\Delta V_{p,k+j}$. Note that, in a similar way as in Eq. (3.39), the matrix $\Delta\mathbf{R}_{\mathbf{w}_p,\mathbf{c}_{k+j}} = \mathbf{0}_{3\times3}$ if $t_{k+j} \notin [t_{\mathrm{knots},k+j}, t_{\mathrm{knots},k+j+q+1})$. Using the stack vectors and matrices, the following linear propagation, in a compact form, is obtained

$$\mathbf{x}_{\mathbf{S}}(k) \approx \mathbf{F}\mathbf{x}_k + \sum_{p=1}^{n_T} \left[\mathbf{G}_p(\mathbf{c}_{\mathbf{S}})(\Delta\mathbf{V}_{\mathbf{S}p} + \boldsymbol{\xi}_{\mathbf{S}p}) + \mathbf{G}_{p,\mathbf{c}_{\mathbf{S}}}(\Delta\mathbf{V}_{\mathbf{S}p}, \boldsymbol{\sigma}_{\mathbf{S}})\Delta\mathbf{c}_{\mathbf{S}}\right], \tag{3.43}$$

where the dependencies with k have been omitted at the right-hand side of Eq. (3.43) for the sake of clarity. The increments on the impulse amplitude are accurately accounted for as the relative propagation was linear on this variable. On the other hand, changes in the nodes orientation are linearly modelled through the matrix $\mathbf{G}_{p,\mathbf{c_S}}$ though its effect is more complex. Note that if the incremental decision variables are null, the original compact propagation of Eq. (3.24) is recovered.

The reaction wheels angular momentum and its variation are also linearized as

$$\begin{aligned}
\mathbf{H}_{\mathrm{rw}} &\approx \mathbf{H}_{\mathrm{rw}}(\boldsymbol{\sigma},\dot{\boldsymbol{\sigma}}) + \sum_{r=k}^{k+n_c}\left(\frac{\partial \mathbf{H}_{\mathrm{rw}}}{\partial \boldsymbol{\sigma}}\frac{\partial \boldsymbol{\sigma}}{\partial \mathbf{c}_r} + \frac{\partial \mathbf{H}_{\mathrm{rw}}}{\partial \dot{\boldsymbol{\sigma}}}\frac{\partial \dot{\boldsymbol{\sigma}}}{\partial \mathbf{c}_r}\right)\Delta\mathbf{c}_r,\\
\dot{\mathbf{H}}_{\mathrm{rw}} &\approx \dot{\mathbf{H}}_{\mathrm{rw}}(\boldsymbol{\sigma},\dot{\boldsymbol{\sigma}},\ddot{\boldsymbol{\sigma}}) + \sum_{r=k}^{k+n_c}\left(\frac{\partial \dot{\mathbf{H}}_{\mathrm{rw}}}{\partial \boldsymbol{\sigma}}\frac{\partial \boldsymbol{\sigma}}{\partial \mathbf{c}_r} + \frac{\partial \dot{\mathbf{H}}_{\mathrm{rw}}}{\partial \dot{\boldsymbol{\sigma}}}\frac{\partial \dot{\boldsymbol{\sigma}}}{\partial \mathbf{c}_r} + \frac{\partial \dot{\mathbf{H}}_{\mathrm{rw}}}{\partial \ddot{\boldsymbol{\sigma}}}\frac{\partial \ddot{\boldsymbol{\sigma}}}{\partial \mathbf{c}_r}\right)\Delta\mathbf{c}_r,
\end{aligned}$$

which can be expressed for all the constraints enforcement instants $t_{k+j,m}$ in a compact formulation as

$$\begin{aligned}
\mathbf{H}_{\mathbf{S},\mathrm{rw}}(k) &\approx \mathbf{H}_{\mathbf{S},\mathrm{rw}}(\boldsymbol{\sigma}_{\mathbf{S},\mathrm{rw}},\dot{\boldsymbol{\sigma}}_{\mathbf{S},\mathrm{rw}}) + \mathbf{L}_{H_{\mathrm{rw}}}(\boldsymbol{\sigma}_{\mathbf{S},\mathrm{rw}},\dot{\boldsymbol{\sigma}}_{\mathbf{S},\mathrm{rw}})\Delta\mathbf{c}_{\mathbf{S}},\\
\dot{\mathbf{H}}_{\mathbf{S},\mathrm{rw}}(k) &\approx \dot{\mathbf{H}}_{\mathbf{S},\mathrm{rw}}(\boldsymbol{\sigma}_{\mathbf{S},\mathrm{rw}},\dot{\boldsymbol{\sigma}}_{\mathbf{S},\mathrm{rw}},\ddot{\boldsymbol{\sigma}}_{\mathbf{S},\mathrm{rw}}) + \mathbf{L}_{\dot{H}_{\mathrm{rw}}}(\boldsymbol{\sigma}_{\mathbf{S},\mathrm{rw}},\dot{\boldsymbol{\sigma}}_{\mathbf{S},\mathrm{rw}},\ddot{\boldsymbol{\sigma}}_{\mathbf{S},\mathrm{rw}})\Delta\mathbf{c}_{\mathbf{S}},
\end{aligned} \tag{3.44}$$

where the matrices $\mathbf{L}_{H_{\mathrm{rw}}}, \mathbf{L}_{\dot{H}_{\mathrm{rw}}} \in \mathbb{R}^{3n_{\mathrm{rw}}N\times 3n_c}$ stack the reaction wheels angular momentum and its variation first derivative with respect to the control points. The dependency with the current MPC step k has been ommited at the right hand side of Eq. (3.44) for the sake of clarity.

3.4.2 Linearized control program

The linearized control program mimics the NLP planning problem (3.27). However, the terminal constraints are transformed to costs in order to prevent infeasibilities as the MPC step advances over time [Chen98]. As analyzed in [Limon06], relaxing the terminal constraints could potentially improve asymptotic stability (whose study is beyond the scope of this work). Under the previous considerations and using the linearized compact propagation of Eq. (3.43) the NLP problem (3.27) is linearized as

$$\boxed{\begin{aligned}
\underset{\boldsymbol{\xi}_{\mathbf{S}p}(k),\Delta\mathbf{c}_{\mathbf{S}}(k)}{\text{minimize}}\quad & \sum_{p=1}^{n_T}\mathbf{f}_{\xi}^T\boldsymbol{\xi}_{\mathbf{S}p}(k)+(\mathbf{x}_{\mathbf{S}}(k)-\mathbf{x}_{\mathbf{S}f})^T\mathbf{Q}_{\mathbf{S}x_f}(k)(\mathbf{x}_{\mathbf{S}}(k)-\mathbf{x}_{\mathbf{S}f})\\
& +(\boldsymbol{\sigma}_{\mathbf{S}}(k)-\boldsymbol{\sigma}_{\mathbf{S}f})^T\mathbf{Q}_{\mathbf{S}\sigma_f}(k)(\boldsymbol{\sigma}_{\mathbf{S}}(k)-\boldsymbol{\sigma}_{\mathbf{S}f})\\
& +\dot{\boldsymbol{\sigma}}_{\mathbf{S}}^T(k)\mathbf{Q}_{\mathbf{S}\dot{\sigma}_f}(k)\dot{\boldsymbol{\sigma}}_{\mathbf{S}}^T(k),\quad k=1\dots N,\\
\text{subject to}\quad & \mathbf{x}_{\mathbf{S}}(k)=\mathbf{F}\mathbf{x}_k+\sum_{p=1}^{n_T}\big[\mathbf{G}_p(\boldsymbol{\sigma}_{\mathbf{S}})(\Delta\mathbf{V}_{\mathbf{S}p}+\boldsymbol{\xi}_{\mathbf{S}p})\\
& \qquad\qquad +\mathbf{G}_{p,\mathbf{c}_{\mathbf{S}}}(\Delta\mathbf{V}_{\mathbf{S}p},\boldsymbol{\sigma}_{\mathbf{S}})\Delta\mathbf{c}_{\mathbf{S}})\big],\\
& \boldsymbol{\sigma}_{\mathbf{S}}(k)=\mathbf{K}_{\sigma}(k)\mathbf{c}_{\mathbf{S}}(k),\\
& \mathbf{A}_{\mathbf{S},\mathrm{LOS}}\mathbf{x}_{\mathbf{S}}(k)\leq\mathbf{b}_{\mathrm{LOS}},\\
& \mathbf{0}\leq\Delta\mathbf{V}_{\mathbf{S}p}(k)+\boldsymbol{\xi}_{\mathbf{S}p}(k)\leq\overline{\Delta\mathbf{V}}_{\mathbf{S}p},\\
& -\overline{\mathbf{H}}_{\mathbf{S},\mathrm{rw}}\leq\mathbf{H}_{\mathbf{S},\mathrm{rw}}(k)+\mathbf{L}_{H_{\mathrm{rw}}}(k)\Delta\mathbf{c}_{\mathbf{S}}(k)\leq\overline{\mathbf{H}}_{\mathbf{S},\mathrm{rw}},\\
& -\dot{\overline{\mathbf{H}}}_{\mathbf{S},\mathrm{rw}}\leq\dot{\mathbf{H}}_{\mathbf{S},\mathrm{rw}}(k)+\mathbf{L}_{\dot{H}_{\mathrm{rw}}}(k)\Delta\mathbf{c}_{\mathbf{S}}(k)\leq\dot{\overline{\mathbf{H}}}_{\mathbf{S}\mathrm{rw}},\\
& \Delta\boldsymbol{\sigma}(t_k,\Delta\mathbf{c}_{\mathbf{S}}(k))=\tilde{\boldsymbol{\sigma}}_k-\boldsymbol{\sigma}(t_k,\mathbf{c}_{\mathbf{S}}(k)),\\
& \Delta\dot{\boldsymbol{\sigma}}(t_k,\Delta\mathbf{c}_{\mathbf{S}}(k))=\dot{\tilde{\boldsymbol{\sigma}}}_k-\dot{\boldsymbol{\sigma}}(t_k,\mathbf{c}_{\mathbf{S}}(k)),\\
& \Delta\ddot{\boldsymbol{\sigma}}(t_k,\Delta\mathbf{c}_{\mathbf{S}}(k))=\ddot{\tilde{\boldsymbol{\sigma}}}_k-\ddot{\boldsymbol{\sigma}}(t_k,\mathbf{c}_{\mathbf{S}}(k)),\\
& -\overline{\boldsymbol{\xi}}_{\mathbf{S}p}\leq\boldsymbol{\xi}_{\mathbf{S}p}(k)\leq\overline{\boldsymbol{\xi}}_{\mathbf{S}p},\\
& -\overline{\Delta\mathbf{c}}_{\mathbf{S}}\leq\Delta\mathbf{c}_{\mathbf{S}}(k)\leq\overline{\Delta\mathbf{c}}_{\mathbf{S}},
\end{aligned}}\tag{3.45}$$

where $\tilde{\boldsymbol{\sigma}}$, $\dot{\tilde{\boldsymbol{\sigma}}}$ and $\ddot{\tilde{\boldsymbol{\sigma}}}$ are the actual attitude and its derivatives at the end of each MPC interval k. These measurements are necessary because the actual attitude path may mismatch the planned one due to the employed continuous constraints reduction (see Eq. (3.19)-(3.20)). The cost function vector premultiplying the incremental impulses is

$$\mathbf{f}_{\xi}=[1,1,\dots,1]^T.\tag{3.46}$$

Note that minimizing the incremental impulses would reduce impulse amplitudes. The terminal quadratic matrices ($\mathbf{Q}_{\mathbf{S},x_f}$, $\mathbf{Q}_{\mathbf{S}\sigma_f}$, $\mathbf{Q}_{\mathbf{S}\dot{\sigma}_f}$), and terminal stack vectors ($\mathbf{x}_{\mathbf{S},f}$, $\boldsymbol{\sigma}_{\mathbf{S},f}$) are as follows

$$\mathbf{Q}_{\mathbf{S}x_f}=\begin{bmatrix}h(k-N)\mathbf{Q}_{x_f} & \dots & \mathbf{0}_{6\times6}\\ \vdots & \ddots & \vdots\\ \mathbf{0}_{6\times6} & \dots & h(k)\mathbf{Q}_{x_f}\end{bmatrix},\quad \mathbf{x}_{\mathbf{S},f}=\begin{bmatrix}\mathbf{x}_f\\ \vdots\\ \mathbf{x}_f,\end{bmatrix},\tag{3.47}$$

$$\mathbf{Q}_{\mathbf{S}\sigma_f}=\gamma_{\sigma}\begin{bmatrix}h(k-N)\mathbf{I} & \dots & \mathbf{0}_{3\times3}\\ \vdots & \ddots & \vdots\\ \mathbf{0}_{3\times3} & \dots & h(k)\mathbf{I}\end{bmatrix},\quad \boldsymbol{\sigma}_{\mathbf{S},f}=\begin{bmatrix}\boldsymbol{\sigma}_f\\ \vdots\\ \boldsymbol{\sigma}_f\end{bmatrix},\tag{3.48}$$

$$\mathbf{Q}_{\mathbf{S}\dot{\sigma}_f} = \gamma_{\dot{\sigma}} \begin{bmatrix} h(k-N)\mathbf{I} & \dots & \mathbf{0}_{3\times3} \\ \vdots & \ddots & \vdots \\ \mathbf{0}_{3\times3} & \dots & h(k)\mathbf{I} \end{bmatrix}, \tag{3.49}$$

where h is the Heaviside step function which effectively slides the terminal condition forward in time. This potentially helps to stabilize the terminal condition as it is desired not only to reach the terminal state but to maintain it. The relative state cost function yields

$$\mathbf{Q}_{x_f} = \begin{bmatrix} \gamma_\rho \mathbf{I} & \mathbf{0}_{3\times3} \\ \mathbf{0}_{3\times3} & \gamma_{\dot{\rho}} \mathbf{I} \end{bmatrix}. \tag{3.50}$$

The terms $\{\gamma_\rho, \gamma_{\dot{\rho}}, \gamma_\sigma, \gamma_{\dot{\sigma}}\} \geq 0$ are penalty weights for each terminal condition with respect to the fuel consumption. The linearized control program (3.45) is a QP problem because its objective function is quadratic and its constraints are linear. This is due to the relative states linear propagation given by Eq. (3.43) and the linear relation of the MRP (flat output) and its derivatives with the control points (see Eq. (3.16)).

3.4.3 MPC scheme

Using an initial open-loop solution of problem (3.27), a closed-loop MPC scheme can be built with the linearized problem (3.45). The control sequence is updated after each impulsive action. The details of the implemented MPC strategy are expressed as pseudocode in Algorithm 1.

The most computational demanding step 4 can be computed off-line by ground control segment and uplinked prior the operation beggining. This way, no hard real-time requirements arise when computing the NLP problem solution (3.27). The steps 7-17 are performed on-line, thus requiring fast computations in order to update the control sequence. That is the main reason why a QP problem (3.45) (under linearization assumptions) has been developed instead of solving a NLP problem at each step. In [Hartley15b], quadratic programming for elliptic rendezvous operations was proven feasible from a computational perspective using field programmable gate arrays (FPGAs).

Note that steps 8-10 prescribe controls as the horizon is slided forward. Assuming the terminal state is close to the desired one, a null impulse sequence is prescribed (which would be corrected by small increments if needed). The attitudes over the initial control horizon are prescribed to remain motionless forward in time assuming the desired final orientation is met. Consequently, in step 10, the reference B-splines control points are updated by adding the previous considerations to the last computed reference orientations and subsequently solving the linear system of Eq. (3.39).

Algorithm 1: MPC scheme for six-degrees of freedom rendezvous

```
begin
    Obtain a solution of the QCLP problem (3.32);
    Transform the QCLP solution to NLP decision variables (initial
      guess) using Eq. (3.34)-(3.39);
    Obtain a solution of the NLP problem (3.27), $\Delta\mathbf{V}_{\mathbf{S}p}$ and $\mathbf{c}_{\mathbf{S}}$;
    Apply $\Delta V_p(t_0)$ and $\dot{\mathbf{H}}_{\mathrm{rw}}(t, \mathbf{c}_{\mathbf{S}})$ for $t \in [t_0,\ t_1)$;
    Initialize the MPC step $k = 1$;
    while $k < N$ do
        Prescribe reference controls at $N + k$:
        $\Delta V_{p,N+k}$=0,
        $\boldsymbol{\sigma}(t_{N+k}, \mathbf{c}_{\mathbf{S}}(k)) = \boldsymbol{\sigma}_f$, $\dot{\boldsymbol{\sigma}}(t_{N+k}, \mathbf{c}_{\mathbf{S}}(k)) = \mathbf{0}$,
          $\ddot{\boldsymbol{\sigma}}(t_{N+k}, \mathbf{c}_{\mathbf{S}}(k)) = \mathbf{0} \xRightarrow{\text{Eq. (3.39)}} \mathbf{c}_{\mathbf{S}}(k)$;
        Obtain the solution of the QP linearized rendezvous problem
          (3.45), $\boldsymbol{\xi}_{\mathbf{S}p}(k)$ and $\Delta\mathbf{c}_{\mathbf{S}}(k)$;
        Update the control sequence:
        $\Delta\mathbf{V}_{\mathbf{S}p}(k) = \Delta\mathbf{V}_{\mathbf{S}p}(k) + \boldsymbol{\xi}_{\mathbf{S}p}(k)$,
        $\mathbf{c}_{\mathbf{S}}(k) = \mathbf{c}_{\mathbf{S}}(k) + \Delta\mathbf{c}_{\mathbf{S}}(k)$;
        Apply $\Delta V_p(t_k)$ and $\dot{\mathbf{H}}_{\mathrm{rw}}(t)$ for $t \in [t_k,\ t_{k+1})$;
        Update the MPC step, $k \leftarrow k + 1$;
    end
    Apply the final braking impulse $\Delta V_p(t_N)$;
end
```

3.5 Numerical results

The developed formulation allows to freely choose any array of impulsive thrusters (as long as they are aligned with the center of mass) and inertia matrix. To test that feature, two different spacecraft configurations are going to be analyzed. The first one is a traditional heavy cargo chaser spacecraft overequipped with ten thrusters. The second one considers a lightweight spacecraft with only two thrusters available. Additionally, the simulation model is non-linear and mishaps on the impulses application are added. This allows to assess the MPC capability in terms of disturbances rejection.

The simulations have been done in a MATLAB environment using *Gurobi* optimization package (see [Gurobi14]) as QCLP and QP solver. The open-source IPOPT optimization package (see [IPOPT16]) is used as NLP solver.

3.5.1 Simulation model and controller parameters

Next, the detailed simulation and tuning parameters are detailed.

Simulation model

The simulation model assumes a target Keplerian orbit and non-linear relative motion dynamics of Eq. (2.24) without orbital perturbations but with mishaps on the impulses application

$$\begin{aligned}
\ddot{\boldsymbol{\rho}}(t) &= -\dot{\boldsymbol{\omega}}_{L/I} \times \boldsymbol{\rho} - 2\boldsymbol{\omega}_{L/I} \times \dot{\boldsymbol{\rho}} - \boldsymbol{\omega}_{L/I} \times \boldsymbol{\omega}_{L/I} \times \boldsymbol{\rho} - \frac{\mu(\mathbf{r}_t + \boldsymbol{\rho})}{\|\mathbf{r}_t + \boldsymbol{\rho}\|_2^3} + \frac{\mu \mathbf{r}_t}{r_t^3}, \\
\dot{\boldsymbol{\rho}}^+(t_k) &= \dot{\boldsymbol{\rho}}(t_k) + \sum_{p=1}^{n_T} \mathbf{R}^T(\boldsymbol{\sigma}(t_k))\Delta\mathbf{R}(\boldsymbol{\delta\theta})\mathbf{w}_p(1 + \epsilon_{\Delta V_p})\Delta V_p(t_k), \\
\ddot{\mathbf{r}}_t(t) &= -\frac{\mu \mathbf{r}_t(t)}{r_t^3(t)},
\end{aligned}$$

where $\mu = 398600.4$ km^3/s^2 is the Earth's standard gravitational parameter. The dependence with time has been omitted at the right hand side of the relative dynamics for the sake of clarity. Since the target is passive, the only control are the instantaneous velocity changes of the chaser. The impulse mishaps are caused by a multiplicative disturbance, $\epsilon_{\Delta V_p}$, and a thrusters array misalignment matrix $\Delta\mathbf{R}$. These effects are modelled as random Gaussian distributions as stated in Eq. (2.68)-(2.69). The additive noise component has not been considered, thus $\boldsymbol{\delta}\mathbf{V} = \mathbf{0}$.

The attitude model is assumed to perfectly match the prediction one (external torque free), hence Eq. (2.90) and Eq. (2.97) apply. Under the presence of perturbations, a low-level attitude controller, though out of the scope of this work, may further help to acquire the planned orientations. In any case, it should be noted that the impulses orientation is not perfect due to the misalignment matrix.

Controller parameters

In the simulations, the line of sight region is characterized by $c_y = c_z = 1/\tan(\pi/4)$ and $y_0 = z_0 = 2.5$ m. This represents a 90° angular aperture from the docking port. The details on the duration, array of thrusters, reaction wheels, initial and terminal constraints are given in each scenario section.

Regarding MPC tuning parameters (for both scenarios) the MRP B-splines degree is chosen to be quintic. This is equivalent to take $q = 5$ in Eq. (3.16). The intervals between impulses is chosen as $N = 20$, hence the amount of impulses is twenty one. The constraints enforcement parameters are taken as $n_{\text{LOS}} = 2$ (see Eq. (3.18)) and $n_{\text{rw}} = 12$ (see Eq. (3.19)-(3.20)). The objective function weights are tuned as $\gamma_\rho = 10$, $\gamma_{\dot{\rho}} = 5$, $\gamma_\sigma = 2$ and $\gamma_{\dot{\sigma}} = 1$.

3.5.2 Cargo spacecraft

This scenario analyzes a traditional chaser cargo spacecraft (e.g. Soyuz rendezvous with ISS). This spacecraft has the array of thrusters shown in Table 3.1. The target is flying in an eccentric low Earth orbit with $e = 0.1$, $h_p = 600$ km and $\nu(t_0) = \pi/4$. The term h_p is the periapsis altitude. The chaser inertia matrix is chosen to be of the same order of magnitude than the Russian Progress cargo spacecraft [Fehse03],

p	$\mathbf{w}_p$	$\overline{\Delta V}_p$	p	$\mathbf{w}_p$	$\overline{\Delta V}_p$
1	$[1, 0, 0]^T$	1 m/s	6	$[0, 0, -1]^T$	1 m/s
2	$[-1, 0, 0]^T$	1 m/s	7	$[\sqrt{2}/2, \sqrt{2}/2, 0]^T$	1 m/s
3	$[0, 1, 0]^T$	1 m/s	8	$[\sqrt{2}/2, -\sqrt{2}/2, 0]^T$	1 m/s
4	$[0, -1, 0]^T$	1 m/s	9	$[-\sqrt{2}/2, \sqrt{2}/2, 0]^T$	1 m/s
5	$[0, 0, 1]^T$	1 m/s	10	$[-\sqrt{2}/2, -\sqrt{2}/2, 0]^T$	1 m/s

Table 3.1: Array of thrusters for the cargo spacecraft.

$$\mathbf{J} = \begin{bmatrix} 31 & 0 & 0 \\ 0 & 31 & 0 \\ 0 & 0 & 5 \end{bmatrix} \cdot 10^3 \ \text{kg} \cdot \text{m}^2. \tag{3.51}$$

The reaction wheels angular momentum and its variation upper limits are taken as $\overline{\mathbf{H}}_{\text{rw}} = [500, 500, 500]^T$ N·m·s and $\overline{\dot{\mathbf{H}}}_{\text{rw}} = [20, 20, 20]^T$ N·m respectively. The initial and terminal conditions of the 6-DOF maneuver are shown in Table 3.2. The vector $\boldsymbol{\theta}$ is filled with the Euler angles sequence $\{zxz\}$ representing the body orientation with respect to the LVLH frame. Note that with a number of intervals $N = 20$ and a maneuver duration of $t_f - t_0 = 15$ min, the MPC sampling rate is $\Delta t = 45$ s. The initial total angular momentum is $\mathbf{H}_{\text{tot}} = \mathbf{J}\mathbf{R}(\boldsymbol{\sigma}_0)\boldsymbol{\omega}_0 = [0, -33.3649, 0]^T$ N · m · s which is conserved over time. Let recall that $\boldsymbol{\omega} = \boldsymbol{\omega}_{B/L} + \boldsymbol{\omega}_{L/I}$. The impulses mishaps statistical properties are stated

Variable	Initial	Terminal
t	0 min	15 min
$\boldsymbol{\rho}$	$[400, -250, -200]^T$ m	$[2, 0, 0]^T$ m
$\dot{\boldsymbol{\rho}}$	$[1, 1, -1]^T$ m/s	$[0, 0, 0]^T$ m/s
$\boldsymbol{\theta}$	$[0°, 0°, 0°]^T$	$[90°, 90°, 90°]^T$
$\boldsymbol{\omega}_{B/L}$	$[0, 0, 0]^T$ °/s	$[0, 0, 0]^T$ °/s

Table 3.2: Initial and terminal conditions for the cargo spacecraft.

in Table 3.3. A misalignment on the array of thrusters and a multiplicative mishap in the thrust level has been considered. Nonetheless, the additive disturbance has not been taken into account.

	Variable	Bias	Covariance
Misalignment angles	$\boldsymbol{\delta\theta}$	$[1°, 1°, 1°]^T$	$\mathbf{I}^{(\circ)^2}$
Multiplicative	$\epsilon_{\Delta V_p}$	0.02	0.05
Additive	$\boldsymbol{\delta}\mathbf{V}_p$	$[0, 0, 0]$ m/s	$\mathbf{0}_{3\times 3}$ $(\mathrm{m/s})^2$

Table 3.3: Statistical properties of impulses mishaps for the cargo spacecraft.

Under the previous conditions, 100 random realizations of the impulses mishaps have been simulated. For all the realizations, the linear QP program was always feasible and the chaser reaches the proximity of the target without trespassing the LOS region (see Fig. 3.3-3.4). A typical attitude profile is shown in Fig. 3.6. For this attitude evolution, the desired final orientation ($\boldsymbol{\sigma}_f = [0, -0.4142, 0]^T$) is met whereas the angular velocity is driven to a quasi-null value due to the sliding horizon which plans how to maintain the spacecraft in the target neighbourhood over another control horizon. The terminal accuracy details are given in Table 3.4. The operator δ represents the mismatch between the obtained and the desired value (e.g. $\delta\rho(t_f) = \|\boldsymbol{\rho}(t_f) - \boldsymbol{\rho}_f\|_2$). If one observes the planned impulses, for the first random realization in Fig. 3.5, the thrusters {2,5,6,7,9,10} apply relevant firings while thrusters {1,3,4,8} are not operated significantly along the maneuver. In Fig. 3.7 it is shown that the reaction wheels have saturations (both on angular velocity and acceleration) close to the maneuver initial and final instants, but then desaturate immediately and keep providing torque (the reaction wheels angular momentum peak of the converted solution from QCLP was reduced in a 80.31% by the NLP solution).

Regarding fuel consumption, the NLP program reduces the QCLP problem initial guess in a 21.642% (see Table 3.5). This is to be expected as it is more efficient, from the fuel consumption perspective, to align a specific thruster with the control direction (by rotating the spacecraft) than firing three thrusters simultaneously. The closed-loop MPC increases its fuel consumption

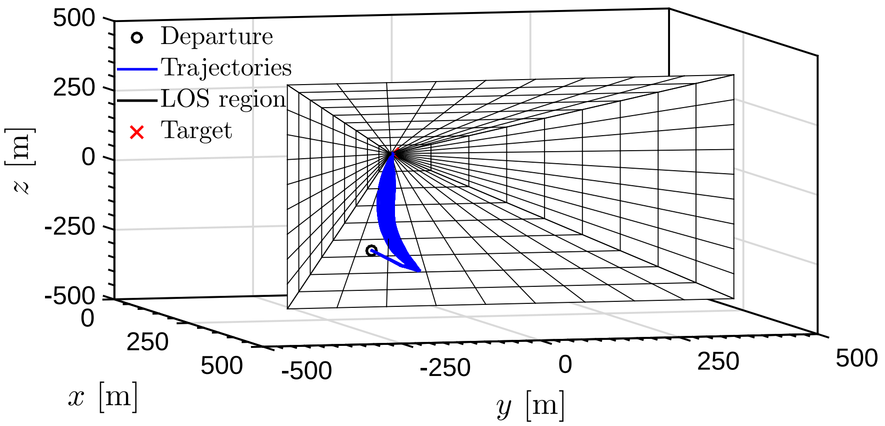

Figure 3.3: Random realizations for the trajectories of the cargo spacecraft.

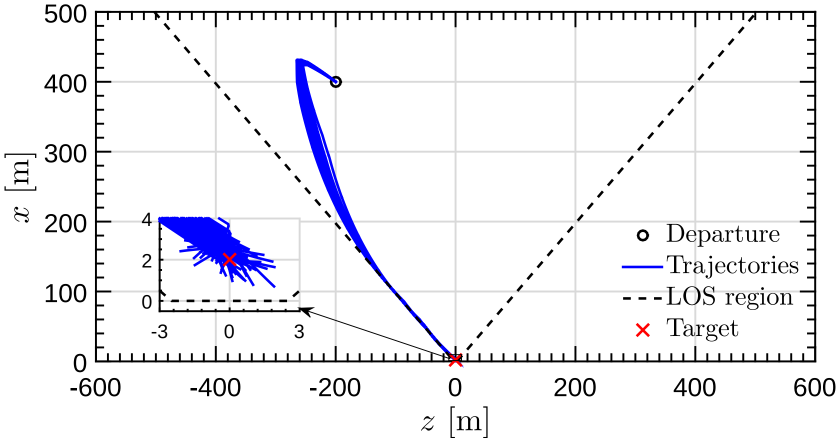

Figure 3.4: Random realizations for the trajectories projection on the target orbital plane of the cargo spacecraft.

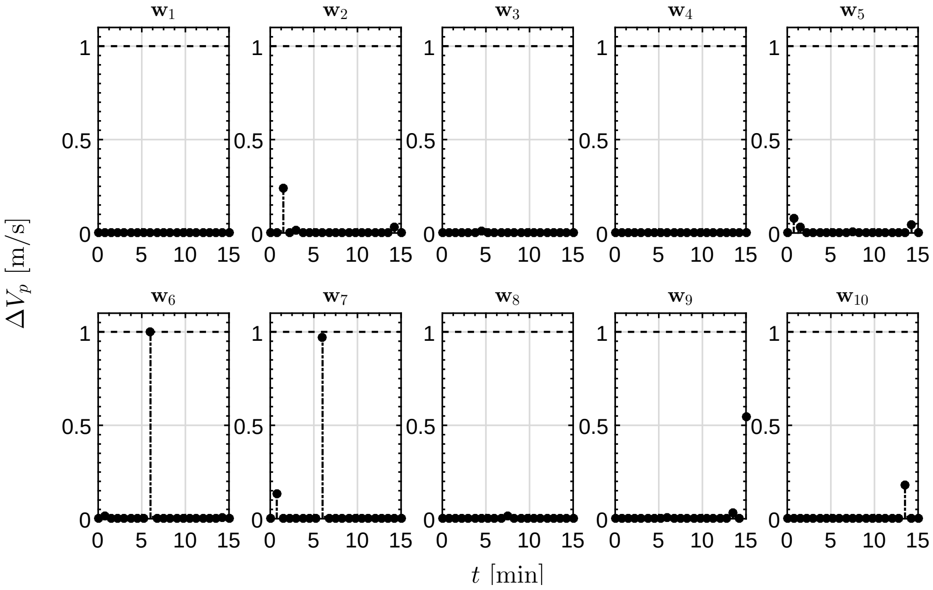

Figure 3.5: Computed impulses for the first random realization of the cargo spacecraft.

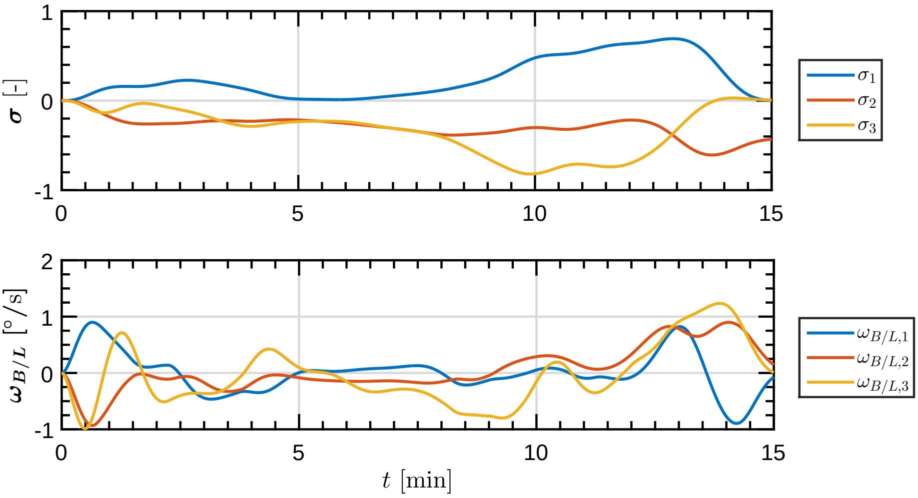

Figure 3.6: Attitude and angular velocity for the first random realization of the cargo spacecraft.

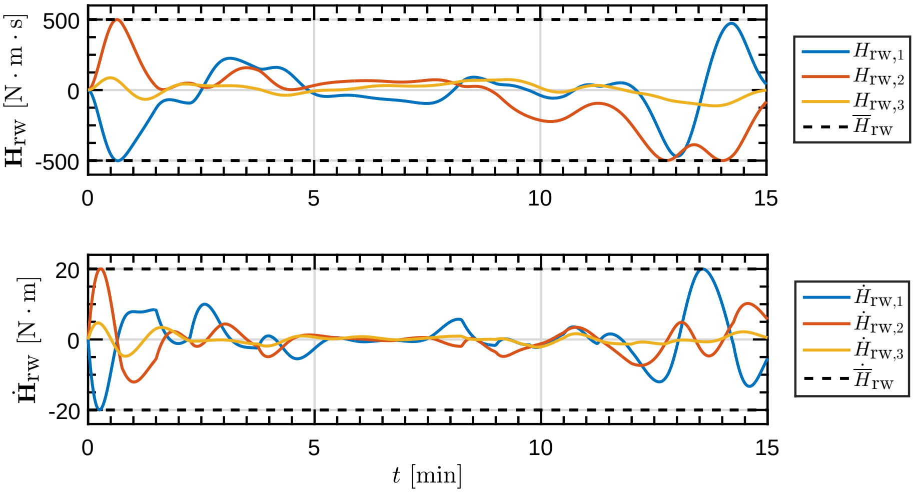

Figure 3.7: Reaction wheels angular momentum and its variation for the first random realization of the cargo spacecraft.

with respect to the NLP solution. This makes sense because compensating the impulses mishaps requires to deviate from the the optimal open-loop plan. The computational times are shown in Table 3.6. The percentage indicates the computational time with respect to the MPC sampling interval (45 s). It is clear that using a NLP optimization (∼ 2 min computation) for closed-loop MPC is infeasible as it overcomes the sampling interval. The QP problem always consumes less than 5% of the sampling interval to update the control plan. This may be still not enough for real-time autonomy but the results provide a good starting point to achieve that.

Variable	Mean	1-sigma
$\delta\rho(t_f)$	1.2258 m	0.6056 m
$\delta\dot{\rho}(t_f)$	2.8354 cm/s	1.0597 cm/s
$\delta\boldsymbol{\theta}(t_f)$	$[90.554°, 91.498°, 90.057°]^T$	$[1.0720°, 1.0840°, 0.5884°]^T$
$\delta\omega_{B/L}(t_f)$	0.1382 °/s	0.0178 °/s

Table 3.4: Control accuracy in the terminal conditions for the random realizations of the cargo spacecraft.

	Mean	1-sigma
QCLP	4.0823 m/s	0 m/s
NLP	3.1988 m/s	0 m/s
MPC (QP)	3.3488 m/s	0.0748 m/s

Table 3.5: Total ΔV of the initial guess, open-loop and closed-loop solutions for the cargo spacecraft.

	Mean	1-sigma	Max.
NLP	118.28 s / 263%	0 / 0%	118.28 s / 263%
MPC (QP)	1.6470 s / 3.66%	0.3636 s / 0.80%	1.8806 s / 4.18%

Table 3.6: Computational time and its percentage over the sampling interval of the cargo spacecraft.

3.5.3 Lightweight spacecraft

In this scenario, a lightweight chaser (equipped with only two thrusters) has to rendezvous with a target in an eccentric low Earth orbit with $e = 0.5$, $h_p = 400$ km and $\nu(t_0) = \pi$. The thrusters are mounted in an orthogonal configuration as shown by Table 3.7. The inertia matrix of the lightweight satellite is chosen to coincide with the CNES small satellite MYRIADE (see [Louembet09])

p	$\mathbf{w}_p$	$\overline{\Delta V}_p$
1	$[0, 0, -1]^T$	0.5 m/s
2	$[-1, 0, 0]^T$	0.5 m/s

Table 3.7: Array of thrusters for the lightweight spacecraft.

$$\mathbf{J} = \begin{bmatrix} 40 & -3 & -0.5 \\ -3 & 28 & -1 \\ -0.5 & -1 & 45 \end{bmatrix} \text{kg} \cdot \text{m}^2. \tag{3.52}$$

The reaction wheels angular momentum and its variation bounds are taken as $\overline{\mathbf{H}}_{\text{rw}} = [1, 1, 1]^T$ N · m · s and $\overline{\dot{\mathbf{H}}}_{\text{rw}} = [0.05, 0.05, 0.05]^T$ N · m, respectively. The initial and terminal conditions for the 6-DOF maneuver are given by Table 3.8. The total angular momentum is computed as $\mathbf{H}_{\text{tot}} = \mathbf{J}\mathbf{R}(\boldsymbol{\sigma}_0)\boldsymbol{\omega}_0 = [0.4619, -4.3110, 0.1540]^T \cdot 10^{-3}$ N · m · s. The impulses mishaps statistical properties for the lightweight satellite are shown in Table 3.9. The noises has been reduced with respect to the heavy cargo spacecraft because a two thrusters configuration is underactuated. It is expected that the closed-loop MPC of this scenario can deal with less perturbations than the heavy cargo spacecraft which can exert control in any direction. Note that no biases have

Variable	Initial	Terminal
t	0 min	15 min
$\boldsymbol{\rho}$	$[350, 200, 200]^T$ m	$[2, 0, 0]^T$ m
$\dot{\boldsymbol{\rho}}$	$[1, 1, -1]^T$ m/s	$[0, 0, 0]^T$ m/s
$\boldsymbol{\theta}$	$[0°, 0°, 0°]^T$	$[90°, 90°, 90°]^T$
$\boldsymbol{\omega}_{B/L}$	$[0, 0, 0]^T$ °/s	$[0, 0, 0]^T$ °/s

Table 3.8: Initial and terminal conditions for the lightweight spacecraft.

been considered for the misalignment angles and the multiplicative term to the thrust level.

	Variable	Bias	Covariance
Misalignment angles	$\boldsymbol{\delta\theta}$	$[0°, 0°, 0°]^T$	$\mathbf{I}^{(°)^2}$
Multiplicative	$\epsilon_{\Delta V_p}$	0	0.01
Additive	$\boldsymbol{\delta}\mathbf{V}_p$	$[0, 0, 0]$ m/s	$\mathbf{0}_{3\times3}$ $(\text{m/s})^2$

Table 3.9: Statistical properties of impulses mishaps for the lightweight spacecraft.

A total of 100 random realizations of the impulses mishaps have been simulated. Similar conclusions with respect to the previous scenario still hold (see Fig. 3.8-3.9). In this case, the desired final orientation is not favourable to brake the spacecraft because the thruster 1 nozzle has to be aligned with the $+x$ LVLH direction and the thruster 2 nozzle aligns with the $-z$ direction. The terminal accuracy is shown in Table 3.10 (it shows a superior accuracy on the final relative state than the heavy cargo scenario due to the lighter perturbations in comparison). Let recall that the Euler angles, between the body and the LVLH frame, are represented in the $\{zxz\}$ sequence through $\boldsymbol{\theta}$. For the first random realization in Fig. 3.10, it can be observed that the final braking impulses are drastically advanced due to the impossibility of braking with the desired final orientation. As a consequence of this, the attitude terminal accuracy degrades with respect to the heavy cargo scenario as it can be observed from the first random realization (see Fig. 3.11), and the overall results of Table 3.10. The reaction wheels saturation peak has been lowered from 5.6927 $\text{N}\cdot\text{m}\cdot\text{s}$ (QCLP solution converted to NLP solution) to its upper limit of 1 $\text{N}\cdot\text{m}\cdot\text{s}$ (see Fig. 3.12).

In this case, the fuel consumption of the initial guess is reduced in a 9.20% with the final NLP solution (see Table 3.11). Again, the computational benefit of the linearized MPC scheme, yielding a QP optimization, can be deduced from Table 3.12. The NLP solution takes $\sim$ 1 min of computation (which overcomes the MPC sampling interval duration) while the worst-case MPC

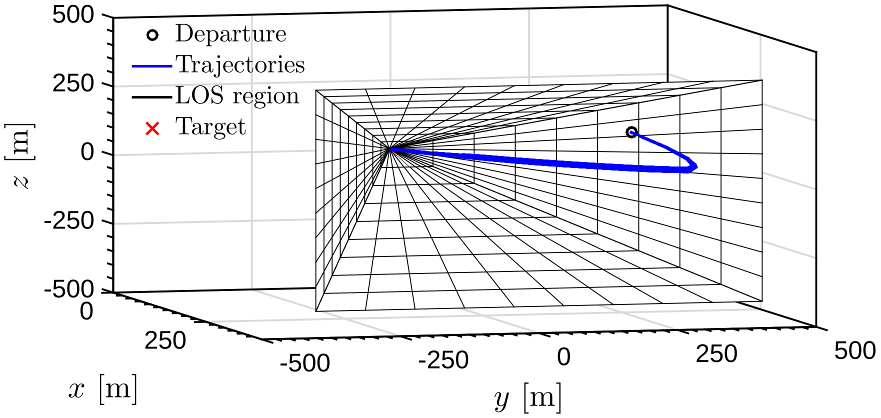

Figure 3.8: Random realizations for the trajectories of the lightweight spacecraft.

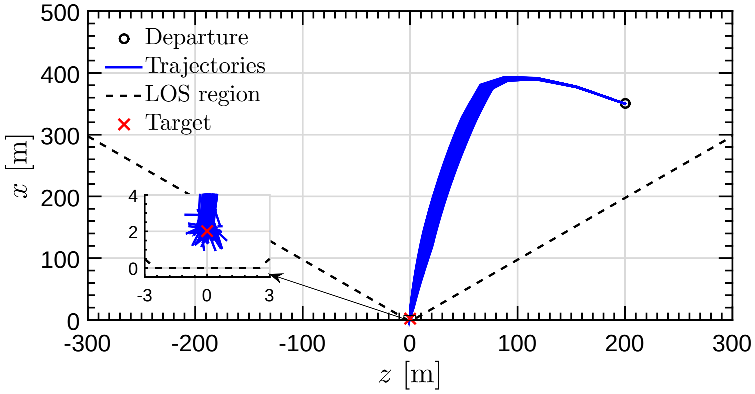

Figure 3.9: Random realizations for the trajectories projection on the target orbital plane of the lightweight spacecraft.

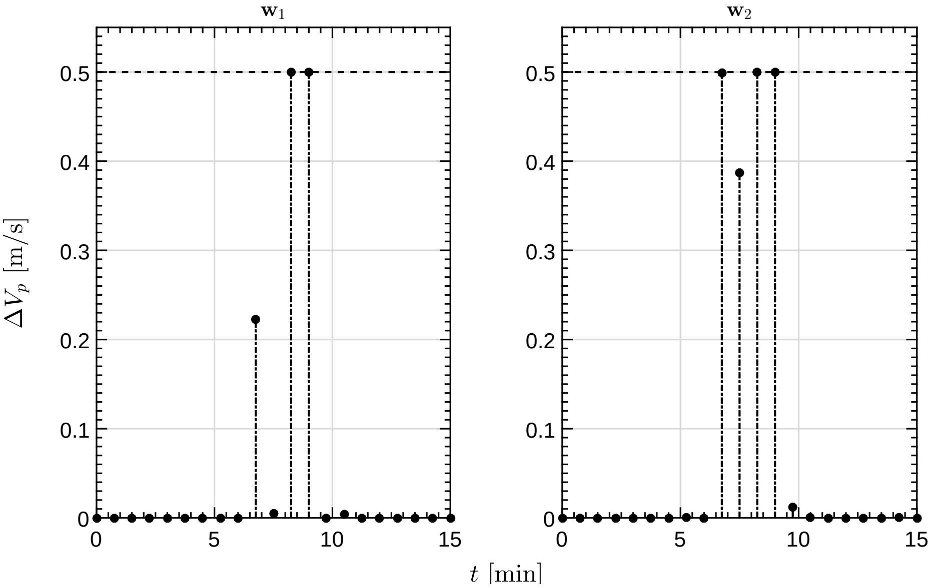

Figure 3.10: Computed impulses for the first random realization of the lightweight spacecraft.

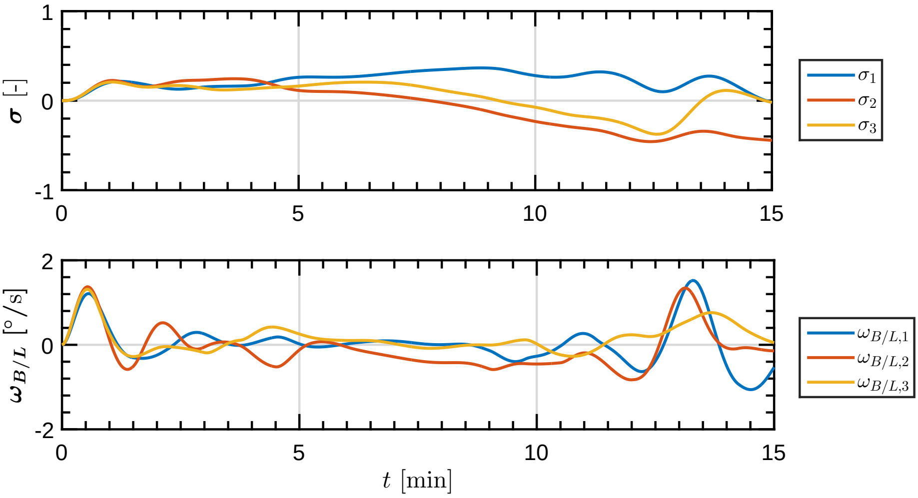

Figure 3.11: Attitude and angular velocity for the first random realization of the lightweight spacecraft.

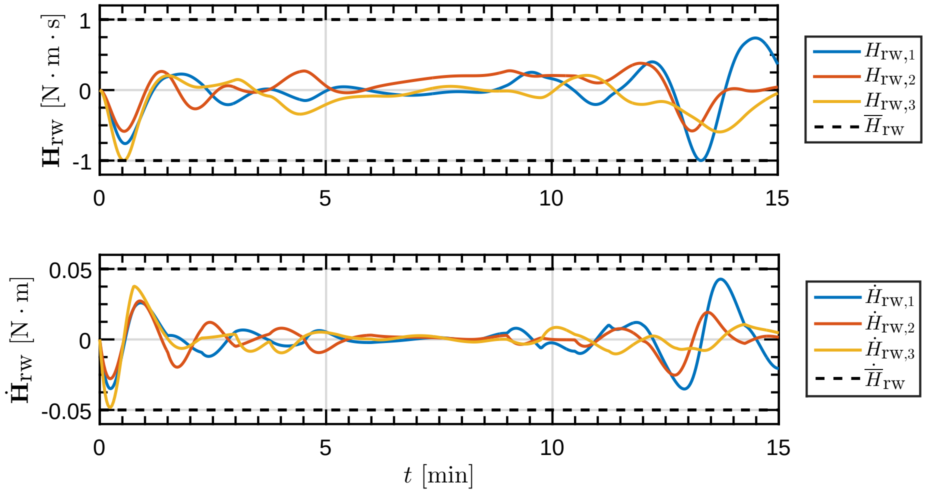

Figure 3.12: Reaction wheels angular momentum and its variation for the first random realization of the lightweight spacecraft.

computation takes $\sim$ 2 s (2.48% of the sampling interval duration) with an average value of $\sim$ 1 s (4.53% of the sampling interval duration).

Variable	Mean	1-sigma
$\delta\rho(t_f)$	0.6962 m	0.2798 m
$\delta\dot{\rho}(t_f)$	1.1286 cm/s	0.5897 cm/s
$\delta\boldsymbol{\theta}(t_f)$	$[94.658°, 94.197°, 89.313°]^T$	$[5.5401°, 2.5801°, 1.8416°]^T$
$\delta\omega_{B/L}(t_f)$	0.3138 °/s	0.1499 °/s

Table 3.10: Control accuracy in the terminal conditions for the random realizations of the lightweight spacecraft.

	Mean	1-sigma
QCLP	3.4254 m/s	0 m/s
NLP	3.1102 m/s	0 m/s
MPC (QP)	3.1481 m/s	0.0266 m/s

Table 3.11: Total ΔV of the initial guess, open-loop and closed-loop solutions for the lightweight spacecraft.

	Mean	1-sigma	Max.
NLP	68.930 s / 153%	0 / 0%	68.930 s / 153%
MPC (QP)	1.1158 s / 2.48%	0.1791 s / 0.40%	2.0403 s / 4.53%

Table 3.12: Computational time and its percentage over the sampling interval of the lightweight spacecraft.

This page is intentionally left blank.

Chapter 4

Robust model predictive control for near-rectilinear halo orbits spacecraft rendezvous

> That's one small step for man,
> one giant leap for mankind.
>
> Neil Armstrong

Contents

4.1 Rendezvous planning problem 95
  4.1.1 Objective function 96
  4.1.2 Constraints 96
4.2 Rendezvous problem robustification 97
  4.2.1 State transition 97
  4.2.2 Gaussian additive disturbances 98
  4.2.3 Robust rendezvous planning problem 99
4.3 Robust control computation 99
  4.3.1 Chance-constrained implementation 100
  4.3.2 Quadratic programming description 102
4.4 Robust MPC scheme with disturbance estimation 107
  4.4.1 Robust control program 107
  4.4.2 On-line disturbance estimator 108
  4.4.3 Robust MPC scheme 109
4.5 Numerical results 111
  4.5.1 Simulation model and controller parameters 111
  4.5.2 Impulsive thrusters scenario 114
  4.5.3 Continuous thrusters scenario 119

This chapter presents a robust model predictive controller to rendezvous with a target placed in a near-rectilinear halo orbit. This work has been published in the journal article [Sanchez20a]. The near-rectilinear halo orbits are a special subset of the halo family that surrounds a Lagrange point in a restricted three-body problem context. This means that the relative motion between both vehicles has to be characterized under the restricted three-body problem model. The previous case is of practical interest to operate the future Lunar Orbital Platform (LOP-G) in cislunar space.

The rendezvous maneuver is assumed to take place in close proximity. This means that the relative distance is negligible with respect to the target distance with each primary, $r_{1t}/\|\boldsymbol{\rho}\|_2 \ll 1$ and $r_{2t}/\|\boldsymbol{\rho}\|_2 \ll 1$. Under the previous assumption, the linear relative motion model for RTBP as per Eq. (2.54) applies. The target is assumed as passive and its orbit is known. Let recall that the RTBP linear system does not admit a closed-form of a transition matrix due to the numerical parameterization of the target orbit. The chaser is considered capable of performing maneuvers in any control direction. Consequently, only the translational control problem is treated. The control thrusters can be either impulsive (see Eq. (2.58)) which models with adequate accuracy chemical or cold gas thrusters; or continuous (see Eq. (2.65)) which models electric thrusters.

In this case, the main control goal is to robustify the closed-loop MPC. A robust method includes any information of the disturbances on its formulation, thus being able to ensure constraints satisfaction (e.g. line-of-sight region) by anticipation. Several forms of robust MPC controllers has been previously employed in Keplerian-based rendezvous operations such: chance-constrained in [Gavilan12]; the worst-case scenario in [Louembet15]; the tube-based method in [Mammarella18]. This work follows the chance-constrained approach of [Gavilan12]. This method considers explicitly the disturbances statistical properties in the prediction model and tightens the constraints accordingly (with a bounding term) so that they are satisfied with a certain probability. By doing so, it is expected that the level of constraints satisfaction improves drastically with respect to a classical non-robust MPC formulation.

The chance-constrained approach largely relies in the prior knowledge of the disturbances statistical properties. As a matter of fact, any robust controller relies on that knowledge (e.g. the worst-case scenario plans for the strongest deviation). However, it may be the case where this information is inaccurate or unavailable from the very beginning. To overcome the previous issue, the methodology is completed with an on-line disturbance estimator. The estimator infers the disturbance by quantifying the discrepancy between the predicted and actual state.

Precisely, the employed methodology is as follows: firstly, the RTBP rendezvous problem is stated in the general continuous form of Eq. (1.1); secondly, a stochastic prediction model is developed; thirdly, the constraints bounding term computation according to the chance-constrained approach is introduced and the associated robust control program is derived; finally, the on-line disturbance estimator is presented. The resulting robust control program is quadratic while the bounding term and on-line disturbance estimator computation only involve algebraic operations. The main source of computational burden is the numerical integration to derive the state transition matrices. Nevertheless, the transition matrices can be precomputed, thus not requiring to compute them along the maneuver.

The chapter concludes with a numerical results section. The analysed scenario is the rendezvous with a target placed in an L2 southern NRHO of the Earth-Moon system. The developed robust MPC algorithm is compared with a classic non-robust MPC. The results show the superior constraints satisfaction of the robust algorithm with respect to its non-robust counterpart.

4.1 Rendezvous planning problem

In a general way, the RTBP rendezvous planning problem (considering both chemical and electric thrusters) states as follows

$$\boxed{\begin{aligned}
\underset{\Delta\mathbf{V}(t_j),\ \mathbf{u}(t)}{\text{minimize}} \quad & J(\Delta\mathbf{V}(t_j), \mathbf{u}(t)), \\
\text{subject to} \quad & \ddot{\boldsymbol{\rho}}(t) = -2\boldsymbol{\omega}_{L/I} \times \dot{\boldsymbol{\rho}} - \dot{\boldsymbol{\omega}}_{L/I} \times \boldsymbol{\rho} - \boldsymbol{\omega}_{L/I} \times (\boldsymbol{\omega}_{L/I} \times \boldsymbol{\rho}) \\
& \qquad - \sum_{i=1}^{2} \left(\mu_i / r_{it}^3\right) \left[\mathbf{I} - 3\left(\mathbf{r}_{it}\mathbf{r}_{it}^T / r_{it}^2\right)\right] \boldsymbol{\rho} + \mathbf{u}, \\
& \dot{\boldsymbol{\rho}}^+(t_j) = \dot{\boldsymbol{\rho}}(t_j) + \Delta\mathbf{V}(t_j), \\
& \mathbf{u}(t) = \sum_{i=1}^{n_c} B_{i,q}(t) \boldsymbol{\zeta}_i, \\
& -\overline{\Delta\mathbf{V}} \leq \Delta\mathbf{V}(t_j) \leq \overline{\Delta\mathbf{V}}, \\
& -\overline{\mathbf{u}} \leq \mathbf{u}(t) \leq \overline{\mathbf{u}}, \\
& \boldsymbol{\rho}(t) \in \mathcal{X}_{\text{LOS}}, \\
& \boldsymbol{\rho}(t_0) = \boldsymbol{\rho}_0, \quad \dot{\boldsymbol{\rho}}(t_0) = \dot{\boldsymbol{\rho}}_0, \\
& \boldsymbol{\rho}(t_f) = \boldsymbol{\rho}_f, \quad \dot{\boldsymbol{\rho}}(t_f) = \mathbf{0}.
\end{aligned}} \tag{4.1}$$

The time dependencies have been omitted at the right-hand side of the relative translational dynamics for the sake of clarity. The following considerations have been made in problem (4.1):

- The relative motion is parameterized through cartesian coordinates in the RTBP LVLH frame (see Fig. 2.3). The linear relative motion model for the restricted three-body problem is considered.

- At $N + 1$ predefined instants t_j, the impulsive thrusters could apply a control impulse. The impulse amplitude is bounded.

- The continuous control acceleration is parameterized with B-splines (see Eq. (2.65)). Then, the underlying decision variable is the set of control points $\boldsymbol{\zeta}_i$.
- During the maneuver, the relative position has to be within the state subset $\mathcal{X}_{\text{LOS}}$. This is the LOS region which guarantees line-of-sight with the docking port and prevents collision with the target.
- The initial relative state is given. The desired terminal relative state would leave the chaser motionless at a certain relative distance from the target.

The objective function and constraints are detailed below.

4.1.1 Objective function

The chosen objective function seeks to minimize the control energy

$$J = \sum_{j=0}^{N} \Delta\mathbf{V}^T(t_j)\Delta\mathbf{V}(t_j) + \frac{\gamma_u}{t_f - t_0}\int_{t_0}^{t_f} \mathbf{u}^T(t)\mathbf{u}(t)dt, \tag{4.2}$$

where $\gamma_u \geq 0$ weights the relative cost of the continuous acceleration with respect to the impulsive action. Since the continuous acceleration is parameterized by B-splines, for the sake of simplicity, the continuous acceleration cost is approximated as

$$J \approx \sum_{j=0}^{N} \Delta\mathbf{V}^T(t_j)\Delta\mathbf{V}(t_j) + \gamma_\zeta \sum_{i=1}^{n_c} \boldsymbol{\zeta}_i^T\boldsymbol{\zeta}_i, \tag{4.3}$$

which follows the logic that $\boldsymbol{\zeta}_i = \mathbf{0}$ $(\forall i = 1 \dots n_c) \longrightarrow \mathbf{u}(t) = \mathbf{0}$.

4.1.2 Constraints

Similarly to the six-degrees of freedom rendezvous (see Chapter 3), three sets of constraints are considered for its RTBP counterpart. These are: path constraints on the relative position; control bounds; initial and terminal conditions on the relative state. From now, on the relative state defined as $\mathbf{x} = [\boldsymbol{\rho}^T, \dot{\boldsymbol{\rho}}^T]^T$ is employed.

Path constraints

As in Keplerian-based rendezvous, for sensing and safety reasons, the rendezvous operation has to take place along a predefined corridor from the docking port. Assuming a V-bar alike approach and using the restricted-three body problem local-vertical local-horizontal frame (see Fig.2.3) the line-of-sight constraints yields

$$\mathbf{A}_{\text{LOS}}\mathbf{x}(t) \leq \mathbf{b}_{\text{LOS}}, \tag{4.4}$$

where the inequality matrix and vector have the same structure of Eq. (3.4).

Control bounds

Both the impulsive and continuous acceleration thrusters have bounds on its control signal due to physical limitations.

Impulsive thrusters: the impulses amplitude are constrained as

$$-\overline{\Delta\mathbf{V}} \leq \Delta\mathbf{V}(t_j) \leq \overline{\Delta\mathbf{V}}, \tag{4.5}$$

where the same limits, in absolute value, apply for the lower and upper bounds.

Continuous thrusters: the exerted control acceleration is limited by

$$-\overline{\mathbf{u}} \leq \mathbf{u}(t) \leq \overline{\mathbf{u}} \longrightarrow -\overline{\mathbf{u}} \leq \sum_{i=1}^{n_c} B_{i,q}(t)\boldsymbol{\zeta}_i \leq \overline{\mathbf{u}}, \tag{4.6}$$

whose treatment is the same as the reaction wheels angular momentum variation case (see Eq. (3.7)).

Boundary constraints

The goal of the rendezvous operation is to depart from an initial relative state in order to reach a final relative position without relative velocity

$$\mathbf{x}(t_0) = \mathbf{x}_0, \quad \mathbf{x}(t_f) = \mathbf{x}_f, \tag{4.7}$$

where $\mathbf{x}_f = [\boldsymbol{\rho}_f^T, \mathbf{0}^T]^T$.

4.2 Rendezvous problem robustification

The first step to robustify the rendezvous planning problem (4.1) is to exploit the state transition matrix and control integration. This allows to express the relative state, at any time, with an explicit mathematical expression. In that expression, a random discrete additive disturbance to the relative state is added. As such, the relative state is also a random variable over time. The disturbance represents statistically the mismatch between the predicted and current state. Finally, the original problem (4.1) is presented in a robust form.

4.2.1 State transition

Under linear RTBP relative dynamics, continuous acceleration and instantaneous changes of velocity, the relative state can be explicitly propagated as

$$\begin{gathered}\mathbf{x}(t) = \mathbf{\Phi}(t,t_0)\mathbf{x}_0 + \int_{t_0}^{t} \mathbf{\Phi}(t,\tau)\mathbf{B}\mathbf{u}(t)dt + \sum_{i=0}^{j} \mathbf{\Phi}(t,t_i)\mathbf{B}\Delta\mathbf{V}(t_i),\\ t_j \leq t \leq t_{j+1}.\end{gathered} \tag{4.8}$$

The state transition matrix is computed by integrating Eq. (2.51) as

$$\dot{\mathbf{\Phi}}(t,t_0) = \mathbf{A}(t)\mathbf{\Phi}(t,t_0), \quad t \geq t_0, \tag{4.9}$$

where

$$\mathbf{A}(t) = \begin{bmatrix} \mathbf{0}_{3\times3} & \mathbf{I} \\ -\dot{\mathbf{\Omega}}_{L/I} - \mathbf{\Omega}_{L/I}^2 - \sum_{i=1}^{2} \frac{\mu_i}{r_{it}^3}\left(\mathbf{I} - 3\frac{\mathbf{r}_{it}\mathbf{r}_{it}^T}{r_{it}}\right) & -2\mathbf{\Omega}_{L/I} \end{bmatrix}. \tag{4.10}$$

4.2.2 Gaussian additive disturbances

Let assume a Gaussian additive disturbance $\boldsymbol{\delta}\mathbf{x} \sim N_6(\widehat{\boldsymbol{\delta}\mathbf{x}}, \mathbf{\Sigma}_{\boldsymbol{\delta}\mathbf{x}})$ affecting the relative state at discrete instants t_j

$$\begin{aligned} \mathbf{x}(t) =& \mathbf{\Phi}(t,t_0)\mathbf{x}_0 + \int_{t_0}^{t} \mathbf{\Phi}(t,\tau)\mathbf{B}\mathbf{u}(t)d\tau + \sum_{i=0}^{j} \mathbf{\Phi}(t,t_i)\mathbf{B}\Delta\mathbf{V}(t_i) \\ &+ \sum_{i=0}^{j} \mathbf{\Phi}(t,t_i)\boldsymbol{\delta}\mathbf{x}(t_i), \quad t_j \leq t \leq t_{j+1}. \end{aligned} \tag{4.11}$$

Then, the relative state is propagated according to a Gaussian stochastic process $\mathbf{x}(t) \sim N_6(\hat{\mathbf{x}}(t), \mathbf{\Sigma}_{\mathbf{x}}(t))$, where

$$\begin{aligned} \hat{\mathbf{x}}(t) =& \mathbf{\Phi}(t,t_0)\mathbf{x}_0 + \int_{t_0}^{t} \mathbf{\Phi}(t,\tau)\mathbf{B}\mathbf{u}(t)d\tau + \sum_{i=0}^{j} \mathbf{\Phi}(t,t_i)\mathbf{B}\Delta\mathbf{V}(t_i) \\ &+ \sum_{i=0}^{j} \mathbf{\Phi}(t,t_i)\widehat{\boldsymbol{\delta}\mathbf{x}}(t_i), \\ \mathbf{\Sigma}_{\mathbf{x}}(t) =& \sum_{i=0}^{j} \mathbf{\Phi}^T(t,t_i)\mathbf{\Sigma}_{\boldsymbol{\delta}\mathbf{x}}(t_i)\mathbf{\Phi}(t,t_i), \quad t_j \leq t \leq t_{j+1}. \end{aligned} \tag{4.12}$$

It should be noticed that a discrete additive Gaussian disturbance may be less realistic than a continuous disturbance. However, the discrete form provides a simplified Gaussian stochastic process of the relative state. Additionally, as it contemplates both position and velocity errors, it can be seen as a measurement of the accumulated uncertainty between the impulses intervals.

4.2.3 Robust rendezvous planning problem

Under the stochastic propagation of the relative state as per Eq. (4.11), the original rendezvous planning problem (4.1) is robustified as follows

$$
\begin{aligned}
\underset{\Delta\mathbf{V}(t_j),\ \boldsymbol{\zeta}_i}{\text{minimize}} \quad & \sum_{j=0}^{N} \Delta\mathbf{V}^T(t_j)\Delta\mathbf{V}(t_j) + \gamma_\zeta \sum_{i=1}^{n_c} \boldsymbol{\zeta}_i^T \boldsymbol{\zeta}_i, \\
\text{subject to} \quad & \mathbf{x}(t) = \boldsymbol{\Phi}(t,t_0)\mathbf{x}_0 + \int_{t_0}^{t} \boldsymbol{\Phi}(t,\tau)\mathbf{B}\mathbf{u}(t)d\tau \\
& \qquad + \sum_{i=0}^{j} \boldsymbol{\Phi}(t,t_i)\mathbf{B}\Delta\mathbf{V}(t_i) + \sum_{i=0}^{j} \boldsymbol{\Phi}(t,t_i)\boldsymbol{\delta}\mathbf{x}(t_i), \\
& \qquad t_j \le t \le t_{j+1}, \\
& \boldsymbol{\delta}\mathbf{x}(t) \sim N_6(\widehat{\boldsymbol{\delta}\mathbf{x}}(t), \boldsymbol{\Sigma}_{\boldsymbol{\delta}\mathbf{x}}(t)), \\
& \mathbf{u}(t) = \sum_{i=1}^{n_c} B_{i,q}(t)\boldsymbol{\zeta}_i, \\
& -\overline{\Delta\mathbf{V}} \le \Delta\mathbf{V}(t_j) \le \overline{\Delta\mathbf{V}}, \\
& -\overline{\mathbf{u}} \le \mathbf{u}(t) \le \overline{\mathbf{u}}, \\
& P(\mathbf{A}_{\text{LOS}}\mathbf{x}(t) \le \mathbf{b}_{\text{LOS}}) \ge p, \\
& \mathbf{x}(t_0) = \mathbf{x}_0, \quad \hat{\mathbf{x}}(t_f) = \mathbf{x}_f.
\end{aligned}
\tag{4.13}
$$

The terminal condition on the relative state is posed in terms of its mean value while the line-of-sight constraint is enforced to be fullfiled above a certain probability p. To achieve the line-of-sight constraint satisfaction in a probabilistic sense, the chance-constrained approach will be further developed in the sequel. The rationale behind this approach is shown in the sketch of Fig. 4.1. It can be observed that knowing the relative state statistical distribution would allow to tighten the constraint in order to enforce its satisfaction in the majority of cases. Note that guaranteeing a 100% of constraints satisfaction is infeasible since the disturbance is a Gaussian distribution which is unbounded by definition.

4.3 Robust control computation

This section implements the chance-constrained approach in order to ensure the probabilistic satisfaction of the LOS constraints. To do so, a deterministic bounding term to the non-robust LOS constraints is added. This bounding term mainly depends on the disturbances statistical properties. Then, the resulting deterministic continuous problem is discretized and some of its constraints are relaxed. The outcome a quadratic program that allows to compute a robust control plan.

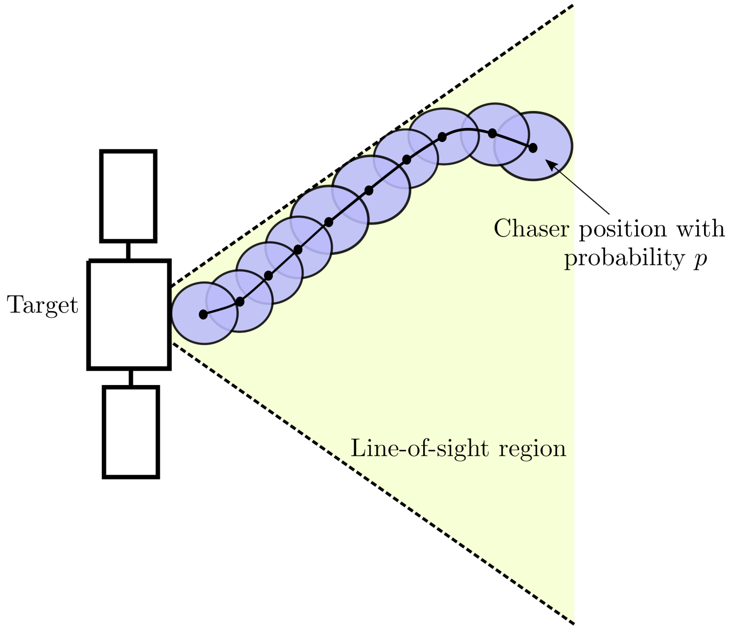

Figure 4.1: Robust satisfaction of constraints.

4.3.1 Chance-constrained implementation

In order to enforce the line-of-sight constraints above a certain probability p, their inequality (under the relative state mean) can be tightened by adding a bounding term $\mathbf{b}_{\delta x} = [b^1_{\delta x}, b^2_{\delta x}, b^3_{\delta x}, b^4_{\delta x}, b^5_{\delta x}]^T$ where each element of the bounding term corresponds to each one of the line-of-sight constraints

$$P(\mathbf{A}_{\text{LOS}}\mathbf{x}(t) \leq \mathbf{b}_{\text{LOS}}) \geq p \longrightarrow \mathbf{A}_{\text{LOS}}\hat{\mathbf{x}}(t) \leq \mathbf{b}_{\text{LOS}} + \mathbf{b}_{\delta x}(t) \leq \mathbf{A}_{\text{LOS}}\mathbf{x}(t). \quad (4.14)$$

The bounding term $\mathbf{b}_{\delta x}$ has to be determined at each instant. In that sense, it should be noted that the minimum probability p of constraints satisfaction presents a tradeoff between infeasibility (if p is chosen the unity, the bounding term would tighten too much the constraint) and mission safeness (p should be close to the unity). Inserting Eq. (4.11) and Eq. (4.12) into Eq. (4.14) and cancelling the respective deterministic terms yields

$$\mathbf{A}_{\text{LOS}} \sum_{i=0}^{j} \boldsymbol{\Phi}(t,t_i)\widehat{\boldsymbol{\delta}\mathbf{x}}_i \leq \mathbf{b}_{\delta x}(t) \leq \mathbf{A}_{\text{LOS}} \sum_{i=0}^{j} \boldsymbol{\Phi}(t,t_i)\boldsymbol{\delta}\mathbf{x}_i, \quad t_j \leq t < t_{j+1}. \quad (4.15)$$

Since the disturbance term was assumed as a Gaussian distribution, the following statistical property holds (see [Rencher98] for the details)

$$\boldsymbol{\delta}\mathbf{x} \sim N_6(\widehat{\boldsymbol{\delta}\mathbf{x}}, \boldsymbol{\Sigma}_{\boldsymbol{\delta}\mathbf{x}}) \longrightarrow (\boldsymbol{\delta}\mathbf{x} - \widehat{\boldsymbol{\delta}\mathbf{x}})^T \boldsymbol{\Sigma}^{-1}_{\boldsymbol{\delta}\mathbf{x}} (\boldsymbol{\delta}\mathbf{x} - \widehat{\boldsymbol{\delta}\mathbf{x}}) \sim \chi^2(6), \quad (4.16)$$

where the time dependencies has been ommited for the sake of clarity. The term $\chi^2(6)$ denotes a chi-square probability distribution function with six-degrees of freedom. Assuming that the disturbances statistical properties are constant during the whole rendezvous operation (quasi-steady hypothesis), then

$$\boldsymbol{\delta}\mathbf{x}_j \sim N_6(\widehat{\boldsymbol{\delta}\mathbf{x}}, \boldsymbol{\Sigma}_{\boldsymbol{\delta}\mathbf{x}}), \quad \widehat{\boldsymbol{\delta}\mathbf{x}} \equiv \text{constant}, \quad \boldsymbol{\Sigma}_{\boldsymbol{\delta}\mathbf{x}} \equiv \text{constant}, \tag{4.17}$$

where $\boldsymbol{\delta}\mathbf{x}_j = \boldsymbol{\delta}\mathbf{x}(t_j)$. Consequently, Eq. (4.16) remains invariant over time

$$(\boldsymbol{\delta}\mathbf{x}_j - \widehat{\boldsymbol{\delta}\mathbf{x}})^T \boldsymbol{\Sigma}^{-1}_{\boldsymbol{\delta}\mathbf{x}} (\boldsymbol{\delta}\mathbf{x}_j - \widehat{\boldsymbol{\delta}\mathbf{x}}) \sim \chi^2(6), \quad j = 0 \dots N, \tag{4.18}$$

hence the following probabilistic relation also holds

$$P(\chi^2(6) \leq \alpha) = p \longrightarrow P[(\boldsymbol{\delta}\mathbf{x}_j - \widehat{\boldsymbol{\delta}\mathbf{x}})^T \boldsymbol{\Sigma}^{-1}_{\boldsymbol{\delta}\mathbf{x}} (\boldsymbol{\delta}\mathbf{x}_j - \widehat{\boldsymbol{\delta}\mathbf{x}}) \leq \alpha] = p. \tag{4.19}$$

The upper bound α has to be found from a given probability p (see Fig. 4.2).

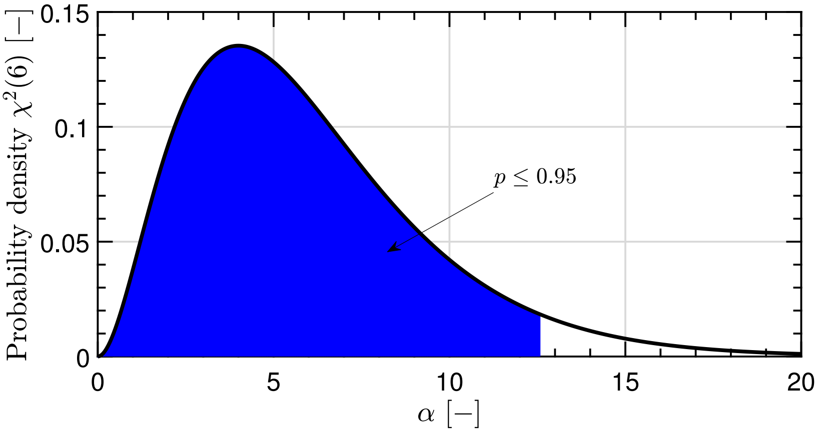

Figure 4.2: Probability density function of the chi-square distribution with six-degrees of freedom.

While fulfilling Eq. (4.19), each element of the bounding term $\mathbf{b}_{\delta x}$ is maximized as (to increase the feasibility of the problem, the bound should be the least restrictive as possible)

$$\begin{aligned} \underset{\boldsymbol{\delta}\mathbf{x}(t_i)}{\text{maximize}} \quad & b^s_{\delta x}(t) = \sum_{i=0}^{j} \mathbf{g}^s_{\text{LOS}}(t)(\boldsymbol{\delta}\mathbf{x}_i - \widehat{\boldsymbol{\delta}\mathbf{x}}), & s = 1 \dots 5, \\ \text{subject to} \quad & (\boldsymbol{\delta}\mathbf{x}_i - \widehat{\boldsymbol{\delta}\mathbf{x}})^T (\alpha \boldsymbol{\Sigma}_{\boldsymbol{\delta}\mathbf{x}})^{-1} (\boldsymbol{\delta}\mathbf{x}_i - \widehat{\boldsymbol{\delta}\mathbf{x}}) \leq 1, & i = 0 \dots j, \end{aligned} \tag{4.20}$$

where $\mathbf{g}^s_{\mathrm{LOS}}$, $s = 1\dots5$, refers to each row of the matrix $\mathbf{A}_{\mathrm{LOS}}\sum_{i=0}^{j}\boldsymbol{\Phi}(t,t_i)$ as

$$\mathbf{A}_{\mathrm{LOS}}\sum_{i=0}^{j}\boldsymbol{\Phi}(t,t_i) = \begin{bmatrix}\mathbf{g}^1_{\mathrm{LOS}}(t)\\ \mathbf{g}^2_{\mathrm{LOS}}(t)\\ \mathbf{g}^3_{\mathrm{LOS}}(t)\\ \mathbf{g}^4_{\mathrm{LOS}}(t)\\ \mathbf{g}^5_{\mathrm{LOS}}(t)\end{bmatrix}. \tag{4.21}$$

By using the following change of variable

$$\mathbf{z}_i = \mathbf{H}^{1/2}(\boldsymbol{\delta}\mathbf{x}_i - \widehat{\boldsymbol{\delta}\mathbf{x}}), \quad \mathbf{H} = (\alpha\boldsymbol{\Sigma}_{\boldsymbol{\delta}\mathbf{x}})^{-1} \succ 0, \tag{4.22}$$

the problem (4.20) is transformed as

$$\begin{aligned} \underset{\mathbf{z}_i}{\text{maximize}} \quad & b^s_{\delta x}(t) = \sum_{i=0}^{j}\mathbf{g}^s_{\mathrm{LOS}}(t)\mathbf{H}^{-1/2}\mathbf{z}_i, \qquad && s = 1\dots5,\\ \text{subject to} \quad & \mathbf{z}_i^T\mathbf{z}_i \le 1, && i = 1\dots j, \end{aligned} \tag{4.23}$$

where each term of the summation is independent from each other, thus the bounding term computation can be decoupled for each disturbance as

$$\begin{aligned} \underset{\mathbf{z}_i}{\text{miminize}} \quad & -\mathbf{g}^s_{\mathrm{LOS}}(t)\mathbf{H}^{-1/2}\mathbf{z}_i,\\ \text{subject to} \quad & \mathbf{z}_i^T\mathbf{z}_i \le 1, \end{aligned} \tag{4.24}$$

where the optimal decision variable can be easily obtained via the Lagrange formalism, yielding the minimum at

$$\mathbf{z}_i^* = \frac{\mathbf{H}^{-1/2}(\mathbf{g}^s_{\mathrm{LOS}}(t))^T}{\sqrt{\mathbf{g}^s_{\mathrm{LOS}}(t)\mathbf{H}^{-1}(\mathbf{g}^s_{\mathrm{LOS}}(t))^T}}. \tag{4.25}$$

Finally, by undoing the change of variable and substituting in the bounding term expresion yields

$$b^s_{\delta_x}(t) = \sum_{i=0}^{j}\left(-\sqrt{\mathbf{g}^s_{\mathrm{LOS}}(t)\alpha\boldsymbol{\Sigma}_{\boldsymbol{\delta}\mathbf{x}}(\mathbf{g}^s_{\mathrm{LOS}}(t))^T} - \mathbf{g}^s_{\mathrm{LOS}}(t)\widehat{\boldsymbol{\delta}\mathbf{x}}\right). \tag{4.26}$$

Then, the robust line-of-sight constraint is expressed deterministically as

$$\mathbf{A}_{\mathrm{LOS}}\hat{\mathbf{x}}(t) \le \mathbf{b}_{\mathrm{LOS}} + \mathbf{b}_{\delta x}(t). \tag{4.27}$$

4.3.2 Quadratic programming description

Now, the continuous robust rendezvous planning problem (4.13) is reduced into a static form by means of discretization and a B-splines parameterization of the control acceleration. The result is a quadratic programming problem guaranteeing probabilistic constraints satisfaction.

Impulses placement

A predefined number of $N+1$ firing times for the impulsive thrusters has been assumed. These control times are equally spaced in time as $t_j = t_0 + j\Delta t,\ j = 0\dots N$ with $\Delta t = (t_f - t_0)/N$. As such, let denote $\Delta\mathbf{V}_j = \Delta\mathbf{V}(t_j)$.

B-splines parameterization of the continuous acceleration

The continuous acceleration control is parameterized in terms of B-splines (see Appendix A) for the details, as

$$\mathbf{u}(t) = \sum_{i=1}^{n_c} B_{i,q}(t)\boldsymbol{\zeta}_i. \tag{4.28}$$

Similar guidelines as in the MRP B-splines parameterization of Section 3.3.1 apply. The term q is the B-splines degree which has to fullfill $q \geq 2$ in order to support a smooth acceleration profile. Note that $q = 0$ corresponds to the pulse amplitude modulation model. The number of control points is a free parameter which is recommended to be chosen as $n_c \geq N+1$. Proceeding like that would allow to make the basis functions of the B-splines coincident with the intervals between impulses. Under the previous considerations, the number of knots must satisfy $n_{\text{knots}} = n_c + q \geq N + q + 1$ which can be enforced as

$$\mathbf{t}_{\text{knots}} = [\ \underbrace{t_0, \dots, t_0}_{>q/2+1 \text{ times}}\ , t_1, \dots, t_{N-1},\ \underbrace{t_f, \dots, t_f}_{>q/2+1 \text{ times}}\ ]^T. \tag{4.29}$$

where the repetition of initial and final nodes does not alter the internal q^{th} order continuity of the control acceleration profile.

Discretization of continuous constraints

Subsequently, the continuous constraints of problem 4.13 are discretized with respect to time.

Line-of-sight constraint: in a similar way as in Section 3.3.1, the probabilistic line-of-sight constraint is only enforced at n_{LOS} equally spaced times, within an interval between impulses, separated by $\Delta t_{\text{LOS}} = \Delta t / n_{\text{LOS}}$

$$\begin{aligned} P(\mathbf{A}_{\text{LOS}}\mathbf{x}_{j,l} \leq \mathbf{b}_{\text{LOS}}) \geq p \quad &\longrightarrow \quad \mathbf{A}_{\text{LOS}}\hat{\mathbf{x}}_{j,l} \leq \mathbf{b}_{\text{LOS}} + \mathbf{b}_{\delta x}(t_{j,l}), \\ t_{j,l} = t_0 + (j-1)\Delta t + l\Delta t_{\text{LOS}}, \quad &j = 1\dots N, \quad l = 1\dots n_{\text{LOS}}. \end{aligned} \tag{4.30}$$

Note that the bounding term $\mathbf{b}_{\delta x}(t_{j,l})$ has to be computed in accordance with Eq. (4.26) at the constraints enforcement instants $t_{j,l}$

$$b^q_{\delta_x}(t_{j,l}) = \sum_{i=0}^{j} \left(-\sqrt{\mathbf{g}^q_{\text{LOS}}(t_{j,l})\alpha\boldsymbol{\Sigma}_{\boldsymbol{\delta}\mathbf{x}}(\mathbf{g}^q_{\text{LOS}}(t_{j,l}))^T} - \mathbf{g}^q_{\text{LOS}}(t_{j,l})\widehat{\boldsymbol{\delta}\mathbf{x}} \right). \tag{4.31}$$

Control acceleration bounds: since the control acceleration is parameterized in a continuous way (different from a PAM model which assumes a constant acceleration over an interval), its bounds constraints are continuous. To discretize this constraint, it is only enforced at n_u equally spaced times, within internal knots, separated by $\Delta t_u = \Delta t / n_u$

$$
\begin{aligned}
-\bar{\mathbf{u}} \leq \sum_{i=1}^{n_c} B_{i.q}(t_{j,m})\boldsymbol{\zeta}_i \leq \bar{\mathbf{u}}, \quad t_{j,m} &= t_0 + (j-1)\Delta t + m\Delta t_u, \\
j &= 1 \dots N, \quad m = 1 \dots n_u.
\end{aligned}
\tag{4.32}
$$

Compact formulation

As in Section 3.3.1, a compact formulation is employed to ease the notation. Let define the stack vectors $\mathbf{x_S} \in \mathbb{R}^{6n_{\mathrm{LOS}}N}$, $\boldsymbol{\zeta}_\mathbf{S} \in \mathbb{R}^{3n_c}$, $\Delta\mathbf{V_S} \in \mathbb{R}^{3(N+1)}$ and $\boldsymbol{\delta}\mathbf{x_S} \in \mathbb{R}^{3(N+1)}$ as

$$
\begin{aligned}
&\mathbf{x_S} = [\mathbf{x}_{1,1}^T, \dots, \mathbf{x}_{1,n_{\mathrm{LOS}}}^T, \mathbf{x}_{2,1}^T, \dots, \mathbf{x}_{2,n_{\mathrm{LOS}}}^T, \mathbf{x}_{3,1}^T, \dots\dots, \mathbf{x}_{N,n_{\mathrm{LOS}}}^T]^T, \\
&\boldsymbol{\zeta}_\mathbf{S} = \begin{bmatrix} \boldsymbol{\zeta}_1 \\ \vdots \\ \boldsymbol{\zeta}_{n_c} \end{bmatrix}, \quad \Delta\mathbf{V_S} = \begin{bmatrix} \Delta\mathbf{V}_0 \\ \vdots \\ \Delta\mathbf{V}_N \end{bmatrix}, \quad \boldsymbol{\delta}\mathbf{x_S} = \begin{bmatrix} \boldsymbol{\delta}\mathbf{x}_0 \\ \vdots \\ \boldsymbol{\delta}\mathbf{x}_N^T \end{bmatrix}.
\end{aligned}
\tag{4.33}
$$

Let also define the stack matrices $\mathbf{F} \in \mathbb{R}^{6n_{\mathrm{LOS}}N \times 6}$, $\mathbf{G}_\zeta \in \mathbb{R}^{6n_{\mathrm{LOS}}N \times 3n_c}$, $\mathbf{G}_{\Delta V} \in \mathbb{R}^{6n_{\mathrm{LOS}}N \times 3(N+1)}$ and $\mathbf{G}_{\delta x} \in \mathbb{R}^{6n_{\mathrm{LOS}}N \times 6(N+1)}$

$$
\begin{aligned}
&\mathbf{F} = \\
&[\boldsymbol{\Phi}^T(t_{1,1}, t_0), \dots, \boldsymbol{\Phi}^T(t_{1,n_{\mathrm{LOS}}}, t_0), \boldsymbol{\Phi}^T(t_{2,n_{\mathrm{LOS}}}, t_0), \dots\dots, \boldsymbol{\Phi}^T(t_{N,n_{\mathrm{LOS}}}, t_0)]^T,
\end{aligned}
$$

$$
\mathbf{G}_\zeta = \begin{bmatrix}
\mathbf{B}_{\zeta_1}(t_{1,1}) & \mathbf{B}_{\zeta_2}(t_{1,1}) & \dots & \mathbf{B}_{\zeta_{n_c}}(t_{1,1}) \\
\vdots & \vdots & \ddots & \vdots \\
\mathbf{B}_{\zeta_1}(t_{1,n_{\mathrm{LOS}}}) & \mathbf{B}_{\zeta_2}(t_{1,n_{\mathrm{LOS}}}) & \dots & \mathbf{B}_{\zeta_{n_c}}(t_{1,n_{\mathrm{LOS}}}) \\
\mathbf{B}_{\zeta_1}(t_{2,1}) & \mathbf{B}_{\zeta_2}(t_{2,1}) & \dots & \mathbf{B}_{\zeta_{n_c}}(t_{2,1}) \\
\vdots & \vdots & \ddots & \vdots \\
\mathbf{B}_{\zeta_1}(t_{2,n_{\mathrm{LOS}}}) & \mathbf{B}_{\zeta_2}(t_{2,n_{\mathrm{LOS}}}) & \dots & \mathbf{B}_{\zeta_{n_c}}(t_{2,n_{\mathrm{LOS}}}) \\
\mathbf{B}_{\zeta_1}(t_{3,1}) & \mathbf{B}_{\zeta_2}(t_{3,1}) & \dots & \mathbf{B}_{\zeta_{n_c}}(t_{3,1}) \\
\vdots & \vdots & \ddots & \vdots \\
\vdots & \vdots & \ddots & \vdots \\
\mathbf{B}_{\zeta_1}(t_{N,n_{\mathrm{LOS}}}) & \mathbf{B}_{\zeta_2}(t_{N,n_{\mathrm{LOS}}}) & \dots & \mathbf{B}_{\zeta_{n_c}}(t_{N,n_{\mathrm{LOS}}})
\end{bmatrix},
\tag{4.34}
$$

$$\mathbf{G}_{\Delta V} = \begin{bmatrix} \boldsymbol{\Phi}(t_{1,1},t_0)\mathbf{B} & \mathbf{0}_{6\times3} & \dots & \mathbf{0}_{6\times3} \\ \vdots & \vdots & \ddots & \vdots \\ \boldsymbol{\Phi}(t_{1,n_{\mathrm{LOS}}},t_0)\mathbf{B} & \mathbf{0}_{6\times3} & \dots & \mathbf{0}_{6\times3} \\ \boldsymbol{\Phi}(t_{2,1},t_0)\mathbf{B} & \boldsymbol{\Phi}(t_{2,1},t_1)\mathbf{B} & \dots & \mathbf{0}_{6\times3} \\ \vdots & \vdots & \ddots & \vdots \\ \boldsymbol{\Phi}(t_{2,n_{\mathrm{LOS}}},t_0)\mathbf{B} & \boldsymbol{\Phi}(t_{2,n_{\mathrm{LOS}}},t_1)\mathbf{B} & \dots & \mathbf{0}_{6\times3} \\ \boldsymbol{\Phi}(t_{3,1},t_0)\mathbf{B} & \boldsymbol{\Phi}(t_{3,1},t_1)\mathbf{B} & \dots & \mathbf{0}_{6\times3} \\ \vdots & \vdots & \ddots & \vdots \\ \vdots & \vdots & \ddots & \vdots \\ \boldsymbol{\Phi}(t_{N,n_{\mathrm{LOS}}},t_0)\mathbf{B} & \boldsymbol{\Phi}(t_{N,n_{\mathrm{LOS}}},t_1)\mathbf{B} & \dots & \mathbf{B} \end{bmatrix}, \tag{4.35}$$

$$\mathbf{G}_{\delta x} = \begin{bmatrix} \boldsymbol{\Phi}(t_{1,1},t_0) & \mathbf{0}_{6\times3} & \dots & \mathbf{0}_{6\times3} \\ \vdots & \vdots & \ddots & \vdots \\ \boldsymbol{\Phi}(t_{1,n_{\mathrm{LOS}}},t_0) & \mathbf{0}_{6\times3} & \dots & \mathbf{0}_{6\times3} \\ \boldsymbol{\Phi}(t_{2,1},t_0) & \boldsymbol{\Phi}(t_{2,1},t_1) & \dots & \mathbf{0}_{6\times3} \\ \vdots & \vdots & \ddots & \vdots \\ \boldsymbol{\Phi}(t_{2,n_{\mathrm{LOS}}},t_0) & \boldsymbol{\Phi}(t_{2,n_{\mathrm{LOS}}},t_1) & \dots & \mathbf{0}_{6\times3} \\ \boldsymbol{\Phi}(t_{3,1},t_0) & \boldsymbol{\Phi}(t_{3,1},t_1) & \dots & \mathbf{0}_{6\times3} \\ \vdots & \vdots & \ddots & \vdots \\ \vdots & \vdots & \ddots & \vdots \\ \boldsymbol{\Phi}(t_{N,n_{\mathrm{LOS}}},t_0) & \boldsymbol{\Phi}(t_{N,n_{\mathrm{LOS}}},t_1) & \dots & \mathbf{I} \\ & & & \end{bmatrix}, \tag{4.36}$$

where the term $\mathbf{B}_\zeta$ of Eq. (4.34) is defined as

$$\mathbf{B}_{\zeta_i}(t_{j,l}) = \int_{t_0}^{t_{j,l}} \boldsymbol{\Phi}(t_{j,l},\tau)\mathbf{B}B_{i,q}(\tau)d\tau, \quad i = 1\dots n_c. \tag{4.37}$$

Finally, by relating the stack vectors with the stack matrices (see Eq. (4.33)-(4.36)), the relative state prediction can be expressed in a compact form

$$\mathbf{x}_\mathbf{S} = \mathbf{F}\mathbf{x}_0 + \mathbf{G}_\zeta\boldsymbol{\zeta}_\mathbf{S} + \mathbf{G}_{\Delta V}\Delta\mathbf{V}_\mathbf{S} + \mathbf{G}_{\delta x}\boldsymbol{\delta}\mathbf{x}_\mathbf{S}. \tag{4.38}$$

The mean of Eq. (4.38) is

$$\hat{\mathbf{x}}_\mathbf{S} = \mathbf{F}\mathbf{x}_0 + \mathbf{G}_\zeta\boldsymbol{\zeta}_\mathbf{S} + \mathbf{G}_{\Delta V}\Delta\mathbf{V}_\mathbf{S} + \mathbf{G}_{\delta x}\widehat{\boldsymbol{\delta}\mathbf{x}}_\mathbf{S}, \tag{4.39}$$

where

$$\begin{aligned} \hat{\mathbf{x}}_\mathbf{S} &= [\hat{\mathbf{x}}_{1,1}^T,\dots,\hat{\mathbf{x}}_{1,n_{\mathrm{LOS}}}^T,\hat{\mathbf{x}}_{2,1}^T,\dots,\hat{\mathbf{x}}_{2,n_{\mathrm{LOS}}}^T,\hat{\mathbf{x}}_{3,1}^T,\dots\dots,\hat{\mathbf{x}}_{N,n_{\mathrm{LOS}}}^T]^T, \\ \widehat{\boldsymbol{\delta}\mathbf{x}}_\mathbf{S} &= [\widehat{\boldsymbol{\delta}\mathbf{x}}^T,\dots,\widehat{\boldsymbol{\delta}\mathbf{x}}_N^T]^T, \end{aligned} \tag{4.40}$$

where the bias of the additive disturbance is invariant due to the quasi-steady assumption.

The continuous acceleration, evaluated at the constraints enforcement instants $t_{j,m}$, can also be compactly expressed as

$$\mathbf{u}_{\mathbf{S}} = \mathbf{K}_u \boldsymbol{\zeta}_{\mathbf{S}}, \tag{4.41}$$

where the stack vector $\mathbf{u}_{\mathbf{S}} \in \mathbb{R}^{3n_u N}$ is

$$\mathbf{u}_{\mathbf{S}} = [\mathbf{u}_{1,1}^T, \ldots, \mathbf{u}_{1,n_u}^T, \mathbf{u}_{2,1}^T, \ldots, \mathbf{u}_{2,n_u}^T, \mathbf{u}_{3,1}^T, \ldots\ldots, \mathbf{u}_{N,n_u}^T]^T, \tag{4.42}$$

being $\mathbf{u}_{j,m} = \mathbf{u}(t_{j,m})$. The stack matrix $\mathbf{K}_u \in \mathbb{R}^{3n_u N \times 3n_c}$ is defined as

$$\mathbf{K}_u = \begin{bmatrix} B_{1,q}(t_{1,1})\mathbf{I} & B_{2,q}(t_{1,1})\mathbf{I} & \ldots & B_{n_c,q}(t_{1,1})\mathbf{I} \\ \vdots & \vdots & \ddots & \vdots \\ B_{1,q}(t_{1,n_u})\mathbf{I} & B_{2,q}(t_{1,n_u})\mathbf{I} & \ldots & B_{n_c,q}(t_{1,n_u})\mathbf{I} \\ B_{1,q}(t_{2,1})\mathbf{I} & B_{2,q}(t_{2,1})\mathbf{I} & \ldots & B_{n_c,q}(t_{2,1})\mathbf{I} \\ \vdots & \vdots & \ddots & \vdots \\ B_{1,q}(t_{2,n_u})\mathbf{I} & B_{2,q}(t_{2,n_u})\mathbf{I} & \ldots & B_{n_c,q}(t_{2,n_u})\mathbf{I} \\ B_{1,q}(t_{3,1})\mathbf{I} & B_{2,q}(t_{3,1})\mathbf{I} & \ldots & B_{n_c,q}(t_{3,1})\mathbf{I} \\ \vdots & \vdots & \ddots & \vdots \\ \vdots & \vdots & \ddots & \vdots \\ B_{1,q}(t_{N,n_u})\mathbf{I} & B_{2,q}(t_{N,n_u})\mathbf{I} & \ldots & B_{n_c,q}(t_{N,n_u})\mathbf{I} \end{bmatrix}. \tag{4.43}$$

Robust static program

By joining the discretization of the continuous constraints discretization with the compact formulation, the following quadratic program is derived

$$\begin{aligned} \underset{\Delta\mathbf{V}_{\mathbf{S}},\, \boldsymbol{\zeta}_{\mathbf{S}}}{\text{minimize}} \quad & \Delta\mathbf{V}_{\mathbf{S}}^T \Delta\mathbf{V}_{\mathbf{S}} + \gamma_\zeta \boldsymbol{\zeta}_{\mathbf{S}}^T \boldsymbol{\zeta}_{\mathbf{S}}, \\ \text{subject to} \quad & \hat{\mathbf{x}}_{\mathbf{S}} = \mathbf{F}\mathbf{x}_0 + \mathbf{G}_\zeta \boldsymbol{\zeta}_{\mathbf{S}} + \mathbf{G}_{\Delta V} \Delta\mathbf{V}_{\mathbf{S}} + \mathbf{G}_{\delta x} \widehat{\boldsymbol{\delta}\mathbf{x}}_{\mathbf{S}}, \\ & \mathbf{A}_{\mathbf{S},\mathrm{LOS}} \hat{\mathbf{x}}_{\mathbf{S}} \leq \mathbf{b}_{\mathbf{S},\mathrm{LOS}} + \mathbf{b}_{\mathbf{S},\delta x}, \\ & -\overline{\Delta\mathbf{V}}_{\mathbf{S}} \leq \Delta\mathbf{V}_{\mathbf{S}} \leq \overline{\Delta\mathbf{V}}_{\mathbf{S}}, \\ & -\bar{\mathbf{u}}_{\mathbf{S}} \leq \mathbf{u}_{\mathbf{S}} \leq \bar{\mathbf{u}}_{\mathbf{S}}, \\ & \mathbf{u}_{\mathbf{S}} = \mathbf{K}_u \boldsymbol{\zeta}_{\mathbf{S}}, \\ & \mathbf{u}(t_0, \boldsymbol{\zeta}_{\mathbf{S}}) = \mathbf{0}, \quad \dot{\mathbf{u}}(t_0, \boldsymbol{\zeta}_{\mathbf{S}}) = \mathbf{0}, \quad \ddot{\mathbf{u}}(t_0, \boldsymbol{\zeta}_{\mathbf{S}}) = \mathbf{0}, \\ & \mathbf{b}_{\mathbf{S},\delta x} \equiv \mathbf{b}_{\mathbf{S},\delta x}(\widehat{\boldsymbol{\delta}\mathbf{x}}, \boldsymbol{\Sigma}_{\boldsymbol{\delta}\mathbf{x}}, \alpha), \\ & \widehat{\boldsymbol{\delta}\mathbf{x}} \equiv \text{constant}, \quad \boldsymbol{\Sigma}_{\boldsymbol{\delta}\mathbf{x}} \equiv \text{constant}. \end{aligned} \tag{4.44}$$

The stack matrix $\mathbf{A}_{\mathbf{S},\mathrm{LOS}}$ and vector $\mathbf{b}_{\mathbf{S},\mathrm{LOS}}$ for the line-of-sight constraints have the same expression of Eq. (3.28). The matrix $\mathbf{A}_{x_f}$ extracts the final state as in Eq. (3.30). The continuous acceleration profile considers the initial transient phase of the thrusters which is the reason why the initial control acceleration and its derivatives (up to second order) are nullified. The term $\mathbf{b}_{\mathbf{S},\delta x} \in \mathbb{R}^{5n_{\mathrm{LOS}}N}$ stacks the bounding terms guaranteeing the probabilistic satisfaction of the line-of-sight constraints as

$$\mathbf{b}_{\mathbf{S},\delta x} = [\mathbf{b}^T_{\delta_x}(t_{1,1}), \ldots \mathbf{b}^T_{\delta_x}(t_{1,n_{\mathrm{LOS}}}), \mathbf{b}^T_{\delta_x}(t_{2,1}), \ldots\ldots, \mathbf{b}^T_{\delta_x}(t_{N,n_{\mathrm{LOS}}})]^T. \tag{4.45}$$

Let recall that the bounding term explicitly depends on the probabilistic parameter α which is not the same as the constraints satisfaction probability p. In order to ensure a satisfaction equal or above a probability p, the corresponding parameter α has to be derived according to Eq. (4.19). It is also assumed that the disturbances mean and covariance are known. Finally, the impulse amplitude and continuous accelerations bounds has been stacked through $\overline{\Delta \mathbf{V}}_{\mathbf{S}} \in \mathbb{R}^{3(N+1)}$ $\overline{\mathbf{u}}_{\mathbf{S}} \in \mathbb{R}^{3n_uN}$ as follows

$$\overline{\Delta \mathbf{V}}_{\mathbf{S}} = \begin{bmatrix} \overline{\Delta \mathbf{V}} \\ \vdots \\ \overline{\Delta \mathbf{V}} \end{bmatrix}, \quad \overline{\mathbf{u}}_{\mathbf{S}} = \begin{bmatrix} \overline{\mathbf{u}} \\ \vdots \\ \overline{\mathbf{u}} \end{bmatrix}. \tag{4.46}$$

4.4 Robust MPC scheme with disturbance estimation

In this section, the robust closed-loop model predictive scheme is presented. Firstly, the robust control program (4.44) is embedded within an MPC form. Then, an on-line disturbance estimator, with the ability of inferring the disturbance statistical properties along the operation, is stated. Finally, the complete MPC algorithm with disturbance estimation is shown as pseudocode.

4.4.1 Robust control program

The robust quadratic programming 4.44 is suitable to be embedded within an MPC scheme. Let recall that very efficient QP solvers, from the computational perspective, are available nowadays. However, as in Section 3.4.2, it is recommended to relax the terminal equality constraints to penalty costs in the objective function. This would prevent infeasibilities as the time horizon is slided forward, thus the equality constraint would have to be repeated over a finite interval. By taking this into account, for an MPC step $k = 0 \ldots N-1$, the robust control program is given by

$$\boxed{\begin{array}{ll}
\underset{\Delta\mathbf{V}_{\mathbf{S}}(k),\,\boldsymbol{\zeta}_{\mathbf{S}}(k)}{\text{minimize}} & (\Delta\mathbf{V}_{\mathbf{S}}(k))^T\Delta\mathbf{V}_{\mathbf{S}}(k)+\gamma_\zeta(\boldsymbol{\zeta}_{\mathbf{S}}(k))^T\boldsymbol{\zeta}_{\mathbf{S}}(k) \\
 & +\,(\hat{\mathbf{x}}_{\mathbf{S}}(k)-\mathbf{x}_{\mathbf{S}f})^T\mathbf{Q}_{\mathbf{S}x_f}(k)(\hat{\mathbf{x}}_{\mathbf{S}}(k)-\mathbf{x}_{\mathbf{S}f}), \\
 & \qquad\qquad k=1\dots N-1, \\
\text{subject to} & \hat{\mathbf{x}}_{\mathbf{S}}(k)=\mathbf{F}\mathbf{x}_k+\mathbf{G}_\zeta\boldsymbol{\zeta}_{\mathbf{S}}+\mathbf{G}_{\Delta V}\Delta\mathbf{V}_{\mathbf{S}}+\mathbf{G}_{\delta x}\widehat{\boldsymbol{\delta}\mathbf{x}}_{\mathbf{S}}, \\
 & \mathbf{A}_{\mathbf{S},\mathrm{LOS}}\hat{\mathbf{x}}_{\mathbf{S}}(k)\le\mathbf{b}_{\mathbf{S},\mathrm{LOS}}+\mathbf{b}_{\mathbf{S},\delta x}(k), \\
 & -\overline{\Delta\mathbf{V}}_{\mathbf{S}}\le\Delta\mathbf{V}_{\mathbf{S}}(k)\le\overline{\Delta\mathbf{V}}_{\mathbf{S}}, \\
 & -\overline{\mathbf{u}}_{\mathbf{S}}\le\mathbf{u}_{\mathbf{S}}(k)\le\overline{\mathbf{u}}_{\mathbf{S}}, \\
 & \mathbf{u}_{\mathbf{S}}(k)=\mathbf{K}_u(k)\boldsymbol{\zeta}_{\mathbf{S}}(k), \\
 & \tilde{\mathbf{u}}_k=\mathbf{u}(t_k,\boldsymbol{\zeta}_{\mathbf{S}}(k)), \\
 & \dot{\tilde{\mathbf{u}}}_k=\dot{\mathbf{u}}(t_k,\boldsymbol{\zeta}_{\mathbf{S}}(k)), \\
 & \ddot{\tilde{\mathbf{u}}}_k=\ddot{\mathbf{u}}(t_k,\boldsymbol{\zeta}_{\mathbf{S}}(k)), \\
 & \mathbf{b}_{\mathbf{S},\delta x}(k)\equiv\mathbf{b}_{\mathbf{S},\delta x}(\widehat{\boldsymbol{\delta}\mathbf{x}}_k,\boldsymbol{\Sigma}_{\boldsymbol{\delta}\mathbf{x}_k},\alpha), \\
 & \widehat{\boldsymbol{\delta}\mathbf{x}}_k\equiv\text{constant},\quad\boldsymbol{\Sigma}_{\boldsymbol{\delta}\mathbf{x}_k}\equiv\text{constant},
\end{array}} \tag{4.47}$$

where, for the sake of clarity, the dependencies with the current MPC step k have been omitted at the right-hand side of the compact propagation equation. The terminal cost matrix $\mathbf{Q}_{\mathbf{S}x_f}$ and vector $\mathbf{x}_{\mathbf{S}f}$ have the same structure as Eq. (3.47). These are modulated by terminal weights $\{\gamma_\rho,\gamma_{\dot{\rho}}\}\ge 0$. Consequently, the sliding MPC does not only consider reaching the terminal relative state but also to remain on its proximity. The final control acceleration and its derivatives are denoted, of the previous interval $k-1$, are denoted by $\tilde{\mathbf{u}}_k$, $\dot{\tilde{\mathbf{u}}}_k$ and $\ddot{\tilde{\mathbf{u}}}_k$. The control acceleration profile, for the MPC step k, has to begin from these conditions in order to maintain its continuity.

4.4.2 On-line disturbance estimator

The robust control program (4.47) requires the disturbance statistical properties, its mean $\widehat{\boldsymbol{\delta}\mathbf{x}}_k$ and covariance $\boldsymbol{\Sigma}_{\boldsymbol{\delta}\mathbf{x}_k}$, in order to compute a robust control sequence. However, these variables are usually inaccurate or unknown a-priori and have to be estimated. In this work, following [Gavilan12], an on-line disturbance estimator is considered. Let first compute the disturbance at the current MPC step k. The disturbance is the mismatch between the current value $\tilde{\mathbf{x}}_k$ and the prediction (without the disturbance term)

$$\begin{aligned}\boldsymbol{\delta}\mathbf{x}_k=&\tilde{\mathbf{x}}_k-\boldsymbol{\Phi}(t_k,t_{k-1})\mathbf{x}_{k-1}-\int_{t_{k-1}}^{t_k}\boldsymbol{\Phi}(t_k,\tau)\mathbf{B}\sum_{i=1}^{n_c}B_{i,q}(\tau)\boldsymbol{\xi}_i d\tau\\&-\boldsymbol{\Phi}(t_k,t_{k-1})\mathbf{B}\Delta\mathbf{V}_{k-1}.\end{aligned} \tag{4.48}$$

Using past disturbances up to the current MPC step k, the disturbance bias and covariance can be estimated as

$$\begin{aligned}\widehat{\boldsymbol{\delta}\mathbf{x}}_k &= \frac{\sum\limits_{i=1}^{k} e^{-\lambda(k-i)}\boldsymbol{\delta}\mathbf{x}_i}{\sum\limits_{i=1}^{k} e^{-\lambda(k-i)}},\\ \boldsymbol{\Sigma}_{\boldsymbol{\delta}\mathbf{x}_k} &= \frac{\sum\limits_{i=1}^{k} e^{-\lambda(k-i)}(\boldsymbol{\delta}\mathbf{x}_i - \widehat{\boldsymbol{\delta}\mathbf{x}}_k)(\boldsymbol{\delta}\mathbf{x}_i - \widehat{\boldsymbol{\delta}\mathbf{x}}_k)^T}{\sum\limits_{i=1}^{k} e^{-\lambda(k-i)}},\end{aligned} \tag{4.49}$$

where $\lambda \geq 0$ is a forgetting factor giving more weight to the recent disturbances. This may help to account for the case where the disturbance statistical properties are time-varying. However, the past disturbances have to be stored which may be an issue if the available memory on-board is scarce. In order to mitigate this issue, following [Gavilan12], alternative recursive formulas will substitute Eq. (4.49). Let define the following variable κ_k

$$\kappa_k = \sum_{i=1}^{k} e^{-\lambda(k-i)} = \frac{e^{-\lambda}(1-e^{-\lambda k})}{1-e^{-\lambda}}. \tag{4.50}$$

Note that the summation has been simplified by the sum of a geometric progression. The previous term can be employed to define the following recursive formulas

$$\begin{aligned}\widehat{\boldsymbol{\delta}\mathbf{x}}_k &= \frac{e^{-\lambda}}{\kappa_k}(\kappa_{k-1}\widehat{\boldsymbol{\delta}\mathbf{x}}_{k-1} + \boldsymbol{\delta}\mathbf{x}_k),\\ \boldsymbol{\Sigma}_{\boldsymbol{\delta}\mathbf{x}_k} &= \frac{e^{-\lambda}}{\kappa_k}\left[\kappa_{k-1}\boldsymbol{\Sigma}_{\boldsymbol{\delta}\mathbf{x}_{k-1}} + (\boldsymbol{\delta}\mathbf{x}_k - \widehat{\boldsymbol{\delta}\mathbf{x}}_k)(\boldsymbol{\delta}\mathbf{x}_k - \widehat{\boldsymbol{\delta}\mathbf{x}}_k)^T\right],\end{aligned} \tag{4.51}$$

which have to be initialized with the initial knowledge of the disturbances statistical properties $\widehat{\boldsymbol{\delta}\mathbf{x}}_0$ and $\boldsymbol{\Sigma}_{\boldsymbol{\delta}\mathbf{x}_0}$. Note that by using Eq. (4.49), only the last mean and covariance estimates have to be stored in memory.

4.4.3 Robust MPC scheme

The complete robust MPC scheme for RTBP spacecraft rendezvous is shown as pseudocode in Algorithm 2. The initial steps 2-3 precompute by integration the transition matrices and contribution of the B-splines based continuous control acceleration. On the contrary to Keplerian motion, the RTBP relative models have to be numerically integrated according to (2.51). Then, with the initial knowledge of the disturbances statistical properties, the line-of-sight constraint bounding terms are computed in step 5. If the disturbances statistical properties are unknown, that is $\widehat{\boldsymbol{\delta}\mathbf{x}}_0 = \mathbf{0}$ and $\boldsymbol{\Sigma}_{\boldsymbol{\delta}\mathbf{x}_0} = \mathbf{0}_{6\times 6}$, the bounding term will

Algorithm 2: Robust MPC scheme with disturbance estimation

```
begin
    Integrate Eq. (2.51) to precompute the state transition matrices
      $\boldsymbol{\Phi}(t_{j+k,l}, t_k)$, $k = 0 \ldots N-1$;
    Integrate Eq. (4.37) to precompute $\mathbf{B}_{\zeta_i}(t_{j+k,l})$, $k = 0 \ldots N-1$;
    Initialize the disturbances statistical properties $\widehat{\boldsymbol{\delta}\mathbf{x}}_0$ and $\boldsymbol{\Sigma}_{\boldsymbol{\delta}\mathbf{x}_0}$;
    Compute the bounding terms $\mathbf{b}_{\delta x}(t_{j,l})$ through Eq. (4.26);
    Obtain a solution of the QP problem (4.44), $\Delta\mathbf{V}_{\mathbf{S}}$ and $\boldsymbol{\zeta}_{\mathbf{S}}$;
    Apply $\Delta\mathbf{V}(t_0)$ and $\mathbf{u}(t)$ for $t \in [t_0, t_1)$;
    Initialize the MPC step $k = 1$;
    while $k < N$ do
        Compute the actual disturbance $\boldsymbol{\delta}\mathbf{x}_k$ according to Eq. (4.48);
        Update the disturbance statistical properties $\widehat{\boldsymbol{\delta}\mathbf{x}}_k$ and $\boldsymbol{\Sigma}_{\boldsymbol{\delta}\mathbf{x}_k}$
          through Eq. (4.51);
        Update the bounding terms $\mathbf{b}_{\mathbf{S},\delta x}(k)$ through Eq. (4.26);
        Obtain the solution of the QP problem (4.47), $\Delta\mathbf{V}_{\mathbf{S}}(k)$ and
          $\boldsymbol{\zeta}_{\mathbf{S}}(k)$;
        Apply $\Delta\mathbf{V}(t_k)$ and $\mathbf{u}(t)$ for $t \in [t_k,\, t_{k+1})$;
        Update the MPC step, $k \leftarrow k + 1$;
    end
    Apply the final braking impulse $\Delta\mathbf{V}(t_N)$;
end
```

be null in the initialization. Using the previous inputs, an initial open-loop plan is computed in step 6. This plan is executed by the application of the first impulse action and continuous control acceleration during the first MPC interval.

Subsequently, the closed-loop MPC controller takes on until the end of the rendezvous operation. After each MPC step, the relative state disturbance is computed in step 10. This serves to update the disturbance statistical properties as per step 11. With this new statistical properties, the line-of-sight constraint bounding term is computed in step 12. Then, the robust control plan is updated by solving the associated QP problem in step 13. The first impulse and continuous acceleration for the first interval of this new plan are applied and the process is repeated until the end of the maneuver. At the instant $t_f = t_N$, the final braking impulse is applied (see step 17). A further station-keeping phase around the final relative position is out of the scope of this work.

4.5 Numerical results

The main contribution of the proposed robust controller for RTBP rendezvous is its capability to explicitly account for disturbances, thus assuring constraints satisfaction in a probabilistic sense. To test the previous feature, the numerical results are mainly devoted to compare the proposed robust controller with respect to a non-robust one. The non-robust controller can be easily recover from the employed formulation by assuming there are no disturbances, thus $\widehat{\boldsymbol{\delta}\mathbf{x}} = \mathbf{0}$ and $\boldsymbol{\Sigma}_{\boldsymbol{\delta}\mathbf{x}} = \mathbf{0}_{6\times 6}$ (which also implies $\mathbf{b}_{\mathbf{S},\delta x} = \mathbf{0}$) in the program (4.47).

The studied scenario consists in a rendezvous operation with a target placed in an Earth-Moon near-rectilinear halo orbit. Two distinct configurations of the chaser propulsive plant have been considered. The first one corresponds to a vehicle equipped with only impulsive thrusters while for the second one only continuous acceleration thrusters are available. The reason to separate both cases (though the employed formulation allows to consider both) is that only a specific type of actuator is usually employed for the same mission phase.

The simulations have been carried out in a MATLAB environment using *Gurobi* optimization package [Gurobi14] as the QP solver. The MATLAB routine *ode45* was used for the computation of the state transition matrices and the contribution of the continuous acceleration. This function implements a 4th order Runge-Kutta numerical integration method with an adaptive time step.

4.5.1 Simulation model and controller parameters

Next, the simulation model and controller parameters are detailed. In order to justify the chosen scenario, an analysis of the rendezvous maneuver with respect to the target position is carried out.

Simulation model

The simulation model assumes a passive target placed in an Earth-Moon periodic orbit. The non-linear restricted three-body problem relative dynamics of Eq. (2.50), without orbital perturbations but with control disturbances as Eq. (2.68)-(2.70), are considered

$$\begin{aligned}
\ddot{\boldsymbol{\rho}}(t) =& -\dot{\boldsymbol{\omega}}_{L/I} \times \boldsymbol{\rho} - 2\boldsymbol{\omega}_{L/I} \times \dot{\boldsymbol{\rho}} - \boldsymbol{\omega}_{L/I} \times (\boldsymbol{\omega}_{L/I} \times \boldsymbol{\rho}) - \frac{\mu_1(\mathbf{r}_{1t} + \boldsymbol{\rho})}{\|\mathbf{r}_{1t} + \boldsymbol{\rho}\|_2^3} \\
& - \frac{\mu_2(\mathbf{r}_{2t} + \boldsymbol{\rho})}{\|\mathbf{r}_{2t} + \boldsymbol{\rho}\|_2^3} + \frac{\mu_1 \mathbf{r}_{1t}}{r_{1t}^3} + \frac{\mu_2 \mathbf{r}_{2t}}{r_{2t}^3} + \Delta\mathbf{R}(\boldsymbol{\delta\theta})[(1+\epsilon_u)\mathbf{u}(t) + \boldsymbol{\delta}\mathbf{u}], \\
\dot{\boldsymbol{\rho}}^+(t_k) =& \dot{\boldsymbol{\rho}}(t_k) + \Delta\mathbf{R}(\boldsymbol{\delta\theta})[(1+\epsilon_{\Delta V})\Delta\mathbf{V}(t_k) + \boldsymbol{\delta}\mathbf{V}], \\
\ddot{\mathbf{r}}_t(t) =& -\frac{\mu_1 \mathbf{r}_{1t}}{r_{1t}^3} - \frac{\mu_2 \mathbf{r}_{2t}}{r_{2t}^3}.
\end{aligned}$$

The main bodies standard gravitational parameters correspond to the Earth $\mu_1 = 398600.4$ km^3/s^2 and the Moon $\mu_2 = 4904.869$ km^3/s^2 respectively. The Earth-Moon distance varies between a minimum of 363104 km and a maximum of 405696 km. Note that $\mathbf{r}_{it}(t) = \mathbf{r}_t(t) - \mathbf{r}_i(t)$ $(i = 1, 2)$ is the target relative position with respect to each one of the primaries. The dependency with time has been omitted at the right-hand side of the chaser and target dynamics.

The target is placed in an Earth-Moon southern L2 NRHO characterized by Table 4.1. The chosen NRHO has an orbital period in a 4:1 resonance with respect to the Moon synodic period (29.5 days). In order to understand these parameters, the reader is referred to Appendix B (see Fig. B.2-B.3) for the details about NRHOs in the Earth-Moon system. The simulation model uses a non-linear dynamics model (see Eq. (2.25)) for the relative motion. The target evolves as per the RTBP model which may deviate its orbit computed under the CRTBP. Let recall that the primaries distance forms an ellipse which causes $\mathbf{r}_1 \equiv \mathbf{r}_1(t)$ and $\mathbf{r}_2 \equiv \mathbf{r}_2(t)$. However, the robustness of the NRHOs against perturbations guarantees that the deviations are weak enough for the duration of the rendezvous operation.

Stability index	Orbital period	Perilune altitude	Apolune altitude
1.625	7.375 days	3996.7 km	74103 km

Table 4.1: Parameters of the target NRHO.

The main perturbation comes from the thrusters control. The mishaps are assumed to be produced by an imperfect alignment of the array and an additive disturbance to the thrust level. The statistical properties of the mishaps are shown in Tables 4.2-4.3 for the impulsive and continuous acceleration thrusters respectively. The term $U_3(-w, w)$, indicates a multivariate uniform distribution (of dimension three) in the interval $[-w, w]$ for each variable. The bias of the additive disturbance is randomly varied for each simulation in order to assess its impact.

	Variable	Bias	Covariance
Misalignment	$\boldsymbol{\delta\theta}$	$[2.5°, 2.5°, 2.5°]^T$	$(2.5°)^2\mathbf{I}$
Multiplicative	$\epsilon_{\Delta V}$	0	0
Additive	$\boldsymbol{\delta}\mathbf{V}$	$U_3(-0.17, 0.17)$ mm/s	$(0.5)^2\mathbf{I}$ (mm/s)^2

Table 4.2: Statistical properties of impulses mishaps.

	Variable	Bias	Covariance
Misalignment	$\boldsymbol{\delta\theta}$	$[2.5°, 2.5°, 2.5°]^T$	$(2.5°)^2\mathbf{I}$
Multiplicative	ϵ_u	0	0
Additive	$\boldsymbol{\delta}\mathbf{u}$	$U_3(-0.17, 0.17)$ μmm/s^2	$(0.5)^2\mathbf{I}$ (μmm/s^2)^2

Table 4.3: Statistical properties of the continuous acceleration mishaps.

Controller parameters

For all the simulations, the target is initially placed at the NRHO perilune. This assumption will be justified below. The rendezvous maneuver duration is chosen as 6 h which consumes a 3.4% of the target orbital period. The LOS parameters are chosen as $c_y = c_z = 1/\tan(\pi/6)$ and $y_0 = z_0 = 5$ m. This corresponds to a 30° half-angle of a cone departing from the docking port along the $+x$ direction.

For the sake of generality, the robust MPC tuning parameters are chosen equally for all the simulations. These are: the number of sampling intervals N; the weights γ_ρ and $\gamma_{\dot{\rho}}$ for the terminal relative position and velocity; the constraints satisfaction probability p; the forgetting factor λ for the on-line disturbance estimator.

The number of sampling intervals is chosen as $N = 40$. This turns out to place 41 impulses along the maneuver for the impulsive scenario. The weights for the terminal relative position and velocity are chosen as $\gamma_\rho = 10^6$ and $\gamma_{\dot{\rho}} = 0$. Since the MPC control horizon is slided forward by adding a new cost to the terminal condition each time, targeting a null relative velocity will be indirectly enforced by the terminal costs in the relative position. The probability threshold of constraints satisfaction is chosen to be equal or above a 95% which implies $\alpha = 12.6$ as per the chi-square distribution with six-degrees of freedom (see Eq. (4.19)). Finally, the forgetting factor for the on-line disturbance estimator is taken as $\lambda = 0.25$.

Rendezvous analysis around the NRHO

Doing the rendezvous maneuver in the vicinity of the perilune is the most challenging case. To demonstrate that, for the controller parameters and 4:1 resonant NRHO, a parametric analysis depending on the initial target position has been carried out. This analysis uses the impulsive model and no mismatch between the prediction and the simulation model is assumed (both linear). Let also assume a V-bar alike approach such that $\boldsymbol{\rho}_0 = [500, 0, 0]^T$ m and $\dot{\boldsymbol{\rho}}_0 = \mathbf{0}$ m/s. The maneuver duration is 6 h and the control sequence is formed by 41 open-loop impulse. Figure 4.3 shows the projection of the relative trajectories in the xz plane. It can be seen that the maneuvers taking place in the target apolune region are straight lines while the ones in the vicinity of the perilune are curved. This suggests that the natural relative motion in the vicinity of the perilune is much faster, thus being more difficult to satisfy line-of-sight constraints in a perturbed scenario. Figure 4.4 shows the total ΔV for the rendezvous maneuver. It can be observed that the consumption when the rendezvous takes place in the vicinity of the perilune doubles the one for the apolune.

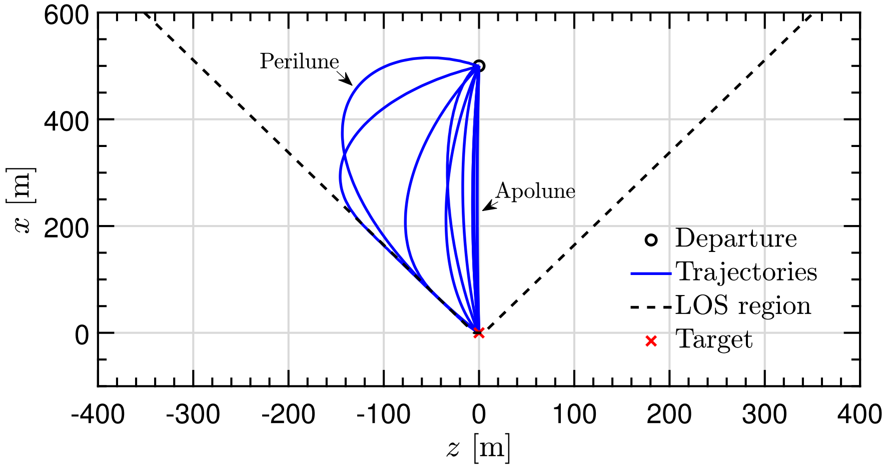

Figure 4.3: Projection of the chaser relative trajectories in the xz plane for different initial NRHO locations.

4.5.2 Impulsive thrusters scenario

Although the developed strategy allows to consider both impulsive and continuous thrusters, these are considered separately in the simulation scenario. The main reason behind the previous consideration is that, in practice, only one of these devices is used for proximity operations. To this end, the impulsive scenario is considered by forcing $\overline{\mathbf{u}} = \mathbf{0}$. The impulse amplitude is

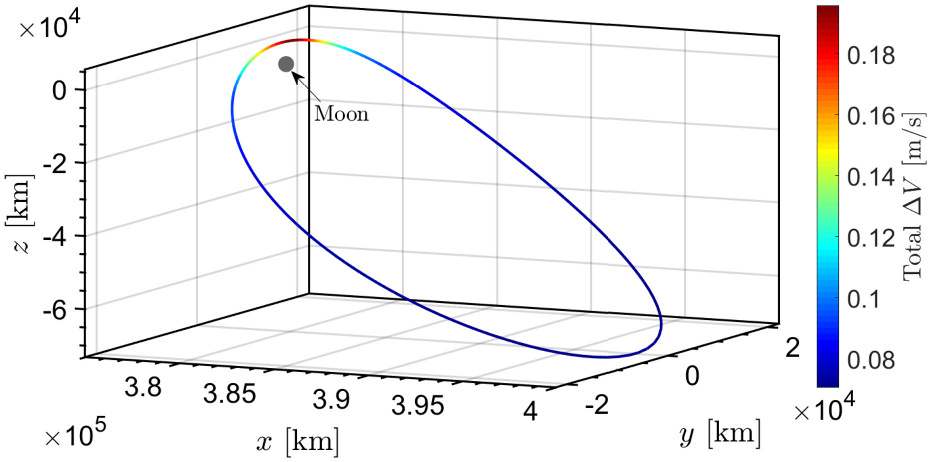

Figure 4.4: Total ΔV for different initial target locations around the NRHO.

bounded by $\overline{\Delta \mathbf{V}} = [10, 10, 10]^T$ cm/s. The chaser is assumed to depart from $\boldsymbol{\rho}_0 = [400, 200, 200]$ m with $\dot{\boldsymbol{\rho}}_0 = [10, 0, 10]$ cm/s. To compare the robust controller with respect to a non-robust one, 100 simulations, that also varies the impulsive bias $\widehat{\boldsymbol{\delta}\mathbf{V}}$ (see Table 4.2) are carried out.

Robust MPC

The robust controller (see Algorithm 2) results are shown in Fig. 4.5-4.8. For the sake of clarity, the trajectory is also projected into the xz plane because it depicts the most conflictive situations arising with the LOS constraints. Figures 4.5-4.6 show that the LOS constraints are satisfied for all the random realizations and the chaser ends in the vicinity of the target. The first conflictive situation arises early with the plane $x \geq c_z(z - z_0)$. Nonetheless, the constraint is respected even if the disturbances statistical properties are poorly known at this stage. The latter one arises at the end of the maneuver where it can be seen that the trajectories brake in advance to avoid trespassing $x \geq 0$. This can be noticed in Fig. 4.7 where the in-track impulses of the last hour are devoted to brake. The relative velocity disturbance mean and 1-sigma uncertainty estimation is shown in Fig. 4.8. The results correspond to the order of magnitude of the impulse mishap (~ 1 mm/s).

Comparison with non-robust MPC

The non-robust controller skips the disturbance estimation step 11 of Algorithm 2. Then, $\boldsymbol{\delta}\hat{\boldsymbol{x}}_k = \mathbf{0}$ and $\boldsymbol{\Sigma}_{\delta x,k} = \mathbf{0}_{6\times 6}$ for $k = 0 \ldots N$, thus the disturbances are not accounted for in the formulation. In order to compare with Figure 4.6

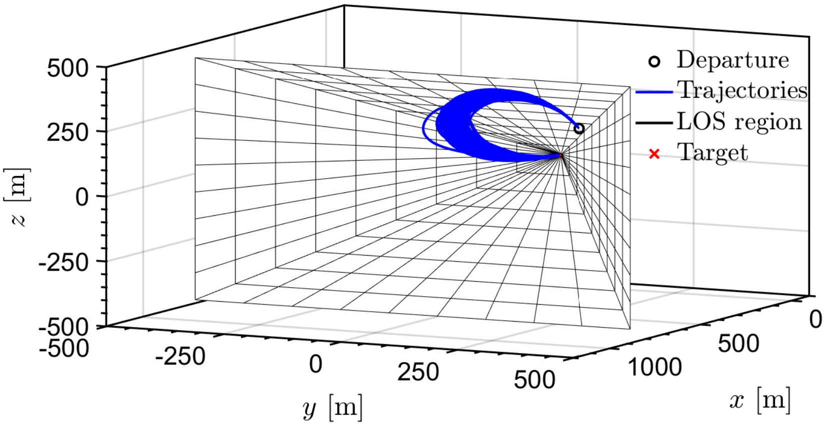

Figure 4.5: Chaser relative trajectories of the robust MPC for the impulsive scenario.

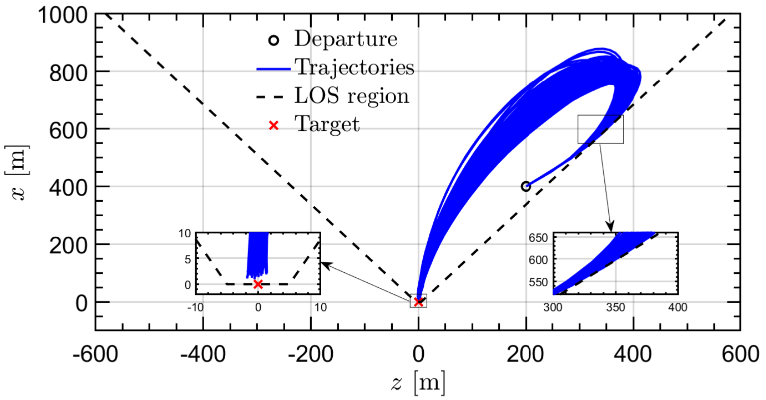

Figure 4.6: Projection of the chaser relative trajectories in the xz plane of the robust MPC for the impulsive scenario.

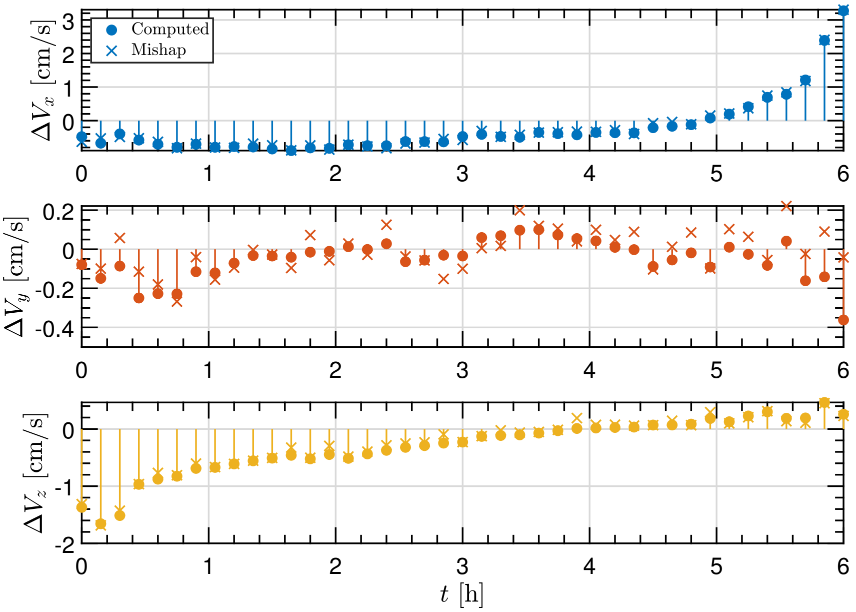

Figure 4.7: Impulse sequence for the first random realization of the robust MPC for the impulsive scenario.

of the robust controller, Figure 4.9 shows the non-robust controller trajectories in the plane xz. It can be observed that some random realizations trespass the LOS region near the departure. Additionally, the final relative position violate the inequality $x \geq 0$ for some random realizations at the final instants of the maneuver (which is a potential collision risk with the target).

Quantitatively, the robust and non-robust controllers results are shown in Fig. 4.10. The LOS satisfaction and total ΔV ($\sum_{k=0}^{N} \|\Delta \mathbf{V}_k\|_1$) are represented with respect to the additive impulse mishap bias. It can be observed that the robust controller has satisfied the LOS satisfaction in the 100% of the simulations while the non-robust controller only satisfies constraints for a 5% of the cases. In order to guarantee the LOS satisfaction by counteracting the disturbances, the robust controller requires an average of 0.4745 m/s while the non-robust control spends 0.4312 m/s. The fuel consumption demands are typically increased by a 10% by the robust controller.

The computational times for the state transition matrix, robust control and non-robust control computations are shown in Table 4.4. The most time-consuming task is the numerical integration of the state transition matrices. However, this step can be precomputed before the maneuver start. The robust MPC and non-robust MPC have similar computational times though the non-robust strategy is slightly faster as expected. The time-consumed percentage

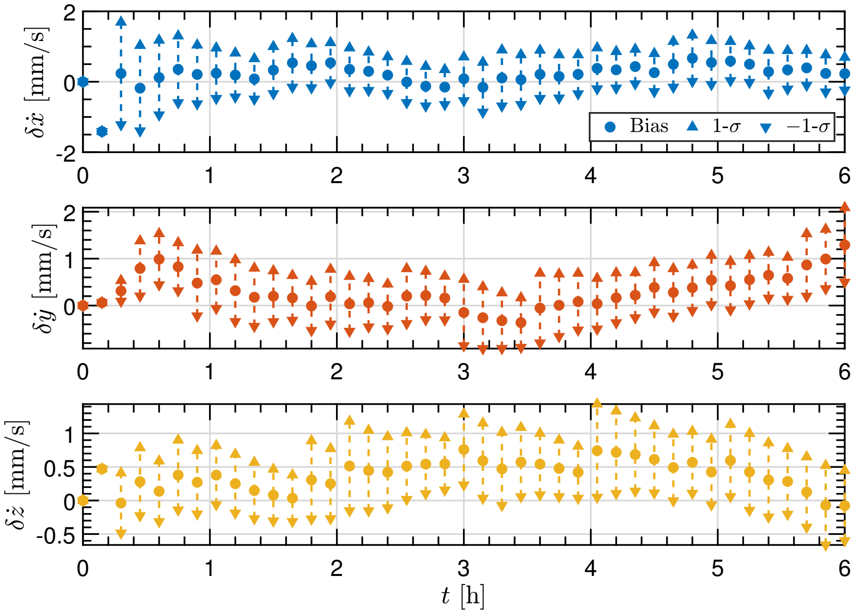

Figure 4.8: Disturbance estimation for the first random realization of the robust MPC for the impulsive scenario.

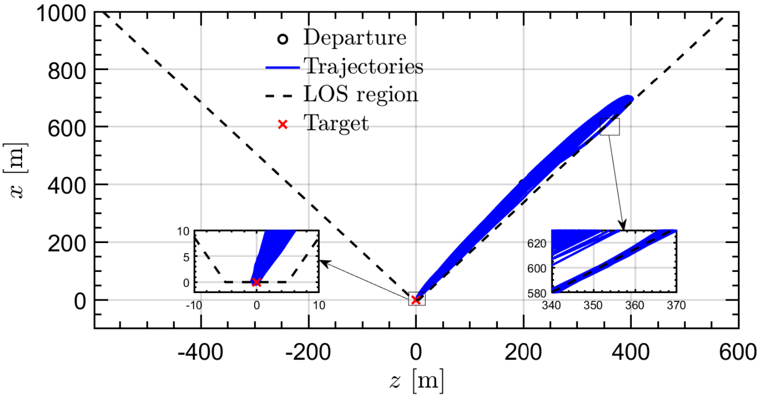

Figure 4.9: Projection of the chaser relative trajectories in the xz plane of the non-robust MPC for the impulsive scenario.

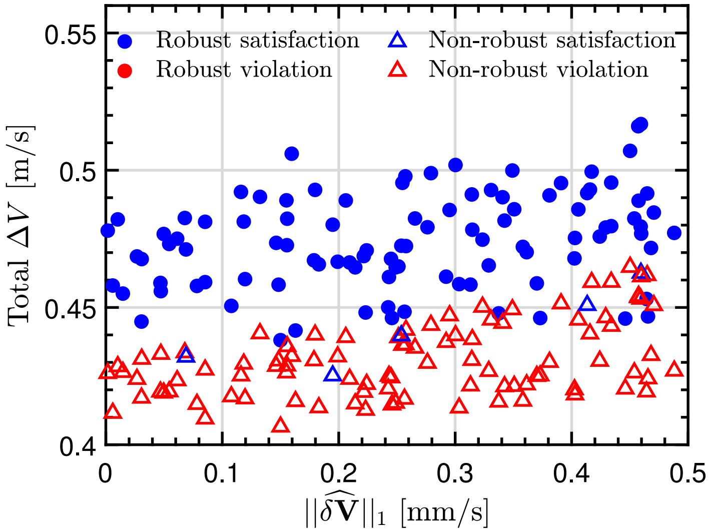

Figure 4.10: Total ΔV and constraints satisfaction of robust and non-robust MPC for the impulsive scenario.

of the sampling interval (9 min) in the computations ($< 0.2\%$) highlights the potential applicability of the proposed robust MPC in an autonomous system.

	Mean	1-sigma	Max.
STM comp.[1]	1.3659 s / 0.25%	0.0777 s / 0.01%	1.5408 s / 0.29%
R-MPC[2]	0.2631 s / 0.05%	0.0508 s / 0.01%	0.7984 s / 0.15%
NR-MPC[3]	0.2467 s / 0.05%	0.2150 s / 0.04%	0.7431 s / 0.14%

Table 4.4: Computational time and its percentage over the sampling interval for the impulsive scenario

4.5.3 Continuous thrusters scenario

Now, let consider the scenario for the continuous thrusters. In that sense, the continuous acceleration profile is characterized by the following B-splines parameters: $q = 4$, $n_c = 44$, and the knots sequence

$$\mathbf{t}_{\text{knots}} = [t_k, t_k, t_k, t_k, t_k, t_{k+1} \dots, t_{k+N-1}, t_{k+N}, t_{k+N}, t_{k+N}, t_{k+N}, t_{k+N}]^T.$$

---

[1] STM comp. ≡ computation of the state transition matrices by numerical integration.

[2] R-MPC ≡ robust model predictive control.

[3] NR-MPC ≡ non-robust model predictive control.

Therefore, the acceleration profile $\mathbf{u}(t)$ has C^4 continuity in time. The control impulses are precluded by forcing $\overline{\mathbf{\Delta V}} = \mathbf{0}$. The maximum continuous acceleration is assumed as $\overline{\mathbf{u}} = [100, 100, 100]^T$ μm/s^2. In this scenario, the chaser departs from $\boldsymbol{\rho}_0 = [600, 300, -200]$ m with a velocity of $\dot{\boldsymbol{\rho}}_0 = [-10, -10, 0]$ cm/s. Again, to compare the robust controller with respect to a non-robust one, 100 simulations, randomly varying the continuous thrust bias as per Table 4.3 are carried out.

Robust MPC

The robust controller (see Algorithm 2) results are shown in Fig. 4.11-4.14. Again, the trajectory is projected into the xz plane as it depicts the situations with a potential to violate the LOS constraints. One of the conflicts arises at the midterm of the maneuver while the other one happens in the vicinity of the target. In this scenario, some random realizations fail to satisfy the LOS constraints for these conflicts. Specifically, 80% of the random realizations satisfied the LOS constraints which is below the probability satisfaction level of a 95%. The potential cause of that underperformance is that the additive disturbances assumption (see Eq. (4.11)) models the continuous acceleration mishap in a very simplified way (the exertion of a continuous mishap is not considered). The final instants braking in the in-track direction can be seen in Fig. 4.13 for the first random realization. The bias on the continuous acceleration is also noticeable. Finally, the disturbance statistical properties (for the velocity) estimation for the first random realization is shown in Fig. 4.14. The order of magnitude of the estimation coincides with the expected cumulative effect of ~ 0.17 μm/s$^2 \cdot 9$ min ≈ 5 mm/s over the sampling interval.

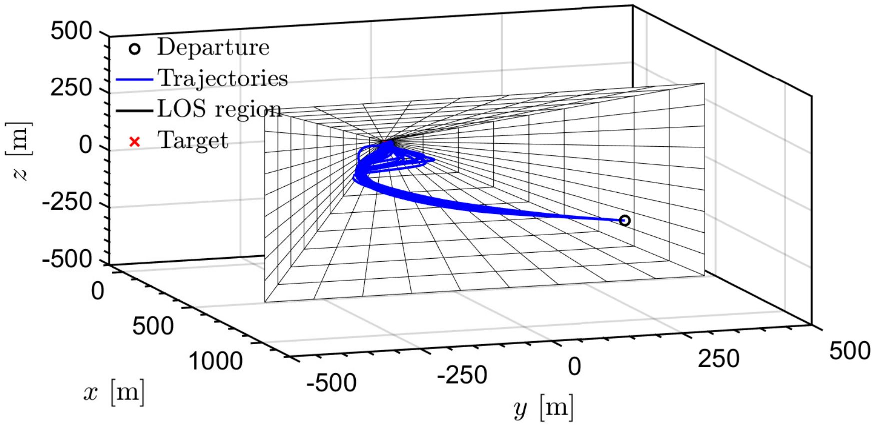

Figure 4.11: Chaser relative trajectories of the robust MPC for the continuous thrusters scenario.

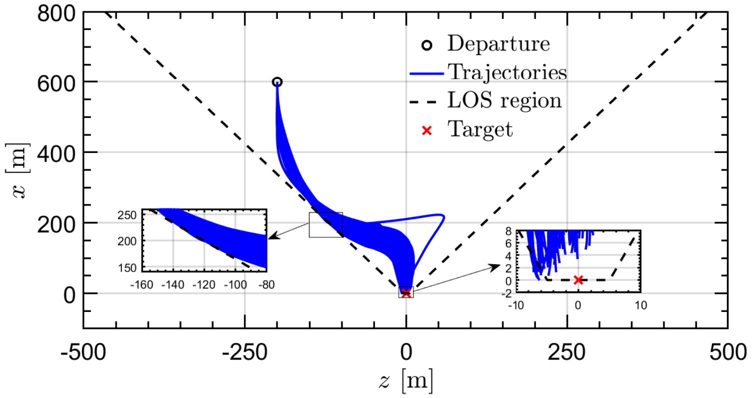

Figure 4.12: Projection of the chaser relative trajectories in the xz plane of the robust MPC for the continuous thrusters scenario.

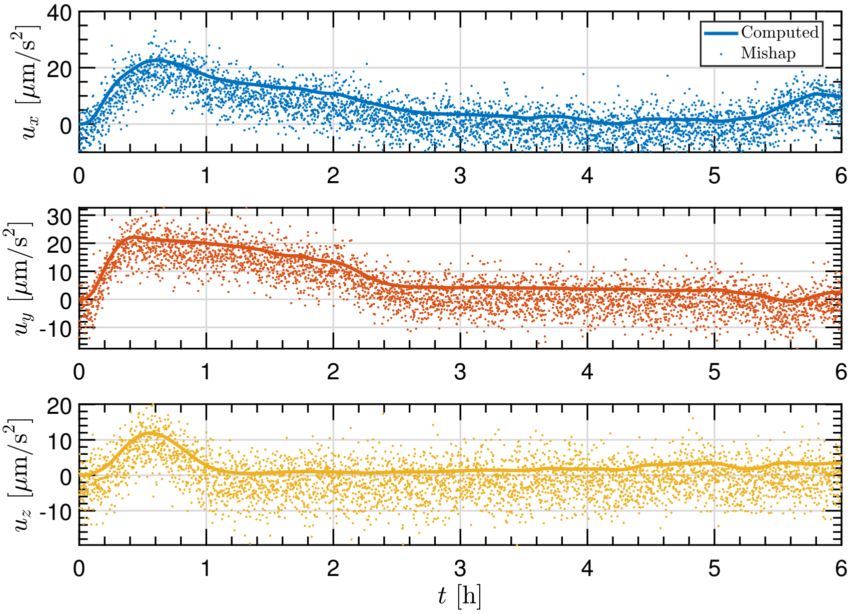

Figure 4.13: Control acceleration evolution for the first random realization of the robust MPC for the continuous thrusters scenario.

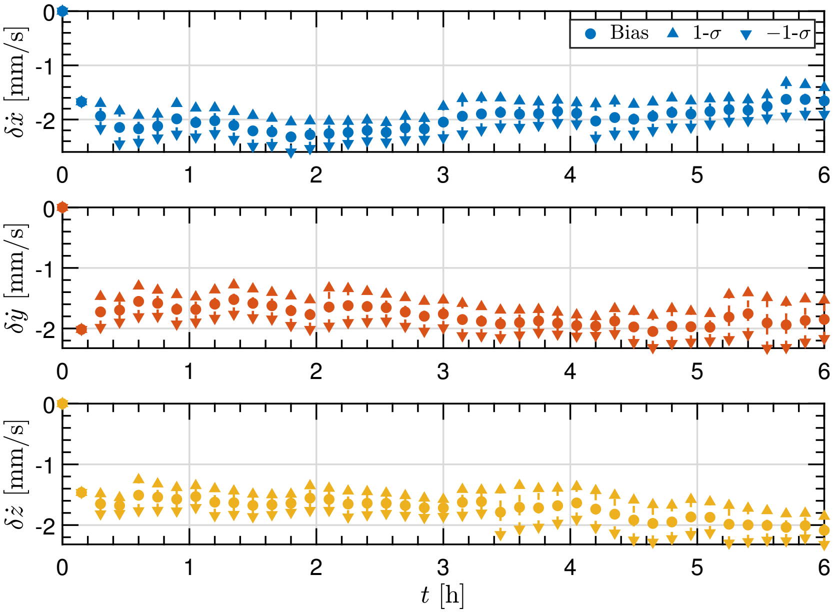

Figure 4.14: Disturbance estimation for the first random realization of the robust MPC for the continuous thrusters scenario.

Comparison with non-robust MPC

Now, let compare the robust MPC with the non-robust MPC. The non-robust MPC trajectories, for all the random realizations, are shown in Fig. 4.15. It can be observed that the majority of the trajectories violate the LOS constraints with even some of them failing to reach the vicinity of the target. The main reason to this behaviour is that the non-robust MPC control program becomes infeasible after a LOS trespassing without the possibility to recompute a feasible rendezvous maneuver from that point.

The comparison between both controllers is shown in Fig. 4.16 where both the LOS constraints satisfaction and cost, in terms of the computed control effort $\int_{t_0}^{t_f} \mathbf{u}^T(t)\mathbf{u}(t)dt/(t_f - t_0)$, are presented with respect to the continuous thrust bias. It can be noticed that the robust MPC LOS violations occur for values of $\|\boldsymbol{\delta}\mathbf{u}\|_1 > 2.2$ μm/s^2, which highlights the important effect of the disturbance bias.. The robust MPC not also achieves a LOS constraints satisfaction level of a 80%, compared to the 7% of the non-robust MPC, but also presents a lower cost. Specifically, the mean cost of the robust MPC is 0.0779 m^2/s^4 against the mean cost of 0.2421 m^2/s^4 for the non-robust MPC.

The computational times for the state transition matrix, robust control and non-robust control computations are shown in Table 4.5. In this case, the numerical integration of the state transition matrices and the continuous control action is three times slower than for the impulsive scenario (see Table 4.4). The robust MPC and non-robust MPC have similar computational times though the non-robust strategy is slightly faster as expected. They are also an order of magnitude higher than the impulsive scenario. Still, the time-consumed percentage of the sampling interval (9 min) in the computations ($< 0.5\%$) is moderate enough.

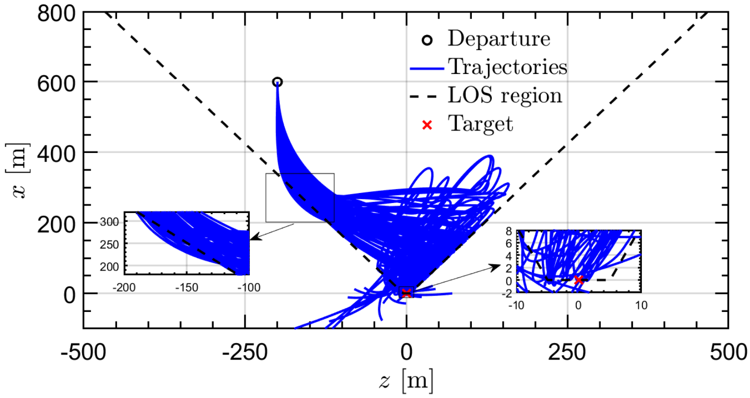

Figure 4.15: Projection of the chaser relative trajectories in the xz plane of the non-robust MPC for the continuous thrusters scenario.

	Mean	1-sigma	Max.
STM comp.[4]	3.2649 s / 0.61%	0.3214 s / 0.06%	4.1210 s / 0.76%
R-MPC[5]	1.1726 s / 0.22%	0.1117 s / 0.02%	2.3129 s / 0.43%
NR-MPC[6]	1.1051 s / 0.21%	0.1083 s / 0.02%	2.4773 s / 0.46%

Table 4.5: Computational time and its percentage over the sampling interval for the continuous thrusters scenario.

---

[4] STM comp. ≡ computation of the state transition matrices by numerical integration.

[5] R-MPC ≡ robust model predictive control.

[6] NR-MPC ≡ non-robust model predictive control.

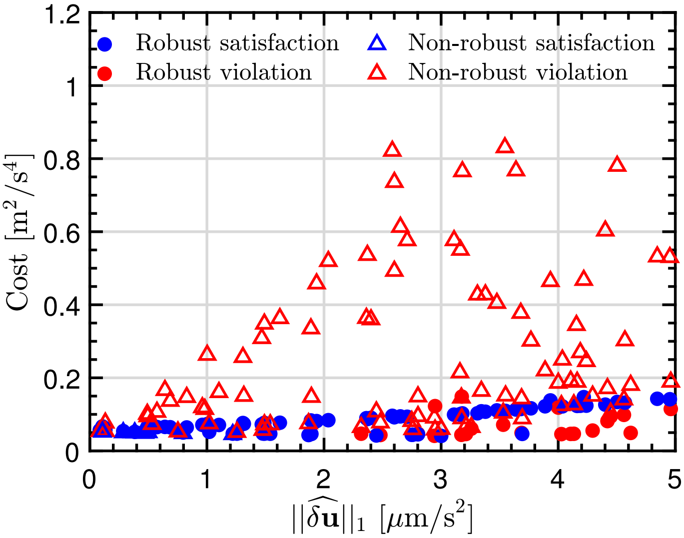

Figure 4.16: Control effort and constraints satisfaction of robust and non-robust MPC for the impulsive scenario.

Chapter 5

Event-based impulsive control for spacecraft rendezvous hovering phases

> The supreme art of war is to subdue the enemy without fighting.
>
> Sun Tzu, *The Art of War*

Contents

5.1 Hovering phase control problem 127
5.2 Constrained periodic relative orbits 128
5.3 Analysis of the admissible set reachability 129
  5.3.1 Instantaneous reachable set 130
  5.3.2 Admissible set reachability 132
  5.3.3 Admissible set proximity 135
  5.3.4 Region of attraction to the admissible set 139
5.4 Event-based predictive controller 140
  5.4.1 Single-impulse control law 141
  5.4.2 Trigger rules 144
5.5 Invariance of the single-impulse approach 146
  5.5.1 Well-posedness for hybrid impulsive systems 146
  5.5.2 Invariance of the hybrid impulsive system 149
  5.5.3 Invariance under the presence of continuous disturbances 158
5.6 Numerical results 159
  5.6.1 Simulation model and controller parameters 159
  5.6.2 Impact of the leader eccentricity 160
  5.6.3 Impact of the impulse thresholds 168

This chapter presents an event-based predictive controller for spacecraft rendezvous hovering phases. The hovering phase aims to maintain the relative position, between a leader (target) and follower (chaser), within a bounded region (see Fig. 1.3). The leader is assumed to be in a known Keplerian orbit and has a passive role (it does not change its orbit). The follower control action is impulsive which models with adequate accuracy chemical or cold gas thrusters. Both vehicles are in close proximity such that the relative distance is negligible with respect to the semi-major axis $\|\boldsymbol{\rho}\|_2/a \ll 1$. The previous hypothesis allows to use the linear relative dynamics of Eq. (2.31). The main results of this chapter have been presented in the journal article [Sanchez21a] and the conference proceeding [Sanchez19].

A natural way to maintain a follower orbiting in the vicinity of a leader is to employ a relative periodic orbit. These orbits can be conveniently described by the vector of relative parameters (see Eq. (2.40)). In addition, the orbit can be enforced to lie within a specific spatial region (namely a constrained periodic relative orbit). Employing the previous concept, the control goal of the hovering phase can be reduced to maintain the follower in the set of constrained periodic relative orbits within the hovering region. An algebraic description of the set of constrained periodic relative orbits was presented in [Arantes-Gilz17].

The main motivation of this chapter is to address some drawbacks of the global stable controller, for spacecraft rendezvous hovering phases, proposed in [Arantes-Gilz19]. The previous work demonstrated that a three-impulse sequence suffices to stabilize the relative state to the set of constrained periodic relative orbits (admissible set). By using the previous control sequence repeatedly, the distance to the admissible set diminishes until the relative state enters it. The global, though under close proximity assumptions, stable property is especially convenient when the follower relative position is far away from the hovering region (approach phase). However, several flaws arose when the phase switches to maintain the relative state within the admissible set (hovering phase). These are: the unnecessary computation of a high number of impulses; the computation of tiny impulses below the minimum impulse bit; no guarantee that the follower is within the hovering region when the three-impulse sequence is executed.

To overcome the previous issues, a local control strategy is developed. For this purpose, the event-based control paradigm [Aström08] is employed. Then, a control is only computed when an event is detected. The event detection process relies on predefined trigger rules associating a proper control response to each possible event. Consequently, the set of trigger rules is the keystone of an event-based controller and must cover every possible situation in order to not let the system drift to an unrecoverable mode. The rationale behind an event-based controller is to reduce the communication frequencies between sensors, on-board computer and actuators.

The developed event-based controller, for spacecraft rendezvous hovering phases, uses a single-impulse control law with the global stable controller (see

Appendix D) as a backup to ensure stability. The trigger rules are designed after a thorough analysis of the admissible set instantaneous reachability with a single-impulse. The outcome of this analysis is the definition of proximity metrics to the admissible set and the existence of a region of attraction. The proximity metrics quantify the distance to the admissible set in terms of the state reachability with a single-impulse. The region of attraction exploits the system periodicity to determine the states from where an instantaneous reachability window opens within the target orbital period. These concepts provide useful information on when a single-impulse should be triggered.

The resulting event-based impulsive controller can be seen as an equivalent hybrid impulsive system. This allows to assess the well-posedness and invariance of the prioritized single-impulse control. The event-based and global stable controllers are compared in terms of numerical simulations for a wide range of leader orbits. The results confirms the event-based controller superiority in terms of control accuracy and computational efficiency, with respect to the global stable controller, without noticeable drawbacks.

5.1 Hovering phase control problem

Generally, the hovering phase consists in maintaining the follower relative position, $\boldsymbol{\rho}$, within a hovering region (state subset) described as a convex polytope $\mathcal{X}_{\text{hov}}$. Assuming three-axis impulsive control and Keplerian-based motion in proximity, which allows to employ Eq. (2.24) linear relative dynamics, the hovering control problem yields

$$\boxed{\begin{array}{ll}
\underset{t_j,\Delta\mathbf{V}(t_j)}{\text{minimize}} & J(\Delta\mathbf{V}(t_j)), \\
\text{subject to} & \ddot{\boldsymbol{\rho}}(t) = -2\boldsymbol{\omega}_{L/I}\times\dot{\boldsymbol{\rho}} - \dot{\boldsymbol{\omega}}_{L/I}\times\boldsymbol{\rho} - \boldsymbol{\omega}_{L/I}\times(\boldsymbol{\omega}_{L/I}\times\boldsymbol{\rho}) \\
& \qquad\quad - \left(\mu/r_t^3\right)\left[\mathbf{I} - 3\mathbf{r}_t\mathbf{r}_t^T/r_t^2\right]\boldsymbol{\rho}, \\
& \dot{\boldsymbol{\rho}}^+(t_j) = \dot{\boldsymbol{\rho}}(t_j) + \Delta\mathbf{V}(t_j), \\
& \boldsymbol{\rho}(t) \in \mathcal{X}_{\text{hov}}, \quad t \in [t_0, t_f], \\
& \boldsymbol{\rho}(t_0) = \boldsymbol{\rho}_0 \in \mathcal{X}_{\text{hov}}, \\
& \|\Delta\mathbf{V}(t_j)\|_2 \in [-\overline{\Delta V}, -\underline{\Delta V}] \cup 0 \cup [\underline{\Delta V}, \overline{\Delta V}].
\end{array}} \tag{5.1}$$

Typically, the hovering phase duration is much greater than the leader orbital period $t_f - t_0 \gg T$. This phase is initiated when the hovering region $\mathcal{X}_{\text{hov}}$ is reached. The previous facts suggest the possibility to treat the impulse application times as a free variable. Maintaining the spacecraft hovering typically induces the computation of a tiny impulse (as the position change over time is limited to the hovering region size), thus the thruster minimum impulse bit $\underline{\Delta V}$ is taken into account.

5.2 Constrained periodic relative orbits

The most fuel efficient way to hover a given region, $\mathcal{X}_{\text{hov}}$ as per problem 5.1, is to insert the follower into a natural constrained periodic relative orbit. This orbit assures the satisfaction of the hovering region polytopic constraints without need of control. Since there could be multiple relative orbits, within the hovering region, the admissible set $\mathcal{S}_D$ is defined as

$$\mathcal{S}_D := \{\boldsymbol{\rho} \in \mathbb{R}^6 \mid \boldsymbol{\rho}(t) = \boldsymbol{\rho}(t+kT) \in \mathcal{X}_{\text{hov}},\ \ k \in \mathbb{N},\ \ t \in [0,T]\}, \tag{5.2}$$

where any constrained relative periodic orbit is admissible. Note that the relative orbit period follows a 1:1 relation with the leader orbit period T (this is due to the Keplerian-based relative motion periodicity as given by Eq. (2.39)).

The hovering region is usually described as a cuboid, in order to reduce the problem dimension without loss of generality, defined by its limits $\{\underline{x}, \overline{x}, \underline{y}, \overline{y}, \underline{z}, \overline{z}\}$ and centered in $[\underline{x}+\overline{x}, \underline{y}+\overline{y}, \underline{z}+\overline{z}]^T/2$. Under the previous consideration, the membership of the relative position to the hovering region is described by six linear inequalities

$$\boldsymbol{\rho}(t) \in \mathcal{X}_{\text{hov}} \equiv \begin{cases} \underline{x} \leq x(t) \leq \overline{x}, \\ \underline{y} \leq y(t) \leq \overline{y}, \\ \underline{z} \leq z(t) \leq \overline{z}. \end{cases} \tag{5.3}$$

For illustrative purposes, Fig. 5.1 shows several constrained relative periodic orbits within a cuboid.

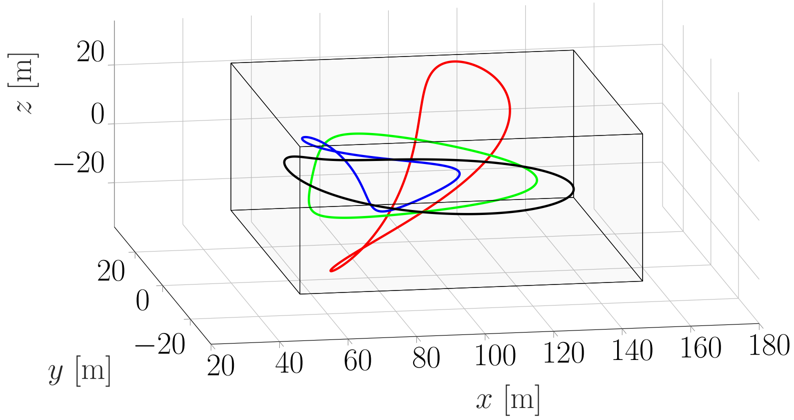

Figure 5.1: Examples of constrained periodic relative orbits.

Using the vector of parameters $\mathbf{d} = [d_0, d_1, d_2, d_3, d_4, d_5]^T$ (see Eq. (2.40)) and changing the independent variable from time t to true anomaly ν the admissible set in Eq. (5.2) can be explicitly described in the vector of parameters space as

$$\mathcal{S}_D := \left\{ \mathbf{d} \in \mathbb{R}^6 \;\middle|\; \begin{bmatrix} \underline{x} \\ \underline{y} \\ \underline{z} \end{bmatrix} \leq \frac{1}{\rho_\nu} \begin{bmatrix} \mathbf{W}_1(\nu)\mathbf{d}(\nu) \\ \mathbf{W}_2(\nu)\mathbf{d}(\nu) \\ \mathbf{W}_3(\nu)\mathbf{d}(\nu) \end{bmatrix} \leq \begin{bmatrix} \overline{x} \\ \overline{y} \\ \overline{z} \end{bmatrix},\ d_0 = 0,\ \forall \nu \geq \nu_0 \right\}, \tag{5.4}$$

where $\mathbf{W}_i,\ i = 1, 2, 3$, are the first three rows of the transformation matrix $\mathbf{W}$ from the relative state to the vector of parameters (see Eq. (2.41)). The necessary and sufficient periodicity condition $d_0 = 0$ was deduced in [Deaconu13]. Note that the non-periodic terms, in the Keplerian-based relative motion, are premultiplied by d_0 (see Eq. (2.39)). Let recall that $\rho_\nu = 1 + e \cos \nu$.

However, Eq. (5.4) is inefficient to verify the membership of a periodic state $\mathbf{d}$ (with $d_0 = 0$) to the admissible set $\mathcal{S}_D$. In its current form, the inequalities should be evaluated over an entire orbital period of the leader. To overcome this issue, [Arantes-Gilz17] eliminated the dependence with the true anomaly by implicitizing the envelope of the inequalities arising in Eq. (5.4). The implicitization of trigonometric functions used [Hong95] method (see Appendix C for the details). Then, a state-dependent expression of the admissible set is available as

$$\mathcal{S}_D := \left\{ \mathbf{d} \in \mathbb{R}^6 \mid d_0 = 0,\ \mathbf{g}(\mathbf{d}) \leq \mathbf{0} \right\}, \tag{5.5}$$

where $\mathbf{g} = [g_{\underline{x}}, g_{\overline{x}}, g_{\underline{y}}, g_{\overline{y}}, g_{\underline{z}}, g_{\overline{z}}]^T$ is a vector composed of multivariate polynomials in the vector of parameters as follows

$$g_{\underline{x}}(d_1, d_2, d_3) = \sum_{i=0}^{6} \sum_{j=0}^{6} \sum_{k=0}^{4} \underline{\theta}_{ijk}(e, \underline{x}) d_1^i d_2^j d_3^k, \quad \underline{\theta}_{ijk} = 0 \text{ if } i + j + k > 6, \tag{5.6}$$

$$g_{\overline{x}}(d_1, d_2, d_3) = \sum_{i=0}^{6} \sum_{j=0}^{6} \sum_{k=0}^{4} \overline{\theta}_{ijk}(e, \overline{x}) d_1^i d_2^j d_3^k, \quad \overline{\theta}_{ijk} = 0 \text{ if } i + j + k > 6, \tag{5.7}$$

$$g_{\underline{y}}(d_4, d_5) = (d_4 - e\underline{y})^2 + d_5^2 - \underline{y}^2, \tag{5.8}$$

$$g_{\overline{y}}(d_4, d_5) = (d_4 - e\overline{y})^2 + d_5^2 - \overline{y}^2, \tag{5.9}$$

$$g_{\underline{z}}(d_1, d_2) = d_1^2 + d_2^2 - \underline{z}^2, \tag{5.10}$$

$$g_{\overline{z}}(d_1, d_2) = d_1^2 + d_2^2 - \overline{z}^2. \tag{5.11}$$

The degree of the multivariate polynomials $g_{\underline{x}}$ and $g_{\overline{x}}$ is 6 for both cases.

As given by Eq. (5.5) the admissible set implicitly describes the set of constrained periodic relative orbits within the cuboid limits $\{\underline{x}, \overline{x}, \underline{y}, \overline{y}, \underline{z}, \overline{z}\}$ in the vector of parameters space. This set is also a convex bounded set in the vector of parameters space.

5.3 Analysis of the admissible set reachability

In this section, the admissible set (composed of constrained relative periodic orbits) reachability, using a single-impulse control, is thoroughly analyzed. An adequate single-impulse structure, reaching a relative periodic orbit, is described. Then, the set of reachable states under that single-impulse is formally expressed. It is demonstrated that the intersection of the previous set of states with the admissible set determines reachability conditions for this last one. Moreover, by transcribing the reachability conditions to the control variables, useful proximity indicators can be derived. Finally, by exploiting the system periodicity, a region of attraction to the admissible set is found.

5.3.1 Instantaneous reachable set

Let define the instantaneous reachable set $\Delta^+_{\mathrm{dz/sat}}$ as the states which can be instantaneously reached through a constrained single-impulse (within dead-zone and saturation thresholds) at a given instant ν. In the Keplerian-based relative motion, out-of-plane $\{d_4, d_5\}$ and in-plane motions $\{d_0, d_1, d_2, d_3\}$ are decoupled (see Eq. (2.45)-(2.46)). The decoupling is also present in the admissible set (see Eq. (5.6)-(5.11)) due to the hovering region characterization (a cuboid with its sides parallel to LVLH axes). Due to the previous facts, the out-of-plane and in-plane motions are treated separately as

$$\Delta^+_{\mathrm{dz/sat}}(\mathbf{d},\nu) = \Delta^+_{\mathrm{dz/sat},xz}(\mathbf{d},\nu) \times \Delta^+_{\mathrm{dz/sat},y}(\mathbf{d}), \tag{5.12}$$

where $\Delta^+_{\mathrm{dz/sat},xz}$ and $\Delta^+_{\mathrm{dz/sat},y}$ are the in-plane and out-of-plane reachable sets which are described in the sequel.

Out-of-plane motion

Let define the out-of-plane state subset $\mathbf{d}_y = [d_4, d_5]^T$ which is naturally periodic as deduced from Eq. (2.45). When an out-of-plane impulse $\Delta V_y = \lambda_y \in \mathbb{R}$ (where λ_y is used for notation consistency with the in-plane case) is applied, the state instantaneously changes as

$$\mathbf{d}^+_y(\mathbf{d}_y,\nu,\lambda_y) = \mathbf{d}_y + \mathbf{B}_{D_y}(\nu)\lambda_y, \tag{5.13}$$

where $\mathbf{B}_{D_y} \in \mathbb{R}^2$ is extracted from the vector of parameters control matrix (see Eq. (2.61))

$$\mathbf{B}_{D_y}(\nu) = \frac{1}{k^2\rho_\nu}\begin{bmatrix} -\mathrm{s}_\nu \\ \mathrm{c}_\nu \end{bmatrix}, \tag{5.14}$$

where $k^2 = \sqrt{\mu/[a(1-e^2)]^3}$. Let recall that $\mathrm{c}_\nu = \cos\nu$, $\mathrm{s}_\nu = \sin\nu$ and $\rho_\nu = 1 + e\cos\nu$. Consequently, the out-of-plane impulse changes the state through the line Δ^+_y

$$\Delta^+_y(\mathbf{d}_y,\nu) := \left\{\mathbf{d}^+_y \in \mathbb{R}^2 \quad \middle| \quad \mathbf{d}^+_y(\mathbf{d}_y,\nu) = \mathbf{d}_y + \mathbf{B}_{D_y}(\nu)\lambda_y, \quad \lambda_y \in \mathbb{R}\right\}. \tag{5.15}$$

However, as per (5.1), the impulse amplitude is constrained due to dead-zone and saturation limits. These constraints are summarized in the set $\Xi_{\mathrm{dz/sat},y}$

$$\Xi_{\mathrm{dz/sat},y} := [-\overline{\Delta V}, -\underline{\Delta V}] \cup [\underline{\Delta V}, \overline{\Delta V}], \tag{5.16}$$

where the possibility of a null impulse has not been included due to its triviality. Then, the out-of-plane instantaneous reachable set is formally described as

$$\begin{aligned}\Delta^{+}_{\mathrm{dz/sat},y}(\mathbf{d}_y,\nu) := \{\mathbf{d}^{+}_{y} \in \mathbb{R}^2 \quad | \quad & \mathbf{d}^{+}_{y}(\mathbf{d}_y,\nu) = \mathbf{d}_y + \mathbf{B}_{D_y}(\nu)\lambda_y, \\ & \lambda_y \in \Xi_{\mathrm{dz/sat},y}\},\end{aligned} \tag{5.17}$$

which consists of two line segments in the out-of-plane state space.

In-plane motion

Let define the in-plane state subset $\mathbf{d}_{xz} = [d_0, d_1, d_2, d_3]^T$ and impulse $\Delta\mathbf{V}_{xz} = [\Delta V_x, \Delta V_z]^T$. The impulse produces the following jump in the state

$$\mathbf{d}^{+}_{xz}(\mathbf{d}_{xz}, \nu, \Delta\mathbf{V}_{xz}) = \mathbf{d}_{xz} + \mathbf{B}_{D_{xz}}(\nu)\Delta\mathbf{V}_{xz}. \tag{5.18}$$

The in-plane control matrix $\mathbf{B}_{D_{xz}} \in \times\mathbb{R}^{4\times 2}$ is extracted from the vector of parameters impulsive control matrix (see Eq. (2.61))

$$\mathbf{B}_{D_{xz}} = \frac{1}{k^2(e^2-1)\rho_\nu}\begin{bmatrix} \rho_\nu^2 & -e\mathrm{s}_\nu\rho_\nu \\ -2\mathrm{c}_\nu - e(1+\mathrm{c}_\nu^2) & \mathrm{s}_\nu\rho_\nu \\ -\mathrm{s}_\nu(2+e\mathrm{c}_\nu) & 2e - \mathrm{c}_\nu\rho_\nu \\ e\mathrm{s}_\nu(2+e\mathrm{c}_\nu) & e\mathrm{c}_\nu\rho_\nu - 2 \end{bmatrix}. \tag{5.19}$$

Let recall that the admissible set is composed of constrained relative periodic orbits. In order to insert the relative state into a periodic orbit, the in-plane control should steer to $d_0^+ = 0$ as

$$d_0^+(d_0, \nu, \Delta\mathbf{V}_{xz}) = d_0 + \mathbf{B}_{d_0,xz}(\nu)\Delta\mathbf{V}_{xz} = 0, \tag{5.20}$$

where

$$\mathbf{B}_{d_0,xz}(\nu) = \frac{1}{k^2(e^2-1)}\begin{bmatrix} \rho_\nu \\ -e\mathrm{s}_\nu \end{bmatrix}, \tag{5.21}$$

is the first row of the in-plane control matrix $\mathbf{B}_{D_{xz}}$ given by Eq. (5.19). To satisfy Eq. (5.20), the impulse should have the following structure

$$\Delta\mathbf{V}_{xz}(d_0, \nu, \lambda_{xz}) = \lambda_{xz}\mathbf{B}^{\perp}_{d_0,xz}(\nu) + \Delta\mathbf{V}^0_{xz}(d_0,\nu), \tag{5.22}$$

where $\lambda_{xz} \in \mathbb{R}$ is the in-plane control variable (a degree of freedom is lost in order to enforce the periodicity condition). The vector $\mathbf{B}^{\perp}_{d_0,xz}$ is perpendicular (kernel space) to $\mathbf{B}_{d_0,xz}$ while $\Delta\mathbf{V}^0_{xz} \in \mathbb{R}^2$ is any particular solution of Eq. (5.20)

$$\mathbf{B}^{\perp}_{d_0,xz}(\nu) = \frac{1}{1+e^2+2e\mathrm{c}_\nu}\begin{bmatrix} e\mathrm{s}_\nu \\ \rho_\nu \end{bmatrix}, \quad \Delta\mathbf{V}^0_{xz}(d_0,\nu) = -d_0\mathbf{B}^{+}_{d_0,xz}(\nu), \tag{5.23}$$

where $\|\mathbf{B}^{\perp}_{d_0,xz}\|_2 = 1$ has been chosen as a unit vector and $\Delta\mathbf{V}^0_{xz}$ is obtained through the pseudoinverse of $\mathbf{B}_{d_0,xz}$. The pseudoinverse $\mathbf{B}^{+}_{d_0,xz}$ is always defined for closed leader orbits as the first term of $\mathbf{B}_{d_0,xz}$ is always negative such that $\rho_\nu/[k^2(e^2-1)] < 0$ for $e \in [0,1)$ and $\nu \in [0, 2\pi]$.

Inserting the periodicity-pursuing, $d_0^+ = 0$, strategy given by Eq. (5.22) into Eq. (5.18) yields

$$\mathbf{d}^{+}_{xz}(\mathbf{d}_{xz}, \nu, \lambda_{xz}) = \mathbf{d}_{xz} + \mathbf{B}_{D_{xz}}(\nu)[\lambda_{xz}\mathbf{B}^{\perp}_{d_0,xz}(\nu) + \Delta\mathbf{V}^0_{xz}(d_0,\nu)]. \tag{5.24}$$

Under Eq. (5.24), the in-plane instantaneous reachable set, without accounting for dead-zone and saturation, is described by

$$\begin{aligned}\Delta^{+}_{xz}(\mathbf{d}_{xz},\nu) := \{\mathbf{d}_{xz} \in \mathbb{R}^4 \ \mid \ \mathbf{d}^{+}_{xz} = \mathbf{d}_{xz} + \mathbf{B}_{D_{xz}}(\nu)[\lambda_{xz}\mathbf{B}^{\perp}_{d_0,xz}(\nu) \\ + \Delta\mathbf{V}^0_{xz}(d_0,\nu)], \quad \lambda_{xz} \in \mathbb{R}\}.\end{aligned} \tag{5.25}$$

The in-plane dead-zone and saturation thresholds can be described through the following set

$$\begin{aligned}\Xi_{\mathrm{dz/sat},xz}(d_0,\nu) :=& \{\lambda_{xz} \in \mathbb{R} \ \mid \ \underline{\Delta V} \leq \|\lambda_{xz}\mathbf{B}^{\perp}_{d_0,xz}(\nu) + \Delta\mathbf{V}^0_{xz}(d_0,\nu)\|_2 \\ & \leq \overline{\Delta V}\} = [\overline{\lambda}_{xz,1}, \underline{\lambda}_{xz,1}] \cup [\underline{\lambda}_{xz,2}, \overline{\lambda}_{xz,2}],\end{aligned} \tag{5.26}$$

where $\overline{\lambda}_{xz,1}$, $\underline{\lambda}_{xz,1}$, $\underline{\lambda}_{xz,2}$ and $\overline{\lambda}_{xz,2}$ are given by

$$\begin{aligned}\underline{\lambda}_{xz,1},\ \underline{\lambda}_{xz,2} =& -(\mathbf{B}^{\perp}_{d_0,xz})^T\Delta\mathbf{V}^0_{xz} \\ & \pm\sqrt{\left[(\mathbf{B}^{\perp}_{d_0,xz})^T\Delta\mathbf{V}^0_{xz}\right]^2 - \|\Delta\mathbf{V}^0_{xz}\|_2^2 + \underline{\Delta V}^2},\end{aligned} \tag{5.27}$$

$$\begin{aligned}\overline{\lambda}_{xz,1},\ \overline{\lambda}_{xz,2} =& -(\mathbf{B}^{\perp}_{d_0,xz})^T\Delta\mathbf{V}^0_{xz} \\ & \pm\sqrt{\left[(\mathbf{B}^{\perp}_{d_0,xz})^T\Delta\mathbf{V}^0_{xz}\right]^2 - \|\Delta\mathbf{V}^0_{xz}\|_2^2 + \overline{\Delta V}^2}.\end{aligned} \tag{5.28}$$

The dependencies with ν and d_0 have been omitted in Eq. (5.27)-(5.28) for the sake of clarity. Inserting the dead-zone and saturation constraints set given by Eq. (5.26) into Eq. (5.25), a formal description of the in-plane instantaneous reachable set is obtained

$$\begin{aligned}\Delta^{+}_{\mathrm{dz/sat},xz}(\mathbf{d}_{xz},\nu) := \{\mathbf{d}_{xz} \in \mathbb{R}^4 \ \mid \ \mathbf{d}^{+}_{xz} = \mathbf{d}_{xz} + \mathbf{B}_{D_{xz}}(\nu)[\lambda_{xz}\mathbf{B}^{\perp}_{d_0,xz}(\nu) \\ + \Delta\mathbf{V}^0_{xz}(d_0,\nu)], \quad \lambda_{xz} \in \Xi_{\mathrm{dz/sat},xz}(d_0,\nu)\},\end{aligned} \tag{5.29}$$

which consists of two line segments in the in-plane state space.

5.3.2 Admissible set reachability

The necessary and sufficient condition to instantaneously reach the admissible set is

$$\Gamma^{+}_{\mathrm{dz/sat}}(\mathbf{d},\nu) = \Gamma^{+}_{\mathrm{dz/sat},xz}(\mathbf{d}_{xz},\nu) \times \Gamma^{+}_{\mathrm{dz/sat},y}(\mathbf{d}_y,\nu) \neq \emptyset, \tag{5.30}$$

where

$$\Gamma^+_{\mathrm{dz/sat},xz}(\mathbf{d}_{xz},\nu) = \Delta^+_{\mathrm{dz/sat},xz}(\mathbf{d}_{xz},\nu) \cap \mathcal{S}_{D_{xz}}, \tag{5.31}$$

$$\Gamma^+_{\mathrm{dz/sat},y}(\mathbf{d}_{y},\nu) = \Delta^+_{\mathrm{dz/sat},y}(\mathbf{d}_{y},\nu) \cap \mathcal{S}_{D_{y}}. \tag{5.32}$$

Note that $\mathcal{S}_{D_{xz}}$ and $\mathcal{S}_{D_y}$ are the projections of the admissible set into the in-plane and out-of-plane space respectively. The sets $\Gamma^+_{\mathrm{dz/sat},xz}$ and $\Gamma^+_{\mathrm{dz/sat},y}$ are formed by the intersection of the in-plane and out-of-plane instantaneous reachable sets with their respective admissible set projections. Since the instantaneous reachable sets were demonstrated to be straight lines segments as per Eq. (5.17) and Eq. (5.29), and the admissible set projections are convex and bounded (as the admissible set is), the sets $\Gamma^+_{\mathrm{dz/sat},xz}$ and $\Gamma^+_{\mathrm{dz/sat},y}$ are concluded to be composed of line segments if non empty. These line segments are parameterized in terms of the control variables λ_{xz} and λ_y respectively. To obtain a tractable form of the line segments $\Gamma^+_{\mathrm{dz/sat},xz}$ and $\Gamma^+_{\mathrm{dz/sat},y}$, let define the following sets

$$\Gamma^+_{xz}(\mathbf{d}_{xz},\nu) = \Delta^+_{xz}(\mathbf{d}_{xz},\nu) \cap \mathcal{S}_{D_{xz}}, \tag{5.33}$$

$$\Gamma^+_{y}(\mathbf{d}_{y},\nu) = \Delta^+_{y}(\mathbf{d}_{y},\nu) \cap \mathcal{S}_{D_{y}}, \tag{5.34}$$

where each one of them is a line segment as formed by the intersection of a line, Δ^+_{xz} and Δ^+_y, with a convex bounded set, $\mathcal{S}_{D_{xz}}$ and $\mathcal{S}_{D_y}$, respectively. The existence of the previous intersections is a necessary condition for the admissible set instantaneous reachability. The intersections described in Eq. (5.33)-(5.34) can be equivalently transcribed in terms of a seminegativity condition for the admissible set multivariate polynomials of Eq. (5.6)-(5.11)

$$\begin{aligned} &\Gamma^+_{xz}(\mathbf{d}_{xz},\nu) := \\ &\{\mathbf{d}^+_{xz} \in \mathbb{R}^4 \ \mid \ \mathbf{d}^+_{xz} = \mathbf{d}_{xz} + \mathbf{B}_{D_{xz}}(\nu)[\lambda_{xz}\mathbf{B}^{\perp}_{d_0,xz}(\nu) + \Delta\mathbf{V}^0_{xz}(d_0,\nu)], \\ &g_{\underline{x}}(\mathbf{d}^+_{xz}) \le 0,\ g_{\overline{x}}(\mathbf{d}^+_{xz}) \le 0,\ g_{\underline{z}}(\mathbf{d}^+_{xz}) \le 0,\ g_{\overline{z}}(\mathbf{d}^+_{xz}) \le 0,\ \lambda_{xz} \in \mathbb{R}\}, \end{aligned} \tag{5.35}$$

$$\begin{aligned} \Gamma^+_{y}(\mathbf{d}_{y},\nu) := \{\mathbf{d}^+_{y} \in \mathbb{R}^2 \ \mid \ &\mathbf{d}^+_{y} = \mathbf{d}_{y} + \mathbf{B}_{D_{y}}(\nu)\lambda_y,\ g_{\underline{y}}(\mathbf{d}^+_{y}) \le 0, \\ &g_{\overline{y}}(\mathbf{d}^+_{y}) \le 0,\ \lambda_y \in \mathbb{R}\}, \end{aligned} \tag{5.36}$$

which are single line segments if non-empty. If Γ^+_{xz} and Γ^+_y are evaluated for a given instant ν and a state $\mathbf{d}$, the only free parameters would be the control variables λ_{xz} and λ_y which can be explicitly inserted into the polynomials

$$\begin{aligned} \Gamma^+_{xz} := \{\mathbf{d}^+_{xz} \in \mathbb{R}^4 \ \mid \ &\mathbf{d}^+_{xz}(\lambda_{xz}) = \mathbf{d}_{xz} + \mathbf{B}_{D_{xz}}(\lambda_{xz}\mathbf{B}^{\perp}_{d_0,xz} + \Delta\mathbf{V}^0_{xz}), \\ &g_{\underline{x}}(\mathbf{d}^+_{xz}(\lambda_{xz})) \le 0,\ g_{\overline{x}}(\mathbf{d}^+_{xz}(\lambda_{xz})) \le 0,\ g_{\underline{z}}(\mathbf{d}^+_{xz}(\lambda_{xz})) \le 0, \\ &g_{\overline{z}}(\mathbf{d}^+_{xz}(\lambda_{xz})) \le 0,\ \lambda_{xz} \in \mathbb{R}\}, \end{aligned} \tag{5.37}$$

$$\begin{aligned} \Gamma^+_{y} := \{\mathbf{d}^+_{y} \in \mathbb{R}^2 \ \mid \ &\mathbf{d}^+_{y}(\lambda_y) = \mathbf{d}_{y} + \mathbf{B}_{D_{y}}\lambda_y,\ g_{\underline{y}}(\mathbf{d}^+_{y}(\lambda_y)) \le 0, \\ &g_{\overline{y}}(\mathbf{d}^+_{y}(\lambda_y)) \le 0,\ \lambda_y \in \mathbb{R}\}, \end{aligned} \tag{5.38}$$

thus, Eq. (5.6)-(5.11) multivariate polynomials are reduced to univariate polynomials in terms of λ_{xz} and λ_y respectively.

From the control perspective, it is convenient to describe the instantaneous reachability conditions in terms of the control variables $(\lambda_{xz}, \lambda_y)$ instead of the reachable states $(\mathbf{d}^+)$. Inserting the state jumps of Eq. (5.24) and Eq. (5.13) into Eq. (5.6)-(5.11), the following intervals are defined

$$\begin{aligned}\Lambda_{xz} := \{\lambda_{xz} \in \mathbb{R} \mid\ & g_{\underline{x}}(\lambda_{xz}) \leq 0,\ g_{\overline{x}}(\lambda_{xz}) \leq 0,\ g_{\underline{z}}(\lambda_{xz}) \leq 0, \\ & g_{\overline{z}}(\lambda_{xz}) \leq 0\} = [\underline{l}_{xz}, \bar{l}_{xz}],\end{aligned} \tag{5.39}$$

$$\Lambda_y := \{\lambda_y \in \mathbb{R} \mid g_{\underline{y}}(\lambda_y) \leq 0,\ g_{\overline{y}}(\lambda_y) \leq 0\} = [\underline{l}_y, \bar{l}_y], \tag{5.40}$$

which are intervals filled by the control variables guaranteeing the admissible set instantaneous reachability from a given state and instant. Consequently, the non-emptiness of the intervals Λ_{xz} and Λ_y is a neccesary condition for the admissible set instantaneous reachability.

Remark 5.1: *if non-empty, the connectedness of the intervals* Λ_{xz}, Λ_y *and consequently of the sets* Γ^+_{xz} *and* Γ^+_y *is ensured by the convexity of* $\mathcal{S}_D$.

The intervals extrema $\underline{l}_{xz}$, $\bar{l}_{xz}$, $\underline{l}_y$, $\bar{l}_y$ can be obtained by computing and pruning the roots of Eq. (5.39)-(5.40) univariate polynomials. Specifically, the out-of-plane ($g_{\underline{y}}$, $g_{\overline{y}}$) and radial ($g_{\underline{z}}$, $g_{\overline{z}}$) polynomials are quadratic with respect to λ_y and λ_{xz} respectively. The in-track polynomials ($g_{\underline{x}}$, $g_{\overline{x}}$) are sextic with respect to λ_{xz}. Accordingly, if Eq. (5.24) and Eq. (5.13) control lines intersect the admissible set, such that $\Gamma^+_{xz} \neq \emptyset$ and $\Gamma^+_y \neq \emptyset$, then the existence of two real roots for each polynomial is ensured. Note that in the state space, the admissible set is convex and the reachable states (unconstrained) form a straight line. This justifies the Remark 5.1. On the contrary, the absence of real roots, for any of the polynomials, reveals that either $\Gamma^+_{xz} = \emptyset$ or $\Gamma^+_y = \emptyset$. In that case, the admissible set is instantaneously unreachable due to the relative geometry between the current state, the control line and the admissible set (regardless of the dead-zone and saturation thresholds).

Taking into account the control dead-zone and saturation sets ($\Lambda_{\mathrm{dz/sat},xz}$ and $\Lambda_{\mathrm{dz/sat},y}$ as per Eq. (5.26) and Eq. (5.16) respectively), the intersections defined in Eq. (5.37)-(5.38) are modified as

$$\begin{aligned}\Gamma^+_{\mathrm{dz/sat},xz} := \{\mathbf{d}^+_{xz} \in \mathbb{R}^4 \mid\ & \mathbf{d}^+_{xz}(\lambda_{xz}) = \mathbf{d}_{xz} + \mathbf{B}_{D_{xz}}(\lambda_{xz}\mathbf{B}^{\perp}_{d0,xz} \\ & + \Delta\mathbf{V}^0_{xz}),\ g_{\underline{x}}(\mathbf{d}^+_{xz}(\lambda_{xz})) \leq 0,\ g_{\overline{x}}(\mathbf{d}^+_{xz}(\lambda_{xz})) \leq 0, \\ & g_{\underline{z}}(\mathbf{d}^+_{xz}(\lambda_{xz})) \leq 0,\ g_{\overline{z}}(\mathbf{d}^+_{xz}(\lambda_{xz})) \leq 0,\ \lambda_{xz} \in \Xi_{\mathrm{dz/sat},xz}\},\end{aligned} \tag{5.41}$$

$$\begin{aligned}\Gamma^+_{\mathrm{dz/sat},y} := \{\mathbf{d}^+_y \in \mathbb{R}^2 \mid\ & \mathbf{d}^+_y(\lambda_y) = \mathbf{d}_y + \mathbf{B}_{D_y}\lambda_y,\ g_{\underline{y}}(\mathbf{d}^+_y(\lambda_y)) \leq 0, \\ & g_{\overline{y}}(\mathbf{d}^+_y(\lambda_y)) \leq 0,\ \lambda_y \in \Xi_{\mathrm{dz/sat},y}\},\end{aligned} \tag{5.42}$$

which correspond to the sets of the necessary and sufficient condition for the admissible set instantaneous reachability (see Eq. (5.30)).

The control variables, within dead-zone and saturation thresholds, enabling the admissible set instantaneous reachability are obtained as

$$\Lambda_{\mathrm{dz/sat},xz} = \Lambda_{xz} \cap \Xi_{\mathrm{dz/sat},xz} = [\lambda_{xz,1}, \lambda_{xz,2}] \cup [\lambda_{xz,3}, \lambda_{xz,4}], \tag{5.43}$$

$$\Lambda_{\mathrm{dz/sat},y} = \Lambda_{y} \cap \Xi_{\mathrm{dz/sat},y} = [\lambda_{y,1}, \lambda_{y,2}] \cup [\lambda_{y,3}, \lambda_{y,4}], \tag{5.44}$$

which are non-connected intervals in general. They result from the intersection of the connected intervals Λ_{xz} and Λ_{y} (see Eq. (5.39)-(5.40)) with the non connected dead-zone and saturation intervals $\Xi_{\mathrm{dz/sat},xz}$ and $\Xi_{\mathrm{dz/sat},y}$ given by Eq. (5.26) and Eq.(5.16) respectively. Then the sufficient condition of Eq. (5.30) for the admissible set instantaneous reachability can be equivalently expressed, in terms of the control variables, as

$$\Delta^{+}_{\mathrm{dz/sat}}(\mathbf{d}, \nu) \neq \emptyset \iff \Lambda_{\mathrm{dz/sat}}(\mathbf{d}, \nu) \neq \emptyset, \tag{5.45}$$

where

$$\Lambda_{\mathrm{dz/sat}}(\mathbf{d}, \nu) = \Lambda_{\mathrm{dz/sat},xz}(\mathbf{d}_{xz}, \nu) \times \Lambda_{\mathrm{dz/sat},y}(\mathbf{d}_{y}, \nu). \tag{5.46}$$

To resume, the non-emptiness of the non-connected intervals $\Lambda_{\mathrm{dz/sat},xz}$ and $\Lambda_{\mathrm{dz/sat},y}$ is assessed through the intersection of the univariate polynomials $\{g_{\underline{x}}, g_{\overline{x}}, g_{\underline{y}}, g_{\overline{y}}, g_{\underline{z}}, g_{\overline{z}}\}$ real roots intervals, if any, with dead-zone and saturation intervals. If the previous intersection does exist, then, there are control variables, within dead-zone and saturation thresholds, that can be employed to instantaneously reach the admissible set with a single-impulse.

5.3.3 Admissible set proximity

The necessary and sufficient admissible set instantaneous reachability condition has been formally defined in Eq. (5.45). However, it may be of interest to quantify the proximity of the admissible set in terms of control. Such indicator would allow to tune the controller reactivity (e.g. do not apply a control until the reachability window is near to be closed). A direct choice for the admissible set proximity indicator is to measure the length of the non-connected intervals $\Lambda_{\mathrm{dz/sat},xz}$ and $\Lambda_{\mathrm{dz/sat},y}$ (see Eq. (5.43)-(5.44))

$$\begin{aligned} L_{xz}(\mathbf{d}, \nu) =& |\lambda_{xz,2} - \lambda_{xz,1}| + |\lambda_{xz,4} - \lambda_{xz,3}|, \\ L_{y}(\mathbf{d}, \nu) =& |\lambda_{y,2} - \lambda_{y,1}| + |\lambda_{y,4} - \lambda_{y,3}|. \end{aligned} \tag{5.47}$$

The state and instant dependencies has been omitted at the right-hand side for the sake of clarity. When these lengths are large, it means there is a huge range of controls enabling the admissible set instantaneous reachability. This offers the possibility to delay the control action (which may be of interest if the number of impulses is to be minimized) if the indicators are continuous functions. On the other hand, when these lengths are small, it means there are few control possibilities that could vanish in the near future. Under the previous fact, it is evident that monitoring the proximity indicator helps to command an optimal control decision.

Additionally, the instantaneous reachability condition can also be expressed in terms of the lengths L_{xz} and L_y as

$$L_{xz}(\mathbf{d}_{xz},\nu) \neq 0 \wedge L_y(\mathbf{d}_y,\nu) \neq 0 \iff \Lambda_{\mathrm{dz/sat}}(\mathbf{d},\nu) \neq \emptyset. \tag{5.48}$$

Nonetheless, the lengths (L_{xz}, L_y) of the non-connected intervals $\Lambda_{\mathrm{dz/sat},xz}$ and $\Lambda_{\mathrm{dz/sat},y}$ are not well-posed proximity indicators (though very intuitive). As a matter of fact, they may suffer discontinuities over time which may compromise the impulse delay strategy. The explanation is that the admissible set $\mathcal{S}_D$, though being a convex bounded set, is defined as the interior region resulting from the intersections of several semi-algebraic sets described as multivariate polynomials in the state space (see Eq. (5.6)-(5.11)). Therefore, $\mathcal{S}_D$ has several edges and vertexes where the disjoint lines $\Gamma^+_{\mathrm{dz/sat},xz}$ and $\Gamma^+_{\mathrm{dz/sat},xz}$ may instantaneously vanish in a discontinuous manner. As a consequence, the lengths L_{xz} and L_y are not guaranteed to be continuous functions. To overcome this issue, the subsequent proximity indicators (G_{xz}, G_y) and its derivatives with respect to the true anomaly $(G_{\nu,xz}$, $G_{\nu,y})$ are defined as

$$\begin{aligned} G_{xz}(\mathbf{d}_{xz},\nu) &= \begin{cases} \max\{g^*_{\underline{x}}, g^*_{\overline{x}}, g^*_{\underline{z}}, g^*_{\overline{z}}\}, & \text{if } \ L_{xz} > 0, \\ 0, & \text{if } \ L_{xz} = 0, \end{cases} \\ G_{\nu,xz}(\mathbf{d}_{xz},\nu) &= \frac{dG_{xz}}{d\nu}, \end{aligned} \tag{5.49}$$

$$\begin{aligned} G_{y}(\mathbf{d}_{y},\nu) &= \begin{cases} \max\{g^*_{\underline{y}}, g^*_{\overline{y}}\}, & \text{if } \ L_{y} > 0, \\ 0, & \text{if } \ L_{y} = 0, \end{cases} \\ G_{\nu,y}(\mathbf{d}_{y},\nu) &= \frac{dG_{y}}{d\nu}, \end{aligned} \tag{5.50}$$

where the dependencies with the current state and instant has been omitted at the right-hand side (and they will be frequently omitted in this paragraph for that reason). The variables $\{g^*_{\underline{x}}, g^*_{\overline{x}}, g^*_{\underline{y}}, g^*_{\overline{y}}, g^*_{\underline{z}}, g^*_{\overline{z}}\}$ are defined as follows

$$\begin{aligned} g^*_{\underline{x}} &= \min_{\lambda_{xz}} \ g_{\underline{x}}(\lambda_{xz}) \ \text{ s.t. } \ \lambda_{xz} \in \Lambda_{\mathrm{dz/sat},xz}, \\ g^*_{\overline{x}} &= \min_{\lambda_{xz}} \ g_{\overline{x}}(\lambda_{xz}) \ \text{ s.t. } \ \lambda_{xz} \in \Lambda_{\mathrm{dz/sat},xz}, \end{aligned} \tag{5.51}$$

$$\begin{aligned} g^*_{\underline{y}} &= \min_{\lambda_{y}} \ g_{\underline{y}}(\lambda_{y}) \ \text{ s.t. } \ \lambda_{y} \in \Lambda_{\mathrm{dz/sat},y}, \\ g^*_{\overline{y}} &= \min_{\lambda_{y}} \ g_{\overline{y}}(\lambda_{y}) \ \text{ s.t. } \ \lambda_{y} \in \Lambda_{\mathrm{dz/sat},y}, \end{aligned} \tag{5.52}$$

$$\begin{aligned} g^*_{\underline{z}} &= \min_{\lambda_{xz}} \ g_{\underline{z}}(\lambda_{xz}) \ \text{ s.t. } \ \lambda_{xz} \in \Lambda_{\mathrm{dz/sat},xz}, \\ g^*_{\overline{z}} &= \min_{\lambda_{xz}} \ g_{\overline{z}}(\lambda_{xz}) \ \text{ s.t. } \ \lambda_{xz} \in \Lambda_{\mathrm{dz/sat},xz}, \end{aligned} \tag{5.53}$$

thus $\{g^*_{\underline{x}}, g^*_{\overline{x}}, g^*_{\underline{y}}, g^*_{\overline{y}}, g^*_{\underline{z}}, g^*_{\overline{z}}\}$ are the minimum values of the univariate polynomials, resulting from the insertion of the expressions for the state after the impulse (see Eq. (5.13) and Eq. (5.18)) into the admissible set description of Eq. (5.6)-(5.11). More precisely, the minimums are computed as

$$\begin{aligned} &g^*_{(\cdot)} = g_{(\cdot)}(\lambda^*_{(\cdot)}), \\ &\lambda^*_{(\cdot)} = \begin{cases} \left.\dfrac{dg_{(\cdot)}}{d\lambda_{(\cdot)}}\right|_{\lambda_{(\cdot)}=\lambda^*_{(\cdot)}} = 0, & \text{if } \lambda^*_{(\cdot)} \in \Lambda_{\mathrm{dz/sat},(\cdot)}, \\ \min\{\lambda_{(\cdot),1}, \lambda_{(\cdot),2}, \lambda_{(\cdot),3}, \lambda_{(\cdot),4}\}, & \text{if } \lambda^*_{(\cdot)} \notin \Lambda_{\mathrm{dz/sat},(\cdot)}, \end{cases} \end{aligned} \tag{5.54}$$

which has been presented in a generic form. Note that the derivative of the univariate polynomials with respect to the control variables is a polynomial with one degree less (e.g. straight lines equations for the out-of-plane and radial constraints). Under the previous definitions, the admissible set proximity indicators G_{xz} and G_y are guaranteed to be continuous functions over time. As such, they are well-posed indicators because they can capture the last control opportunity to instantaneously reach the admissible set. However, the proximity indicators derivatives $G_{\nu,xz}$ and $G_{\nu,y}$ are not continuous functions due to the max operator defining G_{xz} and G_y in Eq. (5.49)-(5.50).

In order to clarify the previous concepts, a sketch in the in-plane state subset $d_0d_2d_3$ space is presented in Fig. 5.2. In that figure, the current state is considered to be quasi-periodic, $|d_0| \approx 0$. This assumption simplifies the analysis because the state evolution would be slow enough to consider the state invariant over one leader orbital period (let recall the vector of relative parameters state transition as per Eq. (2.47))

$$|d_0| \approx 0 \longrightarrow \mathbf{d}(\nu_0) \approx \mathbf{d}(\nu_0 + \Delta\nu), \;\; \Delta\nu \in [0, 2\pi]. \tag{5.55}$$

The quasi-periodic state hypothesis removes the problem dependency with the state as it remains invariant over time. Consequently, the current instant ν is the only free parameter that arises through the control matrix $B_D(\nu)$ (see Eq. (5.18) and Eq. (5.13)). This assumption is supported by the hovering problem (see problem (5.1)) where it is expected that the spacecraft is close to a periodic orbit within the hovering region. Alternatively, if the control goal is to reach the hovering region from a distant position (which is not the problem under consideration), the quasi-periodic assumption would not be valid in general. Returning to the sketch of Fig. 5.2, a quasi-periodic state out of the admissible set is shown as a white dot. The term $\Delta\mathbf{V}^0_{xz}$ of the applied impulse drives the state to the $d_0 = 0$ plane (black dot). From that point, the remaining impulse part, $\lambda_{xz}\mathbf{B}^{\perp}_{d_0,xz}$, allows the state to change along the straight lines Δ^+_{xz}. The intersection of these lines with the admissible set projection in d_2d_3 evidences the possibility of instantaneous reachability. Taking into account impulse dead-zone and saturation thresholds, the reachable sets are reduced to $\Delta^+_{\mathrm{dz/sat}}$. The intersection length of these line segments with the admissible set yields the proximity indicator L_{xz}. An option to instantaneously reach the admissible set would be to choose a point within that intersection (e.g. the black star) and jump to it with $\Delta\mathbf{d} = \Delta\mathbf{V}^0_{xz} + \lambda_{xz}\mathbf{B}^{\perp}_{d_0,xz}$.

Additionally, three different situations at instants $\nu_1 < \nu_2 < \nu_3$, after achieving $d_0 = 0$ by the impulse periodicity component, are analyzed. It is evident that $L_{xz}(\mathbf{d}_{xz}, \nu_1) > L_{xz}(\mathbf{d}_{xz}, \nu_2) > L_{xz}(\mathbf{d}_{xz}, \nu_3) = 0$. Equivalently, it can be deduced that $G_{xz}(\mathbf{d}_{xz}, \nu_1) < G_{xz}(\mathbf{d}_{xz}, \nu_2) < G_{xz}(\mathbf{d}_{xz}, \nu_3) = 0$. This shows that the admissible set is instantaneously reachable at instants ν_1 and ν_2 but it is unreachable at instant ν_3. Let assume that ν_3 is the current instant which lacks admissible set instantanous reachability. Under the previous quasi-periodic assumption, if one looks ahead at future instants within a target orbital period, it will be deduced that $L_{xz}(\nu_1 + 2\pi) \approx L_{xz}(\nu_1) > 0$ and $L_{xz}(\nu_2 + 2\pi) \approx L_{xz}(\nu_2) > 0$. In a general form, $L_{xz}(\nu) \approx L_{xz}(\nu + 2\pi)$ $(G_{xz}(\nu) \approx G_{xz}(\nu + 2\pi))$ due to the control matrix periodicity, $B_D(\nu) = B_D(\nu + 2\pi)$ (see Eq. (2.46)). This periodicity is extended to the reachable sets as $\Delta^+_{\mathrm{dz/sat}}(\nu) \equiv \Delta^+_{\mathrm{dz/sat}}(\nu + 2\pi)$. It can be concluded that, even if the admissible set is instantaneously unreachable, future reachability opportunities (if any) could be predicted by exploiting the periodicity of the system. This fact can be exploited to safely delay a control action by knowing that a window of single-impulse control opportunities will open in the future. The previous deductions also apply to the out-of-plane motion which is naturally periodic, $\mathbf{d}_y(\nu) = \mathbf{d}_y(\nu + 2\pi)$.

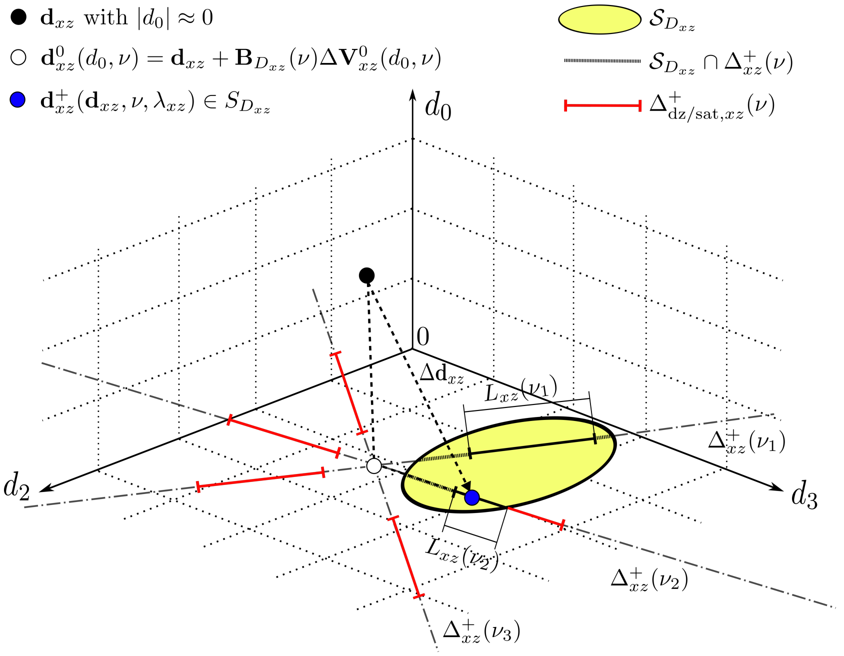

Figure 5.2: Sketch of the in-plane instantaneous reachability and proximity.

5.3.4 Region of attraction to the admissible set

In Section 5.3.1, the reachable set (with a single-impulse) was exploited to derive the admissible set instantaneous reachability conditions and its associated proximity indicators. Moreover, under the quasi-periodic state assumption, the admissible set instantaneous reachability and proximity indicators were demonstrated to be periodic over the next leader orbital period. As such, the set of states allowing the admissible set instantaneous reachability over a leader orbital period can be seen as a region of attraction to the admissible set. Let define the admissible set region of attraction $\mathcal{D}$ as

$$\mathcal{D} = \mathcal{D}_{xz} \times \mathcal{D}_y, \tag{5.56}$$

where its projections into the in-plane and out-of-plane state spaces are formally defined as

$$\mathcal{D}_{xz} := \left\{ \mathbf{d}_{xz} \in \mathbb{R}^4 : \ \mathbf{d}_{xz} \notin \mathcal{S}_{D_{xz}}, \ \frac{1}{2\pi} \int_{\nu}^{\nu+2\pi} L_{xz}(\mathbf{d}_{xz}(\tau), \tau) d\tau > 0 \right\}, \tag{5.57}$$

$$\mathcal{D}_y := \left\{ \mathbf{d}_y \in \mathbb{R}^2 : \ \mathbf{d}_y \notin \mathcal{S}_{D_y}, \ \frac{1}{2\pi} \int_{\nu}^{\nu+2\pi} L_y(\mathbf{d}_y, \tau) d\tau > 0 \right\}, \tag{5.58}$$

which means that a state belongs to the region of attraction if there exists a time window over the next leader orbital period where the admissible set is instantaneously reachable. Note that, even with the quasi-periodic assumption, the in-plane state variation when $d_0 \neq 0$ has been considered in Eq. (5.57). The region of attraction $\mathcal{D}$ to the admissible set is of interest for the event-based predictive controller that will be designed in the sequel. This is due to the fact that if the spacecraft state is within the region of attraction, then it is guaranteed that it could instantaneously reach the admissible set in a finite period of time (a leader orbital period at most) even if at the current instant the admissible set is not reachable. This conclusion is highlighted in Fig. 5.3 which shows the periodic control range (Δ^+ lines in the $\mathbf{d}$ space) for a state in the region of attraction. It can be easily seen that a range of single-impulse controls is able to intersect the admissible set (black region) while the remaining control range is unable to intersect it.

Equations (5.56)-(5.58) can be summarized to provide the necessary and sufficient condition for a state $\mathbf{d}$ to belong to the attractive set $\mathcal{D}$

$$\int_{\nu}^{\nu+2\pi} L_{xz}(\mathbf{d}_{xz}(\tau), \tau) d\tau > 0 \ \wedge \ \int_{\nu}^{\nu+2\pi} L_y(\mathbf{d}_y, \tau) d\tau > 0 \Longleftrightarrow D \in \mathcal{D}. \tag{5.59}$$

In order to obtain a computational tractable form of the integrals arising

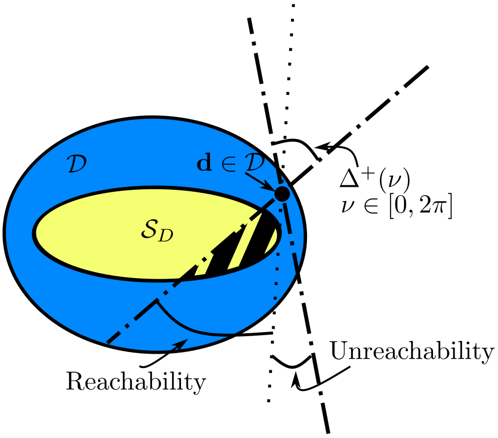

Figure 5.3: Sketch of the region of attraction to the admissible set.

in Eq. (5.59), these are discretized as follows

$$\frac{1}{2\pi}\int_{\nu}^{\nu+2\pi} L_{xz}(\mathbf{d}_{xz}(\tau),\tau)d\tau \approx \sum_{i=1}^{n_\nu} L_{xz}(\mathbf{d}_{xz}(\nu_i),\nu_i), \tag{5.60}$$

$$\frac{1}{2\pi}\int_{\nu}^{\nu+2\pi} L_{y}(\mathbf{d}_{y},\tau)d\tau \approx \sum_{i=1}^{n_\nu} L_{y}(\mathbf{d}_{y},\nu_i), \tag{5.61}$$

where $\nu_i = \nu + 2\pi/n_\nu$, $n_\nu \in \mathbb{N}$. Using the previous approximation, the necessary and sufficient condition for a state to be in the region of attraction (see Eq. (5.59)) boils down to

$$\sum_{i=1}^{n_\nu} L_{xz}(\mathbf{d}_{xz}(\nu_i),\nu_i) > 0 \ \wedge \ \sum_{i=1}^{n_\nu} L_{y}(\mathbf{d}_{y},\nu_i) > 0 \iff \mathbf{d} \in \mathcal{D}, \tag{5.62}$$

which is the expression employed in the subsequent event-based predictive controller.

5.4 Event-based predictive controller

The analysis of the admissible set reachability in Section 5.3 is used for the design of an event-based predictive controller. This controller is based on the computation of a single-impulse control with associated trigger rules. The single-impulse control law computation is highly efficient (from a computational perspective) since it only requires a finite number of objective function evaluations. Then, by using the concepts of admissible set reachability, proximity and region of attraction, the trigger rules are properly defined. These ensure the feasibility of the single-impulse control computation when triggered.

5.4.1 Single-impulse control law

In the previous developments, it was exploited that, under Keplerian linear relative dynamics, the out-of-plane and in-plane motions are decoupled. In principle, the computation of a single-impulse control can be treated separately for each case. However, in the case that both in-plane and out-of-plane controls are required at the same time, their coupling (through the impulse amplitude constraints) has to be considered.

Out-of-plane control

In order to instantaneously steer the state subset $\mathbf{d}_y$ into the out-of-plane admissible set $\mathcal{S}_{D_y}$ at a given instant ν, the following program is considered

$$\begin{aligned} \underset{\lambda_y}{\text{minimize}} \quad & |\Delta V_y|, \\ \text{subject to} \quad & \mathbf{d}_y^+ = \mathbf{d}_y + \mathbf{B}_{D_y}(\nu)\Delta V_y, \\ & \mathbf{d}_y^+ \in \mathcal{S}_{D_y}, \\ & \Delta V_y = \lambda_y, \\ & \lambda_y \in \Xi_{\mathrm{dz/sat},y}, \end{aligned} \tag{5.63}$$

which minimizes the control impulse amplitude. In Section 5.3.2, it was demonstrated that the constraints of the problem (5.63) can be reduced to $\lambda_y \in \Lambda_{\mathrm{dz/sat},y}(\mathbf{d}_y, \nu)$ (see Eq. (5.43)). The state and time dependency will be subsequently omitted for the sake of clarity. Then, the control program (5.63) is simplified as

$$\begin{aligned} \underset{\lambda_y}{\text{minimize}} \quad & |\lambda_y|, \\ \text{subject to} \quad & \lambda_y \in \Lambda_{\mathrm{dz/sat},y}, \\ & \Lambda_{\mathrm{dz/sat},y} \equiv [\lambda_{y,1}, \lambda_{y,2}] \cup [\lambda_{y,3}, \lambda_{y,4}], \end{aligned} \tag{5.64}$$

where it can be easily deduced that the set of possible optimal candidates, Λ_y^*, is composed by the extremas of the non-connected intervals forming $\Lambda_{\mathrm{dz/sat},y}$

$$\Lambda_y^* = \{\lambda_{y,1}, \lambda_{y,2}, \lambda_{y,3}, \lambda_{y,4}\}. \tag{5.65}$$

Finally, the optimal solution can be easily found by evaluating the objective function for this set of possible optimal candidates and taking the minimum

$$\lambda_y^* = \arg \min_{\lambda_y \in \Lambda_y^*} (|\lambda_y|). \tag{5.66}$$

Note that only four objective function evaluations are needed.

In-plane control

To instantaneously steer the in-plane state $\mathbf{d}_{xz}$ to its corresponding admissible set $\mathcal{S}_{D_{xz}}$, the following program is considered

$$\begin{aligned}
\underset{\lambda_{xz}}{\text{minimize}} \quad & \|\Delta\mathbf{V}_{xz}\|_1, \\
\text{subject to} \quad & \mathbf{d}^+_{xz} = \mathbf{d}_{xz} + \mathbf{B}_{D_{xz}}(\nu)\Delta\mathbf{V}_{xz}, \\
& \mathbf{d}^+_{xz} \in \mathcal{S}_{D_{xz}}, \\
& \Delta\mathbf{V}_{xz} = \lambda_{xz}\mathbf{B}^{\perp}_{d_0,xz}(\nu) + \Delta\mathbf{V}^0_{xz}(d_0,\nu), \\
& \underline{\Delta V} \leq \|\Delta\mathbf{V}_{xz}\|_2 \leq \overline{\Delta V},
\end{aligned} \tag{5.67}$$

where, similarly to the out-of-plane case, the goal is to minimize the total in-plane impulse amplitude (directly related to fuel consumption). The constraints arising in the optimization problem (5.67) were shown, in Section 5.3.2, to be equivalent to $\lambda_{xz} \in \Lambda_{\mathrm{dz/sat},xz}(\mathbf{d}_{xz},\nu)$ (the dependency of this set on the state and time will be omitted for the sake of clarity). Using the previous fact, the control program (5.67) is simplified to

$$\begin{aligned}
\underset{\lambda_{xz}}{\text{minimize}} \quad & |\lambda_{xz}B^{\perp}_{d_0,x} + \Delta V^0_x| + |\lambda_{xz}B^{\perp}_{d_0,z} + \Delta V^0_z| \\
\text{subject to} \quad & \lambda_{xz} \in \Lambda_{\mathrm{dz/sat},xz}, \\
& \Lambda_{\mathrm{dz/sat},xz} \equiv [\lambda_{xz,1},\lambda_{xz,2}] \cup [\lambda_{xz,3},\lambda_{xz,4}].
\end{aligned} \tag{5.68}$$

For the previous optimization problem, the set of possible optimal candidates Λ^*_{xz} is formed by the extrema of the non-connected intervals composing $\Lambda_{\mathrm{dz/sat},xz}$ and the points where the slope of the objective function changes its tendency

$$\Lambda^*_{xz} = \left\{\lambda_{xz,1},\lambda_{xz,2},\lambda_{xz,3},\lambda_{xz,4},-\Delta V^0_x/B^{\perp}_{d_0,x},-\Delta V^0_z/B^{\perp}_{d_0,z}\right\}. \tag{5.69}$$

Then, the optimal solution is obtained by evaluating the objective function at the optimal candidates (six times at most) and taking the minimum

$$\lambda^*_{xz} = \underset{\lambda_{xz}\in\Lambda^*_{xz}\cap\Lambda_{\mathrm{dz/sat},xz}}{\arg\min} \left(|\lambda_{xz}B^{\perp}_{d_0,x} + \Delta V^0_x| + |\lambda_{xz}B^{\perp}_{d_0,z} + \Delta V^0_z|\right). \tag{5.70}$$

Note the that the points, where the slope of the objective function changes its tendency, have to be members $\Lambda_{\mathrm{dz/sat},xz}$ in order to be evaluated.

Coupled motion control

In the previous cases, the control is assumed to be purely applied on the in-plane or out-of-plane component. When both in-plane and out-of-plane controls are required at the same time, a coupled program has to be considered. This program has to fully account for the impulse constraint of problem (5.1) while preserving the low complexity level of programs (5.66) and (5.70). Following these programs, the coupled impulse with in-plane and out-of-plane components is

$$\Delta\mathbf{V}(\mathbf{d}_{xz},\nu,\lambda_{xz},\lambda_y)=\begin{bmatrix}\lambda_{xz}B^{\perp}_{d_0,x}(\mathbf{d}_{xz},\nu)+\Delta V^0_x(\mathbf{d}_{xz},\nu)\\ \lambda_y\\ \lambda_{xz}B^{\perp}_{d_0,z}(\mathbf{d}_{xz},\nu)+\Delta V^0_z(\mathbf{d}_{xz},\nu)\end{bmatrix}. \tag{5.71}$$

Then, when control is required in both components, the following program is stated

$$\begin{aligned}\underset{\lambda_{xz},\lambda_y}{\text{minimize}}\quad & \|\Delta\mathbf{V}\|_1,\\ \text{subject to}\quad & \mathbf{d}^+=\mathbf{d}+\mathbf{B}_D\Delta\mathbf{V},\\ & \mathbf{d}^+\in\mathcal{S}_D,\\ & \Delta\mathbf{V}=[\lambda_{xz}B^{\perp}_{d_0,x}+\Delta V^0_x,\ \lambda_y,\ \lambda_{xz}B^{\perp}_{d_0,z}+\Delta V^0_z]^T,\\ & \underline{\Delta V}\leq\|\Delta\mathbf{V}\|_2\leq\overline{\Delta V},\end{aligned} \tag{5.72}$$

where the dependencies with time, ν, and the in-plane state $\mathbf{d}_{xz}$ have been omitted for the sake of clarity. The constraints of the coupled program (5.72) can not be directly related to the sets $\Lambda_{\mathrm{dz/sat},xz}$ and $\Lambda_{\mathrm{dz/sat},y}$ respectively. However, the following non-connected set, $\Lambda_{\mathrm{dz/sat}}\in\mathbb{R}^2$, can be defined over the previous ones

$$\Lambda_{\mathrm{dz/sat}}=\Lambda_{\mathrm{dz/sat},xz}\times\Lambda_{\mathrm{dz/sat},y}. \tag{5.73}$$

Using the set $\Lambda_{\mathrm{dz/sat}}$, the program (5.72) can be equivalently transformed as

$$\begin{aligned}\underset{\lambda_{xz},\lambda_y}{\text{minimize}}\quad & |\lambda_{xz}B^{\perp}_{d_0,x}+\Delta V^0_x|+|\lambda_y|+|\lambda_{xz}B^{\perp}_{d_0,z}+\Delta V^0_z|,\\ \text{subject to}\quad & \lambda_{xz},\lambda_y\in\Lambda_{\mathrm{dz/sat}},\\ & \Lambda_{\mathrm{dz/sat}}\equiv([\lambda_{xz,1},\lambda_{xz,2}]\cup[\lambda_{xz,3},\lambda_{xz,4}])\\ & \qquad\times([\lambda_{y,1},\lambda_{y,2}]\cup[\lambda_{y,3},\lambda_{y,4}])\\ & \underline{\Delta V}\leq\sqrt{(\lambda_{xz}B^{\perp}_{d_0,x}+\Delta V^0_x)^2+\lambda_y^2+(\lambda_{xz}B^{\perp}_{d_0,z}+\Delta V^0_z)^2},\\ & \sqrt{(\lambda_{xz}B^{\perp}_{d_0,x}+\Delta V^0_x)^2+\lambda_y^2+(\lambda_{xz}B^{\perp}_{d_0,z}+\Delta V^0_z)^2}\leq\overline{\Delta V},\end{aligned} \tag{5.74}$$

Note that the membership of the control variables, λ_{xz} and λ_y, to the set $\Lambda_{\mathrm{dz/sat}}$ does not guarantee the fulfilment of the impulse constraint in this case. However, in order to keep a low computational burden, the search space can be restricted to the sixteen vertexes of the set $\Lambda_{\mathrm{dz/sat}}$

$$\Lambda^*\equiv\{(\lambda_{xz},\lambda_y)\in\{\lambda_{xz1},\ \lambda_{xz2},\ \lambda_{xz3},\ \lambda_{xz4}\}\times\{\lambda_{y1},\ \lambda_{y2},\ \lambda_{y3},\ \lambda_{y4}\}\}. \tag{5.75}$$

Consequently, the optimal solution is computed as

$$\begin{aligned}&(\lambda^*_{xz},\lambda^*_y)=\\ &\qquad\underset{(\lambda_{xz},\lambda_y)\in\Lambda^*\cap\Xi_{\mathrm{dz/sat}}}{\arg\min}\ (|\lambda_{xz}B^{\perp}_{d_0,x}+\Delta V^0_x|+|\lambda_y|+|\lambda_{xz}B^{\perp}_{d_0,z}+\Delta V^0_z|),\end{aligned} \tag{5.76}$$

where the set $\Xi_{\mathrm{dz/sat}} \in \mathbb{R}^2$ is defined as follows

$$\Xi_{\mathrm{dz/sat}} \equiv \{(\lambda_{xz}, \lambda_y) \in \mathbb{R}^2 \mid \\ \underline{\Delta V} \leq \sqrt{(\lambda_{xz} B^{\perp}_{d_0,x} + \Delta V^0_x)^2 + \lambda^2_y + (\lambda_{xz} B^{\perp}_{d_0,z} + \Delta V^0_z)^2} \leq \overline{\Delta V}\}.$$

Let recall that the individual components of the search space Λ^* may not fulfil the impulse constraints. The vertexes of the search space violating the constraints are removed as optimal candidates as indicated in Eq. (5.76). Nonetheless, if $\Lambda^*_{xz} \cap \Xi_{\mathrm{dz/sat}} \equiv \emptyset$ which means that all of the candidate solutions violate the impulse constraint, the in-plane control is prioritized at that instant and the out-of-plane control is applied in a subsequent time step. The in-plane control is prioritized because it is found (by numerical experimentation) to be more restrictive that the out-of-plane one. This fact will be highlighted in Section 5.5.

5.4.2 Trigger rules

The trigger rules are the core of the event-based controller because they decide which control actions are applied (if any). These rules are designed in order to achieve a threefold objective: they must ensure the control programs (5.66), (5.70) and (5.74) feasibility when executed; for the sake of efficiency, they should avoid unnecessary control actions; Zeno phenomena (which is the trigger of infinite control actions over a finite time period) must be precluded. In a rough way, the decision tree of the designed trigger rules is summarized as:

- If the relative state is within the admissible set, no control action is required.
- On the contrary, if the relative state is not in the admissible set, a decision is triggered according to the following conditions:
  - If the admissible set is instantaneously reachable and its proximity indicators fall below given thresholds, a single-impulse control is commanded.
  - If the admissible set is not instantaneously reachable but the current state belongs to its region of attraction, the event-based control awaits until the instantaneous reachability window opens (which is guaranteed to open in less than one leader orbital period).
  - If the previous conditions are not met, a global stable controller is commanded. This controller makes the state converge to the admissible set in a finite period of time.

Under the previous trigger rules, the proposed event-based controller is shown as pseudocode in Algorithm 3. The membership of the state $\mathbf{d}$ to the admissible set $\mathcal{S}_D$ and its region of attraction $\mathcal{D}$ is assessed using Eq. (5.5) and Eq. (5.62) respectively (steps 2, 4 and 34). If the relative state belongs to the admissible set, it is guaranteed that the follower is within the hovering region and no action is required (step 3). Alternatively, if the relative state has escaped the admissible set but is on its region of attraction, it means that either a reachability window is open or it will be over the next orbital period (step 4). This guarantees the feasibility of using a single-impulse control to steer the relative state back to the admissible set. On the other hand, if the relative state is not on the admissible set region of attraction (step 34), it means that a single-impulse control will not suffice to steer the relative state back to the admissible set. Under the previous fact, a global stable controller, to the admissible set, with N-impulses will be employed.

Let focus on the case where the state is outside the admissible set but belongs to its region of attraction (step 4). In that situation, a trigger decision tree spans through steps 5-33. The trigger rules take a control decision based on the admissible set proximity indicators G_{xz} and G_y and its derivatives $G_{\nu,xz}$ and $G_{\nu,y}$. If the proximity indicators, G_{xz} or G_y, are equal or above predefined thresholds, δ_{xz} or δ_y, and growing, $G_{\nu,xz} > 0$ or $G_{\nu,y} > 0$, a single-impulse steering the state back to the admissible set is computed and applied (steps 7-8, 10-11, 13-14, 19-20 and 26-27). The single-impulse control is computed by one of the programs: (5.66), (5.70) or (5.76). The one to solve depends on which control direction is required. On the contrary, when the proximity indicators fall below the thresholds or are decreasing, the single-impulse control is postponed (steps 22, 29 and 32). As a matter of fact, the thresholds δ_{xz} or δ_y are used to tune the reactivity of the controller. If the thresholds are too low, the single-impulse will be commanded as soon as the reachability window is opened. Otherwise, if higher values are chosen, the single-impulse will await until the end of the reachability window. This does not alter control accuracy since a necessary condition for the admissible set to be instantaneously reachable is that the relative state lies within the hovering region polytopic constraints. Note that a single-impulse is only able to instantaneously change the velocity but not the position (at least two impulses would be required if the spacecraft is outside the hovering region). These thresholds have to be chosen by assuring a minimum degree of reactivity within the region of attraction. To do so, one should find a lower bound for the smallest possible values of G_{xz} and G_y over the region of attraction domain (during a leader orbital period) and then take more negative values than those for the thresholds δ_{xz} and δ_y respectively. The previous condition can be expressed as

$$\begin{aligned} \delta_{xz} &< \min\left\{\sup_{\mathbf{d}\in\mathcal{D}}\left(\max_{\nu\in[0,2\pi]} G_{xz}(\mathbf{d}_{xz},\nu)\right)\right\}, \\ \delta_{y} &< \min\left\{\sup_{\mathbf{d}\in\mathcal{D}}\left(\max_{\nu\in[0,2\pi]} G_{y}(\mathbf{d}_{y},\nu)\right)\right\}. \end{aligned} \tag{5.77}$$

These upper bounds guarantee that a single-impulse control is triggered for one of the instantaneous reachability windows arising in the region of attraction.

This ensures that the controller reacts at some instant over the next leader orbital period. Note that the proximity thresholds are negative, $\delta_{xz} < 0$ and $\delta_y < 0$, due to the negativity of the proximity indicators (see Eq. (5.49)-(5.50)).

It may be also the case that the admissible set is instantaneously unreachable when $G_{xz} = 0$ or $G_y = 0$, then $G_{\nu,xz} = 0$ and $G_{\nu,y} = 0$. If the state is contained in the admissible set region of attraction $\mathcal{D}$, then it is guaranteed that at least one instantaneous reachability windows will open along the next leader orbital period. Under such condition, it is safe to await until the reachability window opens (step 32). On the other hand, if the state does not belong to the admissible set region of attraction, a N-impulses stable control method has to be employed. In that sense, an adapted version of the global stable controller of [Arantes-Gilz19] (see Algorithm 7 in Appendix D) is used (step 35). The global stable controller repeats a sequence of $N \geq 3$ impulses spaced in time where the admissible set is reached just after the application of the final impulse. The adaptation considers the L2-norm for saturated impulses (instead of the infinity-norm in [Arantes-Gilz19]) and the nullification of impulses below the minimum impulse bit. This algorithm ensures the event-based controller stability though its use has a potential negative impact on control accuracy (as it only the admissible set is reached just once the set of N-impulses is completed). This is the reason why it acts as a backup for the single-impulse control.

5.5 Invariance of the single-impulse approach

As outlined at the end of Section 5.4.2, the prioritized single-impulse control of the event-based algorithm only ensures convergence towards the admissible set within a local domain (admissible set region of attraction). Due to the previous consideration, the invariance of the single-impulse control will be assessed through the theory of hybrid impulsive systems [Haddad06]. Under that theory, the well-posedness of the single-impulse control, in the context of the spacecraft rendezvous hovering phases, is analyzed. Subsequently, the system invariance is studied and demonstrated to be dependant on the problem parameters. Finally, the previous analysis is extended to account for the presence of continuous disturbances.

5.5.1 Well-posedness for hybrid impulsive systems

An impulsive control strategy for the linear Keplerian relative motion can be recasted to a hybrid impulsive system. The hybrid system is composed of the Eq. (2.44) continuous flow dynamics and the instantaneous state changes of Eq. (2.60). For that reason, the main results of [Haddad06] for hybrid impulsive systems apply to the single-impulse control of Algorithm 3. Transforming the event-based controller steps 2-33, associated to the single-impulse control

Algorithm 3: Event-based controller for spacecraft rendezvous hovering phases.

```
begin
    if $\mathbf{d} \in \mathcal{S}_D$ then
        Wait.
    else if $(\mathbf{d} \notin \mathcal{S}_D) \wedge (\mathbf{d} \in \mathcal{D})$ then
        if $(G_{xz}(\mathbf{d},\nu) \geq \delta_{xz}) \wedge (G_{\nu,xz}(\mathbf{d},\nu) > 0) \wedge (G_y(\mathbf{d},\nu) \geq \delta_y) \wedge (G_{\nu,y}(\mathbf{d},\nu) > 0)$ then
            if $(\mathbf{d}_{xz} \notin \mathcal{S}_{D_{xz}}) \wedge (\mathbf{d}_y \in \mathcal{S}_{D_y})$ then
                Compute $\lambda_{xz}$ by solving the program (5.70);
                Apply $\Delta\mathbf{V} \leftarrow \lambda_{xz}\mathbf{B}^{\perp}_{d_0,xz}(\nu) + \Delta\mathbf{V}^0_{xz}(d_0,\nu)$;
            else if $(\mathbf{d}_{xz} \in \mathcal{S}_{D_{xz}}) \wedge (\mathbf{d}_y \notin \mathcal{S}_{D_y})$ then
                Compute $\lambda_y$ by solving the program (5.66);
                Apply $\Delta\mathbf{V} \leftarrow \lambda_y\mathbf{j}_L$;
            else
                Compute $(\lambda_{xz}, \lambda_y)$ by solving the program (5.76);
                Apply $\Delta\mathbf{V} \leftarrow \lambda_{xz}\mathbf{B}^{\perp}_{d_0,xz}(\nu) + \Delta\mathbf{V}^0_{xz}(d_0,\nu) + \lambda_y\mathbf{j}_L$;
            end
        end
        else if $(G_{xz}(\mathbf{d},\nu) \geq \delta_{xz}) \wedge (G_{\nu,xz}(\mathbf{d},\nu) > 0)$ then
            if $\mathbf{d}_{xz} \notin \mathcal{S}_{D_{xz}}$ then
                Compute $\lambda_{xz}$ by solving the program (5.70);
                Apply $\Delta\mathbf{V} \leftarrow \lambda_{xz}\mathbf{B}^{\perp}_{d_0,xz}(\nu) + \Delta\mathbf{V}^0_{xz}(d_0,\nu)$;
            else
                Wait
            end
        else if $(G_y(\mathbf{d},\nu) \geq \delta_y) \wedge (G_{\nu,y}(\mathbf{d},\nu) > 0)$ then
            if $\mathbf{d}_y \notin \mathcal{S}_{D_y}$ then
                Compute $\lambda_y$ by solving the program (5.66);
                Apply $\Delta\mathbf{V} \leftarrow \lambda_y\mathbf{j}_L$;
            else
                Wait
            end
        else
            Wait.
        end
    else if $(\mathbf{d} \notin \mathcal{S}_D) \wedge (\mathbf{d} \notin \mathcal{D})$ then
        Apply the global stabilizing controller of Algorithm 7 (see Appendix D).
    end
end
```

strategy, into a hybrid impulsive system yields

$$\begin{aligned} \mathbf{d}'(\nu) &= \mathbf{A}_D(\nu)\mathbf{d}(\nu), & \mathbf{d}_0 \in \mathcal{D} \cup \mathcal{S}_D, \quad (\mathbf{d},\nu) \notin \mathcal{Z}, \\ \Delta\mathbf{d}(\nu) &= \mathbf{B}_D(\nu)\Delta\mathbf{V}(\nu), & (\mathbf{d},\nu) \in \mathcal{Z}, \end{aligned} \tag{5.78}$$

where $\Delta\mathbf{d} = \mathbf{d}^+ - \mathbf{d}$ denotes the instantaneous change in the state due to an impulsive control. Note that $\mathbf{d}_0 = \mathbf{d}(\nu_0)$. The set $\mathcal{Z}$ denotes the resetting set (which triggers an impulse) as

$$\mathcal{Z} = \mathcal{Z}_{xz} \times \mathcal{Z}_y, \tag{5.79}$$

where the respective in-plane and out-of-plane resetting sets are given by

$$\mathcal{Z}_{xz} := \{(\mathbf{d},\nu) : \mathbf{d} \notin \mathcal{S}_{D_{xz}},\ \mathbf{d} \in \mathcal{D}_{xz},\ G_{xz}(\mathbf{d}_{xz},\nu) \geq \delta_{xz},\ G_{\nu,xz} > 0\}, \tag{5.80}$$

$$\mathcal{Z}_y := \{(\mathbf{d},\nu) : \mathbf{d} \notin \mathcal{S}_{D_y},\ \mathbf{d} \in \mathcal{D}_y,\ G_y(\mathbf{d}_y,\nu) \geq \delta_y,\ G_{\nu,y} > 0\}. \tag{5.81}$$

In this study, the initial state $\mathbf{d}_0$, is assumed to lie within the union of the admissible set $\mathcal{S}_D$ with its region of attraction $\mathcal{D}$. The opposite case, where [Arantes-Gilz19] global stable controller is called (steps 34-36 of Algorithm 3), is out of the scope of this analysis which only concerns the single-impulse control.

For the hybrid impulsive system (5.78), the well-posedness of the resetting set is only guaranteed if the following assumptions are met:

Assumption 5.5.1. *A trajectory can only enter the resetting set through a point lying on its boundary but not from its interior [Haddad06, chapter 2, p.13].*

Assumption 5.5.2. *When a trajectory intersects the resetting set, it exits $\mathcal{Z}$ without returning to it for a finite period of time [Haddad06, Chapter 2, p.13].*

In other words, assumption 5.5.1 guarantees that a control response is given at the exact instant where the trajectory intersects the resetting set. The second assumption 5.5.2 precludes Zeno phenomena as it assures that the state after the impulse cannot be on the resetting set boundary. These assumptions guarantee the uniqueness of the system (5.78) trajectories over a forward interval of time.

Let assess the first assumption 5.5.1 for the event-based controller in Algorithm 3. If the initial state lies within the admissible set $\mathcal{S}_D$ it remains invariant over time as its dynamics are stationary since $d_0 = 0$. As a consequence, it cannot reach the resetting set. On the contrary, if the initial state lies in the region of attraction $\mathcal{D}$, it can only enter the resetting set $\mathcal{Z}$ through its boundary $\partial\mathcal{Z}$ characterized by

$$\partial\mathcal{Z} = \partial\mathcal{Z}_{xz} \times \partial\mathcal{Z}_y, \tag{5.82}$$

where

$$\partial\mathcal{Z}_{xz} := \{(\mathbf{d},\nu) : \mathbf{d} \notin \mathcal{S}_{D_{xz}},\ \mathbf{d} \in \mathcal{D}_{xz},\ G_{xz}(\mathbf{d}_{xz},\nu) = \delta_{xz},\ G_{\nu,xz} > 0\}, \quad (5.83)$$
$$\partial\mathcal{Z}_{y} := \{(\mathbf{d},\nu) : \mathbf{d} \notin \mathcal{S}_{D_{y}},\ \mathbf{d} \in \mathcal{D}_{y},\ G_{y}(\mathbf{d}_{y},\nu) = \delta_{y},\ G_{\nu,y} > 0\}. \quad (5.84)$$

Note that by definition G_{xz} and G_y (see Eq. (5.49)-(5.50)) are continuous functions in time (except when an impulse control is applied), thus it is assured that the state enters the resetting set through its boundary.

The second assumption 5.5.2 requires that when a trajectory intersects the resetting set, it exits $\mathcal{Z}$ without returning to it for some finite time. In the proposed event-based control algorithm, as soon as the state enters the resetting set, a single-impulse instantaneously steers the state to the admissible set. By the resetting set definition (see Eq. (5.79)-(5.81)) it is deduced that its intersection with the admissible set is empty, $\mathcal{S}_D \cap \mathcal{Z} = \emptyset$ (a state cannot be at the same time in the resetting and admissible sets). Consequently, the resetting set is not contained within the admissible set. Let recall that when the state is on the admissible set, its dynamics is stationary and remains there indefinitely. These facts preclude the return of the state $\mathbf{d}$ to the resetting set $\mathcal{Z}$ after the single-impulse control is executed.

5.5.2 Invariance of the hybrid impulsive system

This section presents a result guaranteeing the existence of an invariant attractive set for the hybrid impulsive system (5.78). It is not possible to directly use the invariance principles for linear time invariant systems given in [Haddad06, Chapter 2, p.38] as the Keplerian linear relative motion under consideration is time-varying. However, the system periodicity would be exploited to obtain results aligned with the rationale for time invariant systems.

In order to reach the invariance results, some auxiliary sets needs to be properly defined and its geometrical shapes has to be inferred. These are the reachable set over one period and the dead-zone set.

Geometry of the reachable set over one period

At the end of Section 5.3 and under the quasi-periodic assumption, $|d_0| \approx 0$, it was demonstrated that the instantaneous reachability is periodic with the leader orbital period. Extending the instantaneous reachability condition over a leader orbital period allowed to define a region of attraction to the admissible set (see Eq. (5.56)-(5.58)) Let study now the state reachability over one period. Let define the reachable set of states over one period as

$$\mathcal{F} = \mathcal{F}_{xz} \times \mathcal{F}_{y}. \quad (5.85)$$

The reachable sets will be conveniently expressed in terms of the state increment $\Delta\mathbf{d} = \mathbf{d}^{+} - \mathbf{d} \in \mathbb{R}^6$ which results from the application of a single-impulse.

The out-of-plane $\mathcal{F}_y$ and in-plane $\mathcal{F}_{xz}$ reachable sets over one period are analyzed separately.

<u>Out-of-plane motion:</u> the out-of-plane state increment, $\Delta\mathbf{d}_y = \mathbf{d}_y^+ - \mathbf{d}_y = [\Delta d_4, \Delta d_5]^T$, is given by

$$\Delta\mathbf{d}_y(\nu, \lambda_y) = \lambda_y \mathbf{B}_{D_y}(\nu) = \frac{\lambda_y}{k^2\rho_\nu}\begin{bmatrix}-\mathrm{s}_\nu \\ \mathrm{c}_\nu\end{bmatrix}. \tag{5.86}$$

The out-of-plane state increment forms a geometric shape over one period. This geometric shape can be obtained by implicitizing Eq. (5.86) (see [Hong95] and Appendix C for the details concerning the implicitization of trigonometric functions) with respect to its independent variable ν

$$f_y(\Delta\mathbf{d}_y, \lambda_y) = \frac{\Delta d_4^2}{\left(\dfrac{\lambda_y}{k^2\sqrt{1-e^2}}\right)^2} + \frac{\left(\Delta d_5 + \dfrac{e\lambda_y}{k^2(1-e^2)}\right)^2}{\left(\dfrac{\lambda_y}{k^2(1-e^2)}\right)^2} - 1 = 0, \tag{5.87}$$

which is the equation of an ellipse in the $\Delta d_4 \Delta d_5$ space for a constant λ_y and e. Using Eq. (5.87), the out-of-plane state increment reachable set over one period is expressed as

$$\mathcal{F}_y(\Upsilon_y) := \{\Delta\mathbf{d}_y \in \mathbb{R}^2 \mid f_y(\Delta\mathbf{d}_y, \lambda_y) = 0,\ \lambda_y \in \Upsilon_y\}, \tag{5.88}$$

where the set $\Upsilon_y \subseteq \mathbb{R}$ refers, in a generic way, to the admissible values for the out-of-plane control variable λ_y. If the dead-zone and saturation set $\Xi_{\mathrm{dz/sat},y}$ is taken into account (see Eq. (5.16)), the constrained reachable set $\mathcal{F}_{\mathrm{dz/sat},y}$ is

$$\mathcal{F}_{\mathrm{dz/sat},y} = \mathcal{F}_y(\Xi_{\mathrm{dz/sat},y}), \tag{5.89}$$

which comprises the region between two ellipses with different $\lambda_y = \underline{\Delta V}, \overline{\Delta V}$ according to Eq. (5.87). It is also of interest to describe both the reachable set for impulses below the minimum impulse bit $\mathcal{F}_{\mathrm{dz},y}$ and the unconstrained reachable set $\mathcal{F}_{\infty,y}$

$$\mathcal{F}_{\mathrm{dz},y} = \mathcal{F}_y([-\underline{\Delta V}, \underline{\Delta V}]) \tag{5.90}$$

$$\mathcal{F}_{\infty,y} = \mathcal{F}_y(\mathbb{R}). \tag{5.91}$$

Note that the unconstrained reachable set $\mathcal{F}_{\infty,y}$ is the whole domain $\mathbb{R}^2$ in the $\Delta d_4 \Delta d_5$ space.

<u>In-plane motion:</u> let define $\Delta\mathbf{d}_{xz} = \mathbf{d}_{xz}^+ - \mathbf{d}_{xz} = [\Delta d_0, \Delta d_1, \Delta d_2, \Delta d_3]^T$ as the in-plane state increment. Reorganizing terms in Eq. (5.24), the in-plane state increment yields the following expression

$$\Delta\mathbf{d}_{xz}(\mathbf{d}_{xz}, \nu, \lambda_{xz}) = \mathbf{B}_{D_{xz}}(\nu)\left(\lambda_{xz}\mathbf{B}_{d_0,xz}^{\perp}(\nu) + \Delta\mathbf{V}_{xz}^0(d_0, \nu)\right), \tag{5.92}$$

where the in-plane state increment $\Delta\mathbf{d}_{xz}$ depends on the actual state due to d_0. Due to the previous fact, obtaining insight of the geometrical shape for the in-plane reachable set over one period is more complex than it is for the out-of-plane case. Let define the in-plane state reachable set over one period, in terms of the state increment, as

$$\begin{aligned}\mathcal{F}_{xz}(\Upsilon_{xz}) := \{\Delta\mathbf{d}_{xz} \in \mathbb{R}^4 \mid \Delta\mathbf{d}_{xz} = \mathbf{B}_{D_{xz}}(\nu)\Big(\lambda_{xz}\mathbf{B}^{\perp}_{d_0,xz}(\nu) \\ +\Delta\mathbf{V}^0_{xz}(d_0,\nu)\Big)\,,\ \lambda_{xz} \in \Upsilon_{xz}\}\end{aligned} \tag{5.93}$$

where the set $\Upsilon_{xz} \subseteq \mathbb{R}$ refers to the admissible values of the in-plane control variable λ_{xz}. The dead-zone and saturation constraints are considered through the set $\Xi_{\mathrm{dz/sat},xz}$ (see Eq. (5.26)) hence the constrained in-plane reachable set over one period yields

$$\mathcal{F}_{\mathrm{dz/sat},xz} = \mathcal{F}_{xz}(\Xi_{\mathrm{dz/sat},xz}(d_0,\nu)),\ \ \nu \in [0,2\pi]. \tag{5.94}$$

Similarly to the out-of-plane case, it is of interest to describe the dead-zone reachable set and the unconstrained reachable set

$$\mathcal{F}_{\mathrm{dz},xz} = \mathcal{F}_{xz}([\underline{\lambda}_{xz,1}(d_0,\nu),\underline{\lambda}_{xz,2}(d_0,\nu)]),\ \ \nu \in [0,2\pi], \tag{5.95}$$

$$\mathcal{F}_{\infty,xz} = \mathcal{F}_{xz}(\mathbb{R}). \tag{5.96}$$

Note that $\underline{\lambda}_{xz,1}$ and $\underline{\lambda}_{xz,2}$ are the extremas of the non-connected intervals in $\Xi_{\mathrm{dz/sat},xz}$ (see Eq. (5.26)). Due to the periodicity pursuing strategy $\Delta d_0 = -d_0$, therefore the relevant in-plane state space is reduced to $\Delta d_1 \Delta d_2 \Delta d_3$. If the quasi-equilibrium assumption $|d_0| \approx 0$ is made, some insight on the geometry for the in-plane reachable set over one period can be obtained. Since $|d_0| \approx 0$, the periodicity pursuing component of the in-plane single-impulse can be neglected with respect to its free part such that $\|\lambda_{xz}\mathbf{B}^{\perp}_{d_0,xz}\|_2 \gg \|\Delta\mathbf{V}^0_{xz}\|_2$. Under the previous assumption, Eq. (5.92) can be approximated as follows

$$\Delta\mathbf{d}_{xz}(\nu) \approx \lambda_{xz}\mathbf{B}_{D_{xz}}(\nu)\mathbf{B}^{\perp}_{d_0,xz}(\nu) = \frac{\lambda_{xz}}{k^2\rho}\begin{bmatrix}0\\ -\mathrm{s}_\nu \\ \mathrm{c}_\nu \\ 2+e\mathrm{c}_\nu\end{bmatrix}. \tag{5.97}$$

To obtain a geometrical shape of the in-plane state increment as per Eq. (5.97), the implicitization must get rid of two independent variables. Since the relevant in-plane state increment $\Delta d_1 \Delta d_2 \Delta d_3 \in \mathbb{R}^3$, a surface (defined by two independent parameters) would be obtained as the result of the implicitization. By using a Groebner basis (see [Fix96] for the details), Eq. (5.97) can be implicitized with respect to λ_{xz} and ν such that

$$f_{xz}(\Delta\mathbf{d}_{xz}) = 4\Delta d_1^2 + (4-e^2)\Delta d_2^2 + 2e\Delta d_2\Delta d_3 - \Delta d_3^2 = 0, \tag{5.98}$$

which is the geometrical shape of a conic surface in the $\Delta d_1 \Delta d_2 \Delta d_3$ space. Note that the cone apex is aligned with the Δd_3 direction for $e = 0$. Using

Eq. (5.98), an approximation (due to the quasi-periodic assumption $|d_0| \approx 0$) for the unconstrained reachable set over one period $\mathcal{F}_{\infty,xz}$ is available as

$$\mathcal{F}_{\infty,xz} \approx \{\Delta\mathbf{d}_{xz} \in \mathbb{R}^4 \mid f_{xz}(\Delta\mathbf{d}_{xz}) = 0\}. \tag{5.99}$$

The lost of the control variable, λ_{xz}, in the geometrical shape of the in-plane reachable set over one period hinders the obtention of intuitive geometrical shapes for the constrained $\mathcal{F}_{\mathrm{dz/sat},xz}$ and dead-zone $\mathcal{F}_{\mathrm{dz},xz}$ reachable sets over one period. Nonetheless, they can be formally defined as

$$\begin{aligned}\mathcal{F}_{\mathrm{dz/sat},xz} \approx \{&\Delta\mathbf{d}_{xz} \in \mathbb{R}^4 \mid \Delta\mathbf{d}_{xz} = \lambda_{xz} B_{D_{xz}}(\nu)\mathbf{B}^{\perp}_{d_0,xz}(\nu),\\ &\lambda_{xz} \in \Xi_{\mathrm{dz/sat},xz}(\nu),\ \nu \in [0,2\pi]\},\end{aligned} \tag{5.100}$$

$$\begin{aligned}\mathcal{F}_{\mathrm{dz},xz} \approx \{&\Delta\mathbf{d}_{xz} \in \mathbb{R}^4 \mid \Delta\mathbf{d}_{xz} = \lambda_{xz} B_{D_{xz}}(\nu)\mathbf{B}^{\perp}_{d_0,xz}(\nu),\\ &\lambda_{xz} \in (\underline{\lambda}_{xz,1}(\nu), \underline{\lambda}_{xz,2}(\nu)),\ \nu \in [0,2\pi]\},\end{aligned} \tag{5.101}$$

where a step back with respect to the implicitization process has been done in order to make the control variable λ_{xz} appear again. Note that the constrained and dead-zone in-plane reachable sets are portions of the unconstrained reachable set conical shape since $\mathcal{F}_{\mathrm{dz/sat},xz}, \mathcal{F}_{\mathrm{dz},xz} \subseteq \mathcal{F}_{\infty,xz}$.

Geometry of the dead-zone set

The dead-zone set is composed of the states from where all the admissible set instantaneous reachability opportunities, along one leader orbital period, fall below the dead-zone threshold. Let define the dead-zone set $\mathcal{D}_{\mathrm{dz}}$ as

$$\mathcal{D}_{\mathrm{dz}} = \mathcal{D}_{\mathrm{dz},xz} \times \mathcal{D}_{\mathrm{dz},y}. \tag{5.102}$$

The dead-zone set is of interest because it establishes a sufficient condition for a state to not be in the admissible set region of attraction

$$\mathbf{d} \in \mathcal{D}_{\mathrm{dz}} \implies \mathbf{d} \notin \mathcal{D}, \tag{5.103}$$

thus, if $\mathbf{d} \in \mathcal{D}_{\mathrm{dz}}$, a single-impulse control does not suffice to reach the admissible set. In that case, if the state is outside the admissible set, the event-based control Algorithm 3 will trigger the global stable controller. The dead-zone set may or may not exist as it will be proved in the sequel.

Out-of-plane motion: the out-of-plane dead-zone set is described as

$$\begin{aligned}\mathcal{D}_{\mathrm{dz},y} := \{&\mathbf{d}_y \in \mathbb{R}^2 \mid \mathbf{d}_y \notin \mathcal{S}_{D_y},\ (\mathbf{d}_y \oplus \mathcal{F}_{\mathrm{dz/sat},y}) \cap \mathcal{S}_{D_y} = \emptyset,\\ &(\mathbf{d}_y \oplus \mathcal{F}_{\mathrm{dz},y}) \cap \mathcal{S}_{D_y} \neq \emptyset\},\end{aligned} \tag{5.104}$$

where the Minkowski sum ($\oplus$) has been employed to add the out-of-plane reachable sets over one period, $\mathcal{F}_{\mathrm{dz/sat},y}$ and $\mathcal{F}_{\mathrm{dz},y}$, to the current state. For the states within the dead-zone set and during one orbital period, it is only possible to reach the admissible set with a single-impulse below the minimum impulse bit. Using the Minkowski sum, the out-of-plane region of attraction (see Eq. (5.58)) can also be expressed as

$$\mathcal{D}_y = \mathcal{S}_{D_y} \oplus \mathcal{F}_{\mathrm{dz/sat},y}. \tag{5.105}$$

The direct addition of the reachable state to the admissible set is possible because $\mathcal{F}_{\mathrm{dz/sat},y}$ is independent of the state $\mathbf{d}_y$ (see Eq. (5.89)). Since the out-of-plane reachable set is the region enclosed between an inner and outer ellipse in the $\Delta d_4 \Delta d_5$ space, which is a closed region, it can be deduced that

$$\{\exists \mathbf{d}_y \in \partial \mathcal{S}_{D_y} \ : \ \mathcal{S}_{D_y} \cap (\mathbf{d}_y + \mathcal{F}_{\mathrm{dz/sat},y}) = \emptyset\} \iff \mathcal{D}_{\mathrm{dz},y} \neq \emptyset, \tag{5.106}$$

which implies the existence of the dead-zone set if and only if the out-of-plane reachable set does not intersect the admissible set from any of its boundary points. This is a consequence of the Minkowski sum between a closed region $\mathcal{F}_{\mathrm{dz/sat},y}$ and a convex bounded set $\mathcal{S}_{D_y}$ in Eq. (5.105). The result of this sum would enclose the admissible set but depending on the reachable set empty interior size, a region (dead-zone set) between the admissible set and the Minkowski sum result (region of attraction) arises or not. In that sense, it can be deduced that the existence of the dead-zone set mainly depends on the minimum impulse bit $\underline{\Delta V}$. If the minimum impulse bit is high, the inner ellipse of $\mathcal{F}_{\mathrm{dz/sat},y}$ (see Eq. (5.89)) enlarges until a point where it is larger than the admissible set.

To illustrate the previous result, let consider the circular orbit case $e = 0$. Then, both the out-of-plane admissible set $\mathcal{S}_{D_y}$ and the interior region of the state increment reachable set $\mathcal{F}_{\mathrm{dz/sat},y}$ are circles of radius $\max(|\underline{y}|, |\overline{y}|)$ and $\underline{\Delta V}/k^2$ respectively. In this case, the dead-zone set existence condition of Eq. (5.106) is satisfied if the radius of the reachable set doubles that of the admissible set such that $\underline{\Delta V} > 2k^2 \max(|\underline{y}|, |\overline{y}|)$.

Let consider an example for a leader orbit with $a = 7011$ km and $e = 0.004$. Let assume the out-of-plane hovering region bounds as $\underline{y} = -25$ m and $\overline{y} = 25$ m, and the dead-zone/saturation thresholds as $\underline{\Delta V} = 7.5$ cm/s and $\overline{\Delta V} = 10$ cm/s. In Fig. 5.4, the geometrical situation (constrained reachable set $\mathcal{F}_{\mathrm{dz/sat},y}$, dead-zone reachable set $\mathcal{F}_{\mathrm{dz},y}$ and admissible set $\mathcal{S}_{D_y}$) of the out-of-plane admissible set reachability over one period is shown for two relevant cases. In the left image, the out-of-plane state is $\mathbf{d}_y = [-50, 50]^T$ and it can be seen that the out-of-plane constrained reachable set (over one period) intersects the admissible set. This state lies on the admissible set region of attraction $\mathcal{D}_y$ and has instantaneous reachability opportunities over one orbital period. On the other hand, in the right image, the out-of-plane state is $\mathbf{d}_y = [-25, 25]^T$ and the constrained reachable set over one period does not intersect the admissible set. Consequently, that state does not belong to the region of attraction to the admissible set. Note that, the dead-zone set intersects the admissible set which shows that lower values of the minimum impulse bit $\underline{\Delta V}$ would make this state to lie in the region of attraction $\mathcal{D}_y$.

Let briefly show how the minimum impulse bit may affect the admissible set reachability. For the previous scenario, Fig. 5.5 plots the out-of-plane region of attraction $\mathcal{D}_y$, dead-zone $\mathcal{D}_{\text{dz},y}$ and admissible $\mathcal{S}_{D_y}$ sets. In the left image, for $\underline{\Delta V} = 0.1$ cm/s, the region of attraction surrounds the admissible set on its totality and no dead-zone set arises. On the contrary, in the right image for $\underline{\Delta V} = 7.5$ cm/s there exists a gap between the region of attraction and the admissible set corresponding to the dead-zone set. This highlights the influence of the minimum impulse bit in the existence of the out-of-plane dead-zone set. Actually, for the out-of-plane case, this is the unique parameter driving the dead-zone existence. If there is no minimum impulse bit constraint, that is $\underline{\Delta V} = 0$, then $\mathcal{D}_{\text{dz},y} = \emptyset$ due to the Minkowski sum of a convex set with another convex set as per Eq. (5.105). This would make the region of attraction to surround the admissible set on its totality as in the left image.

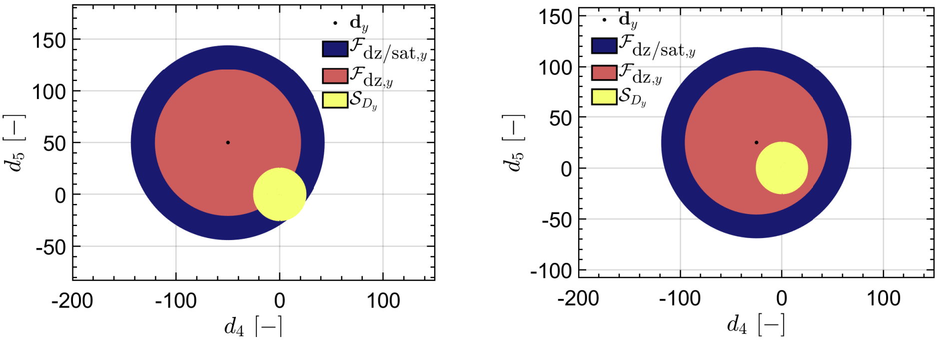

Figure 5.4: Geometry of the out-of-plane admissible set reachability over one period: reachable (*left*) and unreachable (*right*).

<u>In-plane motion:</u> using the previous notation, the in-plane dead-zone set can be defined as

$$\begin{aligned}\mathcal{D}_{\text{dz},xz}(d_0) := \{\mathbf{d}_{xz} \in \mathbb{R}^4 \mid\ & \mathbf{d}_{xz} \notin \mathcal{S}_{D_{xz}}, \\ & (\mathbf{d}_{xz} \oplus \mathcal{F}_{\text{dz/sat},xz}(d_0)) \cap \mathcal{S}_{D_{xz}} = \emptyset, \\ & (\mathbf{d}_{xz} \oplus \mathcal{F}_{\text{dz},xz}(d_0)) \cap \mathcal{S}_{D_{xz}} \neq \emptyset\},\end{aligned} \tag{5.107}$$

and the region of attraction as

$$\mathcal{D}_{xz}(d_0) = \mathcal{S}_{D_{xz}} \oplus \mathcal{F}_{\text{dz/sat},xz}(d_0). \tag{5.108}$$

It should be noted that these sets explicitly depends on the in-plane state as d_0 has an influence on Eq. (5.22) in-plane impulse. Nonetheless, this dependency

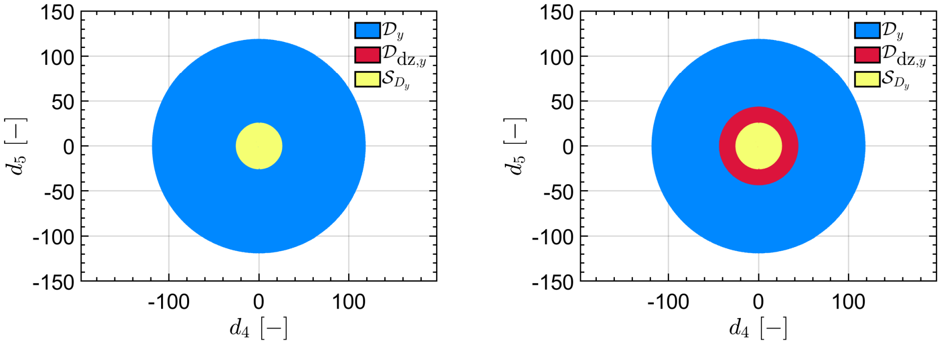

Figure 5.5: Out-of-plane region of attraction, dead-zone and admissible sets: non-existent dead-zone set (*left*) and existing dead-zone set (*right*).

can be eliminated if the quasi-periodic state assumption is done, then

$$\begin{aligned}\mathcal{D}_{\mathrm{dz},xz} :\approx \{\mathbf{d}_{xz} \in \mathbb{R}^4 \mid \mathbf{d}_{xz} \notin \mathcal{S}_{D_{xz}},\ (\mathbf{d}_{xz} \oplus \mathcal{F}_{\mathrm{dz/sat},xz}) \cap \mathcal{S}_{D_{xz}} = \emptyset,\\ (\mathbf{d}_{xz} \oplus \mathcal{F}_{\mathrm{dz},xz}) \cap \mathcal{S}_{D_{xz}} \neq \emptyset\},\end{aligned} \tag{5.109}$$

and

$$\mathcal{D}_{xz} \approx \mathcal{S}_{D_{xz}} \oplus \mathcal{F}_{\mathrm{dz/sat},xz} \ \text{ if } \ |d_0| \approx 0, \tag{5.110}$$

where the in-plane constrained and dead-zone reachable sets approximations has been employed (see Eq. (5.101) and Eq. (5.100)).

In this case, the Minkowksi sum, producing the region of attraction $\mathcal{D}_{xz}$, is composed of a convex closed set $\mathcal{S}_{D_{xz}}$ and a portion of a conic surface $\mathcal{F}_{\mathrm{dz,sat},xz}$ given by Eq. (5.100). Consequently, since a cone is an open surface, it could not be guaranteed that the region of attraction encloses the admissible on its totality even if $\underline{\Delta V} = 0$. Then, the admissible set unreachability by an in-plane single-impulse control could arise due to the combination of the minimum impulse bit and the problem geometrical configuration.

Let analyze an example to assess the previous statement. Let consider a leader on an orbit with $a = 7011$ km and $e = 0.004$. Let assume the in-plane hovering region bounds as $\{\underline{x}, \overline{x}, \underline{z}, \overline{z}\} = \{50, 150, -25, 25\}$ m and the impulse thresholds as $\underline{\Delta V} = 3$ cm/s and $\overline{\Delta V} = 10$ cm/s. Figure 5.6 shows the constrained $\mathcal{F}_{\mathrm{dz/sat},xz}$ and dead-zone $\mathcal{F}_{\mathrm{dz},xz}$ reachable sets over one period as well as the admissible set $\mathcal{S}_{D_{xz}}$. In the left image, $\mathbf{d}_{xz} = [0, 17.5, 17.5, 150]^T$, it is seen that the in-plane constrained reachable set over one period intersects the admissible set. Then, the previous state belongs to the admissible set region of attraction. On the contrary, in the right image for $\mathbf{d}_{xz} = [0, 17.5, 17.5, 110]^T$, the constrained reachable set over one period does not intersect the admissible set. It can be concluded that the previous state does not belong to the admissible set region of attraction. In this case, it can also be seen that the dead-zone set over one period intersects the admissible set. This points out that a lower minimum impulse bit would make this state belong to the admissible set region of attraction. However, observing the constrained reachable set over one period geometry in Fig. 5.6, it is also deduced that a subset of the in-plane space $d_1 d_2 d_3$ would not belong to the admissible set region of attraction regardless of the minimum impulse bit $\underline{\Delta V}$ (e.g. imagine displacing the cone over the space).

For the previous scenario, Fig. 5.7 shows the boundaries of the admissible set $\mathcal{S}_{D_{xz}}$ and its region of attraction $\mathcal{D}_{xz}$ over one period. In that case, the minimum impulse bit was varied from $\underline{\Delta V} = 0.1$ cm/s (left image) to $\underline{\Delta V} = 3$ cm/s (right image). In the left image, the region of attraction encloses on its totality the admissible set. However, in the right panel, the region of attraction does not encloses the region around the admissible set neck. As a consequence, for the right image, a state escaping the admissible set from that neck would not be able to return with a single-impulse control. It has been demonstrated that this degraded situation for the single-impulse control mainly depends on the minimum impulse bit.

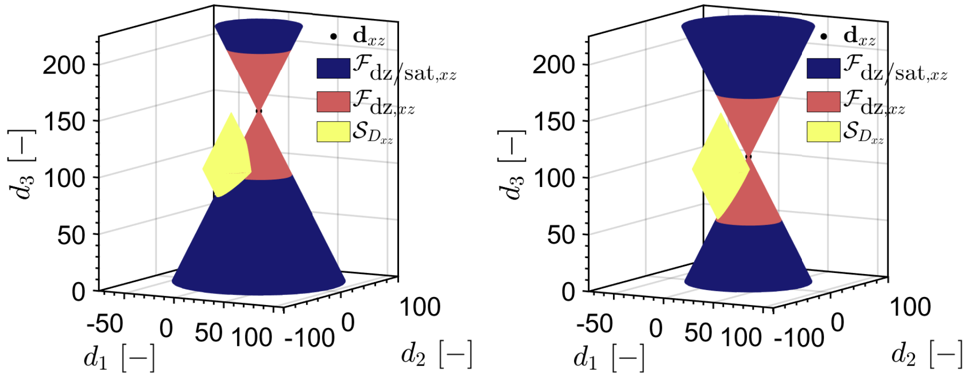

Figure 5.6: Geometry of the in-plane admissible set reachability over one period: reachable (*left*) and unreachable (*right*).

Invariance of the admissible set and its region of attraction

Using the previous results and definitions, this section demonstrates the invariance for the union of the admissible set and its region of attraction.

For the system (5.78), the invariance condition can be expressed as

$$\mathbf{d}(\nu_0) = \mathbf{d}_0 \in \mathcal{D} \cup \mathcal{S}_D \Longrightarrow \mathbf{d}(\nu) \in \mathcal{D} \cup \mathcal{S}_D, \;\; \nu \geq \nu_0. \tag{5.111}$$

This means that a state in the vicinity of the admissible set is ensured to be steered to it after some finite time, thus the following assumption must be

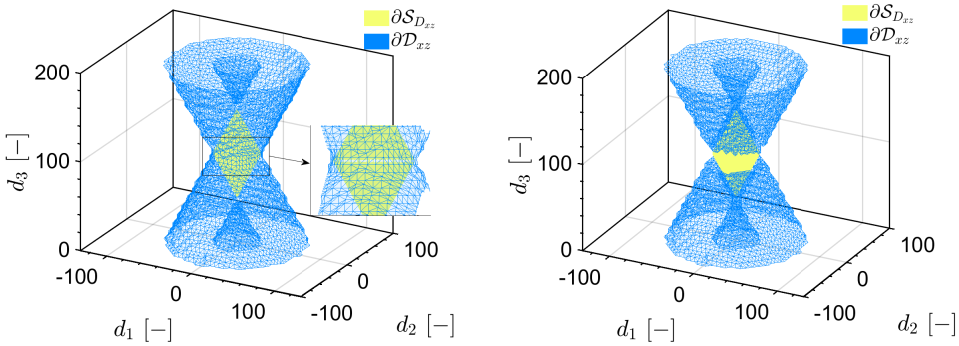

Figure 5.7: In-plane region of attraction, dead-zone and admissible sets: non-existent dead-zone set (*left*) and existing dead-zone set (*right*).

satisfied.

Assumption 5.5.3. *Every state in the admissible set neighborhood can reach the admissible set through an unconstrained single-impulse over a leader orbital period.*

In other terms, it is required that each state $\mathbf{d}$ in the vicinity of $\mathcal{S}_D$ fulfils $(\mathbf{d} \oplus \mathcal{F}_\infty) \cap \mathcal{S}_D \neq \emptyset$. Note that $\mathcal{F}_\infty = \mathcal{F}_{\infty,xz} \times \mathcal{F}_{\infty,y}$ is the unconstrained reachable set in terms of the state increment. It was demonstrated that $\mathcal{F}_{\infty,y}$ is the whole space $\mathbb{R}^2$, (see Eq. (5.91)) while $\mathcal{F}_{\infty,xz}$ is a conic surface (see Eq. (5.96)).

Remark 5.5.1. *If assumption 5.5.3 is not satisfied for some states in the close vicinity of the admissible set, those states do not belong to its region of attraction by definition. Consequently, there exist escape trajectories from the admissible set without any opportunity, over a leader orbital period, to be steered back to the admissible set with a single-impulse control. In such condition, the admissible set invariance can not be guaranteed.*

Even though the admissible set is formally defined with null dynamics ($d_0 = 0 \implies \dot{\mathbf{d}} = \mathbf{0}$) in the vector of parameters space, due to small errors the periodicity state will tend to the quasi-periodicity $|d_0| \approx 0 \implies \dot{\mathbf{d}} \neq \mathbf{0}$. This fact would potentially lead to trajectories escaping from the admissible set. In order to proof the invariance result, the dead-zone set, $\mathcal{D}_{\mathrm{dz}}$, needs to be employed. From the previous paragraph, this set is defined as the set of states whose admissible set reachability opportunities over a 2π period fall below the minimum impulse bit. This set was proven to exist or not depending on the problem parameters (mainly the minimum impulse bit $\underline{\Delta V}$).

Theorem 1. *Let consider the impulsive dynamical system* (5.78)*. Let define the set* $\mathcal{M} = \mathcal{D} \cup \mathcal{S}_D$ *as the union of the admissible set and its region of attraction. If the dead-zone set over one period is empty,* $\mathcal{D}_{\mathrm{dz}} = \emptyset$*, then for* $\mathbf{d}(\nu_0) \in \mathcal{M}$*, it holds that* $\mathbf{d}(\nu) \to \mathcal{M}$ *as* $\nu \geq \nu_0$*.*

Proof. Let recall the assumption 5.5.3 which states that for every state in the admissible set vicinity, it is possible to apply an unconstrained control steering the state back to the admissible set over the next leader orbital period: $(\mathbf{d} \oplus \mathcal{F}_\infty) \cap \mathcal{S}_D \neq \emptyset$. For states which are very close to the admissible set, the control would be small enough so that $(\mathbf{d} \oplus \mathcal{F}_{\mathrm{dz}}) \cap \mathcal{S}_D \neq \emptyset$. At this point, two cases are possible depending if the set $(\mathbf{d} \oplus \mathcal{F}_{\mathrm{dz/sat}}) \cap \mathcal{S}_D$ is empty or not. Recalling that from Eq. (5.102), Eq. (5.104) and Eq. (5.107), the dead-zone set is described as

$$\begin{aligned} \mathcal{D}_{\mathrm{dz}} &= \mathcal{D}_{\mathrm{dz},xz} \times \mathcal{D}_{\mathrm{dz},y} \\ &:= \{\mathbf{d} \in \mathbb{R}^6 \mid (\mathbf{d} \oplus \mathcal{F}_{\mathrm{dz}}) \cap \mathcal{S}_D \neq \emptyset \ \wedge \ (\mathbf{d} \oplus \mathcal{F}_{\mathrm{dz/sat}}) \cap \mathcal{S}_D = \emptyset\}. \end{aligned} \tag{5.112}$$

Then, if the dead-zone set is empty $\mathcal{D}_{\mathrm{dz}} = \emptyset$, any state in the admissible set closest neighbourhood verifies $(\mathbf{d} \oplus \mathcal{F}_{\mathrm{dz/sat}}) \cap \mathcal{S}_D \neq \emptyset$. In other terms, the closest neighbourhood of the admissible set belongs to its region of attraction as

$$\partial \mathcal{D} \cap \partial \mathcal{S}_D = \partial \mathcal{S}_D. \tag{5.113}$$

Accordingly, every escape trajectory from the admissible set is guaranteed to enter the region of attraction. Noting that, by the event-based controller of Algorithm 3), a single-impulse control instantaneously reaching the admissible set would be triggered. Then, it is concluded that the admissible set is attractive for the states on its vicinity which terminates the proof. □

Theorem 1 indicates that, under the event-based control trigger rules of Algorithm 3, the union set $\mathcal{M} = \mathcal{D} \cup \mathcal{S}_D$ is invariant under the single-impulse control.

Remark 5.5.2. *If the dead-zone set is non-empty, some states at the admissible set boundary belong to the dead-zone set. Consequently, the admissible set closest neighborhood does not belong to its region of attraction* $\partial \mathcal{D}_{\mathrm{dz}} \cap \partial \mathcal{S}_D \neq \emptyset \implies \partial \mathcal{D} \cap \partial \mathcal{S}_D \neq \partial \mathcal{S}_D$ *and* $\partial \mathcal{D}_{\mathrm{dz}} \cap \partial \mathcal{S}_D \neq \emptyset$*. Under the previous scenario, there exist trajectories escaping from the admissible set that will not directly enter into the region of attraction. Therefore, the invariance of the union set* $\mathcal{M} = \mathcal{D} \cup \mathcal{S}_D$ *is not ensured for the single-impulse control. Such condition will require the execution of a global stable control for the admissible set.*

5.5.3 Invariance under the presence of continuous disturbances

Next, the hybrid impulsive system of Eq. (5.78) is modified to account for continuous disturbances as

$$\begin{aligned} \mathbf{d}'(\nu) &= \mathbf{A}_D(\nu)\mathbf{d}(\nu) + \mathbf{a}_D(\mathbf{d}, \nu), \quad \mathbf{d}_0 \in \mathcal{D} \cup \mathcal{S}_D, \quad (\mathbf{d}, \nu) \notin \mathcal{Z}, \\ \Delta \mathbf{d}(\nu) &= \mathbf{B}_D(\nu)\Delta \mathbf{V}(\nu), \quad (\mathbf{d}, \nu) \in \mathcal{Z}, \end{aligned} \tag{5.114}$$

where $\mathbf{a}_D(\nu, \mathbf{d}) \in \mathbb{R}^6$ is an unknown Lipschitz continuous disturbance function (perturbing acceleration term transformed to the vector of parameters space). This function is assumed to behave in a way such that it does not modify the validity of the Assumptions 5.5.1-5.5.2 guaranteeing the well-posedness of the resetting set. The invariance under continuous disturbances can only be ensured if Theorem 1 conditions hold. In that case, the admissible set is attractive and the union set, $\mathcal{M}$ is an invariant set if the effect of the continuous disturbance function $\mathbf{a}_D$ is bounded as

$$\varphi_D^{\nu,\nu_0}(\mathbf{d}_0) \in \mathcal{M} \quad \text{for} \quad \mathbf{d}_0 \in \mathcal{S}_D,\ \ \nu \in [\nu_0,\ \nu_0 + 2\pi], \tag{5.115}$$

where $\varphi_D^{\nu,\nu_0} : \mathbb{R}^6 \to \mathbb{R}^6$ is the bundle of flow trajectories under the continuous disturbances system (5.114). In other words, to ensure the validity of Theorem 1, the effect of the disturbances has to be weak enough such that the admissible set instantaneous reachability windows are not suddenly closed (before they open) within the next orbital period. As a matter of fact, remaining in the admissible set region of attraction, $\mathcal{D}$, ensures that an opportunity will raise during the next orbital period as the resetting set, $\mathcal{Z}$, is contained in the region of attraction $\mathcal{Z} \subset \mathcal{D}$. Nonetheless, the case where the disturbance effect is strong enough to drift the state outside the region of attraction is also probable.

5.6 Numerical results

This section validates the proposed event-based controller for spacecraft rendezvous hovering phases. The simulations consider the Earth's oblateness and the atmospheric drag as continuous disturbances. The impact of the target eccentricity, the minimum impulse bit and the saturation threshold is assessed individually. A comparison between the aperiodic event-based algorithm and a periodic implementation of the global stable controller is carried out and discussed. The simulations has been done in a MATLAB software environment.

5.6.1 Simulation model and controller parameters

The relative motion simulator of [Arantes-Gilz16] is employed. This simulator includes non-linear Keplerian relative dynamics with Earth's oblateness and atmospheric drag effects for both leader and follower. More precisely, the simulator dynamics is

$$\begin{aligned}
\ddot{\boldsymbol{\rho}} &= -\boldsymbol{\omega}_{L/I} \times \boldsymbol{\rho} - 2\boldsymbol{\omega}_{L/I} \times \dot{\boldsymbol{\rho}} - \boldsymbol{\omega}_{L/I} \times \boldsymbol{\omega}_{L/I} \times \boldsymbol{\rho} - \frac{\mu(\mathbf{r}_t + \boldsymbol{\rho})}{\|\mathbf{r} + \boldsymbol{\rho}\|_2^3} + \frac{\mu \mathbf{r}_t}{r_t^3} \\
&\quad + \Delta\mathbf{a}_{\mathrm{grav},J2} + \Delta\mathbf{a}_{\mathrm{drag}}, \\
\dot{\boldsymbol{\rho}}^+(t_k) &= \dot{\boldsymbol{\rho}}(t_k) + \Delta\mathbf{V}(t_k), \\
\ddot{\mathbf{r}}_t(t) &= -\frac{\mu \mathbf{r}_t(t)}{r_t^3(t)} + \mathbf{a}_{\mathrm{grav},J2}(\mathbf{r}_t(t)) + \mathbf{a}_{\mathrm{drag}}(\mathbf{r}_t(t), \dot{\mathbf{r}}_t(t)),
\end{aligned}$$

where the time and state dependencies has been omitted at the right-hand side of the relative motion equation for the sake of clarity. The terms $\Delta\mathbf{a}_{\text{grav},J2}$ and $\Delta\mathbf{a}_{\text{drag}}$ are the differential non-Keplerian gravity and atmospheric drag between the follower and leader. The non-Keplerian gravity and atmospheric drag are modelled according to Eq. (2.14) and Eq. (2.21) respectively. The non-Keplerian gravity only considers the Earth's oblateness (the equatorial radius is higher than the polar one), thus $n_{\max} = 2$ with $\tilde{C}_{20} = -J_2/\sqrt{5}$ and $\tilde{C}_{21} = \tilde{C}_{22} = \tilde{S}_{21} = \tilde{S}_{22} = 0$.

The Earth's gravity parameters are $\mu = 398600.4$ km^3/s^2 and $J_2 = 1.08264\cdot 10^{-3}$ with a normalization radius of $R = 6378.14$ km. The ballistic coefficients for leader and follower are chosen in the same order of magnitude for a space station (e.g. ISS) and a cargo spacecraft (e.g. automated transfer vehicle) respectively. That is $B = 175.90$ kg/m^2 and $B_t = 139.80$ kg/m^2.

For all the simulations, the initial orbital elements of the leader are $\{h_{p,0} = 650 \text{ km},\ i_0 = 98°,\ \Omega_0 = \omega_0 = \nu_0 = 0°\}$ while the follower departs from $\boldsymbol{\rho}_0 = [400, 300, -40]^T$ m with $\dot{\boldsymbol{\rho}}_0 = \mathbf{0}$ m/s. The leader's perigee altitude h_p is fixed while the leader eccentricity is varied. The hovering region is characterized by a cuboid bounded by $\{\underline{x} = 50,\ \overline{x} = 150,\ \underline{y} = -25, \overline{y} = 25,\ \underline{z} = -25,\ \overline{z} = 25\}$ m. Note that the origin (target position) is not within the hovering region due to the chosen cuboid bounds along the in-track coordinate. This precludes the follower to collide with the leader by design. The initial relative position is not within the hovering region, thus each simulation carries out an initial approach phase by using the global stable controller of Algorithm 7 (see Appendix D). When a constrained relative periodic orbit within the hovering region is acquired, the hovering phase (which is the scope of this work) begins. For each simulation, the hovering phase lasts during ten leader orbits. The leader initial eccentricity, e_0, minimum impulse bit, $\underline{\Delta V}$, and saturation threshold $\overline{\Delta V}$ are the parameters that will be analyzed in the sequel.

For the event-based controller, the trigger rules are evaluated at a sampling rate of $\Delta\nu = 1°$. The admissible set proximity thresholds are generically taken as $(\delta_{xz} = -3,\ \delta_y = -100)$ though more reactive thresholds will also be studied. The number of discrete evaluations for the membership to the region of attraction (see Eq. (5.62)) is chosen as $n_\nu = 100$. For the global stable controller, the tuning parameters are the number of impulses N, their spacing in time τ_I and the spacing between impulses sequences τ_P. These are nominally taken as $N = 3,\ \tau_I = 30°$ and $\tau_P = 5°$, though the spacing between impulses τ_P will be varied for some simulations.

5.6.2 Impact of the leader eccentricity

The leader eccentricity has a relevant role in the linearized Keplerian relative dynamics through the state and control matrices, $\mathbf{A}_D$ and $\mathbf{B}_D$, (see Eq. (2.45)-(2.46)) and the admissible set $\mathcal{S}_D$ description (see Eq. (5.6)-(5.11)). To analyze its impact, 50 initial eccentricities of the leader are simulated. The dead-zone and saturation values are chosen as $\underline{\Delta V} = 0.1$ cm/s and $\overline{\Delta V} = 10$ cm/s.

The follower relative position, under the event-based controller, is shown for several leader eccentricities, $e_0 = \{0, 0.2, 0.4, 0.6\}$, in Fig. 5.8-5.11. For the sake of clarity, these figures focus on the hovering phase as the approach phase has been by the global stable controller of Algorithm 7 (see Appendix D). The follower relative position is within the hovering region except for some instants in the case $e_0 = 0.6$ (see the upper left corner of Fig. 5.11). However, it can be observed that the follower returns naturally to the hovering region, thus it can be concluded that the relative state was within the region of attraction (which assures that instantaneous reachability windows admissible set reachability opportunities over the next leader orbital period).

The admissible set proximity indicators evolution and triggered impulses are shown in Fig. 5.12-5.13 for $e_0 = \{0, 0.6\}$. It can observed that the admissible set proximity indicators evolve quasi-periodically which confirms the quasi-periodic assumption $|d_0| \approx 0$. The admissible set proximity indicators are also continuous (except at the instants when impulses are executed) which guarantees that reachability opportunities does not vanish instantaneously. However, for the most eccentric case, $e_0 = 0.6$ (see Fig. 5.13), the relative motion at the leader perigee induces fast changes in the proximity indicators which is oftentimes be poorly captured by the trigger rules evaluation sampling rate. This may indicate that the sampling rate should be increased for highly-eccentric orbits.

Figure 5.14 counts the event-based algorithm triggers to the single-impulse and global stable controllers for the hovering phase. The single-impulse triggers ranges between 6-19 with an average of 10.3 events. The global stable controller is not called in all the simulations. In other terms, for the scenario conditions, the single-impulse control permits to not lose track of the admissible set. This illustrates the robustness and invariance of the region of attraction $\mathcal{D}$ to the admissible set even in the presence of continuous disturbances (non-linear model, Earth oblateness and atmospheric drag).

Now, let compare the baseline event-based predictive controller with a highly-reactive version of itself and with the global stable controller. The highly reactive event-based controller decreases the trigger thresholds to $\delta_{xz} = -300$ and $\delta_y = -10^4$. This assures the triggering of impulses regardless of the admissible set proximity indicators as it can be deduced from the values in Fig. 5.12-5.13. The global stable controllers trigger impulses in a periodic way. Two versions of the previous controller are tested by probing two distinct values for the spacing between impulses as $\tau_I = \{5°, 30°\}$. The results of this comparison are shown in Fig. 5.15-5.17.

For each controller, the percentage of time the hovering region constraints are satisfied (that is $\boldsymbol{\rho} \in \mathcal{X}_{\text{hov}}$) is shown in Fig. 5.15. In this context, this is named as the control accuracy. Let recall that the objective of the hovering phase (see the problem (5.1)) is just to ensure that the relative state lies within the hovering region. In that line, the membership of the relative state within

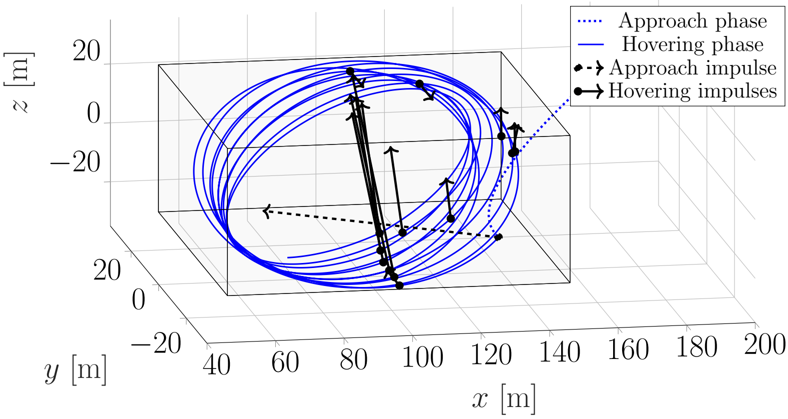

Figure 5.8: Hovering phase trajectory for $e_0 = 0$.

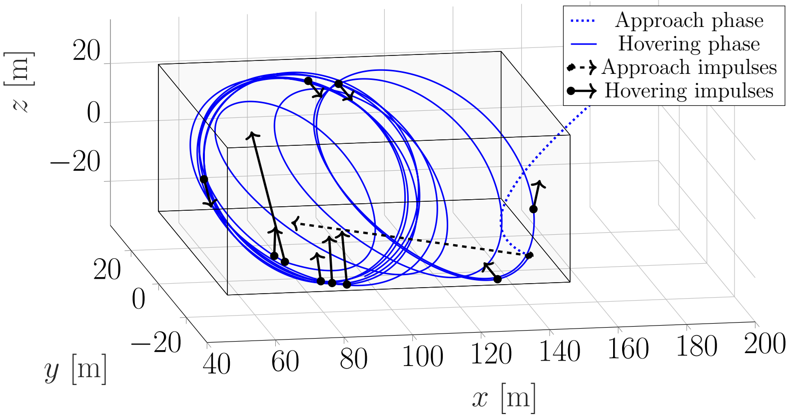

Figure 5.9: Hovering phase trajectory for $e_0 = 0.2$.

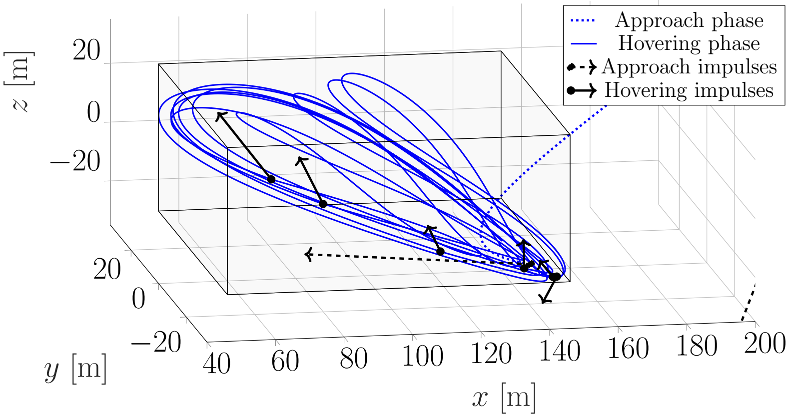

Figure 5.10: Hovering phase trajectory for $e_0 = 0.4$.

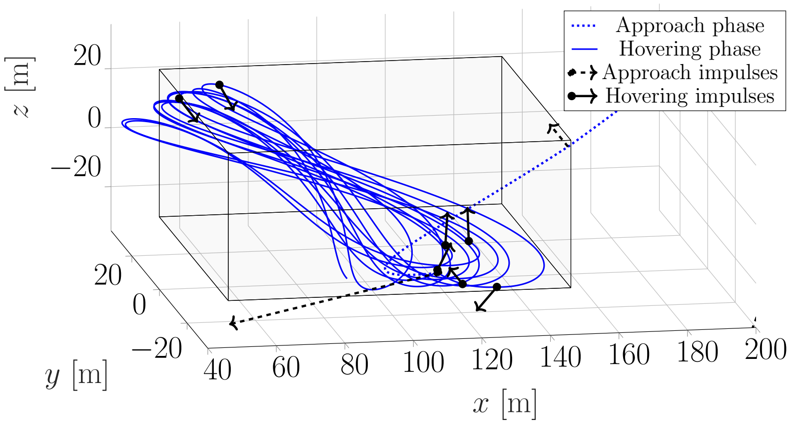

Figure 5.11: Hovering phase trajectory for $e_0 = 0.6$.

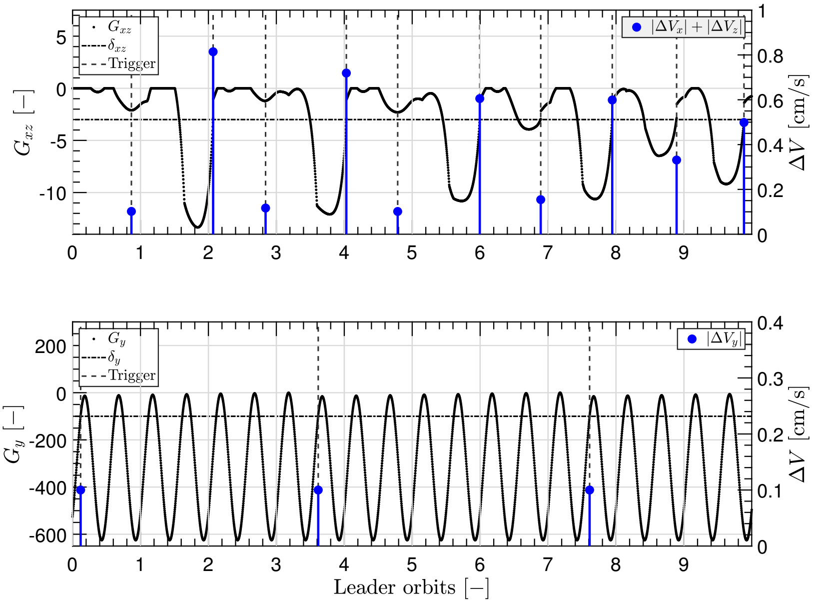

Figure 5.12: Admissible set proximity indicators and triggered impulses for $e_0 = 0$.

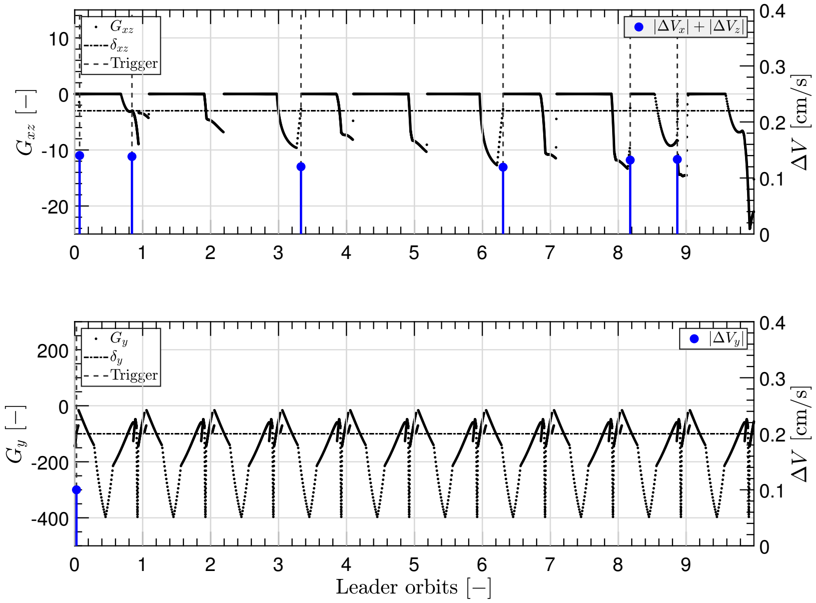

Figure 5.13: Admissible set proximity indicators and triggered impulses for $e_0 = 0.6$.

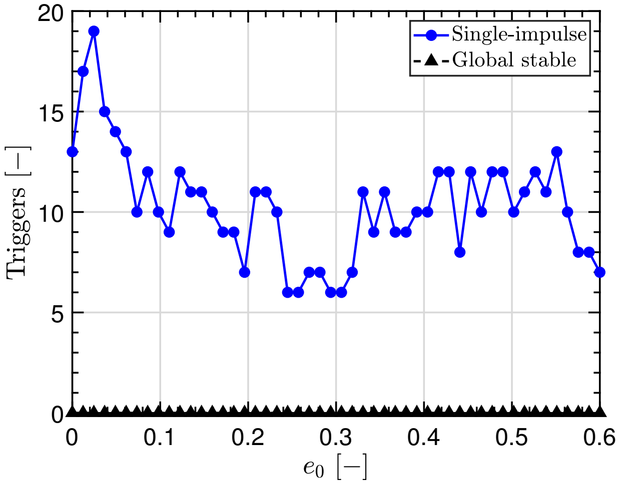

Figure 5.14: Triggers of the event-based predictive controller for different initial eccentricities of the leader.

the admissible set ensured the follower relative position is within the hovering region. Going back to Fig. 5.15, the event-based controller shows its superiority with an accuracy over 96.00% (97.91% for its highly-reactive version) in almost all the cases with an average of 98.66% (99.62% for its highly-reactive version). The periodic global stable controllers provide average results of 95.43% and 91.38% for $\tau_I = 5^\circ$ and $\tau_I = 30^\circ$ respectively. These differences may be relevant as a one-percent of constraints violation ranges from ≈ 10 minutes (if $e_0 = 0$) to ≈ 40 minutes (if $e_0 = 0.6$) in time. Let recall that the leader perigee has been fixed, thus the semi-major axis and orbital period increase with eccentricity. The periodic global stable controllers loss of accuracy, with respect to the event-based algorithm, is due to two causes. Firstly, the global controller does not guarantee constraints satisfaction between the application of impulses. Lastly, the global controller does not explicitly account for the thrusters minimum impulse bit $\underline{\Delta V}$. Consequently, most of the computed controls are not executed due to the dead-zone filtering as per Algorithm 7 (computed impulses below the minimum impulse bit are filtered by nullifying them a-posteriori).

Following the previous discussion, Fig. 5.16 shows the number of executed impulses for each one of the controllers. It should be noted that the global stable controllers compute 723 and 203 impulses (triangles in the upper part of the figure) during the hovering phase. The previous number depends on the spacing between impulses τ_I but not on the leader eccentricity. However, only 3 to 21 of them are above the minimum impulse bit. On the contrary, the event-based controller computes 6 to 19 single-impulses for the nominal case while the highly-reactive controller usually triggers 2 impulses more in average. It is worth noting that the number of applied impulses is of the same magnitude for all the controllers.

The fuel consumption, as the sum of the impulses L1-norm, is shown in Fig. 5.17. The cost is plotted for both the event-based controller and the global controllers with (w. $\underline{\Delta V}$) and without (w/o. $\underline{\Delta V}$) the filtering of the minimum impulse bit. For the instances without minimum impulse bit filtering, only the computed consumption is shown. It can be observed that the event-based controller cost is almost equivalent to the ones of the global stable controllers. More precisely, the event-based controller consumes, at most, less than 4.5 cm/s for $0 \leq e_0 \leq 0.1$, and typically less than 2 cm/s for $e_0 > 0.1$. Similar results are yielded by taking the highly-reactive thresholds as they assure less than 3 cm/s for $0 \leq e_0 \leq 0.1$ and the same performance for $e_0 > 0.1$ in average. It can be concluded that the the event-based and global stable controllers have a similar overall performance in terms of fuel consumption needs.

Now, let assess the numerical efficiency of the event-based controller with respect to the global stable algorithm. The event-based algorithm computational load comes from the evaluation of the trigger rules in Algorithm 3 and the computation of the control programs (5.66), (5.70) or (5.76) when triggered. The elapsed computation times of these modules are shown in Table 5.1. It is

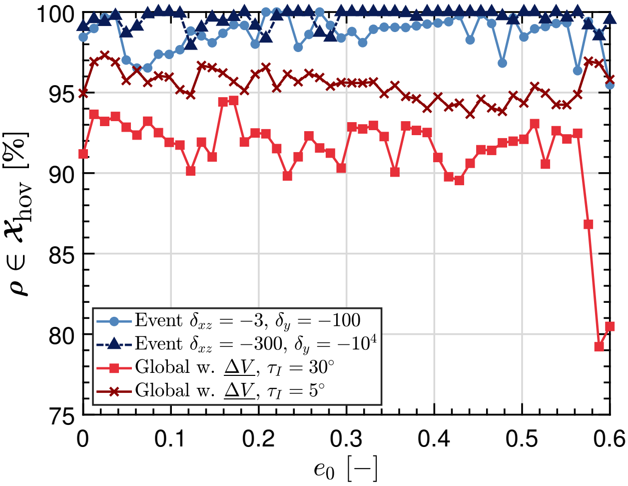

Figure 5.15: Satisfaction of the hovering region constraints for different initial eccentricities of the leader.

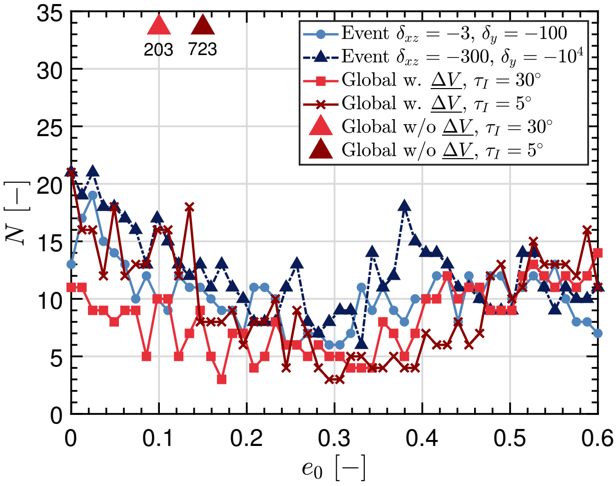

Figure 5.16: Number of impulses for different initial eccentricities of the leader.

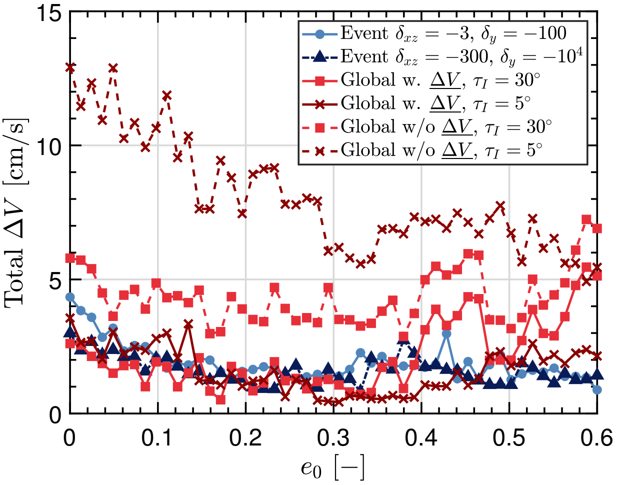

Figure 5.17: Fuel consumption for different initial eccentricities of the leader.

found that the most time-consuming task is the evaluation of the trigger rules which takes 5.895 ms in average. In comparison, the computational times of the control programs are negligible with averages of 0.0299 ms and 0.1314 ms respectively. One can notice that the worst computational time of the trigger rules evaluation highly differs from the mean. This is due to the cases where the state membership to the region of attraction has to be assessed through the computation of Eq. (5.62) condition.

	Mean	1-sigma	Max.
Trigger rules	5.895 ms	15.91 ms	118.6 ms
In-plane control	0.0299 ms	0.0624 ms	0.5813 ms
Out-of-plane control	0.1314 ms	0.0299 ms	0.4824 ms

Table 5.1: Event-based predictive controller computation times.

Table 5.2 shows the cumulated computation time for each one of the controllers along the hovering phase. The cumulated computation time for the event-based controller is between 6 and 79 seconds, whilst, the global stable controller takes between 223 and 266 seconds for $\tau_I = 5^\circ$, and between 60 and 72 seconds for $\tau_I = 30^\circ$. It can be concluded that the event-based algorithm highly reduces the computational burden with respect to the global stable controllers. This superiority of the event-based control is justified by the fact that at five times ($\Delta\nu = 1^\circ$) the global controller sampling rate ($\tau_I = 5^\circ$), the event-based controller computational load is ten times lower in average. By selecting $\tau_I = 30^\circ$, the global controller computational times are still three times higher than the event-based algorithm. Note that increasing the sampling rates, in order to reduce computational burden, has a negative impact on the control accuracy as demonstrated through Fig. 5.15.

Controller	Mean	1-sigma	Max.
Event-based	21.223 s	13.831 s	79.128 s
Global stable $\tau_I = 5°$	245.60 s	11.231 s	265.84 s
Global stable $\tau_I = 30°$	66.500 s	3.143 s	72.191 s

Table 5.2: Cumulated computation times for the hovering phase.

To resume, the comparison between the developed event-based predictive control (see Algorithm 3) and the global stable controller (see Algorithm 7 in Appendix D or [Arantes-Gilz19]) has evidenced the superiority of the event-based approach for certain aspects without disadvantages. In particular, the event-based controller always performed better in terms of control accuracy and computational burden within the range of analyzed initial eccentricities of the leader. Regarding the number of impulses and fuel consumption, it yielded similar results than the global stable controllers. This justifies the use of a local single-impulse control law for spacecraft rendezvous hovering phases. The reactivity of the event-based controller can also be adjusted by tuning the trigger thresholds (or by not awaiting for the proximity indicators to shrink) which showed a positive impact in terms of control accuracy at the expense of augmenting the number of executed impulses.

5.6.3 Impact of the impulse thresholds

The minimum impulse bit ($\underline{\Delta V}$) and saturation threshold ($\overline{\Delta V}$) may have a significant impact in the size of the region of attraction to the admissible set. As a matter of fact, these parameters (which depend on the chosen thrusters for the hovering phase) constrain the control lines where the state can instantaneously change.

Minimum impulse bit

As outlined in Section 5.5.2, the minimum impulse bit can change significantly the geometrical shape of the region of attraction (see Fig. 5.5 and Fig. 5.7). This has an impact on the event-based controller as defined in Algorithm 3. Let carry out a parametric analysis on $\underline{\Delta V}$ for a fixed initial eccentricity of the leader , $e_0 = 0.004$, and saturation threshold, $\overline{\Delta V} = 10$ cm/s. The analysis is done by simulating 50 instances where the minimum impulse bit $\underline{\Delta V}$ is varied logarithmically between 0.01 cm/s and 1 cm/s. The analyzed variables (see Fig. 5.18-5.19) are the satisfaction of the hovering region constraints (in terms of time), fuel consumption and the triggered control law.

Figure 5.18 shows the fuel consumption (in terms of the total velocity increment) and the percentage of time where the hovering region constraints are satisfied. The time percentage of constraints satisfaction is generally high with values above 97% (with several cases of 100%). However, no apparent correlations with the minimum impulse bit can be yielded. It seems to be three regions with almost a 100% of satisfaction while other intermediate regions fall to a 97-98%. These values could be potentially related to small differences in the natural trajectories after the application of the first impulse. Augmenting the minimum impulse bit has a negative impact on fuel consumption. There is an increasing trend in the total ΔV as the dead-zone is enlarged. Actually, the fuel consumption increases by four from the minimum to the maximum dead-zone threshold. Let recall that as the minimum impulse bit increases, the magnitude of the computed impulse is higher.

The event-based controller triggers are shown in Fig. 5.19. They show a decreasing trend as the minimum impulse bit increases. This makes sense as enlarging the dead-zone region reduces the number and duration of the instantaneous reachability windows. For the considered range of minimum impulse bits, no calls to the global stable controller were needed but it is evident that increasing it indefinitely would switch single-impulse strategy to the global stable control.

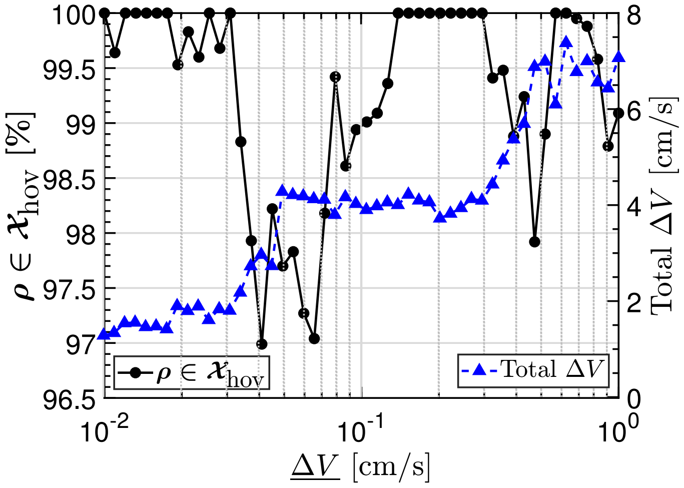

Figure 5.18: Satisfaction of the hovering region constraints and fuel consumption for several minimum impulse bits.

Saturation threshold

Now, let analyze the effect of the saturation threshold $\overline{\Delta V}$. Mimicking the previous study, let assume fixed values for the initial eccentricity of the leader

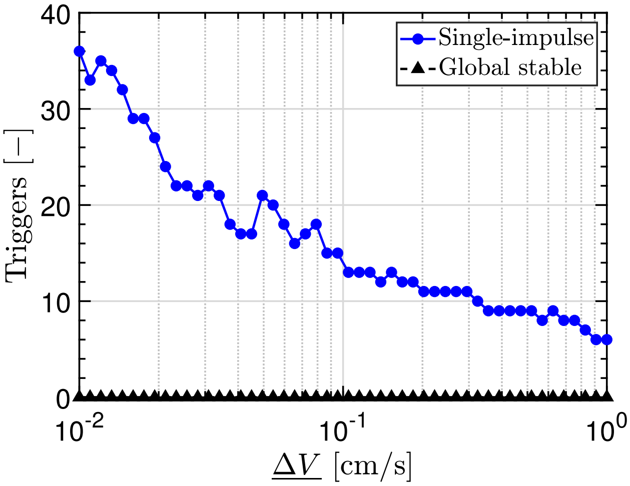

Figure 5.19: Triggers of the event-based predictive controller for several minimum impulse bits.

$e_0 = 0.004$ and the minimum impulse bit $\underline{\Delta V} = 0.1$ cm/s. Then, fifty simulations of the saturation threshold $\overline{\Delta V}$ logarithmically equispaced between 1 mm/s and 0.1 m/s are carried out. Again, the fuel consumption, event-based triggers and satisfaction of the hovering region constraints are presented in Fig. 5.20-5.21.

In Fig. 5.20, it is shown the fuel consumption (in terms of the total velocity increment) and the percentage of time where the hovering region constraints are satisfied. The fuel consumption generally increases as the saturation is enlarged. Actually, from $\overline{\Delta V} = 1$ cm/s the total ΔV remains invariant. This highlights that the tight upper bound constraint on the impulse amplitude causes it to be lower, thus the fuel consumption is keep low (but at the expense of a loss in control accuracy as it will be highlighted). Moreover, from a certain value of the saturation threshold, there are no saturated impulses and the fuel consumption remains the same. The constraints satisfaction generally increases as the saturation threshold is enlarged until a steady value is obtained. This tendency is highly correlated with the low fuel consumption and the calls to the global stable controller for the lower saturation thresholds. The analysis of the saturation threshold may help to determine the minimum required power of the control thrusters in order to obtain an invariant control behaviour.

Additionally, Fig. 5.21 shows that the global stable controller has been often triggered. Specifically, this occurs for low values of the saturation amplitude which may reduce significantly the size of the single-impulse region of attraction to the admissible set. Then, from the previous mentioned value of $\overline{\Delta V} = 1$ cm/s the number of triggers is steady and the same results are obtained.

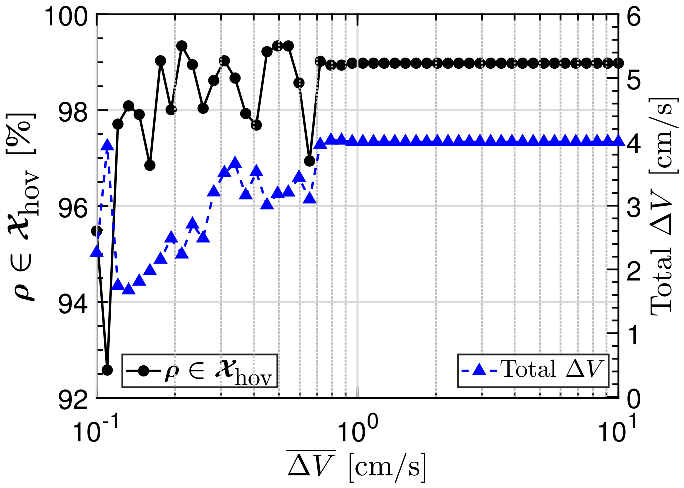

Figure 5.20: Satisfaction of the hovering region constraints and fuel consumption for several saturation thresholds.

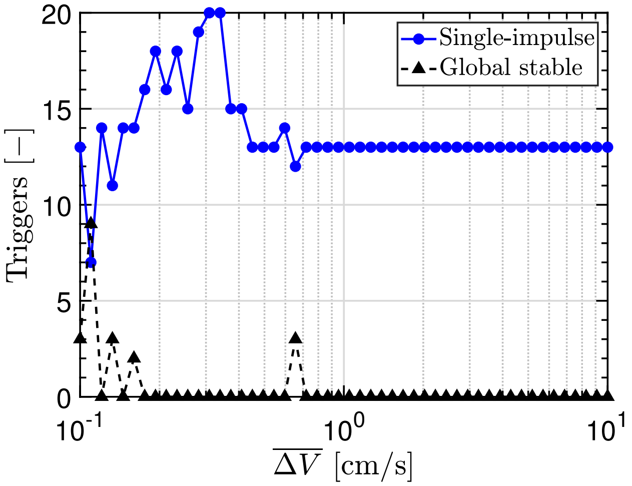

Figure 5.21: Triggers of the event-based predictive controller for several saturation thresholds.

This page is intentionally left blank.

Chapter 6

Learning-based model predictive control in the vicinity of a small body

> It does not do to leave a live dragon out of your calculations, if you live near him.
>
> J.R.R. Tolkien, *The Hobbit*

Contents

6.1 Orbit-attitude station-keeping problem 175
  6.1.1 Frames of reference 175
  6.1.2 Station-keeping problem 178
6.2 Navigation with in-situ gravity estimation 179
  6.2.1 Unscented Kalman filter 179
  6.2.2 Orbit filter 182
  6.2.3 Attitude filter 185
6.3 Model predictive guidance and control 186
  6.3.1 Guidance 186
  6.3.2 Control 188
6.4 Learning-based guidance, navigation and control . 194
  6.4.1 Integrated GNC scheme 194
  6.4.2 Gravity estimation with a satellite constellation . . . 195
6.5 Numerical results 196
  6.5.1 Simulation model, GNC parameters and performance indexes 198
  6.5.2 Efficiency of nullifying the out-of-plane control . . . 201
  6.5.3 Learning-based MPC vs non-learning MPC 202
  6.5.4 Gravity estimation with constellations of satellites . 214

This chapter develops a learning-based model predictive control scheme for orbit-attitude station-keeping in the vicinity of a small body. Maintaining a closed orbit in the vicinity of a small body is challenging due to its inhomogeneous gravity field. This orbital perturbation could degenerate a initial circular orbit into a escape or collision trajectory (see Fig. 6.1-6.2). In order to preclude this phenomena, stable orbits can be found with a stability analysis of the small body dynamical environment (e.g. [Scheeres12]). Nonetheless, in many cases, the small body gravity field is unknown at the early mission phases. In such situation, active control should be employed to avoid escape or collision trajectories. Under the previous considerations, the goal of this work is to design a closed-loop MPC for orbit-attitude station-keeping while undertaking the in-situ estimaton of the inhomogeneous gravity field. The methodology and associated results have been submitted as a journal article [Sanchez20c] and have been presented in a conference [Sanchez21b].

This work considers a high resolution camera, a light detection and ranging device (LIDAR), star trackers and gyroscopes as available on-board sensors. The star trackers and gyroscopes are able to provide measurements of the body orientation and angular velocity with respect to inertial space. The high resolution camera and LIDAR provide relative measurements with respect to landmarks. The landmarks are identified features from the initial mission phases (a fly-by or a high-orbit), as pixels, in the surface of the small body [Miller90]. The previous set of measurements (being its acquisition and processing out of the scope of this work) is employed for both the orbit-attitude determination and the inhomogeneous gravity field estimation. To this end, separate unscented Kalman filters for both the orbit and attitude cases have been developed.

The high resolution camera and LIDAR devices require continuous line-of-sight with the small body surface in order to acquire relative measurements [Li05, Hesar15]. Accordingly, the spacecraft needs to spin with the same rate of its orbital motion. For a circular orbit, under Keplerian motion, this can be enforced using passive gravity-gradient stabilization by choosing the satellite inertia to lie within the stable region. Unfortunately, in an inhomogeneous gravity field the gravity-gradient stable regions may differ from the Keplerian case depending on the gravity parameters [Wang13]. It may be also the case where it is not possible, in terms of the whole mission, to explicitly choose the inertia configuration enabling gravity-gradient stabilization. As a consequence, closed-loop attitude control has to be used in order to ensure the line-of-sight between the high resolution camera and LIDAR with the small body surface.

The overarching control goal translates to maintain a circular orbit and a stationary orientation with respect to the asteroid surface. To this end, a reference tracking approach is followed. This allows to pose the control optimization as a quadratic program by linearizing the dynamics around the reference and discretizing the problem over time. By joining the reference tracking MPC with the unscented Kalman filters, a learning-based control strategy is obtained. Initially, the control is inaccurate due to the poor knowledge of the gravity model. Nonetheless, the filter convergence (as the gravity estimates are more accurate) improves the accuracy of the model predictive control [Hewing20].

In order to speed up the gravity model estimation process, a satellite constellation concept is studied. Having multiple spacecraft simultaneously estimating its own gravity parameters offers the opportunity to gather, process and compute a centralized estimation for all the constellation. Finally, numerical simulations are carried out for a 433 Eros asteroid exploration. The results show the superior control accuracy of the learning-based MPC against a non-learning MPC. The gravity estimation of the satellite constellation is demonstrated to speed up the convergence of the gravity estimation process with respect to single satellites.

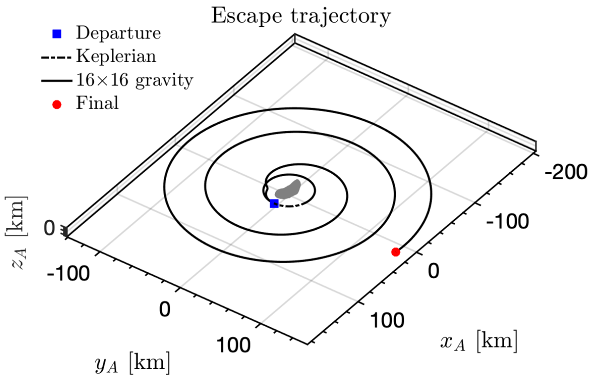

Figure 6.1: Escape trajectory due to 433 Eros inhomogeneous gravity field.

6.1 Orbit-attitude station-keeping problem

This section is devoted to present the orbit-attitude station-keeping problem. Firstly, useful frames of reference, that will be employed along this chapter, are defined. Then, the continuous form of the station-keeping problem is stated. The objective of this problem is to maintain a circular orbit with a stationary attitude relative to the small body.

6.1.1 Frames of reference

In order to understand the problem, the following frames of reference are defined. These are depicted in Fig. 6.3.

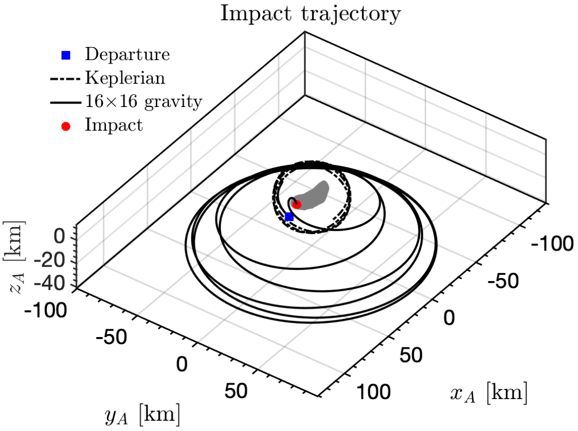

Figure 6.2: Collision trajectory due to 433 Eros inhomogeneous gravity field.

- Asteroid centered inertial frame (I): its origin is the asteroid center of mass $\mathbf{O}$. The direction $\mathbf{k}_I$ is aligned with the asteroid rotation axis while $\mathbf{i}_I$ and $\mathbf{j}_I$ are fixed directions, with respect to inertial space, contained in the asteroid equatorial plane.

- Asteroid centered fixed frame (A): its origin is the asteroid center of mass $\mathbf{O}$. This frame rotates with angular velocity $\boldsymbol{\omega}_{A/I} = [0, 0, \omega_A]^T$ with respect to the inertial frame. Then, the direction $\mathbf{k}_A$ is aligned with the asteroid rotation axis which is coincident with its major inertia axis (as it is the case for the majority of small bodies). The directions $\mathbf{i}_A$ and $\mathbf{j}_A$ are aligned with the remaining principal axes of inertia defining the asteroid equatorial plane. The rotation matrix from the inertial to the asteroid frame is given by

$$\mathbf{R}_I^A = \begin{bmatrix} \cos(\omega_A t + \theta_A) & \sin(\omega_A t + \theta_A) & 0 \\ -\sin(\omega_A t + \theta_A) & \cos(\omega_A t + \theta_A) & 0 \\ 0 & 0 & 1 \end{bmatrix}, \tag{6.1}$$

  where θ_A is the initial phasing angle.

- Local orbital frame (O): its origin is the satellite center of mass $\mathbf{r}$. It is constructed as follows

$$\mathbf{i}_O = \frac{\mathbf{r}}{\|\mathbf{r}\|_2}, \quad \mathbf{j}_O = \frac{\mathbf{k}_O \times \mathbf{i}_O}{\|\mathbf{k}_O \times \mathbf{i}_O\|_2}, \quad \mathbf{k}_O = \frac{\mathbf{r} \times \dot{\mathbf{r}}}{\|\mathbf{r} \times \dot{\mathbf{r}}\|_2}, \tag{6.2}$$

  where $\mathbf{i}_O$ is the radial direction pointing from the asteroid center of mass to the satellite. The out-of-plane direction $\mathbf{k}_O$ is aligned with the satellite angular momentum. The in-track direction $\mathbf{j}_O$ closes the right-handed frame. The rotation matrix from the inertial to the orbit frame is given by

$$\mathbf{R}_I^O = [\mathbf{i}_O \,|\, \mathbf{j}_O \,|\, \mathbf{k}_O]^T. \tag{6.3}$$

- Body frame (B): its origin is the satellite center of mass $\mathbf{r}$. Its directions $\{\mathbf{i}_B, \mathbf{j}_B, \mathbf{k}_B\}$ are aligned with the satellite principal inertia axes. This fact causes the satellite inertia matrix $\mathbf{J}$ to be constant in this frame. This frame can be related to the inertial or orbital frames through its corresponding modified Rodrigues parameter, $\boldsymbol{\sigma}_{B/I}$ and $\boldsymbol{\sigma}_{B/O}$ respectively. Using the formula given by Eq. (2.87), the respective rotation matrices can be computed as $\mathbf{R}_I^B \equiv \mathbf{R}(\boldsymbol{\sigma}_{B/I})$ and $\mathbf{R}_O^B \equiv \mathbf{R}(\boldsymbol{\sigma}_{B/O})$.

- Camera frame (C): its origin is the satellite center of mass $\mathbf{r}$. It is attached to the satellite since its $\mathbf{k}_C$ direction indicates the focal direction of the high resolution camera. It is arbitrarily chosen $\mathbf{k}_C = -\mathbf{x}_B$, such that

$$\mathbf{R}_B^C = \begin{bmatrix} 0 & 0 & 1 \\ 0 & 1 & 0 \\ -1 & 0 & 0 \end{bmatrix}. \tag{6.4}$$

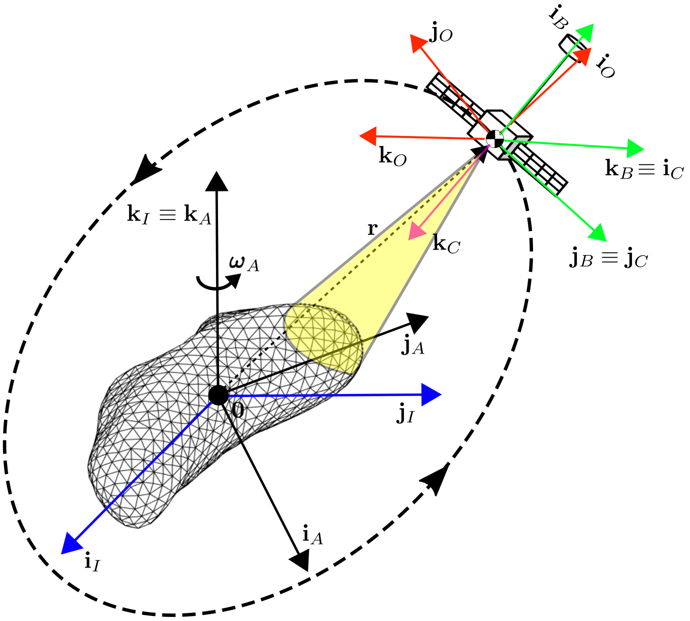

Figure 6.3: Asteroid, body, inertial and orbital reference frames.

6.1.2 Station-keeping problem

The considered station-keeping problem aims to maintain a closed orbit with a stationary attitude with respect to the small body surface. By doing so, the camera is guaranteed to have direct line-of-sight with the small body. The orbit must be designed so that it does not collide with the small body. In this work, a circular orbit would be targeted due to its simplicity. Since this requirement is related to absolute motion, the modified equinoctial elements $\tilde{\boldsymbol{\alpha}} = [p, f, g, h, k, L]^T$ (see Eq. (2.7)) are chosen to parameterize the orbital state. Let recall that the MEE evolve according to the Gauss variational equations (see Eq. (2.10)).

Maintaining a stationary orientation with respect to the small body surface can be translated to keep a stationary orientation of the body B with respect to the orbital frame O. Let recall that the radial direction $\mathbf{i}_O$ of the orbital frame is aligned with the small body and the satellite center of masses. Then, it is concluded that making the body orientation coincident with the orbital frame, that is $\boldsymbol{\sigma}_{B/O} = \mathbf{0}$, guarantees camera line-of-sight with the small body surface since this translates to $\mathbf{k}_C = -\mathbf{i}_B = -\mathbf{i}_O$. Note that the MRP (see Eq. (2.86)) would be used to parameterize the different attitudes.

The previous considerations lead to the following station-keeping problem

$$\boxed{\begin{aligned}
&\underset{\mathbf{u}(t),\mathbf{T}_u(t)}{\text{minimize}} && J(\mathbf{u}(t), \mathbf{T}_u(t)),\\
&\text{subject to} && \dot{\tilde{\boldsymbol{\alpha}}} = \tilde{\mathbf{c}}(\tilde{\boldsymbol{\alpha}}) + \tilde{\mathbf{A}}(\tilde{\boldsymbol{\alpha}})\mathbf{a}_{\text{grav}}(\tilde{\boldsymbol{\alpha}}) + \tilde{\mathbf{A}}(\tilde{\boldsymbol{\alpha}})\mathbf{u},\\
&&& \dot{\boldsymbol{\sigma}}_{B/O} = \mathbf{C}(\boldsymbol{\sigma}_{B/O})[\boldsymbol{\omega}_{B/I} - \mathbf{R}(\boldsymbol{\sigma}_{B/O})\boldsymbol{\omega}^O_{O/I}],\\
&&& \mathbf{J}\dot{\boldsymbol{\omega}}_{B/I} + \boldsymbol{\omega}_{B/I} \times (\mathbf{J}\boldsymbol{\omega}_{B/I}) = \mathbf{T}_{\text{grav}} + \mathbf{T}_u,\\
&&& -\overline{\mathbf{u}} \leq \mathbf{u}(t) \leq \overline{\mathbf{u}},\\
&&& -\overline{\mathbf{T}}_u \leq \mathbf{T}_u(t) \leq \overline{\mathbf{T}}_u,\\
&&& \mathbf{A}_{\text{ref}}\tilde{\boldsymbol{\alpha}}(t) = \mathbf{b}_{\text{ref}}, \quad t_0 \leq t \leq t_f,\\
&&& \boldsymbol{\sigma}_{B/O}(t) = \mathbf{0},\\
&&& \tilde{\boldsymbol{\alpha}}(t_0) = \tilde{\boldsymbol{\alpha}}_0, \quad \boldsymbol{\sigma}_{B/O}(t_0) = \boldsymbol{\sigma}_{B/O,0}, \quad \boldsymbol{\omega}_{B/I}(t_0) = \boldsymbol{\omega}_{B/I,0},
\end{aligned}} \tag{6.5}$$

where

$$\mathbf{A}_{\text{ref}} = \begin{bmatrix} \mathbf{I} & \mathbf{0}_{3\times3} \\ \mathbf{0}_{3\times3} & \mathbf{0}_{3\times3} \end{bmatrix}, \quad \mathbf{b}_{\text{ref}} = \begin{bmatrix} \breve{a} \\ \mathbf{0}_{5\times1} \end{bmatrix}. \tag{6.6}$$

Only the inhomogeneous gravity field perturbation, $\mathbf{a}_{\text{grav}}$, has been explicitly considered because it is the most dominant one in low asteroid orbits. The term $\breve{a}$ is the desired semi-major axis of the circular orbit. Let recall that the relation between the semi-major axis and eccentricity with the MEE (see Eq. (2.7)) is $a = p/(1-e^2)$ and $e = \sqrt{f^2+g^2}$. Then, in order to maintain a circular orbit $\breve{e}$ with a given orbital radius $\breve{a}$, the MEE have to fulfil $\breve{p} = \breve{a}$ and $\breve{f} = \breve{g} = 0$.

6.2 Navigation with in-situ gravity estimation

This section describes the employed navigation strategy in the vicinity of a small body. Unlike previous applications of this manuscript where the state was exactly known, in this case, the state and some model parameters (the ones related to the small body inhomogeneous gravity field) have to be estimated. To this end, unscented Kalman filtering [Wan00] is employed. Separate filters are designed for orbit and attitude respectively. This accounts for the higher sampling frequencies of attitude sensors with respect to ones related with the orbital state determination. The navigation measurements are provided by a high resolution camera, a LIDAR, star-trackers and gyroscopes. The simplified measurement models of the previous devices are subsequently described (the details on their own data acquisition and processing are out of the scope of this dissertation).

6.2.1 Unscented Kalman filter

The UKF mainly relies on the unscented transform (UT) technique. The UT is a particle-based tool to compute the result of applying a non-linear function to a Gaussian distribution. The UT approximates the resulting statistical distribution (which is not Gaussian if the function is non-linear [NRC12]) to a Gaussian one characterized by a mean and a covariance matrix. Let define an initial Gaussian distribution as $\mathbf{y} \sim N_n(\hat{\mathbf{y}}, \mathbf{\Sigma}_\mathbf{y})$. Then, let define a generic non-linear function as $\mathbf{f}(\mathbf{y}) : \mathbb{R}^n \to \mathbb{R}^m$. Finally, let define the result of transforming the initial distribution $\mathbf{y}$ with the non-linear function $\mathbf{f}$ as $\mathbf{z} = \mathbf{f}(\mathbf{y})$. Under the Gaussian assumption the result is statistically characterized by $\mathbf{z} \sim N_m(\hat{\mathbf{z}}, \mathbf{\Sigma}_\mathbf{z})$. Consequently, the non-linear transformation of the initial function is reduced to the computation of the new mean $\hat{\mathbf{z}}$ and covariance matrix $\mathbf{\Sigma}_\mathbf{z}$. In order to do so, it follows a simplified particle-based approach. The particles, named as sigma points $\boldsymbol{\chi}$, are generated by spreading $2n+1$ deterministic samples around the initial distribution mean

$$\boldsymbol{\chi}_\mathbf{y}^{[k]} = \hat{\mathbf{y}} + \mathrm{sgn}(k) \cdot \left(\sqrt{(n+\lambda)\mathbf{\Sigma}_\mathbf{y}}\right)_{|k|}, \quad k = -n \dots n, \tag{6.7}$$

where the subindex $|k|$ denotes each column of the matrix. The scalar λ is a tuning parameter which controls how spreaded apart from the mean are the sigma points distributed. Then, the transforming function $\mathbf{f}$ is applied to each one of the sigma points

$$\boldsymbol{\chi}_\mathbf{z}^{[k]} = \mathbf{f}(\boldsymbol{\chi}_\mathbf{y}^{[k]}), \tag{6.8}$$

which gives the samples of the resulting distribution. Finally, through a weighted mean, the mean $\hat{\mathbf{z}}$ and covariance $\mathbf{\Sigma}_\mathbf{z}$ of the final distribution $\mathbf{z}$ are reconstructed

$$\hat{\mathbf{z}} = \sum_{k=-n}^{n} w_m^{[k]} \boldsymbol{\chi}_\mathbf{z}^{[k]}, \quad \mathbf{\Sigma}_\mathbf{z} = \sum_{k=-n}^{n} w_c^{[k]} (\boldsymbol{\chi}_\mathbf{z}^{[k]} - \hat{\mathbf{z}})(\boldsymbol{\chi}_\mathbf{z}^{[k]} - \hat{\mathbf{z}})^T. \tag{6.9}$$

The UT process comprises Eq. (6.7)-(6.9). Other state-of-the-art techniques transforming Gaussian distributions with non-linear functions are the Monte Carlo method and the extended Kalman filter (EKF). A sketch of these approaches, along with the UKF, is shown in Fig. 6.4. The Monte Carlo method transforms a high number of random realizations, which yields a very accurate result at the expense of a high computational burden. The EKF linearizes the non-linear function around the initial mean which allows to use analytic formulas for the mean and covariance propagation. Its main advantage is the reduction in the computational burden, because only one sample is propagated, though the Jacobian matrix of the system has to be obtained. Its main drawback is that the linearization may result in inaccurate predictions if the distribution is spread from the mean. On the other hand, the employed UKF transformation technique (UT) is usually more accurate than the EKF because the sigma points propagation is exact as the non-linear function is directly employed. Moreover, no computation of the Jacobian matrix is required which simplifies its implementation. The UKF also reduces the high computational burden of the Monte Carlo approach as only a reduced number of samples is propagated. Due to the previous fact, it is also less accurate in comparison.

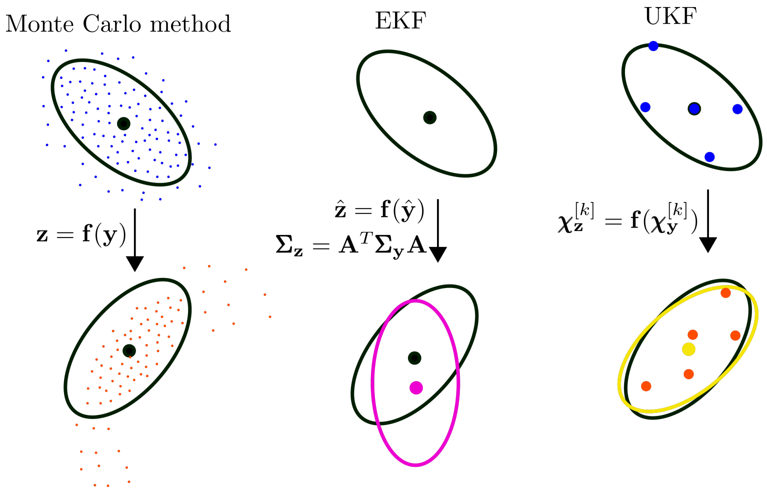

Figure 6.4: Monte Carlo (black), EKF (pink) and UKF (yellow) approaches for uncertainty propagation.

The UKF aims to recursively obtain an statistical estimation of the state $\mathbf{y} \sim N_n(\hat{\mathbf{y}}, \boldsymbol{\Sigma}_{\mathbf{y}})$ through its mean $\hat{\mathbf{y}}$ and covariance $\boldsymbol{\Sigma}_{\mathbf{y}}$. In order to do so, it often receives a vector of measurements modelled as $\mathbf{z} \sim N_m(\hat{\mathbf{z}}, \boldsymbol{\Sigma}_{\mathbf{z}})$ being $\hat{\mathbf{z}}$ its mean and $\boldsymbol{\Sigma}_{\mathbf{z}}$ its covariance matrix. The state and measurements are related through the transformation function $\mathbf{g}(\mathbf{y}) : \mathbb{R}^n \rightarrow \mathbb{R}^m$. This function transforms the state to the space of measurements. Along the interval without measurements, the state and its distribution evolves dynamically (named as process in the UKF nomenclature). Let define the process function as $\mathbf{f}(\mathbf{y}) : \mathbb{R}^n \to \mathbb{R}^n$. The process function may not capture the real evolution of the system (e.g. unmodelled dynamics). Assuming the process errors are not biased, their uncertainty is simply considered by the addition of the process uncertainty covariance matrix $\mathbf{\Sigma_f} \in \mathbb{R}^{n \times n}$ after the process UT. The process uncertainty covariance matrix is usually an unknown parameter (since it represents the mismatch between modelling and reality) which has to be tuned or inferred.

Using the previous definitions, the unscented Kalman filter is presented in Algorithm 4. Given an initial mean $\hat{\mathbf{y}}_0$ and covariance $\mathbf{\Sigma}_{\mathbf{y}_0}$ of the state, the UT of the previous distribution with the process function $\mathbf{f}$ is applied in step 2. The propagation comprises the duration of the interval between measurements Δt_{UKF}. The results are the state mean $\hat{\mathbf{y}}$ and covariance $\mathbf{\Sigma_y}$ after the process. After that, the process uncertainty covariance $\mathbf{\Sigma_f}$ is added to the resulting state covariance in step 3. The next step 4 applies the UT of the processed state with the function $\mathbf{g}$ transforming the state to the space of measurements. This yields the expected measurements distribution $\mathbf{z}' \sim N_m(\hat{\mathbf{z}}', \mathbf{\Sigma}_{\mathbf{z}'})$ after the process. Since the measurements are also uncertain, their covariance matrix $\mathbf{\Sigma_z}$ is added to the expected one in step 5.

The step 6 computes the cross-correlation matrix $\mathbf{H} \in \mathbb{R}^{n \times m}$ between the processed state $\mathbf{f}(\mathbf{y}_0)$ and its expected measurements $\mathbf{z}'$. Then, the Kalman gain $\mathbf{K} \in \mathbb{R}^{n \times m}$ is computed in step 7. The subsequent step 8 uses the Kalman gain and the vector of measurements $\mathbf{z}$ to update the expected estimation mean $\hat{\mathbf{y}}$ and covariance $\mathbf{\Sigma_y}$. The update in the state estimation is based on the mismatch between the current measurements $\mathbf{z}$ and the average of the expected ones $\mathbf{z}'$. Note that the state covariance matrix always diminish.

The steps 2-8 correspond to the standard UKF algorithm as presented in [Wan00]. However, two additional steps (9-10) have been added with the purpose of updating the process uncertainty $\mathbf{\Sigma_f}$. Additionally, it is assumed that the measurements uncertainty $\mathbf{\Sigma_z}$ is characterized by the sensors datasheet, thus it is a known data. As previously mentioned, the state update is proportional to the discrepancy between the measurements and the mean of the expected ones from the process. This mismatch can be related to discrepancies between the process function and the real system dynamics. Then, the process mismatch can be quantified by the Kalman innovation as $\hat{\mathbf{w}} = \mathbf{K}(\mathbf{z} - \hat{\mathbf{z}}')$ (see step 9) which is the quantity added to the state in the Kalman update. Finally, by using the previous Kalman innovation, step 10 updates the process uncertainty covariance matrix. Following [Akhlaghi17], the process uncertainty covariance matrix is updated with a fading factor, $\eta \in [0, 1]$, which balances the importance given to the present innovation with respect to the past history.

The unscented transform, in Eq. (6.9), and the step 6 of the UKF Algorithm 4 require the computation of weighted means with weights w_m and w_c respectively. Following the choice of the initial work [Wan00], these weights

Algorithm 4: UKF with process noise estimation

```
begin
    Apply the UT Eq. (6.7)-(6.9) to the process:
      $(\hat{\mathbf{y}}, \mathbf{\Sigma}_{\mathbf{y}}) \equiv \mathrm{UT}(\hat{\mathbf{y}}_0, \mathbf{\Sigma}_{\mathbf{y}_0}, \mathbf{f}, \Delta t_{\mathrm{UKF}})$;
    Add the uncertainty of the process: $\mathbf{\Sigma}_{\mathbf{y}} \leftarrow \mathbf{\Sigma}_{\mathbf{y}} + \mathbf{\Sigma}_{\mathbf{f}}$;
    Apply the UT Eq. (6.7)-(6.9) to transform from state to
      measurement space $(\hat{\mathbf{z}}', \mathbf{\Sigma}_{\mathbf{z}'}) \equiv \mathrm{UT}(\hat{\mathbf{y}}, \mathbf{\Sigma}_{\mathbf{y}}, \mathbf{g})$;
    Add the uncertainty of measurements: $\mathbf{\Sigma}_{\mathbf{z}'} \leftarrow \mathbf{\Sigma}_{\mathbf{z}'} + \mathbf{\Sigma}_{\mathbf{z}}$;
    Compute the cross-correlation matrix between the state and
      measurements: $\mathbf{H} = \sum_{k=-n}^{n} w_c^{[k]} \left(\boldsymbol{\chi}_{\mathbf{y}}^{[k]} - \hat{\mathbf{y}}\right) \left(\boldsymbol{\chi}_{\mathbf{z}'}^{[k]} - \hat{\mathbf{z}}'\right)^T$;
    Compute the Kalman gain: $\mathbf{K} = \mathbf{H}\mathbf{\Sigma}_{\mathbf{z}'}^{-1}$;
    Update the state estimation with the vector of measurements:
      $\hat{\mathbf{y}} \leftarrow \hat{\mathbf{y}} + \mathbf{K}(\mathbf{z} - \hat{\mathbf{z}}'), \quad \mathbf{\Sigma}_{\mathbf{y}} \leftarrow \mathbf{\Sigma}_{\mathbf{y}}(\mathbf{I} - \mathbf{H}\mathbf{K}^T)$;
    Compute the Kalman innovation: $\mathbf{w} = \mathbf{K}(\mathbf{z} - \hat{\mathbf{z}}')$;
    Update the process uncertainty covariance matrix:
      $\mathbf{\Sigma}_{\mathbf{f}} \leftarrow (1 - \eta)\mathbf{w}\mathbf{w}^T + \eta\mathbf{\Sigma}_{\mathbf{f}}$;
end
```

are defined as

$$\begin{aligned} w_m^{[0]} &= \frac{\lambda}{n+\lambda}, \quad w_c^{[0]} = \frac{\lambda}{n+\lambda} + (1 - \theta^2 + \beta), \\ w_c^{[k]} &= w_m^{[k]} = \frac{1}{2(n+\lambda)} \quad \text{for} \quad k \neq 0, \end{aligned} \tag{6.10}$$

where λ, θ and β are tuning parameters. The variable λ controls the spread of sigma points. The variables θ and β are exclusively related to the weight $w_c^{[0]}$ of the covariance matrix reconstruction. The tuning parameter β is used to encode information about the underlying probabilistic distribution. If the real statistical distribution, after the UT, is Gaussian its optimal choice is $\beta = 2$. The variable θ is used to control the relevance of the mean with respect to the spread of sigma points in the reconstruction of the covariance matrix.

6.2.2 Orbit filter

The orbit estimation process infers the orbital state, in terms of MEE, and the small body gravity field spherical harmonics up to a certain degree and order $n_{\mathrm{orb}} \times n_{\mathrm{orb}}$. The previous variables are grouped in the orbital extended state $\mathbf{y}_{\mathrm{orb}} \in \mathbb{R}^{6+\sum_{n=2}^{n_{\mathrm{orb}}} 2n+1}$

$$\mathbf{y}_{\mathrm{orb}} = [p,\ f,\ g,\ h,\ k,\ L,\ \widetilde{\mathbf{CS}}_{\mathrm{orb}}^T]^T, \tag{6.11}$$

where the vector $\widetilde{\mathbf{CS}}_{\mathrm{orb}} \in \mathbb{R}^{\sum_{n=2}^{n_{\mathrm{orb}}} 2n+1}$ stacks the gravity parameters as

$$\widetilde{\mathbf{CS}}_{\mathrm{orb}} = \left[\tilde{C}_{20}, \ldots, \tilde{C}_{n_{\mathrm{orb}},n_{\mathrm{orb}}}, \tilde{S}_{21}, \ldots \tilde{S}_{n_{\mathrm{orb}},n_{\mathrm{orb}}}\right]^T. \tag{6.12}$$

Orbit process function

The orbit process dynamics combines the MEE Gauss variational equations (see Eq. (2.10)) with constant evolutions of the spherical harmonics

$$\dot{\mathbf{y}}_{\text{orb}} = \begin{bmatrix} \tilde{\mathbf{c}}(\tilde{\boldsymbol{\alpha}}) + \tilde{\mathbf{A}}(\tilde{\boldsymbol{\alpha}})\mathbf{a}_{\text{grav}}(\tilde{\boldsymbol{\alpha}}, \widetilde{\mathbf{CS}}_{\text{orb}}) + \tilde{\mathbf{A}}(\tilde{\boldsymbol{\alpha}})\mathbf{u} \\ 0 \\ \vdots \\ 0 \end{bmatrix}. \tag{6.13}$$

Note that only the orbital perturbation of the small body inhomogeneous gravity field, up to $n_{\text{orb}} \times n_{\text{orb}}$ degree and order, is considered. The solar radiation pressure and Sun third-body gravity perturbations are very weak in low orbits (when compared to the small body inhomogeneous gravity field), thus they have not been added in the process. For an interval duration of $\Delta t^{\text{orb}}_{\text{UKF}}$ between measurements, a simple forward Euler integration method defines the orbit process function

$$\mathbf{f}_{\text{orb}}(\mathbf{y}_{\text{orb}}) = \mathbf{y}_{\text{orb}} + \Delta t^{\text{orb}}_{\text{UKF}}\dot{\mathbf{y}}_{\text{orb}}, \tag{6.14}$$

where the extended state $\mathbf{y}_{\text{orb}}$ and the orbit process dynamics $\dot{\mathbf{y}}_{\text{orb}}$ are evaluated at the beginning of the interval.

Orbit measurements transformation function

The orbital navigation sensors are a high resolution camera and a LIDAR. They provide relative measurements with respect to landmarks. The landmarks are previously identified features on the small body surface (e.g. craters). Specifically, the high resolution camera provides the pixel location of a landmark, in the camera plane, as $\mathbf{p}_q = [p_{x_q}, p_{y_q}]^T$. The LIDAR measures the ranging distance between the satellite and the landmark ρ_q. The subindex q denotes the corresponding landmark. Then, for a current instant, the available set of orbital measurements $\mathbf{z}_{\text{orb}} \in \mathbb{R}^{3l}$ is

$$\mathbf{z}_{\text{orb}} = \begin{bmatrix} \mathbf{p}_{q'_1} \\ \vdots \\ \mathbf{p}_{q'_l} \\ \rho_{q'_1} \\ \vdots \\ \rho_{q'_l} \end{bmatrix}, \quad q' = \{q \in \mathbb{N} \mid (\mathbf{r}^A - \mathbf{r}^A_{\text{lmk},q}) \cap \Omega_{\text{body}} = \emptyset\}, \tag{6.15}$$

where the prime symbol refers to the landmarks with line-of-sight with respect to the satellite. The term Ω_{body} is the volume of the small body. This is a necessary but not sufficient condition for the landmarks to be visible from the high resolution camera and LIDAR. The visibility of a landmark also depends on the small body surface lighting conditions and the orientation of the camera focal direction. The first aspect has not been modelled in this dissertation for the sake of simplicity. The second aspect is considered and is the main motivation to develop an attitude controller. The term l refers to the limitation in the maximum number of landmarks that can be processed by the feature identification algorithm (out of the scope of this work) between filter calls.

Now, let relate the orbital extended state $\mathbf{y}_{\text{orb}}$ to its corresponding measurements $\mathbf{z}_{\text{orb}}$ through the transformation function $\mathbf{g}_{\text{orb}} : \mathbb{R}^{6+\sum_{n=2}^{n_{\text{orb}}} 2n+1} \to \mathbb{R}^{3l}$. Let define the relative position between landmarks and the satellite center of mass as

$$\boldsymbol{\rho}_q^A = \mathbf{r}^A - \mathbf{r}_{\text{lmk},q}^A = [x_q, y_q, z_q]^T. \tag{6.16}$$

Note that the landmarks coordinates are constant in the asteroid centered frame A. The transformation from MEE, $\tilde{\boldsymbol{\alpha}}$, to inertial Cartesian coordinates, $\mathbf{r}^I$, is given by Eq. (2.11). Let define the previous mapping as the function $\mathbf{f}_{\tilde{\boldsymbol{\alpha}}\to\mathbf{r}} : \mathbb{R}^6 \to \mathbb{R}^3$ which receives a MEE and computes the corresponding Cartesian position in inertial space. Using the previous mapping function and transforming the landmarks position to inertial space yields

$$\boldsymbol{\rho}_q^I = \mathbf{f}_{\tilde{\boldsymbol{\alpha}}\to\mathbf{r}}(\tilde{\boldsymbol{\alpha}}) - (\mathbf{R}_I^A)^T \mathbf{r}_{\text{lmk},q}^A, \tag{6.17}$$

where the rotation matrix $\mathbf{R}_A^I$ has been defined in Eq. (6.1). Then, the LIDAR ranging measurement can be computed as

$$\rho_q = ||\boldsymbol{\rho}_q^I||_2. \tag{6.18}$$

To obtain the pixels coordinates of the high resolution camera, the relative distance has to be projected into the camera plane. Let start by expressing the satellite-landmark relative distance into the camera frame

$$\boldsymbol{\rho}_q^C = \mathbf{R}_B^C \mathbf{R}_O^B(\boldsymbol{\sigma}_{B/O}) \mathbf{R}_I^O \boldsymbol{\rho}^I, \tag{6.19}$$

where $\mathbf{R}_I^O$, which depends on the satellite position and velocity, is given by Eq. (6.3). The orientation of the satellite arises through the MRP, $\boldsymbol{\sigma}_{B/O}$. Since the camera focal direction is aligned with the z_C direction, the landmark coordinates, u_q and v_q, in the image plane are expressed by

$$u_q = f_{\text{foc}} \frac{x_q}{z_q}, \quad v_q = f_{\text{foc}} \frac{y_q}{z_q}, \tag{6.20}$$

where f_{foc} is the camera focal length. Finally, the pixel row and column $\mathbf{p}_q$ are obtained as

$$\mathbf{p}_q = \begin{bmatrix} p_{u_q} \\ p_{v_q} \end{bmatrix} = \begin{bmatrix} \lfloor u_q/p_{\text{w}} \rfloor \\ \lfloor v_q/p_{\text{w}} \rfloor \end{bmatrix}, \tag{6.21}$$

where p_{w} is the pixel width and the floor operator $\lfloor\rfloor$ guarantees the resulting pixel is a natural number. Let recall that the pixel has to be within the camera resolution in order to be visible. Under the previous steps of Eq. (6.17)-(6.21), the orbit transformation function can be summarized to

$$\mathbf{g}_{\text{orb}}(\mathbf{y}_{\text{orb}}) = \left[\mathbf{p}_{q_1'}^T(\tilde{\boldsymbol{\alpha}}), \ldots, \mathbf{p}_{q_l'}^T(\tilde{\boldsymbol{\alpha}}), \rho_{q_1'}(\tilde{\boldsymbol{\alpha}}), \ldots, \rho_{q_l'}(\tilde{\boldsymbol{\alpha}})\right]^T. \tag{6.22}$$

6.2.3 Attitude filter

The attitude filter infers the satellite rotational state (MRP and angular velocity), the small body spherical harmonics up to a certain degree and order $n_{\text{att}} \times n_{\text{att}}$ (sensed through the gravity-gradient torque) and the gyroscope bias. The previous variables are grouped in the attitude extended state $\mathbf{y}_{\text{att}} \in \mathbb{R}^{9+\sum_{n=2}^{n_{\text{att}}} 2n+1}$

$$\mathbf{y}_{\text{att}} = [\boldsymbol{\sigma}_{B/I}^T,\ \boldsymbol{\omega}_{B/I}^T,\ \widetilde{\mathbf{CS}}_{\text{att}}^T,\ \Delta\boldsymbol{\omega}_{\text{gyro}}^T]^T, \tag{6.23}$$

where $\boldsymbol{\sigma}_{B/I}$ and $\boldsymbol{\omega}_{B/I}$ are the body orientation and angular velocity with respect to the inertial frame. The vector $\widetilde{\mathbf{CS}}_{\text{att}}$ groups the gravity parameters as in Eq. (6.12) but up to $n_{\text{att}} \times n_{\text{att}}$ degree and order. The attitude filter gravity degree and order shall be chosen as $n_{\text{att}} < n_{\text{orb}}$ because the inhomogeneous gravity effects are lesser observable through the gravity-gradient torque. The variable $\Delta\boldsymbol{\omega}_{\text{gyro}}$ is the gyroscope bias which is also estimated.

The attitude filter computes the body orientation with respect to the inertial frame $\boldsymbol{\sigma}_{B/I}$. This may seem contradictory as the station-keeping problem (6.5) aims to maintain a stationary orientation with respect to the orbital frame as $\boldsymbol{\sigma}_{B/O} = \mathbf{0}$. The motivation behind this procedure is that the attitude sensors (star-trackers and gyroscopes) provide measurements with respect to inertial space, hence the state and measurements relation is direct. Nonetheless, by joining the attitude and orbit filter outputs, the orientation with respect to the orbital frame can be reconstructed by applying the MRP composition rule (see Eq. (2.88))

$$\begin{gathered}\boldsymbol{\sigma}_{B/I} \xrightarrow{-\boldsymbol{\sigma}_{O/I}} \boldsymbol{\sigma}_{B/O},\\ \boldsymbol{\sigma}_{B/O} = \frac{\left(1-\|\boldsymbol{\sigma}_{O/I}\|_2^2\right)\boldsymbol{\sigma}_{B/I} - \left(1-\|\boldsymbol{\sigma}_{B/I}\|_2^2\right)\boldsymbol{\sigma}_{O/I} - 2\boldsymbol{\sigma}_{B/I}\times\boldsymbol{\sigma}_{O/I}}{1+\left(\|\boldsymbol{\sigma}_{O/I}\|_2\|\boldsymbol{\sigma}_{B/I}\|_2\right)^2 - 2\boldsymbol{\sigma}_{O/I}^T\boldsymbol{\sigma}_{B/I}},\end{gathered} \tag{6.24}$$

where $\boldsymbol{\sigma}_{O/I} \equiv \boldsymbol{\sigma}_{O/I}(\tilde{\boldsymbol{\alpha}})$ is the MRP expressing the orientation of the orbital frame with respect to inertial space. This orientation depends on the orbit MEE (see Eq. (6.3)).

Attitude process function

The attitude process dynamics is

$$\dot{\mathbf{y}}_{\text{att}} = \begin{bmatrix} \mathbf{C}(\boldsymbol{\sigma}_{B/I})\boldsymbol{\omega}_{B/I} \\ \mathbf{J}^{-1}[\mathbf{T}_{\text{grav}} + \mathbf{T}_u - \boldsymbol{\omega}_{B/I}\times(\mathbf{J}\boldsymbol{\omega}_{B/I})] \\ 0 \\ \vdots \\ 0 \end{bmatrix}, \tag{6.25}$$

where again constant evolutions of the gravity parameters and gyroscope bias are assumed through the process. Since measurements are received at intervals with a duration of $\Delta t^{\text{att}}_{\text{UKF}}$, a forward Euler integration method yields the attitude process function

$$\mathbf{f}_{\text{att}}(\mathbf{y}_{\text{att}}) = \mathbf{y}_{\text{att}} + \Delta t^{\text{att}}_{\text{UKF}}\dot{\mathbf{y}}_{\text{att}}, \tag{6.26}$$

where the attitude extended state is evaluated at the beginning of the interval.

Attitude measurements transformation function

The attitude sensors are a star-tracker and gyroscopes. In a simplified way, it is considered that the star-tracker provides a direct measurement of the body orientation with respect to the inertial frame, namely $\boldsymbol{\sigma}_{\text{star}}$. The gyroscopes provide the body angular velocity with respect to the inertial frame as $\boldsymbol{\omega}_{\text{gyro}}$. Then, the set of attitude measurements is $\mathbf{z}_{\text{att}} \in \mathbb{R}^6$

$$\mathbf{z}_{\text{att}} = \begin{bmatrix} \boldsymbol{\sigma}_{\text{star}} \\ \boldsymbol{\omega}_{\text{gyro}} \end{bmatrix}. \tag{6.27}$$

In this case, the transformation function from the attitude state and its associated measurements is very simple

$$\mathbf{g}_{\text{att}}(\mathbf{y}_{\text{att}}) = \begin{bmatrix} \boldsymbol{\sigma}_{B/I} \\ \boldsymbol{\omega}_{B/I} + \Delta\boldsymbol{\omega}_{\text{gyro}} \end{bmatrix}, \tag{6.28}$$

where the gyroscope bias is persistently added to the process output in order to match it with the measurements.

6.3 Model predictive guidance and control

In order to meet the station-keeping goals (circular orbit and stationary attitude) of problem (6.5), an MPC-based guidance and control strategy is developed. Separate controllers are developed for orbit and attitude control. This is motivated by the weak coupling of the system through the gravity-gradient torque (the array of thrusters is assumed to provide control in any direction). As such, decoupling the control problems is convenient for the sake of simplicity. Both station-keeping controllers are based on a reference tracking strategy.

6.3.1 Guidance

The guidance block generates the reference that has to be tracked by the control program. The reference is the desired system evolution from the station-keeping perspective.

Orbital reference

For the orbital motion, the satellite is guided into a circular orbit with semi-major axis $\breve{a}$. The remaining orbital elements such as the inclination i, right ascension of the ascending node, Ω, argument of periapsis, ω, and true anomaly, ν, are let to evolve freely. In terms of MEE, this was demonstrated to translate into $\breve{p} = \breve{a}$ and $\breve{f} = \breve{g} = 0$. To prescribe the previous MEE subset, the inhomogeneous gravity field perturbation is counteracted with the following control acceleration

$$\breve{\mathbf{u}}(t) = -\begin{bmatrix} \breve{a}_{\text{grav},r}(t) \\ \breve{a}_{\text{grav},t}(t) \\ 0 \end{bmatrix}. \tag{6.29}$$

The normal component to the orbital plane $\breve{u}_n$ can take an arbitrary value since the radial-tangential motion is independent of the out-of-plane motion (see Eq. (2.10)). Then, for the sake of efficiency, the normal component in the reference control acceleration is nullified. The dynamics of the reference is

$$\frac{d}{dt}\begin{bmatrix} \breve{p} \\ \breve{f} \\ \breve{g} \\ \breve{h} \\ \breve{L} \end{bmatrix} = \begin{bmatrix} 0 \\ 0 \\ 0 \\ 0 \\ 0 \\ \sqrt{\mu/\breve{a}^3} \end{bmatrix} + \frac{\breve{a}_{\text{grav},n}}{2}\sqrt{\frac{\breve{a}}{\mu}}\begin{bmatrix} 0 \\ 0 \\ 0 \\ \breve{s}^2\cos\breve{L} \\ \breve{s}^2\sin\breve{L} \\ 2(\breve{h}\sin\breve{L} - \breve{k}\cos\breve{L}) \end{bmatrix}. \tag{6.30}$$

The numerical integration (e.g. with a Runge-Kutta method) of the previous first order system of differential equations provides a time-varying orbital reference as

$$\breve{\mathbf{x}}_{\text{orb}}(t) = [\breve{a},\ 0,\ 0,\ \breve{h}(t),\ \breve{k}(t),\ \breve{L}(t)]^T, \tag{6.31}$$

where $\mathbf{x}_{\text{orb}}$ denotes the orbit control state composed of the MEE. Note that the MEE subset $\{h, k, L\}$ is let to evolve naturally because it does not influence the station-keeping of a circular orbit (however, the orbital plane may change along time).

The extension of the previous formulation to a reference elliptic orbit is also possible. It can be deduced that $\dot{e} = (f\dot{f} + g\dot{g})/\sqrt{f^2+g^2} = 0$ under the control of Eq. (6.29). Then, the system is only affected by the out-of-plane gravity perturbation $a_{\text{grav},n}$. This perturbation cancels itself for the radial-tangential components as $f\dot{f} + g\dot{g} = 0$ (see Eq. (2.10)) causes $\dot{e} = 0$. However, the reference of the elements f and g would be time-varying.

Attitude reference

The attitude control aims to maintain the body frame aligned with the orbital frame, $\breve{\boldsymbol{\sigma}}_{B/O} = \mathbf{0}$, thus guaranteeing camera line-of-sight with the asteroid surface. This translates to $\dot{\breve{\boldsymbol{\sigma}}}_{B/O} = \mathbf{0}$ which is achieved by imposing the following angular velocity profile (see Eq. (2.90))

$$\breve{\boldsymbol{\omega}}_{B/I}^{B}(t) = \boldsymbol{\omega}_{O/I}^{O}(\breve{\mathbf{x}}_{\mathrm{orb}}(t)), \tag{6.32}$$

which means that the satellite has to rotate with respect to inertial space with the same rate of the orbital frame. In order to acquire the previous angular velocity profile, by clearing Eq. (2.91), the control torque has to fulfil

$$\begin{aligned}\breve{\mathbf{T}}_u(t) &= \mathbf{J}\dot{\breve{\boldsymbol{\omega}}}_{B/I}^{B}(t) + \breve{\boldsymbol{\omega}}_{B/I}^{B}(t) \times (\mathbf{J}\breve{\boldsymbol{\omega}}_{B/I}^{B}(t)) - \breve{\mathbf{T}}_{\mathrm{grav}}(t),\\ \dot{\breve{\boldsymbol{\omega}}}_{B/I}^{B}(t) &= \dot{\boldsymbol{\omega}}_{O/I}^{O}(\breve{\mathbf{x}}_{\mathrm{orb}}(t)).\end{aligned} \tag{6.33}$$

However, in order to ease the computational burden of the attitude reference computation, $\breve{\mathbf{T}}_u \approx \mathbf{0}$ is assumed. This causes the attitude reference to be fictitious but close to the real one if the required counteracting control torque is low enough. Let define the attitude control state as $\mathbf{x}_{\mathrm{att}} = [\boldsymbol{\sigma}_{B/O}^T, (\boldsymbol{\omega}_{B/I}^B)^T]^T$. Then, the fictitious attitude reference is

$$\breve{\mathbf{x}}_{\mathrm{att}}(t) = \begin{bmatrix} \mathbf{0} \\ \breve{\boldsymbol{\omega}}_{O/I}^{O}(\breve{\mathbf{x}}_{\mathrm{orb}}(t)) \end{bmatrix}, \tag{6.34}$$

which is computed in a straightforward way because it only requires the orbital reference of Eq. (6.31) as an input. The fictitious attitude reference generates a drift along time that has to be compensated by the control program.

6.3.2 Control

The orbit-attitude controllers aim to track their respective references $\breve{\mathbf{x}}_{\mathrm{orb}}$ and $\breve{\mathbf{x}}_{\mathrm{att}}$. Since the problem is the same, a common reference tracking MPC is presented. Firstly, the generic reference tracking problem is stated in a continuous form. Then, the orbit-attitude non-linear dynamics are linearized around the reference. This way, a linear system is obtained. Finally, a QP form of the reference tracking problem is obtained by means of discretization. In any case, the specific orbit-attitude control programs are explicitly declared at the end of the section.

Continuous reference tracking problem

Let define a generic state $\mathbf{x}$ and a control $\mathbf{u}$ with their respective references $\breve{\mathbf{x}}$ and $\breve{\mathbf{u}}$. Then, let define the reference tracking error and control increment as $\Delta\mathbf{x} = \mathbf{x} - \breve{\mathbf{x}}$ and $\Delta\mathbf{u} = \mathbf{u} - \breve{\mathbf{u}}$ respectively. Using the previous definitions, a reference tracking control program can be stated in terms of the tracking error and control increment as

$$
\begin{array}{ll}
\underset{\Delta\mathbf{x}(t),\Delta\mathbf{u}(t)}{\text{minimize}} & \displaystyle\int_{t_0}^{t_f} \left(\gamma\Delta\mathbf{x}^T(t)\mathbf{Q}_x\Delta\mathbf{x}(t) + \Delta\mathbf{u}^T(t)\Delta\mathbf{u}(t)\right) dt, \\
\text{subject to} & \Delta\dot{\mathbf{x}}(t) = \dot{\mathbf{x}} - \dot{\breve{\mathbf{x}}}, \\
& \dot{\mathbf{x}}(\mathbf{x}(t), \mathbf{u}(t)) = \mathbf{c}(\mathbf{x}) + \mathbf{f}(\mathbf{x}) + \mathbf{B}(\mathbf{x})\mathbf{u}, \\
& \Delta\mathbf{x}(t) = \mathbf{x} - \breve{\mathbf{x}}, \\
& \Delta\mathbf{u}(t) = \mathbf{u} - \breve{\mathbf{u}}, \\
& -\overline{\mathbf{u}} \leq \mathbf{u}(t) \leq \overline{\mathbf{u}},
\end{array}
\tag{6.35}
$$

where the time dependencies of the non-incremental variables have been frequently omitted for the sake of compactness. The restrictive station-keeping condition of problem 6.5 is relaxed to minimize the reference tracking error in the objective function. The scalar $\gamma > 0$ weights the relative importance given to the reference tracking accuracy with respect to the control effort. The matrix $\mathbf{Q}_x$ extracts the tracked states as

$$
\mathbf{Q}_x = \begin{bmatrix} \mathbf{I} & \mathbf{0}_{3\times3} \\ \mathbf{0}_{3\times3} & \mathbf{0}_{3\times3} \end{bmatrix}, \tag{6.36}
$$

where for both attitude and orbit controllers, the tracked variables are the first three components of their states, that is $\boldsymbol{\sigma}^B_{B/I}$ and $\{p, f, g\}$ respectively. In the generic problem reference tracking problem (6.35), the state dynamics are composed by a natural term $\mathbf{c}$ (Keplerian motion / gyroscopic terms), the perturbations term $\mathbf{f}$ (inhomogeneous gravity / gravity-gradient torque) and a matrix $\mathbf{B}$ premultiplying the control.

Linearized model

Both orbital and attitude dynamics are non-linear (see Eq. (2.10) and Eq. (2.90)-(2.91) respectively). However, in a station-keeping phase, the state should be close to the reference as $\mathbf{x}(t) \approx \breve{\mathbf{x}}(t)$. Specifically, it is expected that the position tracking errors are negligible when compared to the orbital semi-major axis $\|\Delta\mathbf{r}\|_2/a \ll 1$. Under the previous assumption, the dynamics can be linearized around its reference as

$$
\dot{\mathbf{x}}(\mathbf{x}(t), \mathbf{u}(t)) \approx \dot{\breve{\mathbf{x}}}(t) + \mathbf{A}(\breve{\mathbf{x}}(t), \breve{\mathbf{u}}(t))\Delta\mathbf{x}(t) + \mathbf{B}(\breve{\mathbf{x}}(t))\Delta\mathbf{u}(t) + \Delta\dot{\breve{\mathbf{x}}}(t), \tag{6.37}
$$

where $\mathbf{A} \in \mathbb{R}^{6\times6}$ is the linearized tracking error matrix which has the following expression

$$
\mathbf{A}(\breve{\mathbf{x}}(t), \breve{\mathbf{u}}(t)) = \left.\frac{\partial\mathbf{c}}{\partial\mathbf{x}}\right|_{\breve{\mathbf{x}}} + \left.\frac{\partial\mathbf{f}}{\partial\mathbf{x}}\right|_{\breve{\mathbf{x}}} + \left.\frac{\partial\mathbf{B}\breve{\mathbf{u}}}{\partial\mathbf{x}}\right|_{\breve{\mathbf{x}}}. \tag{6.38}
$$

The term $\Delta\dot{\breve{\mathbf{x}}}$ accounts for the possibility of drift if the reference is not consistent with the system dynamics

$$
\Delta\dot{\breve{\mathbf{x}}}(t) = \dot{\mathbf{x}}(\mathbf{x}(t), \breve{\mathbf{u}}(t)) - \dot{\breve{\mathbf{x}}}(t). \tag{6.39}
$$

By clearing the reference variation to the left side of Eq. (6.37), the linearized tracking error dynamics is

$$\Delta\dot{\mathbf{x}}(t) = \mathbf{A}(\breve{\mathbf{x}}(t), \breve{\mathbf{u}}(t))\Delta\mathbf{x}(t) + \mathbf{B}(\breve{\mathbf{x}}(t))\Delta\mathbf{u}(t) + \Delta\dot{\breve{\mathbf{x}}}(t), \tag{6.40}$$

which is a LTV system due to the time-varying reference. The general explicit solution to the LTV system of Eq. (6.40) is

$$\Delta\mathbf{x}(t) = \mathbf{\Phi}(t, t_0)\Delta\mathbf{x}_0 + \int_{t_0}^{t} \mathbf{\Phi}(t, \tau)\mathbf{B}(\breve{\mathbf{x}}(\tau))\Delta\mathbf{u}(\tau)d\tau + \Delta\breve{\mathbf{x}}(t), \tag{6.41}$$

where the reference tracking error transition matrix $\mathbf{\Phi}$ is obtained by integrating its own dynamics

$$\dot{\mathbf{\Phi}}(t, t_0) = \mathbf{A}(\breve{\mathbf{x}}(t), \breve{\mathbf{u}}(t))\mathbf{\Phi}(t, t_0), \quad \mathbf{\Phi}(t_0, t_0) = \mathbf{I}. \tag{6.42}$$

For both orbit-attitude motions, the ODE system of Eq. (6.42) is composed of 36 linear differential equations.

Discretization

Still, even under the linearized dynamics of Eq. (6.41), the reference tracking problem is continuous with infinite degrees of freedom. In order to reduce it to a finite tractable form, the control horizon will be discretized in time.

Pulse amplitude modulation: let consider pulse PAM control models for thrust and torque as defined in Eq. (2.62) and Eq. (2.98) respectively. Under the PAM model, the control signal is constant over an interval $t \in [t_{j-1}, t_j)$ of duration $\Delta t = t_j - t_{j-1}$

$$\mathbf{u}(t) = \{\mathbf{u}_j, \quad t \in [t_{j-1}, t_j), \quad j = 1 \dots N\}. \tag{6.43}$$

Note that the control amplitude changes instantaneously under that the PAM model. Then, Eq. (6.41) explicit expression of the tracking error can be evaluated at discrete instants $\Delta\mathbf{x}_j = \Delta\mathbf{x}(t_j)$ (coincident with the end of each control PAM interval) as

$$\Delta\mathbf{x}_j = \mathbf{\Phi}(t_j, t_0)\Delta\mathbf{x}_0 + \sum_{i=1}^{j} \mathbf{\Phi}(t_j, t_i) \int_{t_{i-1}}^{t_i} \mathbf{\Phi}(t_i, \tau)\mathbf{B}(\breve{\mathbf{x}}(\tau))d\tau\Delta\mathbf{u}_i + \Delta\breve{\mathbf{x}}_j, \tag{6.44}$$

where $\Delta\breve{\mathbf{x}}_j = \Delta\breve{\mathbf{x}}(t_j)$ is the cumulated drift at the instant t_j. The control reference (for the orbit case) has to be converted into a PAM formulation as

$$\breve{\mathbf{u}}_j = \frac{1}{t_j - t_{j-1}} \int_{t_{j-1}}^{t_j} \breve{\mathbf{u}}(t)dt. \tag{6.45}$$

Objective function: let now discretize the integrals of the objective function in the continuous reference tracking problem (6.35)

$$\begin{aligned}&\frac{1}{t_f - t_0}\int_{t_0}^{t_f}\left(\gamma\Delta\mathbf{x}^T(t)\mathbf{Q}_x\Delta\mathbf{x}(t) + \Delta\mathbf{u}^T(t)\Delta\mathbf{u}(t)\right)dt \approx \\ &\sum_{j=1}^{N}\left(\gamma\Delta\mathbf{x}_j^T\mathbf{Q}_x\mathbf{x}_j + \Delta\mathbf{u}_j^T\Delta\mathbf{u}_j\right),\end{aligned} \tag{6.46}$$

Note that the tracking error is evaluated at the end of each control interval which is aligned with Eq. (6.44).

Control bounds: due to the PAM formulation, the control signal bounds can be easily discretized as

$$-\bar{\mathbf{u}} \leq \breve{\mathbf{u}}_j + \Delta\mathbf{u}_j \leq \bar{\mathbf{u}}, \quad j = 1\dots N. \tag{6.47}$$

Compact formulation

In order to ease the notation, a compact formulation is developed. Let recall that the control horizon spans from $t_f - t_0$ but it is indefinitely slided forward in time until the station-keeping phase ends. Consequently, let denote the current MPC interval as k. This causes the MPC prediction horizon timespan to be $[t_k, t_{k+N}) = [t_0 + k\Delta t, t_f + k\Delta t)$. Note that the control program is slided after an interval of duration Δt which is coincident with the interval of the PAM control signal. Let define stack vectors for the tracking error $\Delta\mathbf{x}_{\mathbf{S}}(k) \in \mathbb{R}^{6N}$, the reference drift $\Delta\breve{\mathbf{x}}_{\mathbf{S}}(k) \in \mathbb{R}^{6N}$ and the control increment $\Delta\mathbf{u}_{\mathbf{S}}(k) \in \mathbb{R}^{3N}$ as

$$\begin{gathered}\Delta\mathbf{x}_{\mathbf{S}}(k) = \begin{bmatrix}\Delta\mathbf{x}_{k+1}\\ \vdots \\ \Delta\mathbf{x}_{k+N}\end{bmatrix}, \quad \Delta\breve{\mathbf{x}}_{\mathbf{S}}(k) = \begin{bmatrix}\Delta\breve{\mathbf{x}}_{k+1}\\ \vdots \\ \Delta\breve{\mathbf{x}}_{k+N}\end{bmatrix}, \\ \Delta\mathbf{u}_{\mathbf{S}}(k) = \begin{bmatrix}\Delta\mathbf{u}_{k+1}^T & \dots & \Delta\mathbf{u}_{k+N}^T\end{bmatrix}^T.\end{gathered} \tag{6.48}$$

Let also define stack vectors for the reference state $\breve{\mathbf{x}}_{\mathbf{S}}(k) \in \mathbb{R}^{6N}$ and the reference control $\breve{\mathbf{u}}_{\mathbf{S}}(k) \in \mathbb{R}^{3N}$ as

$$\breve{\mathbf{x}}_{\mathbf{S}}(k) = \begin{bmatrix}\breve{\mathbf{x}}_{k+1}\\ \vdots \\ \breve{\mathbf{x}}_{k+N}\end{bmatrix}, \quad \breve{\mathbf{u}}_{\mathbf{S}}(k) = \begin{bmatrix}\breve{\mathbf{u}}_{k+1}\\ \vdots \\ \breve{\mathbf{u}}_{k+N}\end{bmatrix}. \tag{6.49}$$

Finally, let define the following stack matrices $\mathbf{F} \in \mathbb{R}^{6N\times 6}$ and $\mathbf{G}_{\Delta u} \in \mathbb{R}^{6N\times 3N}$

$$\mathbf{F}(k) = [\mathbf{\Phi}^T(t_{k+1}, t_k), \ldots, \mathbf{\Phi}^T(t_{k+N}, t_k)]^T,$$

$$\mathbf{G}(k) =$$

$$\begin{bmatrix} \int_{t_k}^{t_{k+1}} \mathbf{\Phi}_{(}t_{k+1}, \tau)\mathbf{B}(\check{\mathbf{x}}(\tau))d\tau & \ldots & \mathbf{0}_{6\times 3} \\ \vdots & \ddots & \vdots \\ \mathbf{\Phi}_{k+N,k+1} \int_{t_k}^{t_{k+1}} \mathbf{\Phi}_{(}t_{k+1}, \tau)\mathbf{B}(\check{\mathbf{x}}(\tau))d\tau & \ldots & \int_{t_{k+N-1}}^{t_{k+N}} \mathbf{\Phi}_{(}t_{k+1}, \tau)\mathbf{B}(\check{\mathbf{x}}(\tau))d\tau \end{bmatrix},$$

where $\mathbf{\Phi}_{k+N,k+1} = \mathbf{\Phi}_{(}t_{k+N}, t_{k+1})$. The relation between the previous stack matrices with the stack vectors of Eq. (6.48) yields the linear propagation equation of the tracking error in a compact form

$$\Delta\mathbf{x_S}(k) = \mathbf{F}(\check{\mathbf{x}}_\mathbf{S}, \check{\mathbf{u}}_\mathbf{S})\Delta\mathbf{x}_k + \mathbf{G}(\check{\mathbf{x}}_\mathbf{S}, \check{\mathbf{u}}_\mathbf{S})\Delta\mathbf{u_S} + \Delta\check{\mathbf{x}}_\mathbf{S}, \tag{6.50}$$

where the dependency with the current MPC step k has been omitted at the right-hand side of Eq. (6.50) for the sake of clarity. Note that the stack matrices **F** and **G** depend on the reference state and control due to the transition matrix dependency with the tracking error matrix **A** (see Eq. (6.38)).

Adapting the discrete objective function (see Eq. (6.46)) and the control bounds constraint (see Eq. (6.47)) to the compact formulation, the reference tracking problem states as follows

$$\begin{aligned} \underset{\Delta\mathbf{u_S}(k)}{\text{minimize}} \quad & \gamma(\Delta\mathbf{x_S}(k))^T\mathbf{Q}_{\mathbf{S}x}\Delta\mathbf{x_S}(k) + (\Delta\mathbf{u_S}(k))^T\Delta\mathbf{u_S}(k), \\ \text{subject to} \quad & \Delta\mathbf{x_S}(k) = \mathbf{F}(\check{\mathbf{x}}_\mathbf{S}, \check{\mathbf{u}}_\mathbf{S})\Delta\mathbf{x}_k + \mathbf{G}(\check{\mathbf{x}}_\mathbf{S}, \check{\mathbf{u}}_\mathbf{S})\Delta\mathbf{u_S} + \Delta\check{\mathbf{x}}_\mathbf{S}, \\ & -\bar{\mathbf{u}}_\mathbf{S} \leq \check{\mathbf{u}}_\mathbf{S}(k) + \Delta\mathbf{u_S}(k) \leq \bar{\mathbf{u}}_\mathbf{S}, \end{aligned} \tag{6.51}$$

where $\mathbf{Q}_{\mathbf{S}x} \in \mathbb{R}^{6N\times 6N}$ and $\mathbf{u_S} \in \mathbb{R}^{3N}$ stack the weighting matrix $\mathbf{Q}_x$ and the control bounds $\bar{\mathbf{u}}$ as

$$\mathbf{Q}_{\mathbf{S}x} = \begin{bmatrix} \mathbf{Q}_x & \ldots & \mathbf{0}_{6\times 6} \\ \vdots & \ddots & \vdots \\ \mathbf{0}_{6\times 6} & \ldots & \mathbf{Q}_x \end{bmatrix}, \quad \bar{\mathbf{u}}_\mathbf{S} = \begin{bmatrix} \bar{\mathbf{u}} \\ \vdots \\ \bar{\mathbf{u}} \end{bmatrix}. \tag{6.52}$$

Note that the reference tracking optimization problem (6.51) is a QP problem with $3N$ decision variables. The stack vector of the tracking error is related to the control increment by an equality constraint that can be directly introduced into the objective function. Once the QP optimization is solved, the control sequence is constructed as $\mathbf{u_S}(k) = \check{\mathbf{u}}_\mathbf{S}(k) + \Delta\mathbf{u_S}(k)$.

Orbit-attitude reference tracking programs

Now, the generic reference tracking QP optimization (6.51) is explicitly stated for both orbit and attitude control.

Orbit reference tracking program: let recall that the orbit state is defined as $\mathbf{x}_{\text{orb}} = [p, f, g, h, k, L]^T$ and the control variable is the thrusters exerted acceleration as $\mathbf{u} = [u_r, u_t, u_n]^T$. Then, the compact control program for the orbit reference tracking is

$$\boxed{\begin{aligned} \underset{\Delta\mathbf{u}_{\mathbf{S}}(k)}{\text{minimize}} \quad & \gamma_{\text{orb}}(\Delta\mathbf{x}_{\mathbf{S}\text{orb}}(k))^T\mathbf{Q}_{\mathbf{S}x}\Delta\mathbf{x}_{\mathbf{S}\text{orb}}(k)+(\Delta\mathbf{u}_{\mathbf{S}}(k))^T\Delta\mathbf{u}_{\mathbf{S}}(k),\\ \text{subject to} \quad & \Delta\mathbf{x}_{\mathbf{S}\text{orb}}(k)=\mathbf{F}_{\text{orb}}(\breve{\mathbf{x}}_{\mathbf{S}},\breve{\mathbf{u}}_{\mathbf{S}})\Delta\mathbf{x}_{\text{orb},k}\\ &\qquad\qquad + \mathbf{G}_{\text{orb}}(\breve{\mathbf{x}}_{\mathbf{S}\text{orb}},\breve{\mathbf{u}}_{\mathbf{S}})\Delta\mathbf{u}_{\mathbf{S}}+\Delta\breve{\mathbf{x}}_{\mathbf{S}},\\ & -\bar{\mathbf{u}}_{\mathbf{S}} \le \breve{\mathbf{u}}_{\mathbf{S}}(k)+\Delta\mathbf{u}_{\mathbf{S}}(k)\le\bar{\mathbf{u}}_{\mathbf{S}},\\ & \mathbf{A}_{\mathbf{S}u_n}\Delta\mathbf{u}_{\mathbf{S}}(k)=\mathbf{0}, \end{aligned}} \tag{6.53}$$

where the matrix $\mathbf{A}_{\mathbf{S}u_n} \in \mathbb{R}^{N\times 3N}$ nullifies the out-of-plane control by imposing $\Delta u_n = 0$

$$\mathbf{A}_{\mathbf{S}u_n} = \begin{bmatrix} 0 & 0 & 1 & \dots & 0 & 0 & 0 \\ \vdots & \vdots & \vdots & \ddots & \vdots & \vdots & \vdots \\ 0 & 0 & 0 & \dots & 0 & 0 & 1 \end{bmatrix}. \tag{6.54}$$

This is consistent with the control reference as per Eq. (6.29). In [Tavakoli14], which developed an MPC-based station-keeping control for low-Earth orbits station-keeping, it was demonstrated that nullifying the out-of-plane reduces significantly the control effort if only orbit semi-major axis and eccentricity is controlled. The rationale behind the previous fact is that the most direct way to induce changes in the orbit shape is by applying a control contained in the orbital plane (see the classical orbital elements GVE in Eq. (2.4)). However, an optimizer may found that by changing the orbital angular momentum or the line of apsides, indirect changes on the semi-major axis and eccentricity can be induced. This leads to an efficient control in the short-term (over the prediction horizon) but inefficient at the long-term (the whole duration of the station-keeping phase).

Attitude reference tracking program: let recall that the attitude state is $\mathbf{x}_{\text{att}} = [\boldsymbol{\sigma}_{B/I}^T, (\boldsymbol{\omega}_{B/I}^B)^T]^T$ and the control torque is $\mathbf{T}_u = [T_{u_1}, T_{u_2}, T_{u_3}]^T$. Using the previous variables, the attitude tracking reference program is

$$\boxed{\begin{aligned} \underset{\Delta\mathbf{T}_{\mathbf{S}u}(k)}{\text{minimize}} \quad & \gamma_{\text{att}}(\Delta\mathbf{x}_{\mathbf{S}\text{att}}(k))^T\mathbf{Q}_{\mathbf{S}x}\Delta\mathbf{x}_{\mathbf{S}\text{att}}(k)+(\Delta\mathbf{T}_{\mathbf{S}u}(k))^T\Delta\mathbf{T}_{\mathbf{S}u}(k),\\ \text{subject to} \quad & \Delta\mathbf{x}_{\mathbf{S}\text{att}}(k)=\mathbf{F}_{\text{att}}(\breve{\mathbf{x}}_{\mathbf{S}\text{att}},\breve{\mathbf{T}}_{\mathbf{S}u})\Delta\mathbf{x}_{\text{att},k}\\ &\qquad\qquad + \mathbf{G}_{\text{att}}(\breve{\mathbf{x}}_{\mathbf{S}\text{att}},\breve{\mathbf{T}}_{\mathbf{S}u})\Delta\mathbf{T}_{\mathbf{S}u}+\Delta\breve{\mathbf{x}}_{\mathbf{S}\text{att}},\\ & -\overline{\mathbf{T}}_{\mathbf{S}u} \le \breve{\mathbf{T}}_{\mathbf{S}u}(k)+\Delta\mathbf{T}_{\mathbf{S}u}(k)\le\overline{\mathbf{T}}_{\mathbf{S}u}, \end{aligned}} \tag{6.55}$$

where $\mathbf{T}_{\mathbf{S}u}(k) = [\mathbf{T}_{u_k}^T, \dots, \mathbf{T}_{u_{k+N}}^T]^T$ stacks the control torque.

6.4 Learning-based guidance, navigation and control

The previous UKF navigation (see Section 6.2) and MPC-based guidance and control (see Section 6.3) are integrated to obtain a learning-based GNC scheme. The model learning is enabled by the navigation block which recursively updates the gravity parameters. Since the guidance and control is MPC-based, a more accurate model enhances the state prediction, thus increasing the reference tracking accuracy.

The previous GNC architecture is valid for a single spacecraft. As a consequence, the gravity estimation would largely rely on the asteroid regions that the satellite flew over. Under the previous consideration, it arises the idea of using multiple satellites (e.g. constellation) for the mission. The main assumption is that communication links between the multiple satellites are available. This allows to simultaneously orbit several regions of the small body, thus increasing the amount of available information for the gravity estimation. In this case, it is chosen to weight the individual estimates across the constellation in order to compute a common gravity estimation.

6.4.1 Integrated GNC scheme

The integrated GNC scheme for a single orbiting satellite is summarized in Fig. 6.5. Four blocks can be distinguished: dynamics driven by the control actuators (yellow); sensors (orange); navigation filters (green); MPC-based guidance and control (blue). The focus of this thesis has been the GNC algorithm as formed by the filters and MPC. As it was previously mentioned in this chapter, the specific details of the sensors are out of the scope of this work.

The orbit-attitude dynamics would employ a high-fidelity model for small bodies (see the next Section 6.5). Measurements of such realistic model are taken by the sensors. These measurements feed the filters in order to estimate the satellite state and the small body gravity. Let recall that the GNC algorithm is based on a low-fidelity dynamical model with only gravity terms up to $n_{\text{orb}} \times n_{\text{orb}}$ or $n_{\text{att}} \times n_{\text{att}}$ degree and order. The attitude filter works at a higher sampling rate than the orbit one as the attitude sensors take measurements faster. However, they exchange their own estimates (orientation for the camera / orbit state for the gravity-gradient torque) when possible. They also update each other gravity estimation.

Finally, using the respective state and gravity estimations of the filters, the guidance and control module computes a thrust and a torque command which closes the loop. The guidance algorithm generates references to be tracked by the subsequent control programs. The output of the control algorithm is an increment that is added to the control reference in order to construct the control command. The control command (thrust or torque) is applied to the high-fidelity orbit-attitude dynamics.

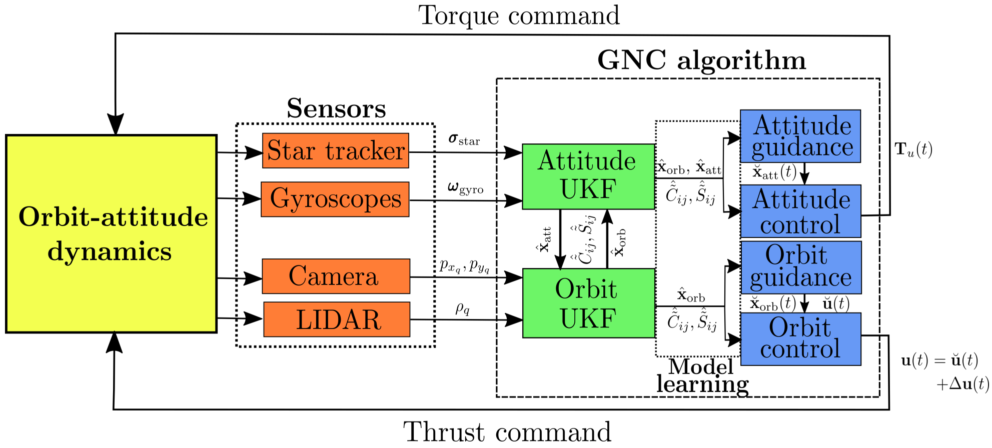

Figure 6.5: GNC scheme for a single spacecraft orbiting around the asteroid.

6.4.2 Gravity estimation with a satellite constellation

Let consider now a constellation of N_{sat} satellites orbiting the asteroid as it can be seen Fig. 6.6. Assuming there are always communication links between them, and that the filters are synchronized in time, it is possible to compute a weighted average of the gravity parameters as

$$\hat{\tilde{C}}_{nm} = \sum_{\iota=1}^{N_{\text{sat}}} w^{[\iota]}_{\tilde{C}_{nm}} \hat{\tilde{C}}^{[\iota]}_{nm}, \quad \hat{\tilde{S}}_{nm} = \sum_{\iota=1}^{N_{\text{sat}}} w^{[\iota]}_{\tilde{S}_{nm}} \hat{\tilde{S}}^{[\iota]}_{nm}, \tag{6.56}$$

where the index ι denotes each satellite and $(w^{[\iota]}_{\tilde{C}_{nm}}, w^{[\iota]}_{\tilde{S}_{nm}})$ are the weights of each satellite estimation. There could be multiple choices to these weights. However, a smart choice could be to assign more weight to the less uncertain estimates as

$$w^{[\iota]}_{\tilde{C}_{nm}} = \frac{\left(1/\sigma^{[\iota]}_{\tilde{C}_{nm}}\right)^2}{\sum\limits_{\iota=1}^{N_{\text{sat}}} \left(1/\sigma^{[\iota]}_{\tilde{C}_{nm}}\right)^2}, \quad w^{[\iota]}_{\tilde{S}_{nm}} = \frac{\left(1/\sigma^{[\iota]}_{\tilde{S}_{nm}}\right)^2}{\sum\limits_{\iota=1}^{N_{\text{sat}}} \left(1/\sigma^{[\iota]}_{\tilde{S}_{nm}}\right)^2}, \quad \iota = 1 \ldots N_{\text{sat}}, \tag{6.57}$$

where $\sigma^{[\iota]}_{\tilde{C}_{nm}}$ and $\sigma^{[\iota]}_{\tilde{S}_{nm}}$ are the 1-sigma standard deviations of each gravity parameter (square root of the covariance matrix diagonal). Using those weights, the weighted mean mitigates outliers, thus potentially enhancing the gravity estimation convergence and accuracy. As there is a cross-correlation between the state and spherical harmonics in the filters, the individual covariances are not updated. The UKF requires the covariance extended state matrix to be positive definite. As such, updating the gravity model block of the covariance matrix may not guarantee the resulting extended state covariance matrix to be positive definite in the next call. The complete methodology is shown as pseudocode in Algorithm 5. The constellation concept arises through step 15, where the joint gravity estimation is computed and shared across the constellation after the output of each satellite individual filter. Note that each satellite carries out its own navigation process and control computation in parallel.

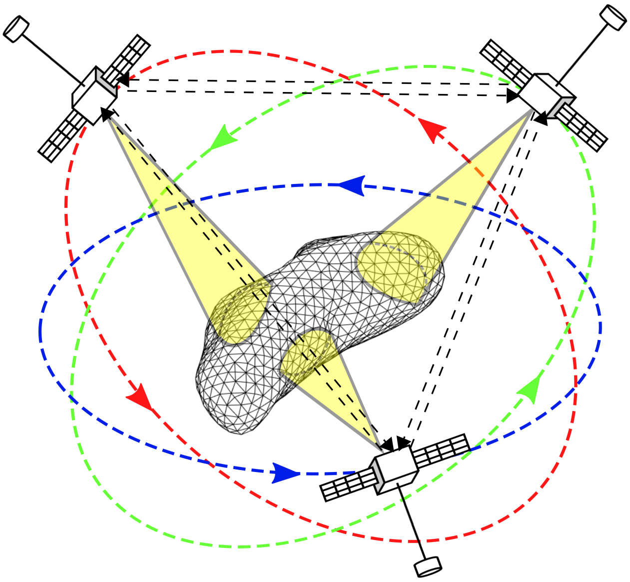

Figure 6.6: Gravity estimation with a satellite constellation.

6.5 Numerical results

The key feature of the designed learning-based GNC scheme is its ability to improve the control accuracy by updating the gravity parameters estimation. In that sense, the proposed methodology is compared to a non-learning based MPC scheme. The effect of nullifying the out-of-plane control is also assessed in terms of its control accuracy and efficiency. Finally, the proposed satellite constellation is compared with single satellites for the gravity estimation.

To assess the previous facts, a small body mission to asteroid 433 Eros is considered. This is usually the benchmark scenario for small bodies applications as a huge amount of data is available from the NEAR Shoemaker mission. The asteroid 433 Eros is a near-Earth object with a distinctive elongated shape.

Algorithm 5: Learning-based GNC scheme

```
1  begin
2      for $i = 1 \dots N_{\text{UKF}}^{\text{orb}}$ do
3          for $j = 1 \dots N_{\text{UKF}}^{\text{att}}$ do
4              Execute the attitude UKF Algorithm 4 to update the
                 extendend state $\hat{\mathbf{y}}_{\text{att}}, \mathbf{\Sigma}_{\mathbf{y}_{\text{att}}}$ with incoming measurements
                 $\mathbf{z}_{\text{att}}$;
5          end
6          Update the attitude guidance reference with Eq. (6.34),
             $\breve{\mathbf{x}}_{\text{att}}(k_{\text{att}})$;
7          Solve QP (6.55) to obtain the torque control sequence
             $\mathbf{T}_u(k_{\text{att}}) \leftarrow \Delta\mathbf{T}_u(k_{\text{att}})$;
8          Apply the first control of the sequence $\mathbf{T}_{u_1}(k_{\text{att}})$;
9          Update the current MPC step $k_{\text{att}} \leftarrow k_{\text{att}} + 1$;
10         Update a subset of the orbit filter gravity parameters with the
             attitude filter estimation $\widehat{\widetilde{\mathbf{CS}}}_{\text{orb}} \leftarrow \widehat{\widetilde{\mathbf{CS}}}_{\text{att}}$ for $n, m = 2 \dots n_{\text{att}}$;
11         Execute the orbit UKF Algorithm 4 to update the extendend
             state $\hat{\mathbf{y}}_{\text{orb}}, \mathbf{\Sigma}_{\mathbf{y}_{\text{orb}}}$ with incoming measurements $\mathbf{z}_{\text{orb}}$;
12     end
13     Do the weighted average to the constellation gravity estimates
         $\hat{\tilde{C}}_{nm} = \sum_{\iota=1}^{N_{\text{sat}}} w_{\tilde{C}_{nm}}^{[\iota]} \hat{\tilde{C}}_{nm}^{[\iota]},\ \hat{\tilde{S}}_{nm} = \sum_{\iota=1}^{N_{\text{sat}}} w_{\tilde{S}_{nm}}^{[\iota]} \hat{\tilde{S}}_{nm}^{[\iota]}$;
14     Update each individual satellite estimation
         $\hat{\tilde{C}}_{nm}^{[\iota]} \leftarrow \hat{\tilde{C}}_{nm}\ , \hat{\tilde{S}}_{nm}^{[\iota]} \leftarrow \hat{\tilde{S}}_{nm},\ \iota = 1 \dots N_{\text{sat}}$;
15     Update the orbit guidance reference with Eq. (6.31), $\breve{\mathbf{x}}_{\text{orb}}(k_{\text{orb}})$ and
         $\breve{\mathbf{u}}(k_{\text{orb}})$;
16     Solve the QP (6.53) to obtain the control acceleration sequence
         $\mathbf{u}(k_{\text{orb}}) \leftarrow \breve{\mathbf{u}}(k_{\text{orb}}) + \Delta\mathbf{u}(k_{\text{orb}})$;
17     Apply the first control of the sequence $\mathbf{u}_1(k_{\text{orb}})$;
18     Update the current MPC step $k_{\text{orb}} \leftarrow k_{\text{orb}} + 1$;
19     Go to step 2;
20 end
```

6.5.1 Simulation model, GNC parameters and performance indexes

Subsequently, the employed simulation model composed of the system dynamics and the satellite characteristics is presented. Next, the GNC tuning parameters for all the simulations are stated. Finally, to ease the analysis of the results, some performance indexes are described

Simulation model

System dynamics: the orbit-attitude simulation model assumes a satellite orbiting in the vicinity of a small body. In that regime, the relevant orbital perturbations are the small body inhomogeneous gravity field, the Sun's third-body gravity and the solar radiation pressure

$$\begin{aligned}\dot{\boldsymbol{\alpha}}(t) &= \tilde{\mathbf{c}}(\tilde{\boldsymbol{\alpha}}) + \tilde{\mathbf{A}}(\tilde{\boldsymbol{\alpha}})(\mathbf{a}_{\text{grav}} + \mathbf{a}_{\text{sun}} + \mathbf{a}_{\text{SRP}} + \mathbf{u}),\\ \dot{\boldsymbol{\sigma}}_{B/O}(t) &= \mathbf{C}(\boldsymbol{\sigma}_{B/O})[\boldsymbol{\omega}_{B/I} - \mathbf{R}(\boldsymbol{\sigma}_{B/O})\boldsymbol{\omega}^{O}_{O/I}],\\ \dot{\boldsymbol{\omega}}_{B/I}(t) &= \mathbf{J}^{-1}[-\boldsymbol{\omega}_{B/I} \times (\mathbf{J}\boldsymbol{\omega}_{B/I}) + \mathbf{T}_{\text{grav}} + \mathbf{T}_{u}].\end{aligned} \tag{6.58}$$

The asteroid 433 Eros has a standard gravitational parameter of $\mu = 4.4628 \cdot 10^5$ m^3/s^2 and a rotation period of $T_A = 5.27$ h. The inhomogeneous gravity of field of 433 Eros is characterized by a 15×15 degree and order normalized ($R_e = 16$ km) spherical harmonics model determined during the NEAR Shoemaker mission [Konopliv02]. The Sun is assumed to be placed at $\mathbf{r}^I_\odot = [1.46, 0, 0]^T$ AU distance from the asteroid.

Satellite characteristics: each satellite is assumed to have a mass of $m =$ 1000 kg. Its mass distribution model consists of five discrete masses being four of them contained in the same plane and the remaining one placed in an axis perpendicular to that plane (see Table 6.1). The coefficient of reflectivity and exposed area to SRP are $C_R = 1.4$ and $A = 10$ m^2 (see Eq.(2.23)).

l	x^B_l [m]	y^B_l [m]	z^B_l [m]	m_l [kg]
1	8	0	0	200
2	-2	-2	0	200
3	-2	2	0	200
4	-2	0	-1	200
5	-2	0	1	200

Table 6.1: Mass distribution of the satellite.

The associated inertia matrix to the previous mass distribution is

$$\mathbf{J} = \begin{bmatrix} 2000 & 0 & 0 \\ 0 & 16400 & 0 \\ 0 & 0 & 17600 \end{bmatrix} \text{ kg} \cdot \text{m}^2. \tag{6.59}$$

The control bounds of the exerted acceleration and torque are taken as $\overline{\mathbf{u}} = [1,1,1]^T$ cm/s^2 and $\overline{\mathbf{T}}_u = [10,10,10]^T$ mN $\cdot$ m. Although a PAM control was assumed in the GNC scheme, the transient of the thrust and torque signals is considered according to Eq. (2.63). The time constant is taken as $\tau = 0.1$ s^{-1}.

The satellite is equipped with a high resolution camera, a LIDAR, star-trackers and gyroscopes. The camera resolution is of 2048×2048 pixels with a 30° field of view and a focal length of $f_{\text{foc}} = 300$ mm. This yields a pixel width of $p_{\text{w}} = 75.8$ μm. The maximum number of landmarks, from which the camera and LIDAR can take measurements between filter calls, is $l = 3$. Following the simplified models presented in Section 6.2, the sensors accuracy is statistically characterized as Gaussian variables with their bias and standard deviation stated in Table 6.2. Note that the star tracker uncertainty is introduced via the rotation angle of the MRP (see Eq. (2.86)).

Sensor	Variable	Bias	1-σ noise
Camera	$\mathbf{p}_q$	$[0,0]^T$ px	$[0.5,0.5]^T$ px
LIDAR	ρ_q	0 m	5 m
Star tracker	θ_{rot}	0 arcsec	10 arcsec
Gyroscopes	$\boldsymbol{\omega}_{\text{gyro}}$	$[5,5,5]^T$ °/h	$[0.05,0.05,0.05]^T$ °/h

Table 6.2: Sensors datasheet.

GNC parameters

Navigation filters: the orbit-attitude filters estimate gravity parameters up to 4×4 and 2×2 degree and order respectively. This makes $n_{\text{orb}} = 4$ and $n_{\text{att}} = 2$. As such, the orbit estimation variable is composed of 27 estimates where 6 of them correspond to the MEE components and the remaining 21 to gravity parameters. The attitude estimation variable is composed of 14 estimates where 3 corresponds to the MRP, 3 are the components of the body angular velocity, 5 are the gravity parameters and 3 are the gyroscope bias.

The UKF parameters are tuned as $\{\lambda, \theta, \beta, \eta\} = \{(\theta^2-1)n, 10^{-3}, 2, 0.98\}$ for both orbit and attitude filters. The term n is the dimension of the estimated variables (27 for the orbit and 14 for the attitude case). The parameters λ, θ and β follow the canonical choice of [Wan00]. The fading factor η is chosen near to the unity to provide a slow update pace of the process noise. This prevents excessive covariance inflation due to outliers.

The filters are called each $\Delta t^{\text{att}}_{\text{UKF}} = 3.6$ s and $\Delta t^{\text{orb}}_{\text{UKF}} = 36$ s for the attitude and orbit respectively. These sampling rates are driven by the speed of the sensors measurements acquisition. In that sense, the attitude sampling rate has been considered one order of magnitude faster than the orbit one. The orbit filter has to leave enough margin so that the camera feature identification process recognizes the landmarks on the taken image. However, it has to be also fast enough in order to capture the frequency of the highest order estimated gravity parameter.

Guidance and control: the MPC-based guidance and control algorithm parameters are the control horizon duration $t_N - t_0$, the number of discretization intervals N and the tracking error weight γ in the objective function. The duration of a sampling interval is given by $\Delta t = (t_N - t_0)/N$. The control is applied for the entire interval $[t_k, t_k + \Delta t)$ and the control program is slided forward in time to recompute a new control sequence. The specific values of the previous variables for both orbit and attitude control programs are shown in Table 6.3.

	$t_N - t_0$ [min]	N [−]	Δt [s]	γ [−]
Attitude	6	10	36	1000
Orbit	240	40	360	1000

Table 6.3: Guidance and control algorithm parameters.

Performance indexes

In order to compare the different simulations, some performance indexes are defined. These indexes apply to the whole scenario timespan which last two weeks for each simulation.

Orbit control: the orbit control efficiency is measured through the fuel consumption as

$$m_F = \int_{t_0}^{t_f} \dot{m}(t)dt \approx \int_{t_0}^{t_f} \frac{m_0 \mathbf{u}(t)}{g_0 I_{\text{sp}}} dt, \tag{6.60}$$

where $g_0 = 9.8066$ m/s^2 is the gravity at Earth's sea level. The mass has been assumed constant as m_0 because it is expected that the fuel consumption is very low $m_0 \gg m_F$. Due to the continuous application of control acceleration, the most suitable propulsion plant may be electric thrusters, thus $I_{\text{sp}} = 2900$ s has been assumed. Since the goal is to station-keep a circular orbit, the orbit control accuracy is measured as the average ΔR and maximum $\overline{\Delta R}$ tracking error on the orbital radius

$$\Delta R = \frac{1}{t_f - t_0} \int_{t_0}^{t_f} |\Delta r(t)| dt, \quad \overline{\Delta R} = \max\{|\Delta r(t)|\}, \tag{6.61}$$

where $\Delta r = \|\mathbf{r}\|_2 - \breve{a}$. Let recall that the semi-major axis coincides with the radius for a circular orbit.

Attitude control: the attitude control efficiency is measured as the integral of the control torque norm over the scenario timespan

$$T_U = \frac{1}{t_f - t_0} \int_{t_0}^{t_f} \|\mathbf{T}_u(t)\|_2 dt. \tag{6.62}$$

The attitude control accuracy metrics are the average $\Delta\boldsymbol{\Theta}$ and maximum $\overline{\Delta\boldsymbol{\Theta}}$ tracking errors in terms of Euler angles as

$$\Delta\boldsymbol{\Theta} = \frac{1}{t_f - t_0} \int_{t_0}^{t_f} |\Delta\boldsymbol{\theta}(t)| dt, \quad \overline{\Delta\boldsymbol{\Theta}} = \max\{|\Delta\boldsymbol{\theta}(t)|\}, \tag{6.63}$$

where $\boldsymbol{\theta} = [\theta_1,\ \theta_2,\ \theta_3]^T \equiv \{\text{pitch}, \text{roll}, \text{yaw}\}$ defines the following $\{xyz\}$ rotation sequence from the orbit to the body frame

$$O \xrightarrow[x_O]{\theta_3} S' \xrightarrow[y_{S'}]{\theta_2} S'' \xrightarrow[z_{S''}]{\theta_1} B. \tag{6.64}$$

Gravity estimation: the estimation error of each gravity parameter is quantified as

$$\delta\tilde{C}_{nm}(t) = \frac{\hat{\tilde{C}}_{nm}(t) - \tilde{C}_{nm}}{\tilde{C}_{nm}}, \quad \delta\tilde{S}_{nm}(t) = \frac{\hat{\tilde{S}}_{nm}(t) - \tilde{S}_{nm}}{\tilde{S}_{nm}}, \tag{6.65}$$

where the values of interest correspond to the end of the scenario: $\delta\tilde{C}^f_{nm} = \delta\tilde{C}_{nm}(t_f)$ and $\delta\tilde{S}^f_{nm} = \delta\tilde{S}_{nm}(t_f)$. The convergence of a gravity estimation parameter is considered to be achieved when its estimation error is under a 20% and is maintained below this threshold until the end of the simulation. Using the previous condition, a convergence time can be defined for each gravity parameter as

$$\begin{aligned} t_{\tilde{C}_{nm}} &\equiv \{\delta\tilde{C}_{nm}(t) \leq 0.2,\ t \geq t_{\tilde{C}_{nm}}\}, \\ t_{\tilde{S}_{nm}} &\equiv \{\delta\tilde{S}_{nm}(t) \leq 0.2,\ t \geq t_{\tilde{S}_{nm}}\}. \end{aligned} \tag{6.66}$$

6.5.2 Efficiency of nullifying the out-of-plane control

Let assess the impact of nullifying the out-of-plane control in the orbit program 6.53. To this end, five simulations with ($\Delta u_n(t) = 0$) and without ($\Delta u_n(t) \equiv$ free) nullifying the out-of-plane control are carried out. For each scenario, the initial orbital elements are $\boldsymbol{\alpha}_0 = [34\text{ km},\ 0,\ i_0,\ 0°,\ 0°,\ 0°]^T$. The initial inclination is varied as $i_0 = \{30°, 60°, 90°, 120°, 150°\}$ because it masters the asteroid regions that are flew over by the satellite. The reference orbit to station-keep is defined by $\breve{a} = 34$ km and $\breve{e} = 0$.

The results are summarized in Table 6.4. It is demonstrated that nullifying the out-of-plane control reduces fuel consumption for all cases. In average, the fuel consumption is reduced in a 32% when compared to allowing out-of-plane control. Regarding the orbit reference tracking accuracy, the gain, when allowing out-of-plane control, is marginal as it only improves ΔR a 3% in average while the maximum errors $\overline{\Delta R}$ are higher in a 6.5% with respect to nullifying the out-of-plane control. Consequently, it can be concluded that, in general, nullifying the out-of-plane control saves fuel consumption without impacting the reference tracking accuracy.

	$u_n(t) = 0$			$u_n(t) \equiv$ free		
Simulation	m_F [kg]	ΔR [m]	$\overline{\Delta R}$ [m]	m_F [kg]	ΔR [m]	$\overline{\Delta R}$ [m]
$i_0 = 30°$	1.7962	160.12	615.16	1.8458	146.39	636.14
$i_0 = 60°$	1.3505	251.39	609.87	2.4677	319.78	583.50
$i_0 = 90°$	1.3926	298.72	811.80	2.4366	314.82	1026.7
$i_0 = 120°$	1.3392	155.36	485.75	1.4218	95.206	475.35
$i_0 = 150°$	1.7338	123.90	465.42	1.8441	85.028	459.81
Average	**1.5225**	**197.90**	**597.60**	**2.0032**	**192.25**	**636.30**

Table 6.4: Orbit control performance with and without nullifying the out-of-plane control.

6.5.3 Learning-based MPC vs non-learning MPC

In this section, the proposed learning-based MPC scheme of Fig. 6.5 is compared to a non-learning MPC. The non-learning MPC is equivalent to the learning-based MPC except from the fact that the filter does not update the gravity parameters of the guidance and control block. Consequently, the non-learning MPC computes a control under a Keplerian gravity model which is potentially more inaccurate than the learning-based MPC estimated model. This allow to assess the benefits of a learning-based strategy in terms of control performance. Note that for both schemes the navigation filters are identical, thus performing an internal estimation of the gravity parameters.

Orbit-attitude control performance

Let first assess the orbit and attitude control performances for the same scenarios of the previous Section 6.5.2.

Orbit control: the numerical results for the learning-based and non-learning based MPC are shown in Fig. 6.7-6.10 and Table 6.5. Figure 6.7 shows the orbital radius evolution for all the scenarios of the learning-based MPC and the non-learning MPC. It can be observed that the learning-based MPC succeeds in tracking the reference in all the cases while the non-learning MPC presents a persistent offset in the tracking error for $i_0 = 30°, 90°, 150°$. These facts are also observed in Fig. 6.8 where the tracking error accuracy index and fuel consumption per day has been plotted. There are no clear conclusions regarding the superior efficiency of one method above the other (for some scenarios the learning-based MPC performs better while in others it is the non-learning MPC). Table 6.5 shows the fuel consumption, error tracking index and its maximum for each scenario and the average of these. In average, the learning-based MPC fuel consumption is practically the same as the non-learning MPC. However, its superiority comes from the orbit reference tracking accuracy which reduces in a factor of three the one assocciated to the non-learning MPC and the maximum error by almost the half.

Figures 6.9-6.10 show individual results for the initial polar orbit case. Again, the semi-major axis and eccentricity evolutions evidence the superiority in the reference orbit tracking of the learning-based MPC (see Fig. 6.9). The radial and tangential control accelerations for both controllers can be seen in Fig. 6.10. It is observed that the control is quite similar during the first week of the simulation but a phasing between the signals starts to arise during the second week. This is probably due to the model learning process which allows to predict inhomogeneous gravity perturbations and counteract these with suitable control actions. The non-learning MPC model is more inaccurate and reacts later just when the tracking error has enlarged.

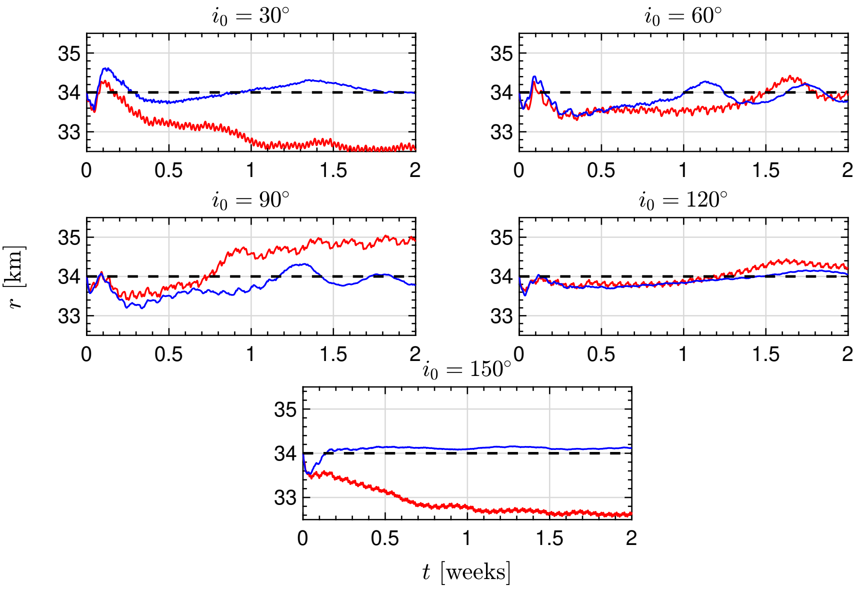

Figure 6.7: Orbital radius for different initial inclinations. Blue: learning-based MPC; red: non-learning MPC; black: reference.

Attitude control: the attitude control performance of the learning-based and non-learning MPC are shown in Tables 6.6-6.7. The attitude control accuracy

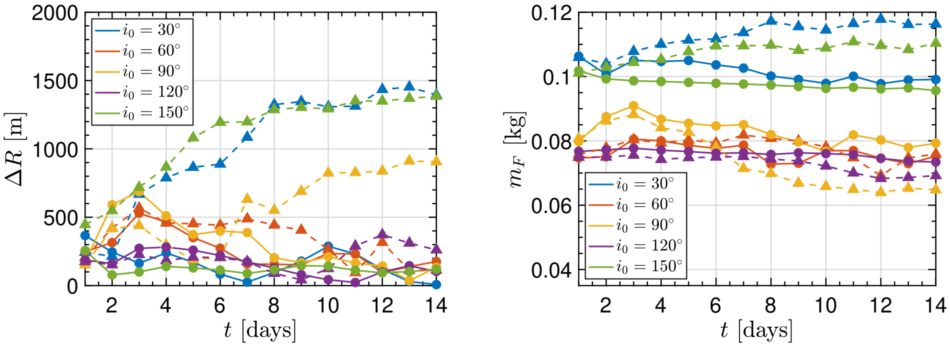

Figure 6.8: Average tracking error per day (*left*) and fuel consumption per day (*right*). Dots: learning-based MPC; triangles: non-learning MPC.

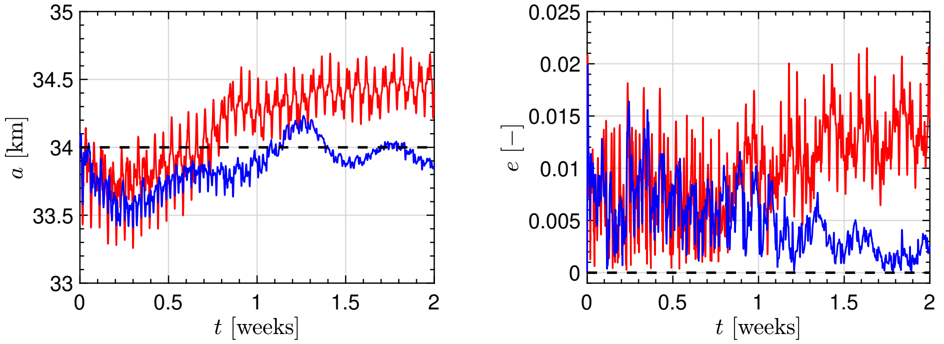

Figure 6.9: Semi-major axis (*left*) and eccentricity (*right*) for $i_0 = 90°$. Blue: learning-based MPC; red: non-learning MPC.

	Learning-based MPC			Non-learning MPC		
Simulation	m_F [kg]	ΔR [m]	$\overline{\Delta R}$ [m]	m_F [kg]	ΔR [m]	$\overline{\Delta R}$ [m]
$i_0 = 30°$	1.7962	160.12	615.16	1.9958	1023.0	1533.4
$i_0 = 60°$	1.3505	251.39	609.87	1.3788	341.06	704.45
$i_0 = 90°$	1.3926	298.72	811.80	1.2560	562.58	1043.1
$i_0 = 120°$	1.3392	155.36	485.75	1.2886	201.06	443.44
$i_0 = 150°$	1.7338	123.90	465.42	1.9121	1099.2	1437.5
Average	**1.5225**	**197.90**	**597.60**	**1.5663**	**645.38**	**1032.4**

Table 6.5: Orbit control performance of learning-based MPC and non-learning MPC.

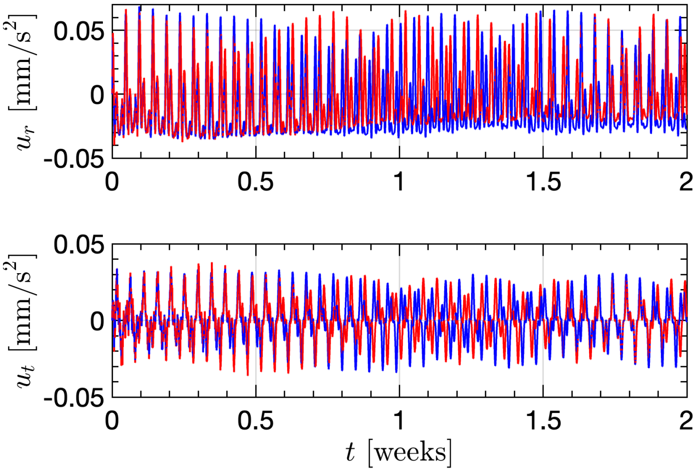

Figure 6.10: Control acceleration for $i_0 = 90°$. Blue: learning-based MPC; red: non-learning MPC.

is practically independent, in terms of mean and maximum tracking errors, of learning the model or not. The roll and yaw are driven to almost null mean values while the pitch angle presents, for all the simulations, a persistent offset in the tracking error of $\approx -1.5°$. This may be explained by the fact that the target attitude is not an equilibrium of the system. An offset-free tracking MPC is only guaranteed if the target is an equilibrium. Still, the discrepancy is low enough, thus enabling camera and LIDAR line-of-sight with the small body. In terms of control effort, T_U, the learning-based MPC reduces the torque demands in a 39% with respect to the non-learning MPC. The previous fact highlights the superiority of the learning-based MPC in terms of attitude control efficiency without a loss in the tracking accuracy. Again, results of

	Learning-based MPC		
Simulation	T_U [mN · m]	$\Delta\boldsymbol{\Theta}$ [°]	$\overline{\Delta\boldsymbol{\Theta}}$ [°]
$i_0 = 30°$	0.6346	$[1.52, 0.02, 0.05]^T$	$[2.53, 0.16, 0.39]^T$
$i_0 = 60°$	0.5996	$[1.55, 0.02, 0.05]^T$	$[2.53, 0.15, 0.38]^T$
$i_0 = 90°$	0.5005	$[1.57, 0.02, 0.05]^T$	$[2.54, 0.13, 0.42]^T$
$i_0 = 120°$	0.6027	$[1.55, 0.02, 0.04]^T$	$[2.54, 0.16, 0.29]^T$
$i_0 = 150°$	0.6011	$[1.52, 0.01, 0.04]^T$	$[2.54, 0.09, 0.38]^T$
Average	**0.5877**	$\mathbf{[1.54, 0.02, 0.05]^T}$	$\mathbf{[2.54, 0.14, 0.37]^T}$

Table 6.6: Attitude control performance of learning-based MPC.

interest for the initial polar orbit simulation are shown in Fig. 6.11-6.12. The pitch, roll and yaw evolutions for both controllers can be seen in Fig. 6.11.

	Non-learning MPC		
Simulation	T_U [mN · m]	$\Delta\boldsymbol{\Theta}$ [°]	$\overline{\Delta\boldsymbol{\Theta}}$ [°]
$i_0 = 30°$	1.0519	$[1.67, 0.02, 0.05]^T$	$[2.53, 0.16, 0.40]^T$
$i_0 = 60°$	0.9424	$[1.56, 0.02, 0.05]^T$	$[2.53, 0.13, 0.36]^T$
$i_0 = 90°$	0.7773	$[1.49, 0.02, 0.05]^T$	$[2.54, 0.12, 0.41]^T$
$i_0 = 120°$	0.9671	$[1.53, 0.02, 0.03]^T$	$[2.54, 0.11, 0.27]^T$
$i_0 = 150°$	1.0465	$[1.68, 0.01, 0.03]^T$	$[2.54, 0.10, 0.27]^T$
Average	**0.9570**	$\mathbf{[1.59, 0.02, 0.04]}^T$	$\mathbf{[2.54, 0.12, 0.34]}^T$

Table 6.7: Attitude control performance of non-learning MPC.

These evolutions are practically the same for both controllers, thus being in accordance with Tables 6.6-6.7. In Fig. 6.12, which shows the applied torque in the body frame, the higher torque demand of the non-learning MPC can be easily seen.

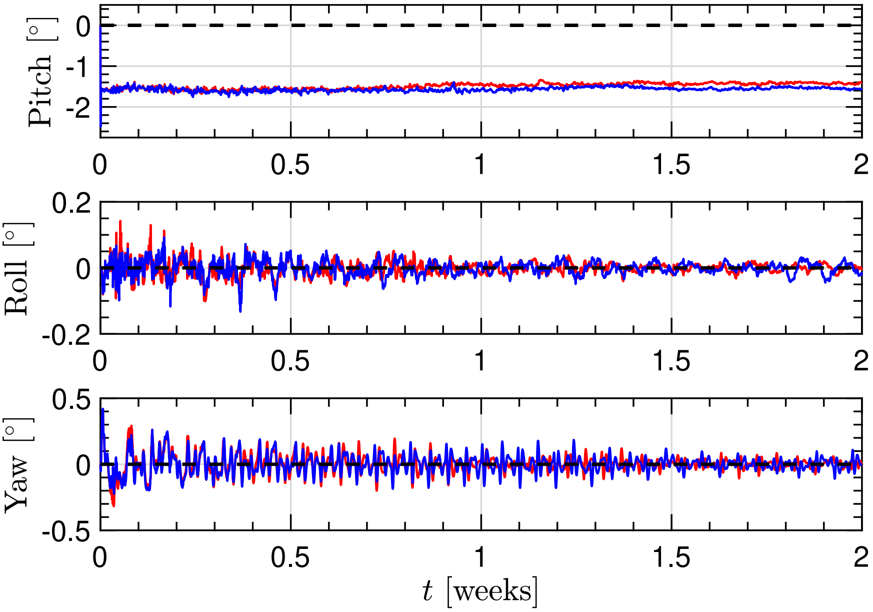

Figure 6.11: Pitch, roll and yaw for $i_0 = 90°$. Blue: learning-based MPC; red: non-learning MPC; black: reference.

Initial orbit sensitivity analysis

Now, the sensitivity of the controllers, with respect to an initial orbit which does not match the orbit reference, is studied. This may be a practical sce-

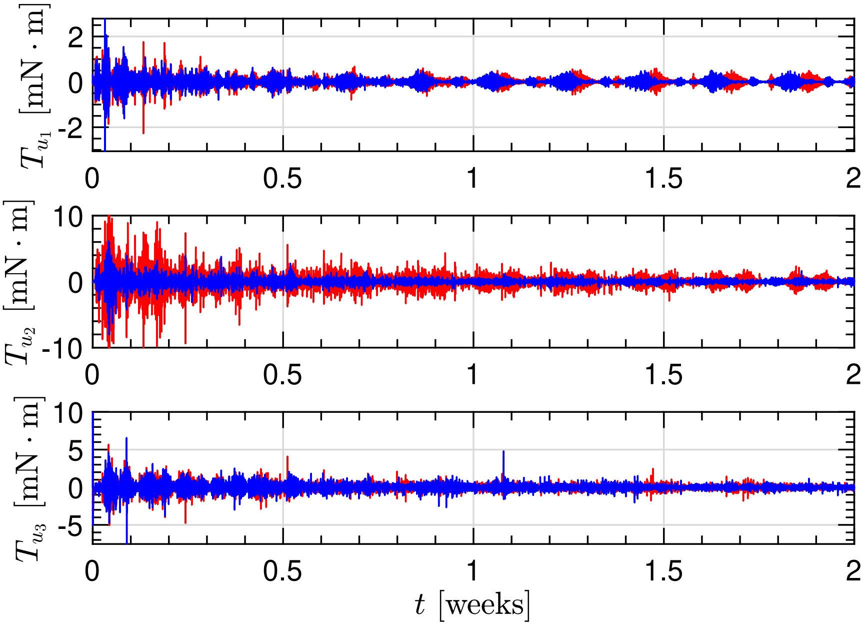

Figure 6.12: Control torque for $i_0 = 90°$. Blue: learning-based MPC; red: non-learning MPC.

nario where there exist an error in the orbit insertion. To this end, only the initial semi-major axis will be varied as $a_0 = \{33, 33.5, 34, 34.5, 35\}$ km. For the sake of conciseness, for each inclination, the average orbit control performance results (by varying the initial semi-major axis) are shown in Table 6.8. Typically, in exchange for a slight increase in fuel consumption ($\approx 7\%$), the learning-based MPC reduces the tracking accuracy index ΔR in a factor of four. The maximum tracking error is also reduced. The gain in orbit control performance for the learning-based MPC depends on the initial inclination, but it is observed that the reference tracking accuracy is enhanced for all of them. This demonstrates the superiority of the learning-based MPC for the sensitivity analysis.

The orbital radius of each initial condition, for the initial polar orbit, is shown in Fig. 6.13. It can be observed that the learning-based MPC succeeds in tracking the reference orbit while the non-learning MPC ends with a persistent tracking error offset in all cases. This evidences the learning-based MPC control capability to reduce the initial tracking error even if the control program is based on linearization around the reference orbit.

	Learning-based MPC			Non-learning MPC		
Simulation	m_F [kg]	ΔR [m]	$\overline{\Delta R}$ [m]	m_F [kg]	ΔR [m]	$\overline{\Delta R}$ [m]
$i_0 = 30°$	1.7943	159.17	864.67	1.9668	1280.5	1829.2
$i_0 = 60°$	1.3547	264.84	983.92	1.2640	284.90	921.90
$i_0 = 90°$	1.4034	316.38	971.50	1.0903	797.04	1247.9
$i_0 = 120°$	1.3378	167.35	840.81	1.1330	241.13	820.26
$i_0 = 150°$	1.7447	129.85	847.83	1.6742	1390.8	1681.5
Average	**1.5270**	**207.52**	**901.75**	**1.4257**	**798.87**	**1300.2**

Table 6.8: Average orbit control performance of the learning-based MPC and non-learning MPC for the sensitivity analysis.

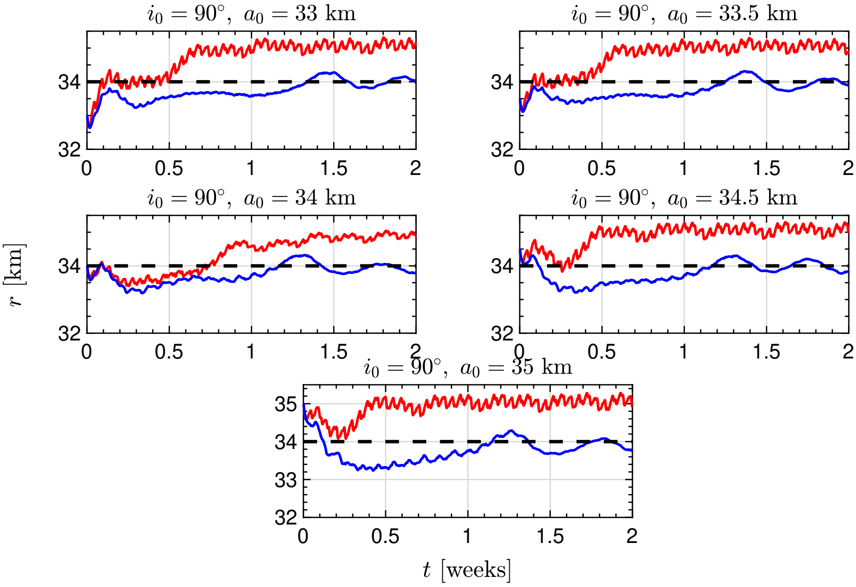

Figure 6.13: Orbital radius of the initial polar orbit in the sensitivity analysis. Blue: learning-based MPC; red: non-learning MPC; black: reference.

Filters performance

Let now assess the performance of the orbit and attitude filters for the initial polar orbit simulation ($i_0 = 90°$).

Orbit filter: the navigation errors in position and the orbit filter residuals are shown in Fig. 6.14-(6.15). It can be observed that the navigation error is less dispersed for the radial coordinate (x^O) than for the tangential (y^O) and normal (z^O) components. This is mainly due to the higher observability of the radial coordinate due to the LIDAR ranging measurement. Table 6.9 shows the mean and maximum absolute navigation errors (e.g. $|\delta x^O|$). It can be seen that the results in the last two days outperforms the ones corresponding to the whole scenario (14 m in average against 19 m). This demonstrates the filter success in reducing the navigation errors which is mainly due to the gravity estimation process convergence.

The filter consistency can be assessed through Table 6.10 which shows statistical information (bias and 1-sigma standard deviation) about the residuals. It is observed that, for both the pixels and range, the residuals biases are one or two order of magnitudes below their 1-sigma dispersions. This correlates well with the non-biased statistical properties of the high-resolution camera and LIDAR as per Table 6.2. Specially, the 1-sigma dispersion is highly correlated in the case of the ranging distance ($\approx$ 4 m with respect to the assumed one of 5 m). In the case of the pixel row and column, the obtained dispersions are three times higher than the introduced ones. However, they diminished along the simulation if one compares the last two days to the overall scenario (see also Fig. (6.15)). This may indicate that more room for improvement is available if the filter is kept running for an extended duration of the scenario.

	Days 1-14		Days 13-14	
Navigation error	Mean	Max.	Mean	Max.
Radial [m]	1.7455	12.243	1.3531	6.2559
Tangential [m]	14.067	136.37	9.0449	33.459
Normal [m]	9.7575	80.250	8.4733	26.227
Total [m]	**19.023**	**152.53**	**13.936**	**34.780**

Table 6.9: Absolute navigation errors in position of learning-based MPC for $i_0 = 90°$.

Attitude filter: the navigation errors in Euler angles and the attitude filter residuals are shown in Fig. 6.16-(6.17). Since the star-tracker and gyroscope measurements are directly related to the navigation variables, the estimation error in Euler angles is low ($< 0.2°$). Table 6.11 shows the mean and maximum value of the attitude navigation errors, in terms of Euler angles, and the gyroscope bias estimation. The filter is demonstrated to be converging as the

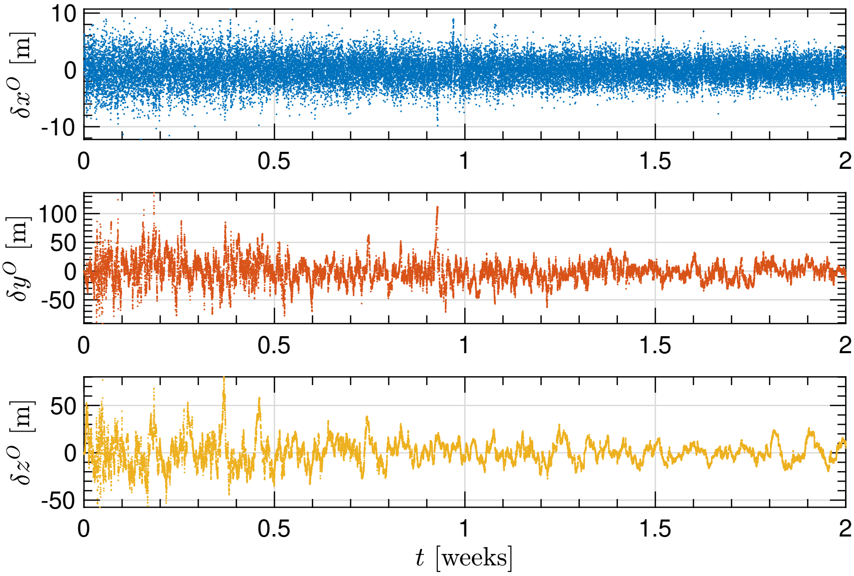

Figure 6.14: Navigation errors in radial, tangential and normal position coordinates.

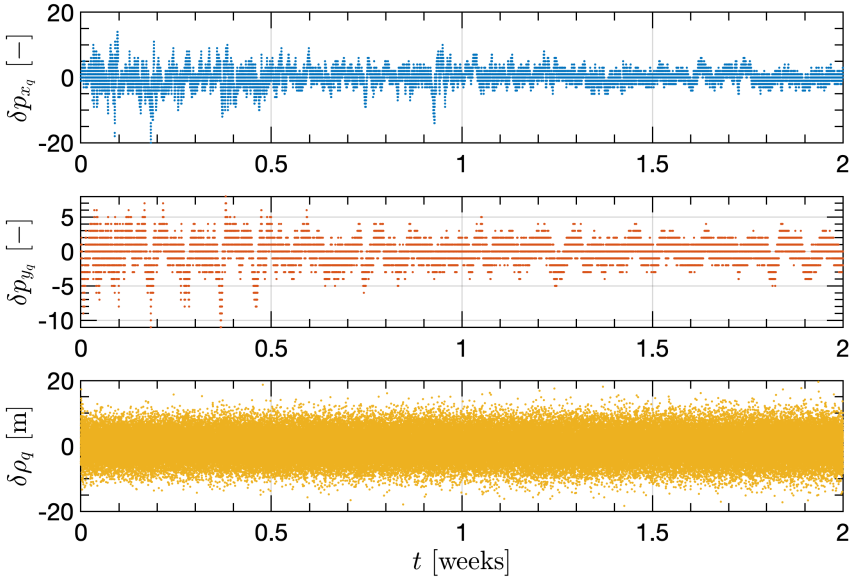

Figure 6.15: Orbit filter residuals of pixels and range.

	Days 1-14		Days 13-14	
Residual	Bias	1-sigma	Bias	1-sigma
Pixel row [-]	0.1019	2.4239	-0.0696	1.5749
Pixel column [-]	-0.1121	1.7373	-0.2088	1.4419
Range [m]	0.0158	4.2282	0.0598	4.4095

Table 6.10: Orbit filter residuals statistics of learning-based MPC for $i_0 = 90°$.

mean and peaks are reduced when the whole scenario is compared to the last two days. The gyroscope bias is well captured as the maximum committed error during the days 13-14 is just 0.052%.

The filter consistency is assessed through the statistical information (bias and 1-sigma standard deviation) of the attitude filter residuals, which can be seen in Table 6.12. For both the star-tracker MRP and the angular velocity of the gyroscopes, the biases are one or two order of magnitude below the standard deviation. This correlates well with Table 6.2 where the only biased variable is the gyroscope angular velocity which is estimated within the filter. The 1-sigma standard deviations also show a good correlation with the sensors Gaussian distribution. The gyroscope angular velocity 1-sigma was assumed to be 0.05 °/h, on each component, which is in the vicinity of the obtained values for the residuals

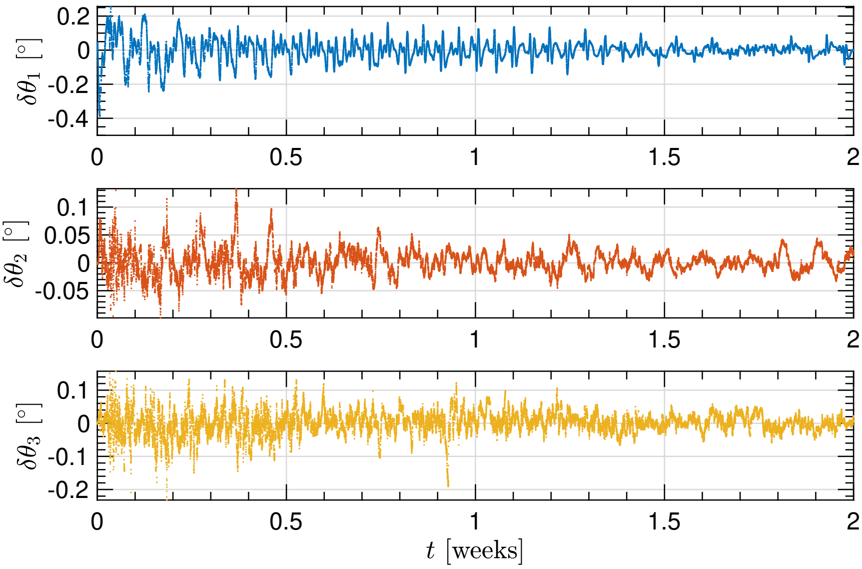

Figure 6.16: Navigation errors in pitch, roll and yaw angles.

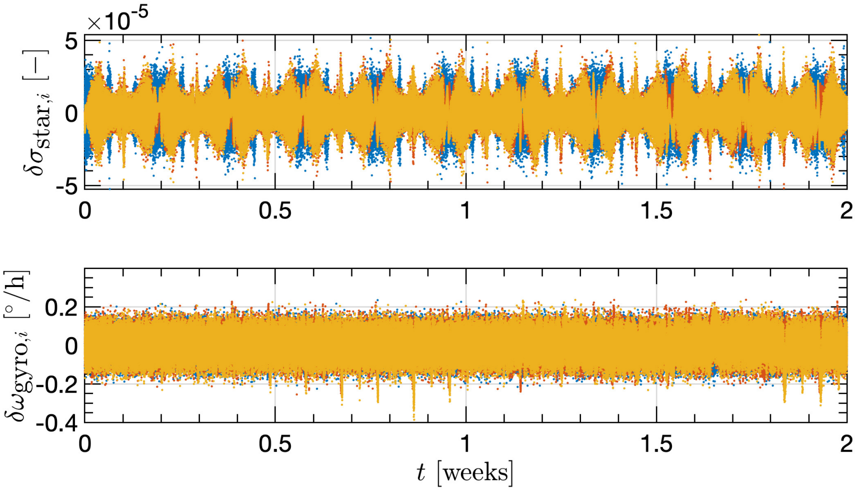

Figure 6.17: Attitude filter residuals of star-tracker MRP and gyroscope angular velocity.

	Days 1-14		Days 13-14	
Navigation error	Mean	max	Mean	max
Pitch [°]	0.0239	0.2318	0.0153	0.0587
Roll [°]	0.0166	0.1363	0.0143	0.0447
Yaw [°]	0.0426	0.3857	0.0191	0.0899
Gyroscope bias [°/h]	0.0014	0.1265	0.0025	0.0026

Table 6.11: Absolute navigation errors in pitch, roll, yaw and gyroscope bias of learning-based MPC for $i_0 = 90°$.

	Days 1-14		Days 13-14	
Residual	Bias	1-sigma	Bias	1-sigma
$\delta\sigma_{\text{star},1}$ [−]	$-2.125\cdot10^{-8}$	$7.851\cdot10^{-6}$	$-1.052\cdot10^{-7}$	$9.128\cdot10^{-6}$
$\delta\sigma_{\text{star},2}$ [−]	$8.334\cdot10^{-8}$	$7.830\cdot10^{-6}$	$-9.768\cdot10^{-8}$	$8.528\cdot10^{-6}$
$\delta\sigma_{\text{star},3}$ [−]	$-6.633\cdot10^{-8}$	$7.945\cdot10^{-6}$	$-7.879\cdot10^{-8}$	$8.469\cdot10^{-6}$
$\delta\omega_{\text{star},1}$ [°/h]	$-4.345\cdot10^{-4}$	0.0510	$5.291\cdot10^{-4}$	0.0509
$\delta\omega_{\text{star},2}$ [°/h]	$4.590\cdot10^{-4}$	0.0541	$-1.160\cdot10^{-3}$	0.0548
$\delta\omega_{\text{star},3}$ [°/h]	$-2.734\cdot10^{-3}$	0.0559	$-4.179\cdot10^{-3}$	0.0603

Table 6.12: Attitude filter residuals statistics of learning-based MPC for $i_0 = 90°$.

Computational effort

Finally, let assess the computational burden of the proposed GNC scheme. The computational times (mean, 1-σ standard deviation and maximum), of filters and guidance and control algorithms, are shown in Table 6.13 for the initial polar orbit simulation. In that table, MPC refers to the whole guidance and control module. As expected, the execution of the guidance and control algorithms is the most time-consuming task being two orders of magnitude slower than the filters computation. The orbit modules (UKF and MPC) execution times are higher than its attitude counterparts which is due, in part, to their longer propagations periods. Translating the worst-case computation as a percentage of the sampling rates yields 2.30% and 0.33% execution times with respect to the period between filter calls for attitude and orbit respectively. The guidance and control execution takes a 6.69% (attitude) and 1.04% (orbit) with respect to their sampling rates. These results are promising in terms of justifying the potential mission autonomy, at least for the orbit modules. Nonetheless, the attitude modules computational burden may be reduced if one renounces to estimate gravity within its filter. Then, the higher control torque demand of the non-learning MPC would have to be assumed.

	Mean	1-sigma	Max.
Att. UKF	0.0482 s / 1.34%	$0.8242\cdot10^{-4}$ s / 0.02%	0.0827 s / 2.30%
Orb. UKF	0.0698 s / 0.19%	$0.9421\cdot10^{-4}$ s / 0.00% /	0.1171 s / 0.33%
Att. MPC	1.645 s / 4.57%	0.0134 s / 0.04%	2.408 s / 6.69%
Orb. MPC	3.721 s / 1.55%	0.0406 s / 0.02%	4.097 s / 1.71%

Table 6.13: Computational times and its percentage over the sampling interval of the GNC modules for the learning-based MPC for $i_0 = 90°$.

6.5.4 Gravity estimation with constellations of satellites

This section is devoted to demonstrate the positive impact in the gravity estimation by using a satellite constellation instead of a single spacecraft. The following constellations are defined:

- 3 sats: $\breve{a}^{[\iota]} = a_0^{[\iota]} = \{34, 36, 38\}$ km, $\breve{e}^{[\iota]} = e_0^{[\iota]} = \{0, 0, 0\}$, $\Omega_0^{[\iota]} = \omega_0^{[\iota]} = \nu_0^{[\iota]} = \{0°, 0°, 0°\}$, $i_0^{[\iota]} = \{45°, 90°, 135°\}$, $\iota = 1, 2, 3$.
- 6 sats: $\breve{a}^{[\iota]} = a_0^{[\iota]} = \{31, 33, 35, 37, 39, 41\}$ km, $\breve{e}^{[\iota]} = e_0^{[\iota]} = \{0, 0, 0, 0, 0, 0\}$, $\Omega_0^{[\iota]} = \omega_0^{[\iota]} = \nu_0^{[\iota]} = \{0°, \ldots, 0°\}$, $i_0^{[\iota]} = \{15°, 45°, 75°, 105°, 135°, 165°\}$, $\iota = 1, \ldots, 6$.
- 9 sats: $\breve{a}^{[\iota]} = a_0^{[\iota]} = \{28, 30, 32, 34, 36, 38, 40, 42, 44\}$ km, $\breve{e}^{[\iota]} = e_0^{[\iota]} = \{0, \ldots, 0\}$, $\Omega_0^{[\iota]} = \omega_0^{[\iota]} = \nu_0^{[\iota]} = \{0°, \ldots, 0°\}$, $i_0^{[\iota]} = \{18°, 36°, 54°, 72°, 90°, 108°, 126°, 144°, 162°\}$, $\iota = 1, \ldots, 9$.

Note that the constellations orbits are circular with a significant separation between satellites (2 km) in order to prevent potential collisions. The term "satι" denotes each satellite in the subsequent figures. The trajectories of the 9 sats constellation are shown in Fig. 6.18-6.19 respectively. Figure 6.18 represents the satellite trajectories in the asteroid centered inertial frame where the nodal precession phenomena is clearly seen. This is due to the decision of not controlling the right ascension of the ascending node. Figure 6.19 shows the satellite trajectories in the asteroid centered fixed frame. This validates that the satellites do not collide with the asteroid while providing insight of the asteroid overflown regions.

The orbital radius and inclinations, for the 9 sats constellation, are represented in Fig. 6.20. The orbital radius evolution shows convergence to the reference after some transient time for all the satellites. The initial transient period will be related to the gravity estimation process in the sequel. Moreover, it can be seen that the initial tracking errors are higher in lower asteroid orbits where the inhomogeneous gravity field effects are stronger. The orbital inclination is maintained constant in average through the simulation, which is partly due to the decision of not applying out-of-plane control. Under such condition, the natural perturbations do not affect, in average, the orbital inclination. This is an interesting fact as the asteroid overflew latitudes can be chosen (at a certain extent) beforehand with the initial inclination i_0.

For the 9 sats constellation, each satellite orientation (in terms of Euler angles) of the body with respect to the orbital frame is shown in Fig. 6.21. The roll and yaw are driven to the reference (null value) in average for all the satellites. Nonetheless, a tracking error offset ($0.4° - 2.5°$) arises in the pitch angle for all of them (this was expected in light of Table 6.6). The tracking error offset intensifies as the satellite orbits closer to the asteroid. This fact could be directly related to the stronger inhomogeneous gravity field perturbations in the gravity-gradient torque for lower orbits.

In order to analyze the orbit control accuracy and fuel consumption performance of each satellite, let observe the left illustration of Fig. 6.22. The orbit reference tracking index shows no meaningful correlation with the reference semi-major axis. This index can be assured to be below ≈ 400 m for all the satellites while the initial inclination may also play a role (that is not analyzed) on its tendency. The fuel consumption shows a clear decreasing trend as the reference semi-major axis increases. This highlights the high influence of the inhomogeneous gravity field perturbation in lower-asteroid orbits.

The joint estimation of the gravity parameters, of the 9 sats constellation, is shown in Fig. 6.22-6.23. The second-order gravity converges rapidly while the third and fourth-order gravity terms are much more slower. Nonetheless, the 1-sigma uncertainty follows a decreasing trend at all cases which confirms the well-posed behaviour of the filters. The gravity estimation convergence process is directly related to the convergence of the orbital radius to the tracking reference as seen in Fig. 6.20. It can be deduced that the initial transient in the orbital radius, with large initial tracking errors, is caused by the initial inaccurate gravity model.

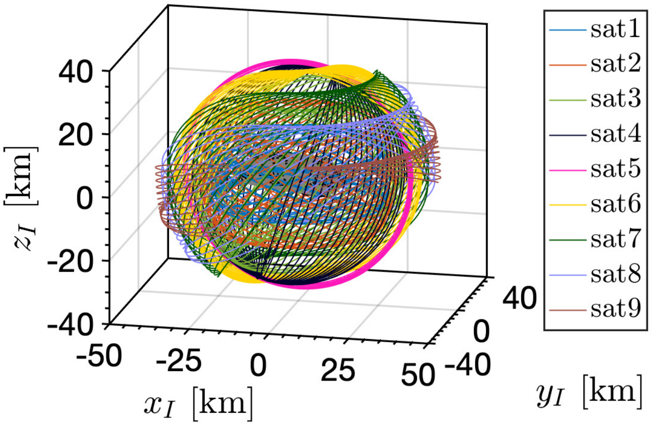

Figure 6.18: Trajectories in the asteroid centered inertial frame of the 9 sats constellation. Black dots: surface landmarks.

Finally, let compare the gravity parameters estimation between the satellite constellation and the single satellite missions of Section 6.5.3. To do so, only the estimation of the relevant gravity parameters is analyzed. A gravity parameter

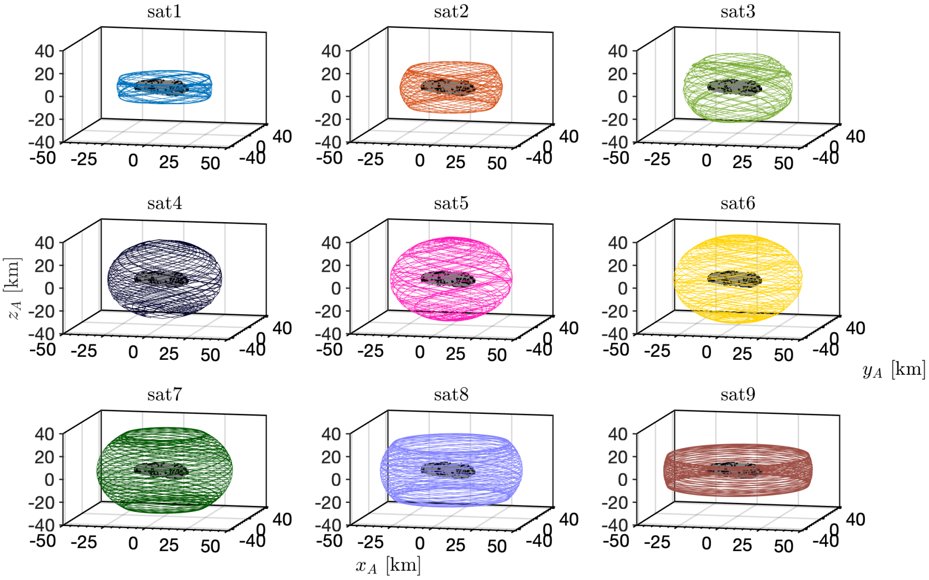

Figure 6.19: Trajectories in the asteroid centered fixed frame of the 9 sats constellation. Black dots: landmarks.

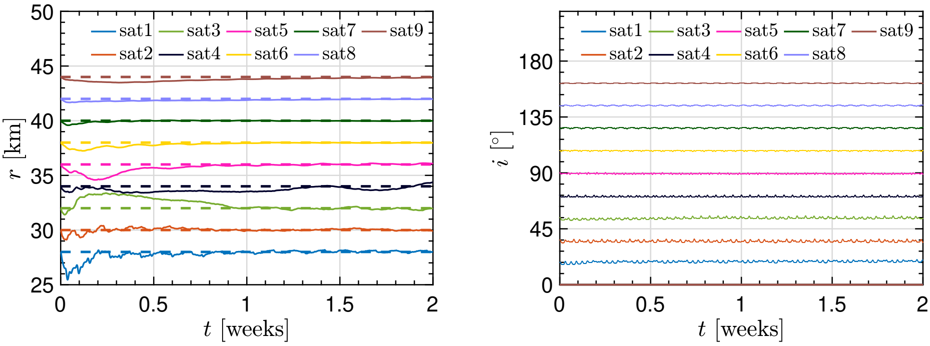

Figure 6.20: Orbital radius (*left*) and inclination (*right*) of 9 sats constellation.

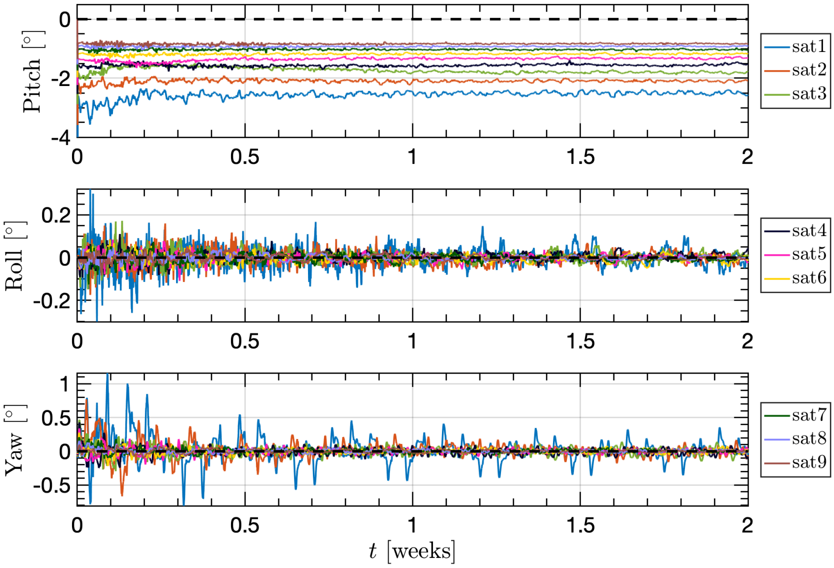

Figure 6.21: Pitch, roll and yaw of 9 sats constellation.

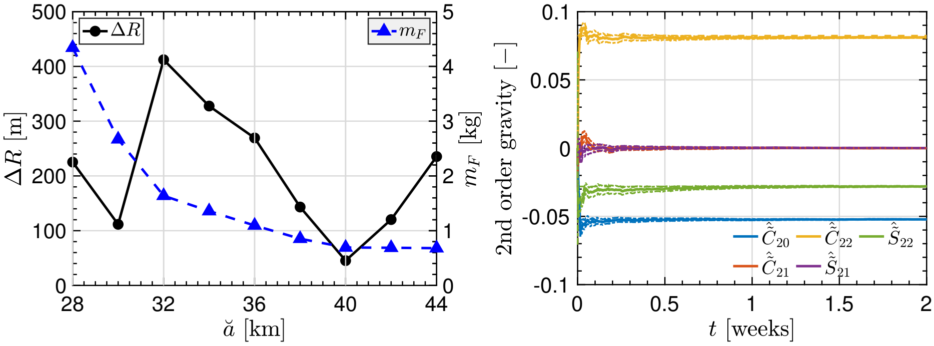

Figure 6.22: Orbit reference tracking index, fuel consumption (*left*) and second-order gravity parameters (*right*) of 9 sats constellation. Dashed:truth; solid:estimation; dot-dashed:1-σ uncertainty.

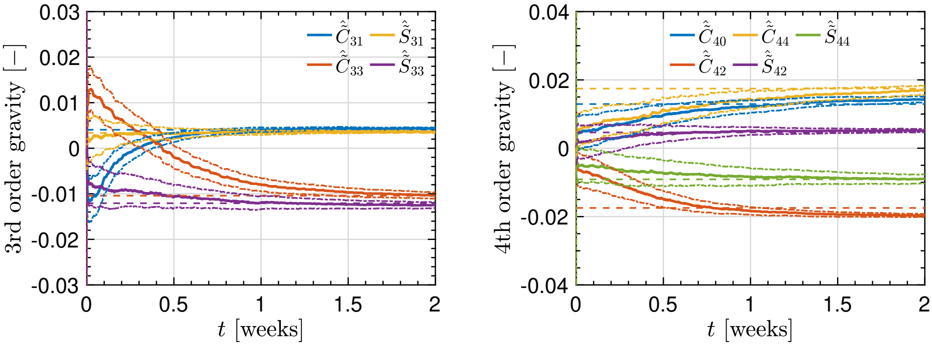

Figure 6.23: Relevant third-order (*left*) and fourth-order gravity parameters (*right*) of 9 sats constellation. Dashed:truth; solid:estimation; dot-dashed:1-σ uncertainty

is considered relevant if $|\tilde{C}_{nm}|, |\tilde{S}_{nm}| > 2 \cdot 10^{-3}$, such that

$$\begin{array}{llllll}
\tilde{C}_{20} = & -5.2462 \cdot 10^{-2}, & \tilde{C}_{22} = & 8.2399 \cdot 10^{-2}, & \tilde{S}_{22} = & -2.8110 \cdot 10^{-2}, \\
\tilde{C}_{31} = & 4.0602 \cdot 10^{-3}, & \tilde{C}_{33} = & -1.0416 \cdot 10^{-2}, & \tilde{S}_{31} = & 3.3685 \cdot 10^{-3}, \\
\tilde{S}_{33} = & -1.2071 \cdot 10^{-2}, & \tilde{C}_{40} = & 1.2932 \cdot 10^{-2}, & \tilde{C}_{42} = & -1.7469 \cdot 10^{-2}, \\
\tilde{C}_{44} = & 1.7455 \cdot 10^{-2}, & \tilde{S}_{42} = & 4.6291 \cdot 10^{-3}, & \tilde{S}_{42} = & -9.1053 \cdot 10^{-3},
\end{array}$$

is the set of 433 Eros relevant gravity parameters. The spherical harmonics that are below that threshold do not provide useful insight in the gravity estimation accuracy as their dynamical effect is weak. This causes them to be less observable which usually results in random variations around very small values.

The gravity parameters final estimation errors ($\delta\tilde{C}^f_{nm}$, $\delta\tilde{S}^f_{nm}$) (see Eq. (6.65)) and convergence times ($t_{\hat{C}_{nm}}$, $t_{\hat{S}_{nm}}$) (see Eq. (6.66)) are shown in Tables 6.14-6.16. When no convergence is acquired for a gravity parameter, because its estimation error is not below the 20% threshold, a “no” is marked in the corresponding field of the table. The second-order gravity estimation results are shown in Table 6.14. The final estimation errors of these parameters are always below 2.5% except for $\tilde{S}_{22}$ in the initial polar orbit case. Moreover, the convergence is always acquired during the first week of the simulation for all the single satellites (except from the previous exception) and during the first two days for the constellations. This fact evidences the superiority of the satellite constellation as it provides a faster convergence in the gravity estimation. Moreover an outlier, such as $\tilde{S}_{22}$ for the initial polar orbit, has not appeared in any of the constellations.

The third and fourth order gravity estimation results are shown in Tables 6.15-6.16. The first issue that one observes is that many of the third and fourth order gravity parameters ($\tilde{C}_{31}$, $\tilde{C}_{33}$, $\tilde{C}_{44}$, $\tilde{S}_{42}$ and $\tilde{S}_{44}$) fail to achieve convergence for the single satellites. On the contrary, the 6 sats and 9 sats constellations acquire convergence for all the relevant gravity parameters with final estimation errors below 20%. Note that the 3 sats constellation does not acquire convergence of some parameters. In any case, the accuracy of the third and fourth order gravity terms can be considered poor when compared to the second-order ones. As an example, the 9 sats constellation provides final estimation errors below a 5% for just five ($\tilde{C}_{33}$, $\tilde{S}_{31}$, $\tilde{S}_{33}$, $\tilde{C}_{42}$ and $\tilde{C}_{44}$) of the nine relevant parameters. This confirms that the estimation of higher order gravity terms is more challenging because their dynamical effect is weak when compared to second-order gravity (augmenting an order makes the perturbing acceleration to decrease in a factor of $1/r$ as deducted by Eq. (2.14)). This causes the higher order gravity terms to be less observable and prone to absorb uncertainty coming from other sources (e.g. solar radiation pressure, Sun third-body perturbation).

The analysis of the gravity estimation results has proven that second-order gravity is estimated accurately for both single satellite and constellations (errors below 2.5% except from an outlier). However, satellite constellations are able to speed up the estimation convergence in 2 to 3.5 times faster. The third and fourth order gravity estimation was more challenging to estimate and the results were worst in general. In particular, single satellites usually failed (except the $i_0 = 30°$ case) to achieve convergence for these parameters, thus yielding inaccurate estimations above a 20% of error.

Simulation	$\delta\tilde{C}^f_{20}$[%]	$t_{\tilde{C}_{20}}$[h]	$\delta\tilde{C}^f_{22}$[%]	$t_{\tilde{C}_{22}}$[h]	$\delta\tilde{S}^f_{22}$[%]	$t_{\tilde{S}_{22}}$[h]
$i_0 = 30°$	0.2027	6.4	0.5796	6.5	2.2642	74.8
$i_0 = 60°$	0.6010	2.0	0.0815	1.3	1.3459	7.8
$i_0 = 90°$	0.1482	1.9	0.1400	1.7	7.3956	193.1
$i_0 = 120°$	0.1856	2.5	0.5236	0.6	0.6305	38.5
$i_0 = 150°$	0.3760	3.5	0.2751	0.5	2.2060	34.1
Average	**0.3027**	**3.3**	**0.3200**	**2.1**	**2.7684**	**69.7**
3 sats	0.3490	1.7	0.6779	0.8	2.4628	43.2
6 sats	0.5284	1.7	0.3093	1.0	1.1560	5.7
9 sats	0.4747	1.7	1.6169	1.0	0.2184	6.0
Average	**0.4507**	**1.7**	**0.8680**	**0.9**	**1.2719**	**18.3**

Table 6.14: Relevant second order gravity parameters estimation.

Simulation	$\delta\tilde{C}^f_{31}$[%]	$t_{\tilde{C}_{31}}$[h]	$\delta\tilde{C}^f_{33}$[%]	$t_{\tilde{C}_{33}}$[h]	$\delta\tilde{S}^f_{31}$[%]	$t_{\tilde{S}_{31}}$[h]	$\delta\tilde{S}^f_{33}$[%]	$t_{S_{33}}$[h]
$i_0 = 30°$	13.712	279.0	18.729	320.3	10.179	187.1	0.0732	80.9
$i_0 = 60°$	4.7739	104.2	55.491	no	14.222	172.6	0.0951	159.7
$i_0 = 90°$	11.943	140.2	73.011	no	21.608	no	0.1352	185.3
$i_0 = 120°$	30.669	no	45.803	no	5.9831	248.5	8.4806	134.7
$i_0 = 150°$	47.641	no	31.365	no	0.0857	156.6	1.4666	37.3
Average	**21.748**	**no**	**44.880**	**no**	**10.416**	**no**	**2.0501**	**119.6**
3 sats	1.3464	122.9	40.868	no	1.2289	120.0	10.096	180.9
6 sats	10.7600	117.0	5.9992	254.9	9.6157	31.2	4.6747	82.9
9 sats	7.2493	109.7	0.3219	176.0	4.5998	26.6	3.4082	61.7
Average	**6.4519**	**116.5**	**15.730**	**no**	**5.1484**	**59.3**	**6.0596**	**108.5**

Table 6.15: Relevant third order gravity parameters estimation.

Simulation	$\delta\tilde{C}^f_{40}$[%]	$t_{\tilde{C}_{40}}$[h]	$\delta\tilde{C}^f_{42}$[%]	$t_{\tilde{C}_{42}}$[h]	$\delta\tilde{C}^f_{44}$[%]	$t_{\tilde{C}_{44}}$[h]	$\delta\tilde{S}^f_{42}$[%]	$t_{\tilde{S}_{42}}$[h]	$\delta\tilde{S}^f_{44}$[%]	$t_{\tilde{S}_{44}}$[h]
$i_0 = 30°$	2.4286	180.9	11.680	93.0	17.764	204.7	4.0302	187.1	1.6548	152.7
$i_0 = 60°$	15.562	268.9	3.3268	84.4	14.513	197.6	2.2619	39.1	31.160	no
$i_0 = 90°$	8.1015	125.0	3.3383	114.6	32.887	no	14.194	329.5	56.613	no
$i_0 = 120°$	3.8394	80.6	0.3583	97.2	24.283	no	26.187	no	26.900	no
$i_0 = 150°$	12.150	145.9	3.9113	168.7	25.408	no	32.276	no	7.2245	142.7
Average	**8.4163**	**160.3**	**4.5229**	**111.6**	**22.971**	**no**	**15.790**	**no**	**24.711**	**no**
3 sats	6.0512	172.6	1.6459	113.3	24.165	no	3.0307	99.7	22.265	no
6 sats	3.9950	105.1	4.9765	106.6	5.8115	198.8	3.2776	150.2	7.2308	225.4
9 sats	10.202	99.3	12.684	73.2	3.1098	171.7	11.797	57.4	1.0366	92.5
Average	**6.7493**	**125.7**	**6.4355**	**97.7**	**11.029**	**no**	**6.0351**	**102.4**	**10.178**	**no**

Table 6.16: Relevant fourth order gravity parameters estimation.

This page is intentionally left blank.

Chapter 7

Conclusions and future work

> Something Ends, Something Begins.
>
> Andrzej Sapkowski / Epilogue quest of The Witcher 3

Contents

7.1 Conclusions 224
7.2 Future work 226

7.1 Conclusions

This dissertation has designed multiple model predictive controllers for four space applications. These include: spacecraft rendezvous with coupled orbit-attitude control; spacecraft rendezvous in cislunar space; spacecraft rendezvous hovering phases; orbit-attitude station-keeping in the vicinity of a small body. The main goals of this thesis were: 1) to develop optimal closed-loop control algorithms; 2) to compare the control accuracy and efficiency of the proposed techniques with other state-of-the-art approaches; 3) to assure the problem is feasible and the computational burden is moderate; 4) to test the developed techniques with scenarios of interest in spacecraft proximity operations. To achieve the previous objectives, a profound literature review of the problems of interest have been done. This has led to the consideration of different controllers for each application. However, the baseline of the specific approach, for each scenario, is model predictive control. Model predictive control is a closed-loop control technique relying on the prediction of the future state by using a model of the system. This allows to compute an optimal control sequence over a future control horizon, but only the first control is applied. Recursively updating the control sequence as the time advances closes the loop. From a computational perspective, the optimization process is the critical part of model predictive control. In space applications, the dynamics is non-linear due to the main bodies gravity which increases the complexity of the optimization problem. In order to obtain a finite tractable and computationally efficient optimization program (usually in a quadratic programming form), which are the key ingredients of autonomous systems, linearization and discretization techniques have been widely employed for the closed-loop control computation. The feasibility of the optimization problem has been achieved by transforming the terminal equality constraints into penalty terms for the objective function (constraints relaxation).

The previous approach has led to innovative advances over other state-of-the-art control techniques in the literature. As a matter of fact, the developed algorithms and their associated results have been published in prestigious journals [Sanchez20b, Sanchez20a, Sanchez21a], with [Sanchez20c] still under review, and conferences proceedings [Sanchez18, Sanchez19, Sanchez21b] of the aerospace engineering research field. The presented scientific and technical advances offer novel options to achieve higher levels of autonomy and robustness in the context of spacecraft proximity operations. Under the approach mentioned in the above paragraph distinct control methodologies have been employed for each space application. These comprise flatness theory, the chance-constrained robust approach, event-based control and learning-based control. Each scenario has been tested under the presence of disturbances in order to analyze the robustness of the closed-loop response. The obtained results with the developed model predictive controllers have been compared with respect to other state-of-the-art controllers. The highlights of each one of the developed controllers are:

- Six-degrees of freedom model predictive control for Keplerian-based spacecraft rendezvous, Chapter 3, [Sanchez18, Sanchez20b].
    - The attitude flatness property and transition matrix of the Keplerian linear relative motion have been exploited to obtain an integrated six-degrees of freedom model predictive controller.
    - The control loop was closed by linearizing the system around the initial solution of the open-loop non-linear program. This results in a quadratic program.
    - The method supports any number of impulsive thrusters and inertia matrix. The simulations have been carried out for a heavy cargo and a lightweight spacecraft.
- Chance-constrained model predictive control for near-rectilinear halo orbits rendezvous, Chapter 4, [Sanchez20a].
    - A linear relative motion model for the restricted three-body problem was used in order to design a robust control for spacecraft rendezvous.
    - The chance-constrained approach guarantees line-of-sight constraints satisfaction in a probabilistic sense. An on-line estimator is used to compute the disturbance statistical properties.
    - The robust controller satisfied line-of-sight constraints in $\geq 80\%$ of the simulations while a non-robust controller only achieves $< 10\%$ of constraints satisfaction.
- Event-based predictive control for spacecraft rendezvous hovering phases, Chapter 5, [Sanchez19, Sanchez21a].
    - By combining a single-impulse control with a set of trigger rules, an aperiodic local controller to station-keep a set of constrained periodic relative orbits is developed.
    - The well-posedness and invariance of the single-impulse control is demonstrated by using reachability concepts from hybrid impulsive systems theory.
    - The event-based controller is tested against Earth's oblateness and atmospheric drag perturbations. The control accuracy and computational efficiency outperforms a recent periodic global stable controller.
- Learning-based model predictive control in the vicinity of a small body, Chapter 6, [Sanchez21b, Sanchez20c].

  - Combining unscented Kalman filtering with model predictive control, a learning-based scheme has been designed to station-keep a circular orbit with a stationary attitude.
  - The recursive update of the prediction model enhances control accuracy over time. A satellite constellation concept is also shown to speed up the gravity estimation process.
  - When compared to a non-learning controller, the developed learning-based predictive control demonstrated a superior performance in terms of orbital reference tracking accuracy (at the expense of a slight increase in fuel consumption) and attitude control efficiency.

Overall, the developed controllers of this dissertation have shown to achieve superior performances than other state-of-the-art or recent control approaches in the literature. Being related to the proximity operations domain, the benefits of the presented approaches are mainly related to the control accuracy in terms of constraints satisfaction using a moderate or low computational footprint (linear and quadratic programs with very reliable state-of-the-art solvers). However, the control effort usually increases to acquire higher levels of mission safeness. In the context of a space mission, fuel consumption for the proximity operations phase is usually a small percentage of the total one (e.g. orbit transfers). Under the previous consideration, the developed control methodologies and their results contribute to enable higher levels of autonomy in space proximity operations where a constraint violation could result in a catastrophic loss of the mission (e.g. a collision).

7.2 Future work

The work carried out in this dissertation opens up several research directions. In this section, the most promising ones are presented:

- The developed controllers for six-degrees of freedom rendezvous, hovering phases and orbit-attitude station-keeping in the vicinity of small bodies are not inherently robust. These controllers may be extended to robust control forms such as the chance-constrained approach of Chapter 4. In six-degrees of freedom rendezvous and hovering phases which rely on impulsive control, a main source of uncertainty is the thrusters actuation. In the first case, a similar approach to the chance-constrained one may be employed as it is expected that these mishaps are biased. If the bias is inferred, the line-of-sight constraints could be tightened accordingly. By doing so, the controller would be able to cope with higher levels of disturbance. In the event-based controller for spacecraft rendezvous hovering phases, under the possibility of an impulse mishap, it will be interesting to compute a single-impulse that maximizes the probability of steering back the state to the set of relative constrained periodic orbits. The current methodology just minimizes the impulse amplitude which may left the state very close to the admissible set boundary. As a consequence, an impulse mishap could cause the control to fail in reaching the admissible set. Finally, for the learning-based approach, a superior reference tracking accuracy could be achieved if not only the mean of the tracking error is minimized but a combination with its own spread over time. In that sense, the filter provides useful information of the state and model parameters uncertainty that is currently unused.

- Under the restricted three-body problem, the spacecraft proximity operations literature is still an emergent (though very rapidly) field when compared to the well-studied Keplerian relative motion. Specifically, for a near-rectilinear halo orbit, the relative dynamics response highly depends on target position along its orbit. Around the apoapsis, with respect to the secondary, the natural relative dynamics is so slow that the natural relative trajectory is a straight line. The problem becomes more interesting if the proximity operation takes place in the periapsis where the natural relative motion is faster. Under the previous consideration, the control is specially challenging in the vicinity of the target periapsis. In that line, mastering the hovering phase in the context of the restricted three-body problem can be viewed as future work. In order to do so, there are multiple lines of work that need to be explored. The restricted three-body problem orbits does not admit, in general, a mathematical closed-form expression as their Keplerian counterparts (e.g. ellipse). Instead, a table of numerical positions and velocities is provided. Since the orbit is periodic, the state can be fitted into a mathematical expression (e.g. Fourier series). Using that mathematical expression of the orbit, an explicit solution (though cumbersome) of the resulting linear relative motion system could be found. Then, by cancelling the non-periodic terms, some conditions for relative periodic orbits can be stated. These can be made to lie within a region in the relative space by constraining their amplitudes. The final step would involve the design of a controller to station-keep the set of relative constrained periodic orbits in the context of the restricted three-body problem.

- Regarding, learning-based model predictive control in the vicinity of small bodies, several future work is identified. The direct use of modified equinoctial elements may lead to fuel expenditure in cancelling short-periodic variations. The extension of the methodology to control mean modified equinoctial elements may reduce considerably the current fuel consumption needs. The presented work is view as a proof of concept of the learning-based control concept, thus it did not dig excessively in all the uncertain variables of a small body (just its inhomogeneous gravity field). In that line, the estimation of the small body mass, its rotation state, the landmarks position and the solar radiation pressure effect on the satellite may be added. This increase in the uncertainty of the system may be dampened by considering more optimistic (the analyzed scenario considered them as initially unknown) initial estimates of the inhomogeneous gravity parameters. This can be enabled by the preliminary knowledge of the asteroid shape (via shape images or lightcurves information). From the estimation perspective, the use of a Kalman filter is a conservative choice, though a sound state-of-the-art tool, as there may be recent advances in machine-learning that are worth exploring. The model-learning process is an inverse problem where one aims to infer the model parameters according to some data acquired by sensors. In that sense, artificial neural networks could be adapted to a guidance, navigation and control scheme by a batch computation combined with a state-of-the-art filter for fast estimations.

Bibliography

[Abdulrahman12] A. Abdulrahman, M. Bagash, and O. Abdelkhalik. Model predictive control for formation keeping in an orbit. *International Conference on Integrated Modeling and Analysis in Applied Control and Automation*, 1:21–25, September 2012.

[Akhlaghi17] S. Akhlaghi, N. Zhou, and Z. Huang. Adaptive Adjustment of Noise Covariance in Kalman Filter for Dynamic State Estimation. In *IEEE Power & Energy Society General Meeting*. July 2017. doi:10.1109/PESGM.2017.8273755.

[Açıkmeşe11] B. Açıkmeşe and L. Blackmore. Lossless convexification of a class of optimal control problems with non-convex control constraints. *Automatica*, 47(2):341–347, 2011. doi:10.1016/j.automatica.2010.10.037.

[Arantes-Gilz15] P. R. Arantes-Gilz and C. Louembet. Predictive control algorithm for spacecraft rendezvous hovering phases. In *Control Conference (ECC), 2015 European*, pages 2085–2090. IEEE, 2015. doi:10.1109/ECC.2015.7330847.

[Arantes-Gilz16] P. R. Arantes-Gilz. A Matlab®/Simulink® non-linear simulator for orbital spacecraft rendezvous applications., December 2016.

[Arantes-Gilz17] P. R. Arantes-Gilz, M. Joldes, C. Louembet, and F. Camps. Model predictive control for rendezvous hovering phases based on a novel description of constrained trajectories. In *IFAC World Congress*, pages 7490–7495. Toulouse, France, July 2017. doi:10.1016/j.ifacol.2017.08.1367.

[Arantes-Gilz18] P. R. Arantes-Gilz. *Embedded and validated control algorithms for the spacecraft rendezvous*. Ph.D. thesis, Université de Toulouse 3 Paul Sabatier, Toulouse, France, 2018.

[Arantes-Gilz19] P. R. Arantes-Gilz, M. Joldes, C. Louembet, and F. Camps. Stable Model Predictive Strategy for Rendezvous Hovering Phases Allowing for Control Saturation. *Journal of Guidance, Control, and Dynamics*, 42(8):1658–1675, 2019. doi:10.2514/1.G003558.

[Ariba16] Y. Ariba, D. Arzelier, L. S. Urbina, and C. Louembet. V-bar and R-bar Glideslope Guidance Algorithms for Fixed-Time Rendezvous: A Linear Programming Approach. In *20^{th} IFAC Symposium on Automatic Control in Aerospace*. Sherbrooke, Canada, August 2016. doi:10.1016/j.ifacol.2016.09.066.

[Aström08] K. J. Aström. *Analysis and Design of Nonlinear Control Systems*, chapter Event Based Control, pages 127–147. Springer, Berlin, Heidelberg, 2008. doi:10.1007/978-3-540-74358-3.

[Bai20] S. Bai, C. Han, X. Sun, H. Zhang, and Y. Jiang. Teardrop hovering formation for elliptical orbit considering j2 perturbation. *Aerospace Science and Technology*, 106, 2020. doi:10.1016/j.ast.2020.106098.

[Balmino94] G. Balmino. Gravitational potential harmonics from the shape of an homogeneous body. *Celestial Mechanics and Dynamical Astronomy*, 60:331–364, 1994. doi:10.1007/BF00691901.

[Bennet16] T. Bennet and H. Schaub. Continuous-Time Modeling and Control Using Nonsingular Linearized Relative-Orbit Elements. *Journal of Guidance, Control, and Dynamics*, 39(12):2605–2614, 2016. doi:10.2514/1.G000366.

[Betts98] J. T. Betts. Survey of Numerical Methods for Trajectory Optimization. *Journal of Guidance, Control, and Dynamics*, 21(2):193–207, 1998. doi:10.2514/2.4231.

[Biggs18] J. D. Biggs and H. Henninger. Motion planning on a class of 6-D Lie groups via a covering map. *IEEE Transactions on Automatic Control*, pages 1–12, 2018. doi:10.1109/TAC.2018.2885241.

[Biggs19] J. D. Biggs and E. Ciccarelli. In-situ tracking of a solar sail's characteristic acceleration using a robust active disturbance estimator. In *5th International Symposium on Solar Sailing*. Aachen, Germany, August 2019.

[Bowen15] J. Bowen, A. Tsuda, J. Abel, and M. Villa. CubeSat Proximity Operations Demonstration (CPOD) mission update. In *2015 IEEE Aerospace Conference*, pages 1–8. Big Sky, United States of America, March 2015. doi:10.1109/AERO.2015.7119124.

[Breger08] L. Breger and J. P. How. Safe Trajectories for Autonomous Rendezvous of Spacecraft. *Journal of Guidance, Control and Dynamics*, 31(5):1–8, 2008. doi:10.2514/1.29590.

[Bridges13] C. P. Bridges, B. Taylor, N. Horri, C. Underwood, S. Kenyon, J. Barrera-Ars, L. Pryce, and R. Bird. STRaND-2: Visual inspection, proximity operations and nanosatellite docking. In *2013 IEEE Aerospace Conference*, pages 1–8. Big Sky, United States of America, March 2013. doi:10.1109/AERO.2013.6497348.

[Broschart05] S. B. Broschart and D. J. Scheeres. Control of Hovering Spacecraft Near Small Bodies: Application to Asteroid 25143 Itokawa. *Journal of Guidance, Control, and Dynamics*, 28(2):343–354, 2005. doi:10.2514/1.3890.

[Bryson75] A. E. Bryson and Y.-C. Ho. *Applied Optimal Control: Optimization, Estimation and Control.* John Wiley & Sons, 1975. doi:10.1002/zamm.19790590826.

[Bucci17] L. Bucci, M. Lavagna, and R. Jehn. Station Keeping Techniques for Near Rectilinear Halo Orbits in the Earth-Moon system. In *10th International ESA Conference on GNC Systems.* Salzburg, Austria, May 2017.

[Bucci18] L. Bucci, A. Colagrossi, and M. Lavagna. Rendezvous in Lunar Near Rectilinear Halo Orbits. *Advances in Astronautics Science and Technology*, 1:39–43, 2018. doi:10.1007/s42423-018-0012-6.

[Butkus07] A. Butkus, K. Roe, B. L. Mitchell, and T. Payne. Space Surveillance Network and Analysis Model (SSNAM) Performance Improvements. In *2007 DoD High Performance Computing Modernization Program Users Group Conference*, pages 469–473. 2007. doi:10.1109/HPCMP-UGC.2007.67.

[Cairano12] S. D. Cairano, H. Park, and I. Kolmanovsky. Model Predictive Control approach for guidance of spacecraft rendezvous and proximity maneuvering. *International Journal of Robust and Nonlinear Control*, 22(12):1398–1427, 2012. doi:10.1002/rnc.2827.

[Calafiore06] G. C. Calafiore and M. C. Campi. The scenario approach to robust control design. *IEEE Transactions on Automatic Control*, 51(5):742–753, 2006. doi:10.1109/TAC.2006.875041.

[Camacho04] E. F. Camacho and C. Bordons. *Model Predictive Control*, chapter 9, pages 249–287. Springer-Verlag, London, 2 edition, 2004. doi:10.1007/978-0-85729-398-5.

[Caubet15] A. Caubet and J. Biggs. A Motion Planning Method for Spacecraft Attitude Maneuvers Using Single Polynomials. In *AAS/AIAA Astrodynamics Specialist Conference*. 2015.

[Ceccaroni13] M. Ceccaroni and J. Biggs. Analytic perturbative theories in highly inhomogenous gravitational fields. *Icarus*, 224(1):74–85, June 2013. doi:10.1016/j.icarus.2013.01.007.

[Chanut15] T. G. Chanut, S. Aljbaae, and V. Carruba. Mascon gravitation model using a shaped polyhedral source. *Monthly Notices of the Royal Astronomical Society*, 450(4):3742–3749, 05 2015. doi:10.1093/mnras/stv845.

[Chen98] H. Chen and F. Allgöwer. A Quasi-Infinite Horizon Nonlinear Predictive Control Scheme with Guaranteed Stability. *Automatica*, 34(10):1205–1217, 1998. doi:10.1016/S0005-1098(98)00073-9.

[Cheng18] A. Cheng, A. Rivkin, P. Michel, J. Atchison, O. Barnouin, L. Benner, N. Chabot, C. Ernst, E. Fahnestock, M. Kueppers, P. Pravec, E. Rainey, D. Richardson, A. Stickle, and C. Thomas. AIDA DART asteroid deflection test: Planetary defense and science objectives. *Planetary and Space Science*, 157:104–115, 2018. doi:10.1016/j.pss.2018.02.015.

[Chupin17] M. Chupin, T. Haberkorn, and E. Trélat. Transfer Between Invariant Manifolds: From Impulse Transfer to Low-Thrust Transfer. *Journal of Guidance, Control, and Dynamics*, 41:1–15, 2017. doi:10.2514/1.G002922.

[Clohessy60] W. Clohessy and R. Wiltshire. Terminal Guidance System for Satellite Rendezvous. *Journal of Aerospace Sciences*, 27(9):653–658, 1960. doi:10.2514/8.8704.

[Conte19] D. Conte. *Semi-Analytical Solutions for Proximity Operations in the Circular Restricted Three-Body Problem*. Ph.D. thesis, The Pennsylvania State University, State College, United States of America, 2019.

[Davis11] K. E. Davis, R. L. Anderson, D. J. Scheeres, and G. H. Born. Optimal transfers between unstable periodic orbits using invariant manifolds. *Celestial Mechanics and Dynamical Astronomy*, 109:241–264, 2011. doi:10.1007/s10569-010-9327-x.

[Deaconu12a] G. Deaconu, C. Louembet, and A. Theron. Constrained periodic spacecraft relative motion using non-negative polynomials. In *Proceedings of the American Control Conference*, pages 6715–6720. Montreal, Canada, 06 2012. ISBN 978-1-4577-1095-7. doi:10.1109/ACC.2012.6314659.

[Deaconu12b] G. Deaconu, C. Louembet, and A. Théron. A two-impulse method for stabilizing the spacecraft relative motion with respect to a periodic trajectory. In *2012 IEEE 51st IEEE Conference on Decision and Control (CDC)*, pages 6541–6546. 2012. doi:10.1109/CDC.2012.6426542.

[Deaconu13] G. Deaconu. *On the trajectory design, guidance and control for spacecraft rendezvous and proximity operations*. Ph.D. thesis, Université de Toulouse 3 Paul Sabatier, Toulouse, France, 2013.

[Deaconu15] G. Deaconu, C. Louembet, and A. Théron. Designing continuously constrained spacecraft relative trajectories for proximity operations. *Journal of Guidance, Control, and Dynamics*, 38(7):1208–1217, 2015.

[delPortillo19] I. del Portillo, B. G. Cameron, and E. F. Crawley. A technical comparison of three low earth orbit satellite constellation systems to provide global broadband. *Acta Astronautica*, 159:123–135, 2019. doi:10.1016/j.actaastro.2019.03.040.

[Di Giorgio14] A. Di Giorgio, F. Liberati, and S. Canale. Electric vehicles charging control in a smart grid: A model predictive control approach. *Control Engineering Practice*, 22:147–162, 2014. doi:10.1016/j.conengprac.2013.10.005.

[Dietrich17] A. Dietrich and J. W. McMahon. Orbit Determination Using Flash Lidar Around Small Bodies. *Journal of Guidance, Control, and Dynamics*, 40(3):650–665, 2017. doi:10.2514/1.G000615.

[Doedel03] E. J. Doedel, R. C. Paffenroth, H. B. Keller, D. J. Dichmann, J. Galan-Vioque, and A. Vanderbauwhede. Computation of Periodic Solutions of Conservative Systems with Application to the 3-Body Problem. *International Journal of Bifurcation and Chaos*, 13(6):1353–1381, 2003. doi:10.1142/S0218127403007291.

[Doedel07] E. J. Doedel, V. Romanov, R. C. Paffenroth, H. B. Keller, D. J. Dichmann, J. Galan-Vioque, and A. Vanderbauwhede. Elemental Periodic Orbits Associated With the Libration Points in the Circular Restricted 3-Body Problem. *International Journal of Bifurcation and Chaos*, 17(8):2625–2677, 2007. doi:10.1142/S0218127407018671.

[Fehse03] W. Fehse. *Automated Rendezvous and Docking of Spacecraft*, pages 171–215. Cambridge University Press. Cambridge, UK, 1 edition, 2003. doi:10.1017/CBO9780511543388.

[Filipe15] N. Filipe and P. Tsiotras. Adaptive Position and Attitude-Tracking Controller for Satellite Proximity Operations Using Dual Quaternions. *Journal of Guidance, Control and Dynamics*, 38(4):566–577, 2015. doi:10.2514/1.G000054.

[Fix96] G. Fix, C.-P. Hsu, and T. Luo. Implicitization of Rational Parametric Surfaces. *Journal of Symbolic Computation*, 21(3):329–336, 1996. doi:10.1006/jsco.1996.0015.

[Fliess95] M. Fliess, J. Lévine, P. Martin, and P. Rouchon. Flatness and defect of non linear systems: introductory theory and examples. *International Journal of Control*, 61(6):13–27, 1995. doi:10.1080/00207179508921959.

[Forshaw20] J. L. Forshaw, G. S. Aglietti, S. Fellowes, T. Salmon, I. Retat, A. Hall, T. Chabot, A. Pisseloup, D. Tye, C. Bernal, F. Chaumette, A. Pollini, and W. H. Steyn. The active space debris removal mission RemoveDebris. Part 1: From concept to launch. *Acta Astronautica*, 168:293–309, March 2020. doi:10.1016/j.actaastro.2019.09.002.

[Foster17] C. Foster, J. Mason, V. Vittaldev, L. Leung, V. Beukelaers, L. Stepan, and R. Zimmerman. Constellation phasing with differential drag on planet labs satellites. *Journal of Spacecraft and Rockets*, 55:1–11, 2017. doi:10.2514/1.A33927.

[Franzini17] G. Franzini and M. Innocenti. Relative motion equations in the local-vertical local-horizontal frame for rendezvous in lunar orbits. In *2017 AAS/AIAA Astrodynamics Specialist Conference*. Stevenson, United States of America, August 2017.

[Franzini19a] G. Franzini and M. Innocenti. Relative Motion Dynamics in the Restricted Three-Body Problem. *Journal of Spacecraft and Rockets*, 56(5):1322–1337, 2019. doi:10.2514/1.A34390.

[Franzini19b] G. Franzini, M. Innocenti, and M. Casasco. Impulsive Rendezvous Maneuvers in the Restricted Three-Body Problem. In *AIAA Scitech 2019 Forum*. San Diego, United States of America, January 2019. doi:10.2514/6.2019-1429.

[Fredrickson03] S. Fredrickson, L. Abbott, S. Duran, J. Jochim, J. Studak, J. Wagenknecht, and N. Williams. Mini AERCam: Development of a free flying nanosatellite inspection robot. In *Proceedings of SPIE - The International Society for Optical Engineering*. August 2003. doi:10.1117/12.498108.

[Fujimoto16] K. Fujimoto, N. Stacey, and J. M. Turner. *Stereoscopic Image Velocimetry as a Measurement Type For Autonomous Asteroid Gravimetry*. Long Beach, United States of America, September 2016. doi:10.2514/6.2016-5566.

[García89] C. E. García, D. M. Prett, and M. Morari. Model predictive control: Theory and practice—A survey. *Automatica*, 25(3):335–348, 1989. doi:10.1016/0005-1098(89)90002-2.

[Gaudet20] B. Gaudet, R. Linares, and R. Furfaro. Six degree-of-freedom body-fixed hovering over unmapped asteroids via LIDAR altimetry and reinforcement meta-learning. *Acta Astronautica*, 172:90–99, 2020. doi:10.1016/j.actaastro.2020.03.026.

[Gavilan12] F. Gavilan, R. Vazquez, and E. F. Camacho. Chance-constrained model predictive control for spacecraft rendezvous with disturbance estimation. *Control Engineering Practice*, 60:111–122, 2012. doi:10.1016/j.conengprac.2011.09.006.

[Gavilan15] F. Gavilan, R. Vazquez, and E. F. Camacho. A high-level model predictive control guidance law for unmanned aerial vehicles. In *2015 European Control Conference (ECC)*, pages 1362–1369. Linz, Austria, November 2015. doi:10.1109/ECC.2015.7330728.

[Gaylor07] D. Gaylor and B. Barbee. Algorithms for safe spacecraft proximity operations. *Advances in the Astronautical Sciences*, 127:133–152, January 2007.

[Genta14] G. Genta. Private space exploration: A new way for starting a spacefaring society? *Acta Astronautica*, 104:480–486, 2014. doi:10.1016/j.actaastro.2014.04.008.

[Gil-Fernandez18] J. Gil-Fernandez and G. Ortega-Hernando. Autonomous vision-based navigation for proximity operations around binary asteroids. *CEAS Space Journal*, 10:287–294, 2018. doi:10.1007/s12567-018-0197-5.

[Gim05] D.-W. Gim and K. T. Alfriend. Satellite Relative Motion Using Differential Equinoctial Elements. *Celestial Mechanics and Dynamical Astronomy*, 92:295–336, 2005. doi:10.1007/s10569-004-1799-0.

[Glassmeier07] K.-H. Glassmeier, H. Boehnhardt, D. Koschny, E. Kührt, and I. Richter. The ROSETTA Mission: Flying towards the origin of the solar system. *Space Science Reviews*, 128:1–21, February 2007. doi:10.1007/s11214-9140-8.

[Gomez04] G. Gomez, W. S. Koon, M. W. Lo, J. E. Marsden, J. J. Masdemont, and S. D. Ross. Connecting orbits and invariant manifolds in the spatial restricted three-body problem. *Nonlinearity*, 17(5):1571–1606, 2004. doi:10.1088/0951-7715/17/5/002.

[Gong09] S. Gong, H. Baoyin, and J. Li. Coupled attitude-orbit dynamics and control for displaced solar orbits. *Acta Astronautica*, 65(5-6):730–737, 2009. doi:10.1016/j.actaastro.2009.03.006.

[Guiggiani15] A. Guiggiani, I. Kolmanovsky, P. Patrinos, and A. Bemporad. Fixed-Point Constrained Model Predictive Control of Spacecraft Attitude. In *American Control Conference*. Chicago, Ilinois, United States of America, July 2015. doi:10.1109/ACC.2015.7171078.

[Gurobi14] Gurobi. *Gurobi optimizer reference manual*. Gurobi Optimization, Inc., 2014. URL **http://www.gurobi.com**.

[Guzzetti17] D. Guzzetti, E. Zimovan, K. Howell, and D. Davis. Stationkeeping analysis for spacecraft in lunar near rectilinear halo orbits. In *27th AAS/AIAA Space Flight Mechanics Meeting*. San Antonio, United States of America, February 2017.

[Haddad06] W. M. Haddad, V. Chellaboina, and S. G. Nersesov. *Impulsive and Hybrid Dynamical Systems*, chapter Stability Theory for Nonlinear Impulsive Dynamical Systems, pages 9–80. Princeton Series in Applied Mathematics, 2006. ISBN 978-1-4008-6524-6.

[Han20] C. Han, S. Bai, X. Sun, and Y. Rao. Hovering Formation Control Based on Two-Stage Constant Thrust. *Journal of Guidance, Control, and Dynamics*, 43(3):504–517, 2020. doi:10.2514/1.G004595.

[Hartley12] E. N. Hartley, P. A. Trodden, A. G. Richards, and J. M. Maciejowski. Model predictive control system design and implementation for spacecraft rendezvous. *Control Engineering Practice*, 20(7):695–713, 2012. doi:10.1016/j.conengprac.2012.03.009.

[Hartley15a] E. N. Hartley. A tutorial on model predictive control for spacecraft rendezvous. In *2015 European Control Conference (ECC)*, pages 1355–1361. 2015. doi:10.1109/ECC.2015.7330727.

[Hartley15b] E. N. Hartley and J. M. Maciejowski. Field programmable gate array based predictive control systen for spacecraft rendezvous in elliptical orbits. *Optimal Control Applications and Methods*, 36(5):585–607, 2015. doi:10.1002/oca.2117.

[Hayne15] P. O. Hayne, A. Hendrix, E. Sefton-Nash, M. A. Siegler, P. G. Lucey, K. D. Retherford, J.-P. Williams, B. T. Greenhagen, and D. A. Paige. Evidence for exposed water ice in the Moon's south polar regions from Lunar Reconnaissance Orbiter ultraviolet albedo and temperature measurements. *Icarus*, 255(15):58–69, 2015. doi:10.1016/j.icarus.2015.03.032.

[Hegrenæs05] O. Hegrenæs, J. T. Gravdahl, and P. Tøndel. Spacecraft Attitude Control using Explicit Model Predictive Control. *Automatica*, 41(12):2107–2114, 2005. doi:10.1016/j.automatica.2005.06.015.

[Hein20] A. M. Hein, R. Matheson, and D. Fries. A techno-economic analysis of asteroid mining. *Acta Astronautica*, 168:104–115, 2020. doi:10.1016/j.actaastro.2019.05.009.

[Herzog07] F. Herzog, G. Dondi, and H. P. Geering. Stochastic Model Predictive Control and Portfolio Optimization. *International Journal of Theoretical and Applied Finance*, 10(02):203–233, 2007. doi:10.1142/S0219024907004196.

[Hesar15] S. Hesar, J. Parker, J. Mcmahon, and G. Born. Small Body Gravity Field Estimation Using LiAISON Supplemented Optical Navigation. In *36th AAS Guidance and Control conference*. Breckenridge, United States of America, 2015.

[Hewing20] L. Hewing, K. P. Wabersich, M. Menner, and M. N. Zeilinger. Learning-Based Model Predictive Control: Toward Safe Learning in Control. *Annual Review of Control,* *Robotics, and Autonomous Systems*, 3(1):269–296, 2020. doi:10.1146/annurev-control-090419-075625.

[Holdridge02] M. Holdridge. NEAR Shoemaker Spacecraft Mission Operations. *Johns Hopkins Apl Technical Digest*, 23:58–70, 2002.

[Hong95] H. Hong. Implicitization of curves parameterized by generalized trigonometric polynomials. In *Applied Algebra, Algebraic Algorithms and Error-Correcting Codes*, volume 948, pages 285–296. Springer Berlin Heidelberg, 1995. ISBN 978-3-540-60114-2. doi:10.1007/3-540-60114-7_21.

[Hope03] A. Hope and A. Trask. Field programmable gate array based predictive control systen for spacecraft rendezvous in elliptical orbits. In *AAS/AIAA Astrodynamics Specialist Conference Meeting*. Big Sky, United States of America, 2003.

[Hrovat12] D. Hrovat, S. D. Cairano, H. Tseng, and I. Kolmanovsky. The development of Model Predictive Control in automotive industry: A survey. In *2012 IEEE International Conference on Control Applications*, pages 295–302. Dubrovnik, Croatia, October 2012. doi:10.1109/CCA.2012.6402735.

[Hull97] D. G. Hull. Conversion of Optimal Control Problems into Parameter Optimization Problems. *Journal of Guidance, Control, and Dynamics*, 20(1):57–60, 1997. doi:10.2514/2.4033.

[Inhalan02] G. Inhalan, M. Tillerson, and J. P. How. Relative Dynamics and Control of Spacecraft Formations in Eccentric Orbits. *Journal of Guidance, Control, and Dynamics*, 25(1):48–59, 2002. doi:10.2514/2.4874.

[IPOPT16] IPOPT. *Introduction to IPOPT: A tutorial for downloading, installing and using IPOPT*. COIN-OR, 2016. URL **https://projects.coin-or.org/Ipopt**.

[Irvin07] D. J. Irvin. *Optimal Control Strategies for Constrained Relative Orbits*. Ph.D. thesis, Air Force Institute of Technology, 2007.

[Irvin09] D. J. Irvin, R. G. Cobb, and T. A. Lovell. Fuel-optimal maneuvers for constrained relative satellite orbits. *Journal of guidance, control, and dynamics*, 32(3):960–973, 2009. doi:10.2514/1.36618.

[Jewison15] C. Jewison, R. S. Erwin, and A. Saenz-Otero. Model Predictive Control with Ellipsoid Obstacle Constraints for Spacecraft Rendezvous. volume 48, pages 257–262. 2015. doi:10.1016/j.ifacol.2015.08.093. 1st IFAC Workshop on Advanced Control and Navigation for Autonomous Aerospace Vehicles ACNAAV'15.

[Jorda16] L. Jorda, R. Gaskell, C. Capanna, S. Hviid, P. Lamy, J. Ďurech, G. Faury, O. Groussin, P. Gutiérrez, C. Jackman, S. Keihm, H. Keller, J. Knollenberg, E. Kührt, S. Marchi, S. Mottola, E. Palmer, F. Schloerb, H. Sierks, J.-B. Vincent, M. A'Hearn, C. Barbieri, R. Rodrigo, D. Koschny, H. Rickman, M. Barucci, J. Bertaux, I. Bertini, G. Cremonese, V. Da Deppo, B. Davidsson, S. Debei, M. De Cecco, S. Fornasier, M. Fulle, C. Güttler, W.-H. Ip, J. Kramm, M. Küppers, L. Lara, M. Lazzarin, J. Lopez Moreno, F. Marzari, G. Naletto, N. Oklay, N. Thomas, C. Tubiana, and K.-P. Wenzel. The global shape, density and rotation of Comet 67P/Churyumov-Gerasimenko from preperihelion Rosetta/OSIRIS observations. *Icarus*, 277:257–278, 2016. doi:10.1016/j.icarus.2016.05.002.

[Kalabic15] U. Kalabic, A. Weiss, S. D. Cairano, and I. Kolmanovsky. Station-keeping and momentum-management on halo orbits around L2: Linear-quadratic feedback and model predictive control approaches. In *AAS Spaceflight Mechanics Meeting*. Williamsburg, United States of America, 2015.

[Kamen10] E. W. Kamen. *The Control Systems Handbook*, chapter 3, pages 1–33. CRC Press, Boca Raton, 2 edition, 2010. doi:10.1201/b10384.

[Kelso09] T. Kelso. Analysis of the Iridium 33-Cosmos 2251 Collision. In *Proceedings of the 19th AIAA/AAS Astrodynamics Specialist Conference*, volume 135. Pittsburgh, United States of America, September 2009.

[Konopliv02] A. Konopliv, J. Miller, W. Owen, D. Yeomans, J. Giorgini, R. Garmier, and J.-P. Barriot. A Global Solution for the Gravity Field, Rotation, Landmarks, and Ephemeris of Eros. *Icarus*, 160(2):289–299, 2002. doi:10.1006/icar.2002.6975.

[Konopliv18] A. Konopliv, R. Park, A. Vaughan, B. Bills, S. Asmar, A. Ermakov, N. Rambaux, C. Raymond, J. Castillo-Rogez, C. Russell, D. Smith, and M. Zuber. The Ceres gravity field, spin pole, rotation period and orbit from the Dawn radiometric tracking and optical data. *Icarus*, 299:411–429, 2018. doi:10.1016/j.icarus.2017.08.005.

[Koon06] W. S. Koon, M. W. Lo, J. E. Marsden, and S. D. Ross. *Dynamical Systems, the Three-Body Problem and Space Mission Design*, chapter 4, pages 100–107. Springer, 2006. ISBN 978-0-615-24095-4.

[Kress98] R. Kress. *Numerical Analysis*, chapter 8, pages 169–179. Graduate Texts in Mathematics. Springer, 1998. doi:10.1007/978-1-4612-0599-9.

[Kristiansen08] R. Kristiansen, P. J. Nicklasson, and J. T. Gravdahl. Spacecraft coordination control in 6DOF: Integrator backstepping vs passivity-based control. *Automatica*, 44(11):2896–2901, 2008. doi:10.1016/j.automatica.2008.04.019.

[Lee18] K. Lee, C. Park, and Y. Eun. Real-time collision avoidance maneuvers for spacecraft proximity operations via discrete-time Hamilton–Jacobi theory. *Aerospace Science and Technology*, 77:688–695, 2018. doi:10.1016/j.ast.2018.04.010.

[Lei19] H. Lei, C. Circi, E. Ortore, E. Condoleo, and B. Xu. Quasi-Frozen Orbits Around a Slowly Rotating Asteroid. *Journal of Guidance, Control, and Dynamics*, 42(4):794–809, 2019. doi:10.2514/1.G003837.

[Leomanni13] M. Leomanni, A. Garulli, A. Giannitrapani, and F. Scortecci. An MPC-based attitude control system for all-electric spacecraft with on/off actuators. In *52nd IEEE Conference on Decision and Control*, pages 4853–4858. Florence, Italy, December 2013. doi:10.1109/CDC.2013.6760650.

[Leve15] F. A. Leve, B. J. Hamilton, and M. A. Peck. *Spacecraft Momentum Control Systems.* Space Technology Library. Springer, 2015. doi:10.1007/978-3-319-22563-0.

[Li05] S. Li, C. Hutao, and C. Pingyuan. Autonomous optical navigation for landing on asteroids. *Aircraft Engineering and Aerospace Technology*, 77(4):317–323, August 2005. doi:10.1108/00022660510606402.

[Lim18] Y. Lim, Y. Jung, and H. Bang. Robust model predictive control for satellite formation keeping with eccentricity/inclination vector separation. *Advances in Space Research*, 61(10):2661–2672, 2018. doi:10.1016/j.asr.2018.02.036.

[Limon06] D. Limon, T. Alamo, F. Salas, and E. F. Camacho. On the Stability of Constrained MPC Without Terminal Constraint. *IEEE Transactions on Automatic Control*, 51(5):832–836, 2006. doi:10.1109/TAC.2006.875014.

[Lizy-Destrez19] S. Lizy-Destrez, L. Beauregard, E. Blazquez, A. Campolo, S. Manglativi, and V. Quet. Rendezvous Strategies in the Vicinity of Earth-Moon Lagrangian Points. *Frontiers in Astronomy and Space Sciences*, 5(45):1–19, 2019. doi:10.3389/fspas.2018.00045.

[Lorenz18] R. D. Lorenz, E. P. Turtle, J. W. Barnes, M. G. Trainer, D. S. Adams, K. E. Hibbard, C. Z. Sheldon, K. Zacny, P. N. Peplowski, D. J. Lawrence, M. A. Ravine, T. G. McGee, K. S. Sotzen, S. M. MacKenzie, J. W. Langelaan, S. Schmitz, L. S. Wolfarth, and P. D. Bedini. Dragonfly: A rotorcraft lander concept for scientific exploration at titan. *Johns Hopkins APL Technical Digest (Applied Physics Laboratory)*, 34:374–387, October 2018.

[Louembet09] C. Louembet, F. Cazaurang, A. Zolghadri, C. Charbonnel, and C. Pittet. Path planning for satellite slew manoeuvres: a combined flatness and collocation-based approach. *IET Control Theory and Applications*, 3(4):481–491, 2009. doi:10.1049/iet-cta.2008.0054.

[Louembet15] C. Louembet, D. Arzelier, and G. Deaconu. Robust Rendezvous Planning Under Maneuver Execution Errors. *Journal of Guidance, Control and Dynamics*, 38(1):76–93, 2015. doi:10.2514/1.G000391.

[Lu13] P. Lu and X. Liu. Autonomous Trajectory Planning for Rendezvous Proximity Operations by Conic Optimization. *Journal of Guidance, Control and Dynamics*, 36(2):375–389, 2013. doi:10.2514/1.58436.

[Lu21] L. Lu, H. Li, W. Zhou, and J. Liu. Design and analysis of a direct transfer trajectory from a near rectilinear halo orbit to a low lunar orbit. *Advances in Space Research*, 67(3):1143–1154, 2021. doi:10.1016/j.asr.2020.11.003.

[Madison00] R. W. Madison. Micro-satellite based, on-orbit servicing work at the Air Force Research Laboratory. In *2000*

IEEE Aerospace Conference, volume 4, pages 215–226. 2000. doi:10.1109/AERO.2000.878421.

[Mammarella18] M. Mammarella, E. Capello, H. Park, G. Guglieri, and M. Romano. Tube-based robust model predictive control for spacecraft proximity operations in the presence of persistent disturbance. *Aerospace Science and Technology*, 77:585–594, 2018. doi:10.1016/j.ast.2018.04.009.

[Manikonda99] V. Manikonda, P. O. Arambel, M. Gopinathan, R. K. Mehra, and F. Y. Hadaegh. A model predictive control-based approach for spacecraft formation keeping and attitude control. In *Proceedings of the 1999 American Control Conference*, volume 6, pages 4258–4262. 1999. doi:10.1109/ACC.1999.786367.

[Marandi87] S. Marandi and V. Modi. A preferred coordinate system and the associated orientation representation in attitude dynamics. *Acta Astronautica*, 15(11):833–843, 1987. doi:10.1016/0094-5765(87)90038-5.

[Mattingley10] J. Mattingley, Y. Wang, and S. Boyd. Code generation for receding horizon control. In *Proceedings of the IEEE International Symposium on Computer-Aided Control System Design*, pages 985–992. October 2010. doi:10.1109/CACSD.2010.5612665.

[Mayne00] D. Mayne, J. B. Rawlings, C. V. Rao, and P. Scokaert. Constrained model predictive control: Stability and optimality. *Automatica*, 36(6):789 – 814, 2000. doi:10.1016/S0005-1098(99)00214-9.

[Mayne05] D. Q. Mayne, M. M. Seron, and S. V. Raković. Robust model predictive control of constrained linear systems with bounded disturbances. *Automatica*, 41(2):219–224, 2005. doi:10.1016/j.automatica.2004.08.019.

[Merri18] M. Merri and M. Sarkarati. Lunar Orbiter Platform - Gateway: a clear use case for CCSDS MO services. In *2018 AIAA Space and Astronautics Forum and Exposition*. Orlando, Florida, United States of America, June 2018. doi:10.2514/6.2018-5337.

[Miller90] J. K. Miller, C. J. Weeks, and L. J. Wood. Orbit determination strategy and accuracy for a Comet Rendezvous mission. *Journal of Guidance, Control, and Dynamics*, 13(5):775–784, 1990. doi:10.2514/3.25402.

[Miller02] J. K. Miller, A. S. Konopliv, P. Antreasian, J. J. Bordi, S. Chesley, C. E. Helfrich, W. M. Owen, T. C. Wang, B. G. Williams, D. K. Yeomans, and D. J. Scheeres. Determination of Shape, Gravity, and Rotational State of Asteroid 433 Eros. *Icarus*, 155:3–17, 2002. doi:10.1006/icar.2001.6753.

[Misra18] G. Misra, H. Peng, and X. Bai. *Halo Orbit Stationkeeping using Nonlinear MPC and Polynomial Optimization*. Kissimmee, United States of America, January 2018. doi:10.2514/6.2018-1454.

[Moon16] G. Moon, B. Lee, M. Tahk, and D. H. Shim. Quaternion Based Attitude Control and Suboptimal Rendezvous Guidance on Satellite Proximity Operation. In *European Control Conference (ECC)*. Aalborg, Denmark, June 2016. doi:10.1109/ECC.2016.7810620.

[Murakami15] N. Murakami, S. Ueda, T. Ikenaga, M. Maeda, T. Yamamoto, and H. Ikeda. Practical rendezvous scenario for transportation missions to cis-lunar station in Earth-Moon L2 Halo orbit. In *25th International Symposium on Space Flight Dynamics (ISSFD)*. Munich, Germany, 2015.

[Muralidharan20] V. Muralidharan, A. Weiss, and U. V. Kalabic. *Control Strategy for Long-Term Station-Keeping on Near-Rectilinear Halo Orbits*. Orlando, United States of America, January 2020. doi:10.2514/6.2020-1459.

[Musk17] E. Musk. Making Humans a Multi-Planetary Species. *New Space*, 5:46–61, June 2017. doi:10.1089/space.2017.29009.emu.

[Naasz03] B. J. Naasz, M. M. Berry, H. Kim, and C. D. Hall. Integrated Orbit and Attitude Control for a Nanosatellite with Power Constraints. In *Proceedings AAS/AIAA Space Flight Mechanics Conference*. Ponce, Puerto Rico, February 2003.

[NASA07] NASA. Overview of the DART Mishap Investigation Results. Technical report, National Aeronautics and Space Administration, 2007.

[Neufeld08] M. J. Neufeld. von Braun and the lunar-orbit rendezvous decision: finding a way to go to the moon. *Acta Astronautica*, 63:540–550, July 2008. doi:10.1016/j.actaastro.2007.12.011.

[Newman18] C. P. Newman, D. C. Davis, R. J. Whitley, J. R. Guinn, and M. S. Ryne. Stationkeeping, Orbit Determination, and

Attitude Control for Spacecraft in Near Rectilinear Halo Orbits. In *AAS/AIAA Astrodynamics Specialists Conference*. Snowbird, United States of America, 2018.

[NRC11] NRC. *Vision and Voyages for Planetary Science in the Decade 2013–2022.* The National Academies Press, Washington DC, United States of America, 2011. doi:10.17226/13117.

[NRC12] NRC. *Continuing Kepler's Quest: Assessing Air Force Space Command's Astrodynamics Standards.* The National Academies Press, Washington DC, United States of America, 2012. ISBN 978-0-309-26142-5. doi:10.17226/13456.

[Pellacani18] A. Pellacani, F. Cabral, A. Alcalde, P. Kicman, J. Lisowski, I. Gerth, and B. Burmann. Semi-autonomous attitude guidance using relative navigation based on line of sight measurements – Aim scenario. *Acta Astronautica*, 152:496–508, 2018. doi:10.1016/j.actaastro.2018.08.051.

[Prince18] E. R. Prince and R. G. Cobb. Optimal inspector satellite guidance to quasi-hover via relative teardrop trajectories. *Acta Astronautica*, 153:201–212, 2018. doi:10.1016/j.actaastro.2018.02.017.

[Qin03] S. Qin and T. A. Badgwell. A survey of industrial model predictive control technology. *Control Engineering Practice*, 11(7):733 – 764, 2003. doi:10.1016/S0967-0661(02)00186-7.

[Reddy18] V. S. Reddy. The SpaceX Effect. *New Space*, 6(2):125–134, 2018. doi:10.1089/space.2017.0032.

[Rencher98] A. C. Rencher. *Multivariate Statistical Inference and Applications*, pages 40–42. Wiley, New York, 1 edition, 1998. ISBN: 978-0-471-57151-3.

[Richards02] A. Richards, T. Schouwenaars, J. P. How, and E. Feron. Spacecraft Trajectory Planning with Avoidance Constraints Using Mixed-Integer Linear Programming. *Journal of Guidance, Control and Dynamics*, 25(4):755–764, 2002. doi:10.2514/2.4943.

[Richards03] A. Richards and J. How. Performance evaluation of rendezvous using model predictive control. In *Proceedings of AIAA Guidance, Navigation and Control Conference*. Austin, Texas, United States of America, August 2003. doi:10.2514/6.2003-5507.

[Russell11] C. Russell and C. Raymond. The Dawn Mission to Vesta and Ceres. *Space Science Reviews*, 163:3–23, December 2011. doi:10.1007/s11214-011-9836-2.

[Sabelhaus07] P. Sabelhaus and J. Decker. James Webb Space Telescope: Project Overview. *Aerospace and Electronic Systems Magazine, IEEE*, 22:3–13, August 2007. doi:10.1109/MAES.2007.4285974.

[Sanchez18] J. C. Sanchez, F. Gavilan, R. Vazquez, and C. Louembet. A Flatness-Based Trajectory Planning Algorithm for Rendezvous of Single-Thruster Spacecraft. In *Networked and Autonomous Air and Space Systems*. Santa Fe, United States of America, June 2018. doi:10.1016/j.ifacol.2018.07.098.

[Sanchez19] J. C. Sanchez, C. Louembet, F. Gavilan, and R. Vazquez. An Event-Triggered Predictive Controller for Spacecraft Rendezvous Hovering Phases. In *21st IFAC Symposium on Automatic Control in Aerospace*. Cranfield, United Kingdom, August 2019. doi:10.1016/j.ifacol.2019.11.076.

[Sanchez20a] J. C. Sanchez, F. Gavilan, and R. Vazquez. Chance-constrained Model Predictive Control for Near Rectilinear Halo Orbit spacecraft rendezvous. *Aerospace Science and Technology*, 100:105827, May 2020. doi:10.1016/j.ast.2020.105827.

[Sanchez20b] J. C. Sanchez, F. Gavilan, R. Vazquez, and C. Louembet. A flatness-based predictive controller for six-degrees of freedom spacecraft rendezvous. *Acta Astronautica*, 167:391–403, 2020. doi:10.1016/j.actaastro.2019.11.026.

[Sanchez20c] J. C. Sanchez, R. Vazquez, J. D. Biggs, and F. Bernelli-Zazzera. Orbit-attitude predictive control in the vicinity of asteroids with in-situ gravity estimation. *submitted to Journal of Guidance, Control and Dynamics*, 2020.

[Sanchez21a] J. C. Sanchez, C. Louembet, F. Gavilan, and R. Vazquez. Event-based Impulsive Control for Spacecraft Rendezvous Hovering Phases. *Journal of Guidance, Control and Dynamics*, 44(10):1794–1810, 2021. doi:10.2514/1.G005507.

[Sanchez21b] J. C. Sanchez, R. Vazquez, J. D. Biggs, and F. Bernelli-Zazzera. Guidance, navigation and control for asteroid orbit station-keeping with in-situ gravity estimation. In *11th International ESA Conference on Guidance, Navigation and Control Systems*. Virtual, June 2021.

[Sasaki19] T. Sasaki, Y. Nakajima, and T. Yamamoto. Proximity Approaches for Active Debris Removal Satellites Considering Trajectory Safety. In *32nd International Symposium on Space Technology and Science*. Fukui, Japan, June 2019.

[Sato15] Y. Sato, K. Kitamura, and T. Shima. Spacecraft Rendezvous Utilizing Invariant Manifolds for a Halo Orbit. *Transactions of the Japan Society for Aeronautical and Space Sciences*, 58(5):261–269, 2015. doi:10.2322/tjsass.58.261.

[Sawai02] S. Sawai, D. J. Scheeres, and S. B. Broschart. Control of Hovering Spacecraft Using Altimetry. *Journal of Guidance, Control, and Dynamics*, 25(4):786–795, 2002. doi:10.2514/2.4947.

[Schaub96] H. Schaub and J. L. Junkins. Stereographic Orientation Parameters for Attitude Dynamics: A Generalization of the Rodrigues Parameters. *Journal of the Astronautical Sciences*, 44(1):1–19, 1996.

[Schaub02] H. Schaub. Spacecraft Relative Orbit Geometry Description through Orbit Elements Differences. In *14th U.S. National Congress of Theoretical and Applied Mechanics*. June 2002.

[Scheeres12] D. J. Scheeres. Orbit Mechanics About Asteroids and Comets. *Journal of Guidance, Control, and Dynamics*, 35(3):987–997, 2012. doi:10.2514/1.57247.

[Scheeres19] D. Scheeres, J. Mcmahon, A. French, D. Brack, S. Chesley, D. Farnocchia, Y. Takahashi, J. Leonard, J. Geeraert, B. Page, P. Antreasian, K. Getzandanner, D. Rowlands, E. Mazarico, J. Small, D. Highsmith, M. Moreau, J. Emery, B. Rozitis, and M. Bernacki. The dynamic geophysical environment of (101955) Bennu based on OSIRIS-REx measurements. *Nature Astronomy*, 3:352–361, 2019. doi:10.1038/s41550-019-0721-3.

[Shkolnik18] E. L. Shkolnik. On the verge of an astronomy Cubesat revolution. *Nature Astronomy*, 2:374–378, 2018. doi:10.1038/s41550-018-0438-8.

[Siguerdidjane17] H. Siguerdidjane, S. Nakasuka, and R. Vazquez. Recent and future trends in space and aeronautics – Special section on selected advanced control systems. *Control Engineering Practice*, 60:196–198, 2017. doi:10.1016/j.conengprac.2017.01.015.

[Siva13] M. S. Siva, R. Padiyan, D. Ghose, M. S. Bhat, and M. P. Ramachandran. Coordinated 6-dof control of dual spacecraft formation. In *5th International Conference on Spacecraft Formation Flying Missions and Technologies*. Munich, Germany, May 2013.

[Souza07] C. D. Souza, C. Hannak, P. Spehar, F. Clark, and M. Jackson. *Orion Rendezvous, Proximity Operations and Docking Design and Analysis*. Hilton Head, United States of America, August 2007. doi:10.2514/6.2007-6683.

[Speretta18] S. Speretta, F. Topputo, J. Biggs, P. D. Lizia, M. Massari, K. Mani, D. D. Tos, S. Ceccherini, V. Franzese, A. Cervone, P. Sundaramoorthy, R. Noomen, S. Mestry, A. Cipriano, A. Ivanov, D. Labate, L. Tommasi, A. Jochemsen, J. Gailis, R. Furfaro, V. Reddy, J. Vennekens, and R. Walker. LUMIO: achieving autonomous operations for Lunar exploration with a CubeSat. In *2018 SpaceOps Conference*. Marseille, France, May 2018. doi:10.2514/6.2018-2599.

[Stacey18] N. Stacey and S. D'Amico. Autonomous Swarming for Simultaneous Navigation and Asteroid Characterization. In *AAS/AIAA Astrodynamics Specialist Conference*. Snowbird, United States of America, 2018.

[Starek16] J. A. Starek, B. Acikmese, I. A. Nesnas, and M. Pavone. *Spacecraft Autonomy Challenges for Next-Generation Space Missions*, pages 1–48. Springer, Berlin, Heidelberg, 2016. doi:10.1007/978-3-662-47694-9_1.

[Subudhi20] C. S. Subudhi, S. Vutukuri, and R. Padhi. A Near Fuel-optimal Station-keeping Strategy for Halo Orbits. In *2020 59th IEEE Conference on Decision and Control (CDC)*, pages 1478–1483. 2020. doi:10.1109/CDC42340.2020.9304327.

[Takahashi13] Y. Takahashi, D. J. Scheeres, and R. A. Werner. Surface Gravity Fields for Asteroids and Comets. *Journal of Guidance, Control, and Dynamics*, 36(2):362–374, 2013. doi:10.2514/1.59144.

[Tapley08] B. D. Tapley. Gravity model determination from the GRACE mission. *The Journal of the Astronautical Sciences*, 56(27):273–285, 2008. doi:10.1007/BF03256553.

[Tavakoli14] M. Tavakoli and N. Assadian. Model predictive orbit control of a Low Earth Orbit satellite using Gauss variational equations. *Proceedings of the Institution of Mechanical Engineers, Part G: Journal of Aerospace Engineering*, 228(13):2385–2398, 2014. doi:10.1177/0954410013516252.

[TayyebTaher17] M. TayyebTaher and S. M. Esmaeilzadeh. Model predictive control of attitude maneuver of a geostationary flexible satellite based on genetic algorithm. *Advances in Space Research*, 60(1):57–64, 2017. doi:10.1016/j.asr.2017.03.013.

[Terui98] F. Terui. Position and Attitude Control of a Spacecraft by Sliding Mode Control. In *Proceedings of the American Control Conference*. Philadelphia, Pennsylvnia, United States of America, June 1998. doi:10.1109/ACC.1998.694662.

[Tolker-Nielsen17] T. Tolker-Nielsen. EXOMARS 2016-Schiaparelli Anomaly Inquiry. Technical Report DG-I/2017/546/TTN, European Space Agency, 2017.

[Topputo05] F. Topputo, M. Vasile, and F. Bernelli-Zazzera. Low Energy Interplanetary Transfers Exploiting Invariant Manifolds of the Restricted Three-Body Problem. *Journal of the Astronautical Sciences*, 53:353–372, 2005. doi:10.1007/BF03546358.

[Tos20] D. A. D. Tos and N. Baresi. Genetic optimization for the orbit maintenance of libration point orbits with applications to equuleus and lumio. In *AIAA Scitech 2020 Forum*. Orlando, United States of America, August 2020. doi:10.2514/6.2020-0466.

[Trofimov20] S. Trofimov, M. Shirobokov, A. Tselousova, and M. Ovchinnikov. Transfers from near-rectilinear halo orbits to low-perilune orbits and the Moon's surface. *Acta Astronautica*, 167:260 – 271, 2020. doi:10.1016/j.actaastro.2019.10.049.

[Tschauner65] J. Tschauner and P. Hempel. Rendezvous zu einem in Elliptischer Bahn Umlaufenden Ziel. *Acta Astronautica*, 11(2):104–109, 1965.

[Tselousova19] A. Tselousova, M. Shirobokov, and S. Trofimov. Direct two-impulse transfers from a low-earth orbit to high circular polar orbits around the moon. In *AIP Conference Proceedings*, volume 2171. November 2019. doi:10.1063/1.5133289.

[Underwood15] C. Underwood, S. Pellegrino, V. Lappas, C. Bridges, and J. Baker. Using CubeSat/micro-satellite technology to demonstrate the Autonomous Assembly of a Reconfigurable

Space Telescope (AAReST). *Acta Astronautica*, 114:112–122, April 2015. doi:10.1016/j.actaastro.2015.04.008.

[Vazquez17] R. Vazquez, F. Gavilan, and E. F. Camacho. Pulse-width predictive control for LTV systems with application to spacecraft rendezvous. *Control Engineering Practice*, 20:199–210, 2017. doi:10.1016/j.conengprac.2016.06.017.

[v.Ehrenfried20] M. v. Ehrenfried. *The Artemis Lunar Program*, pages 7–47. Space Exploration. Springer, 1 edition, 05 2020. doi:10.1007/978-3-030-38513-2.

[Vetrisano16] M. Vetrisano and M. Vasile. Autonomous navigation of a spacecraft formation in the proximity of an asteroid. *Advances in Space Research*, 57(8):1783–1804, 2016. doi:10.1016/j.asr.2015.07.024.

[Vieira11] M. S. Vieira, R. K. Galvão, and K. H. Kienitz. Attitude stabilization with actuators subject to switching-time constraints using explicit MPC. In *2011 Aerospace Conference*, pages 1–8. Big Sky, United States of America, March 2011. doi:10.1109/AERO.2011.5747482.

[Walker85] M. Walker, B. Ireland, and J. Owens. A set of modified equinoctial orbit elements. *Celestial Mechanics*, 36:409–419, 1985. doi:10.1007/BF01227493.

[Wan00] E. Wan and R. Merwe. The Unscented Kalman Filter for Nonlinear Estimation. In *Adaptive Systems for Signal Processing, Communications, and Control Symposium*. Alberta, Canada, 2000. doi:10.1109/ASSPCC.2000.882463.

[Wang12] J. Wang and Z. Sun. 6-DOF robust adaptive terminal sliding mode control for spacecraft formation flying. *Acta Astronautica*, 73:76–87, 2012. doi:10.1016/j.actaastro.2011.12.005.

[Wang13] Y. Wang and S. Xu. Attitude stability of a spacecraft on a stationary orbit around an asteroid subjected to gravity gradient torque. *Celestial Mechanics and Dynamical Astronomy*, 115:333–352, 04 2013. doi:10.1007/s10569-012-9463-6.

[Weiss15a] A. Weiss, M. Baldwin, R. S. Erwin, and I. Kolmanovsky. Model Predictive Control for Spacecraft Rendezvous and Docking Strategies for Handling Constraints and Case Studies. *IEEE Transactions on Control Systems Technology*, 23(4):1638–1647, 2015. doi:10.1109/TCST.2014.2379639.

[Weiss15b] A. Weiss, U. Kalabic, and S. D. Cairano. Model Predictive Control for Simultaneous Station Keeping and Momentum Management of Low-Thrust Satellites. In *American Control Conference*. Chicago, Illinois, United States of America, July 2015. doi:10.1109/ACC.2015.7171076.

[Werner96] R. A. Werner and D. J. Scheeres. Exterior gravitation of a polyhedron derived and compared with harmonic and mascon gravitation representations of asteroid 4769 Castalia. *Celestial Mechanics and Dynamical Astronomy*, 65:313–344, 1996. doi:10.1007/BF00053511.

[Whitley16] R. Whitley and R. Martinez. Options for staging orbits in cislunar Space. In *2016 IEEE Aerospace Conference*. Big Sky, Montana, United States of America, March 2016. doi:10.1109/AERO.2016.7500635.

[Wibben12] D. Wibben and R. Furfaro. Integrated Guidance and Attitude Control for Asteroid Proximity Operations using Higher Order Sliding Modes. In *AIAA/AAS Astrodynamics Specialist Conference*. Minneapolis, United States of America, 2012. doi:10.2514/6.2012-5071.

[Wilson16] J. Wilson, M. Charest, and R. Dubay. Non-linear model predictive control schemes with application on a 2 link vertical robot manipulator. *Robotics and Computer-Integrated Manufacturing*, 41:23–30, 2016. doi:10.1016/j.rcim.2016.02.003.

[Wu09] Y. Wu, X. Cao, Y. Xing, P. Zheng, and S. Zhang. Relative Motion Decoupled Control for Spacecraft Formation Translational and Rotational Dynamics. In *Proceedings of the International Conference on Computer Modeling and Simulation*, pages 63–68. Macau, China, 2009. doi:10.1109/ICCMS.2009.12.

[Xu19] N. Xu, J. Lin, Y. Miao, and Z. Gao. Model Predictive Control for Satellite Formation Keeping Based on Genetic Algorithm. In *2019 Chinese Control And Decision Conference (CCDC)*, pages 1918–1923. 2019. doi:10.1109/CCDC.2019.8832671.

[Yamanaka02] K. Yamanaka and F. Ankersen. New State Transition Matrix for Relative Motion on an Arbitrary Elliptical Orbit. *Journal of Guidance, Control and Dynamics*, 25(1):60–66, 2002. doi:10.2514/2.4875.

[Yan16] H. Yan, S. Yan, and Y. Xie. Integrated Translational and Rotational Control for Rendezvous and Docking on Ellipse Orbits. In *Intelligent Control and Automation (WCICA), 12th World Congress*. Guilin, China, June 2016. doi:10.1109/WCICA.2016.7578283.

[Yoshikawa06] M. Yoshikawa, H. Ikeda, H. Yano, J. Saito, T. Kubota, T. Hashimoto, A. Fujiwara, J. Kawaguchi, T. Kominato, M. Matsuoka, K. Shirakawa, T. Ohnishi, S. Abe, T. Mukai, R. Gaskell, and D. J. Scheeres. *Astrodynamics Science About Itokawa, Gravity and Ephemeris*. Keystone, United States of America, August 2006. doi:10.2514/6.2006-6658.

[Yoshikawa15] M. Yoshikawa, J. Kawaguchi, A. Fujiwara, and A. Tsuchiyama. *Hayabusa Sample Return Mission*. January 2015. ISBN 9780816532131.

[Yu12] Y. Yu and H. Baoyin. Generating families of 3d periodic orbits about asteroids. *Monthly Notices of the Royal Astronomical Society*, 427(1):872–881, 2012. doi:10.1111/j.1365-2966.2012.21963.x.

[Zacny13] K. Zacny, P. Chu, J. Craft, M. Cohen, W. James, and B. Hilscher. Asteroid Mining. In *AIAA SPACE 2013 Conference and Exposition*. September 2013. doi:10.2514/6.2013-5304.

[Zhang12] F. Zhang and G. Duan. Integrated Relative Position and Attitude Control of Spacecraft in Proximity Operation Missions. *International Journal of Automation and Computing*, 9(4):342–351, 2012.

[Zhang20] J. Zhang, J. D. Biggs, D. Ye, and Z. Sun. Finite-time attitude set-point tracking for thrust-vectoring spacecraft rendezvous. *Aerospace Science and Technology*, 96, 2020. doi:10.1016/j.ast.2019.105588.

[Zimovan17] E. M. Zimovan, K. C. Howell, and D. C. Davis. Near Rectilinear Halo Orbits and their Application in Cis-Lunar Space. In *3rd IAA Conference on Dynamics and Control of Space Systems*. Moscow, Russia, May 2017.

This page is intentionally left blank.

Appendix A

B-splines

A B-spline function is a combination of basis functions passing through a number of points, named control points, and creates smooth curves. B-splines functions are able to define flexible trajectories with a high continuity degree and a low number of parameters (see [Kress98] for more details about them). The B-splines domain is subdivided by knots and its basis functions are nonzero on a few adjacent intervals. As a result basis functions are quite "local".

Define $\mathbf{t}_{\text{knots}} : \{t_0 \leq t_1 \ldots \leq t_m\}$ as a set of non-decreasing numbers. The components t_i of the previous set are called knots, the set $\mathbf{t}_{\text{knots}}$ is the knots sequence and the half-open interval $[t_i, t_{i+1})$ is the ith knot span. Note that a knot t_i can be repeated k times (multiple knot of multiplicity k). The B-spline basis function are defined by its degree q through the following recursion

$$\begin{aligned} B_{i,0}(t) &= \begin{cases} 1, & t \in [t_i, t_{i+1}), \\ 0, & t \notin [t_i, t_{i+1}), \end{cases} \\ B_{i,q}(t) &= \frac{t - t_i}{t_{i+q} - t_i} B_{i,q-1}(t) + \frac{t_{i+q+1} - t}{t_{i+q+1} - t_{i+1}} B_{i+1,q-1}(t). \end{aligned} \tag{A.1}$$

Remark A1: a basis function $B_{i,p}$ is non-zero on $q+1$ knots spans that are adjacent as $[t_i, t_{i+1}) \ldots [t_{i+q}, t_{i+q+1})$. Equivalently, at most $q+1$ basis functions (of degree q) are non-zero on any ith knots span.

Given n control points $\{\mathbf{c}_1, \mathbf{c}_2 \ldots \mathbf{c}_n\}$ and a knots sequence $\mathbf{t}_{\text{knots}}$, the B-spline curve of degree q defined by these control points and knots is

$$\mathbf{f}(t) = \sum_{i=1}^{n_c} B_{i,q}(t)\mathbf{c}_i. \tag{A.2}$$

Remark A2: B-splines intrinsically assure continuity up to C^q. The knots, control points and degree must satisfy $m = n_c + q + 1$.

An usual interpolation requirement is that the B-spline curve, $\mathbf{f}(t)$, value and derivatives at the beginning, t_0, and end domain, t_f, are prescribed (in terms of $\mathbf{c}_i$). This can be accomplished by repeating $q+p+1$ times the initial, t_0, and final, t_m, knots being p the desired order of the prescribed derivative.

Let show an example for a scalar B-spline function f. Let define the following knots sequence:

$$t_{\text{knots}} = [0, 0, 0, 0, 0.25, 0.5, 0.75, 1, 1, 1, 1]^T. \tag{A.3}$$

c_1	c_2	c_3	c_4	c_5	c_6	c_7
0.6294	0.8116	-0.7460	0.8268	0.2647	-0.8049	-0.4430

Table A.1: Control points for cubic B-spline.

If a cubic continuity is desired, that is $q = 3$, the number of control points should be $n_c = 7$ according to Remark A2. For this situation, the B-splines basis functions are shown in Fig. A.1.

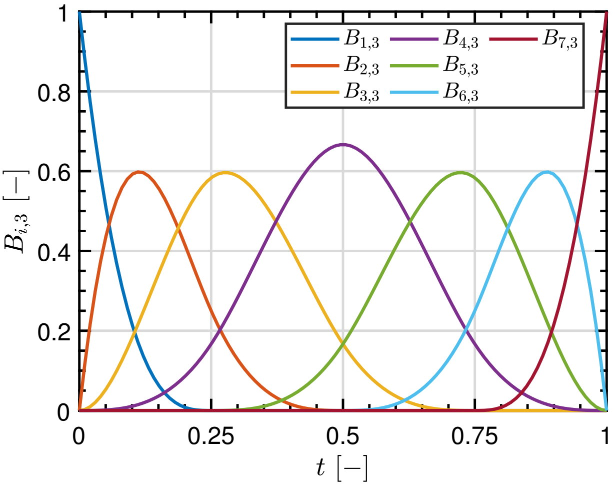

Figure A.1: B-splines cubic basis functions.

Let now assess the continuity property by inserting the randomly chosen control points of Table A.1. The result is the B-spline function f of Fig. A.2. The derivatives of this function, up to the third, have been also plotted. It is confirmed that the function maintains its continuity up to its second derivative being its third derivative formed by step functions as expected for a cubic B-spline.

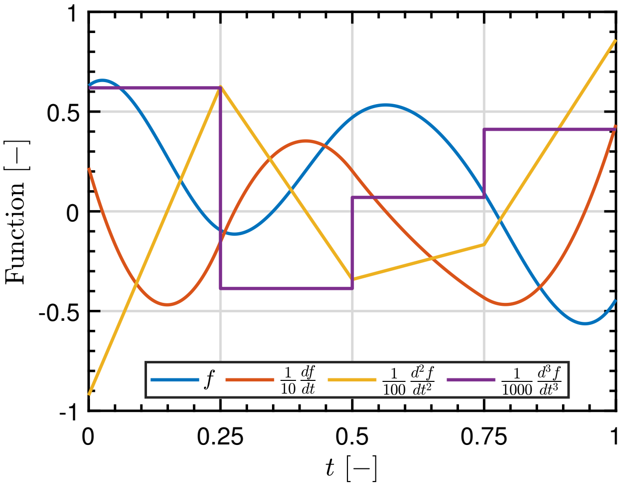

Figure A.2: Example of a cubic B-spline function and its derivatives.

This page is intentionally left blank.

Appendix B

Periodic orbits in the CRTBP

Let assume the natural dynamics of the circular restricted three-body problem (see the paragraph *third bodies gravity* of Section 2.1.1 for the definition of the variables) which are expressed in the synodic frame S as

$$\begin{aligned} \ddot{x} =& \omega^2 x + 2\omega\dot{y} - \frac{\mu_1(x+\beta D)}{r_1^3} - \frac{\mu_2[x-(1-\beta)D]}{r_2^3}, \\ \ddot{y} =& \omega^2 y - 2\omega\dot{x} - \frac{\mu_1 y}{r_1^3} - \frac{\mu_2 y}{r_2^3}, \\ \ddot{z} =& -\frac{\mu_1 z}{r_1^3} - \frac{\mu_2 z}{r_2^3}. \end{aligned} \tag{B.1}$$

The previous system has five libration points (namely the Lagrange points). All of them are contained in the primaries orbital plane xy: three of them, L1, L2 and L3, are placed along the line (x) uniting the primaries; the remaining two, L4 and L5, are placed in an equilateral triangle whose vertexes are the primaries and the Lagrange point. These are shown in Fig. B.1. The blue arrows indicates the decreasing direction of the potential energy while the red arrows from where it augments. In that sense, the collinear Lagrange points (L1, L2 and L3) are placed in a saddle while the L4 and L5 lie in the top of a hill. This causes the collinear Lagrange points to be unstable while the L4 and L5 are stable if the relation between the primaries masses satisfies $M_1/M_2 \geq 24.96$. An interesting feature is that the Lagrange points are surrounded by periodic orbits (also unstable) on their vicinity. To find them, the symmetry of the problem with respect to time is exploited. It can be deduced that the CRTBP dynamics of Eq. (B.1) is invariant under the following transformation

$$\begin{aligned} \{x(t), y(t), z(t), \dot{x}(t), \dot{y}(t), \dot{z}(t)\} \rightarrow \{& x(-t), -y(-t), z(-t), \\ & -\dot{x}(-t), \dot{y}(-t), -\dot{z}(-t)\}, \end{aligned} \tag{B.2}$$

which means that a trajectory lying on one side of a $y \equiv$ constant plane, has a mirror image on the other side of the plane evolving backwards in time. Then, a trajectory whose initial coordinate is perpendicular to the y plane ($\dot{y}(0) = 0$) has to be connected with its symmetric counterpart forming a single path. This fact, combined with the linearized motion around the Lagrange points, is usually exploited to compute CRTBP periodic orbits, $\mathbf{r}(0) = \mathbf{r}(T)$. These initial orbits can be expanded through numerical continuation methods yielding several families of periodic orbits in the CRTBP context (see [Doedel07] for the details):

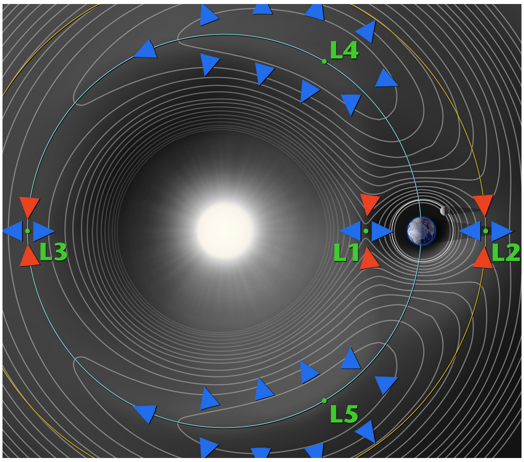

Figure B.1: Lagrange points of the Sun-Earth system. Credits: NASA/WMAP Science Team.

- Planar Lyapunov families at L1, L2, L3 / L4, L5 (short and long periods).
- Vertical families at Li, $i = 1 \dots 5$.
- Halo families at L1, L2 and L3.
- Backflip families from vertical L1, L2 and L3.
- W4/W5 families from vertical L4/L5.
- Circular families from vertical L1 and L2/L3.
- D1, E1 and R2 families.

The CRTBP dynamics Eq. (B.1) is symmetric with respect to the xy plane

$$\{x(t), y(t), z(t), \dot{x}(t), \dot{y}(t), \dot{z}(t)\} \to \{x(t), y(t), -z(t), \dot{x}(t), \dot{y}(t), -\dot{z}(t)\}, \quad \text{(B.3)}$$

which causes the existence of southern ($-z$) and northern ($+z$) orbits for each family.

Near-rectilinear halo orbits: amongst the previous families, the halo orbits have been the most employed one in space exploration. The halo orbits emerge vertically (along the z direction) in the vicinity of the collinear equilibriums. This is convenient for communication purposes because line-of-sight with the two primaries, due to its out-of-plane component, is guaranteed. Due to the symmetry with respect to the xy plane (see Eq. (B.3)) each halo orbit has a northern and southern branch. Being placed in the vicinity of the collinear Lagrange points, the halo orbits are inherently unstable. This means that a satellite would require frequent corrections to maintain its orbit.

For mission design, an interesting aspect is to quantify how unstable an orbit is. For that purpose, the eigenvalues of the monodromy matrix (the state transition matrix evaluated after one period $\mathbf{\Phi}(T,0) \in \mathbb{R}^{6\times 6}$) provide useful information. The CRTBP system Eq. (B.1) is conservative because only gravity forces (which are derived from a potential) are present. For a conservative system, the determinant of its monodromy matrix determinant must be equal to the unity (as well as the product of their eigenvalues), hence it can be demonstrated that the

$$\lambda_1 = \frac{1}{\lambda_2} \in \mathbb{R}, \quad \lambda_3 = \lambda_4 = 1, \quad \lambda_5 = \bar{\lambda}_6 \in \mathbb{C} \ \text{ with } \ \lambda_5 \bar{\lambda}_5 = 1, \tag{B.4}$$

where λ_i refers to each eigenvalue. Consequently, there are two real reciprocals eigenvalues, two equal to the unity and two complex ones lying in the unit circle of the complex domain. The fact that one of the monodromy matrix eigenvalues is above the unity, indicates the unstable behaviour of the halo orbits. This eigenvalue characterizes the orbit tendency towards instability. When its value is closer to the unity (marginally stable case), the orbit would need a longer period of time to be unstabilized. This is an attractive feature as such orbit would need a lesser station-keeping control effort. Under the previous considerations, [Zimovan17] proposed the following stability index

$$\kappa = \frac{1}{2}(|\lambda_1| + |\lambda_2|), \tag{B.5}$$

where $\kappa \geq 1$ being the case $\kappa = 1$ marginally stable and $\kappa > 1$ unstable. An orbit with a higher value of its stability index is more prone to be unstabilized in a fewer period of time.

The stability index defines the near-rectilinear halo orbits. The NRHOs are a subset of the halo family defined by the fact that their stability indexes are bounded (close to the unity). It is unclear how to exactly choose the interval of stability indexes in order to obtain the NRHOs. Let assume the NRHOs are the halo members satisfying $1 \leq \kappa \leq 3$. Under the previous consideration, the L2 southern NRHOs of the Earth-Moon system are depicted in Fig. B.2. The whole family of southern halos has been also represented. The position coordinates are adimensionalized with the mean distance between the Earth and Moon, $D = 384400$ km. The stability indexes and orbital periods for the L2 southern NRHOs of the Earth-Moon system are shown in Fig. B.3. It can be observed that there is a region where the stability index is almost the unity and then suddenly increases with the perilune altitude. The orbital periods oscillate between 6 and 11 days which is an order of magnitude higher than Keplerian geocentric orbits. Two orbits have been highlighted in Fig. B.2-B.3. These correspond to the ones whose orbital periods are in 4:1 and 9:2 resonance with the Moon synodic period (29.5 days). These orbits offer to avoid eclipses with the Moon and Earth shadows by using an appropiate phasing. As a matter of fact, a 4:1 Earth-Moon L2 southern NRHO is the chosen destination to place the LOP-G (see [Whitley16]).

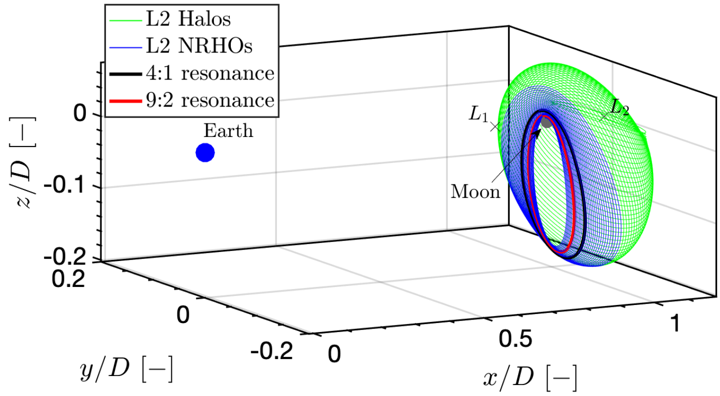

Figure B.2: Southern halos of the Earth-Moon L2.

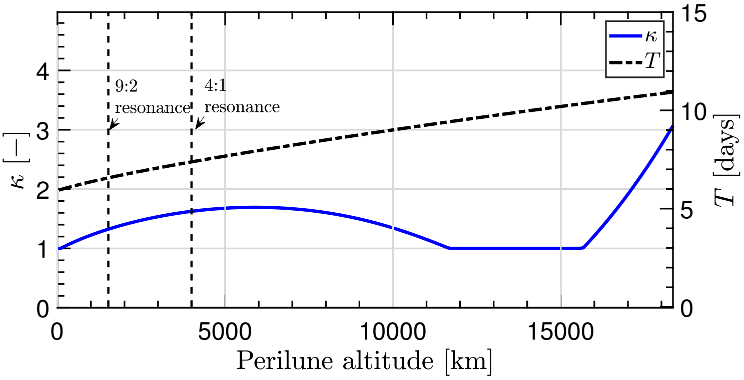

Figure B.3: Stability indexes and orbital periods for the southern halos of the Earth-Moon L2.

Appendix C

Implicitization of trigonometric functions

Implicitizing a parametric function refers to remove the independent variable in order to obtain an expression for its geometrical shape. In the case of functions parameterized by means of trigonometric terms (cosines and sines), [Hong95] developed a general implicitization method as shown in Algorithm 6. Note that the polynomial coefficients in step 4 are complex variables.

Algorithm 6: Implicitization method for trigonometric functions

```
1 begin
2     Rearrange the expressions into:
      $x(t) = c_x + \sum_{m=1}^{m_x} a_{x_m} \cos mt + b_{x_m} \sin mt,$
      $y(t) = c_y + \sum_{m=1}^{m_y} a_{y_m} \cos mt + b_{y_m} \sin mt;$
3     Apply the following change of variable: $\cos mt \leftarrow (w^m + w^{-m})/2,$
      $\sin mt \leftarrow (w^m - w^{-m})/2i;$
4     Rearrange the resulting expressions into polynomial forms:
      $xw^{m_x} - \sum_{m=0}^{m_x} d_{x_m} w^m,\ yw^{m_y} - \sum_{m=0}^{m_y} d_{y_m} w^m;$
5     Form the Sylvester's matrix with the polynomial coefficients
      $S \equiv S(x, y, d_{x_m}, d_{y_m});$
6     The determinant of the Sylvester's matrix yields the implicit
      equation: $\det(S) = \sum_{j=0}^{m_x} \sum_{k=0}^{m_y} c_{jk} x^j y^k = 0;$
7 end
```

Now, an example of the implicitization method, as given by Algorithm 6, is shown. Let consider the following inequality

$$\frac{\cos \nu}{1 + e \cos \nu} d_4 + \frac{\sin \nu}{1 + e \cos \nu} d_5 \leq \overline{y}, \tag{C.1}$$

where: ν is the independent variable; d_4 and d_5 are the parameterized variables; the terms e and $\overline{y}$ are constants. It may be of interest to obtain a formal geometrical description of the inequality envelop. This allows to describe the feasible region $\forall \nu \in [0, 2\pi]$. The envelope is characterized by the frontier of the inequality and its derivative (with respect to the independent variable) as

$$\begin{aligned} d_4 \cos\nu + d_5 \sin\nu - \overline{y}(1 + e\cos\nu) = 0, \\ -d_4 \sin\nu + d_5 \cos\nu + e\overline{y}\sin\nu = 0, \end{aligned} \tag{C.2}$$

which can be rearranged to clear d_4 and d_5 explicitly (step 2)

$$\begin{aligned} d_4 &= \overline{y}(e + \cos\nu), \\ d_5 &= \overline{y}\sin\nu. \end{aligned} \tag{C.3}$$

It is evident that it represents a circle of radius $\overline{y}$ with center $(e\overline{y}, 0)$ (which serves to verify the result). Let apply the change of variable from ν to w (step 3)

$$\begin{aligned} d_4 = \overline{y}\left[e + \frac{w^2+1}{2w}\right], \\ d_5 = \overline{y}\frac{w^2-1}{2iw}, \end{aligned} \tag{C.4}$$

which can be explicitly expressed as a polynomials in w as (step 4)

$$\begin{aligned} \overline{y}w^2 + 2(e\overline{y} - d_4)w + \overline{y} = 0, \\ \overline{y}w^2 + 2id_5w - \overline{y} = 0. \end{aligned} \tag{C.5}$$

Now let form the Sylvester matrix of the previous polynomials in w (step 5)

$$S = \begin{bmatrix} \overline{y} & 2(e\overline{y} - d_4) & \overline{y} & 0 \\ 0 & \overline{y} & 2(e\overline{y} - d_4) & \overline{y} \\ \overline{y} & 2id_5 & -\overline{y} & 0 \\ 0 & \overline{y} & 2id_5 & -\overline{y} \end{bmatrix}, \tag{C.6}$$

then by computing the determinant of the Sylvester matrix (also namely as the resultant of the polynomials)

$$\det(S) = -4e^2\overline{y}^4 + 8d_4e\overline{y}^3 - 4d_4^2\overline{y}^2 - 4d_5^2\overline{y}^2 + 4\overline{y}^4, \tag{C.7}$$

and by equalling that expression to zero, the implicitized equation is found (step 6)

$$\boxed{\frac{(d_4 - e\overline{y})^2}{\overline{y}^2} + \frac{d_5^2}{\overline{y}^2} = 1.} \tag{C.8}$$

The resulting implicitized equation is a circle with a center offset in d_4 as expected from Eq. (C.3). For $e = 0.2$ and $\overline{y} = 25$, the family of inequalities and its associated implicitized envelope function is shown in Fig. C.1.

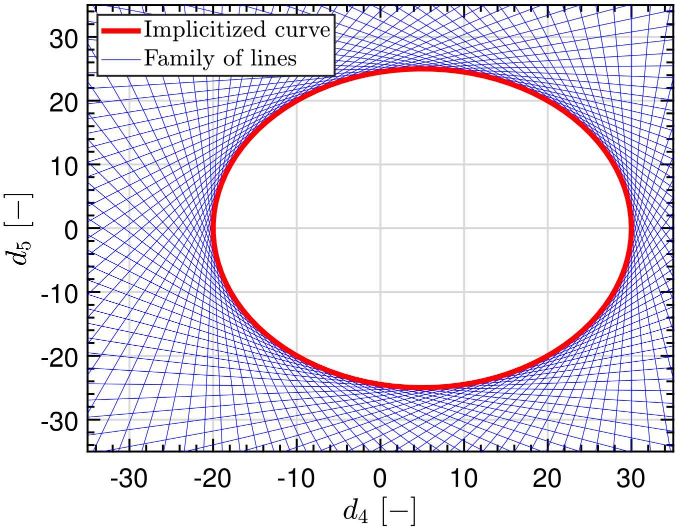

Figure C.1: Result of the implicitization.

This page is intentionally left blank.

Appendix D

Global stable impulsive control for spacecraft rendezvous hovering phases

This appendix summarizes the main result of the manuscript [Arantes-Gilz19]. In that publication, a model predictive controller was developed and proven to globally stabilize a set of constrained relative periodic orbits (admissible set). The hovering region was a cuboid, in terms of Cartesian relative position coordinates, of dimensions $\{\underline{x}, \overline{x}, \underline{y}, \overline{y}, \underline{z}, \overline{z}\}$. Let recall that the global stability property is demonstrated under Keplerian linear relative motion assumptions (if follower and leader have a large initial separation, this linear model is not accurate). The details of the stability proof can be found in [Arantes-Gilz19]. The vector of parameters $\mathbf{d} = [d_0, d_1, d_2, d_3, d_4, d_5]^T$ for Keplerian relative motion is exploited. This state has its own transition as

$$\begin{gathered} \mathbf{d}(\nu) = \mathbf{\Phi}_D(\nu, \nu_0)\mathbf{d}(\nu) + \sum_{j=1}^{N} \mathbf{\Phi}_D(\nu, \nu_0)\mathbf{B}_D(\nu)\Delta\mathbf{V}(\nu_j), \\ \nu \geq \nu_0, \quad \nu_0 \leq \nu \leq \nu_j. \end{gathered} \tag{D.1}$$

The global stable controller uses an initial single-impulse to steer the state towards a periodic relative orbit ($d_0 = 0$) and a subsequent number of N impulses driving the state to the admissible set along the plane $d_0 = 0$. Consequently, the state evolves in relative periodic orbits. An impulse structure fullfiling the previous requirement is as follows

$$\Delta\mathbf{V} = \underbrace{\begin{bmatrix} \lambda_{xz} e \sin\nu/(1 + e^2 + 2e\cos\nu) \\ \Delta V_y \\ \lambda_{xz}(1 + e\cos\nu)/(1 + e^2 + 2e\cos\nu) \end{bmatrix}}_{\lambda_{xz}\mathbf{B}^{\perp}_{d_0}(\nu) + \Delta\mathbf{V}_y} + \underbrace{\begin{bmatrix} \Delta V_{x,0} \\ 0 \\ \Delta V_{z,0} \end{bmatrix}}_{\Delta\mathbf{V}^0}, \tag{D.2}$$

where the first part of the right-hand side does not alter the state d_0 while the second part is employed to nullify d_0.

A single-impulse instantaneously nullifying d_0 has to fulfil

$$d_0^+ = d_0 + \mathbf{B}_{d_0}(\nu)\Delta\mathbf{V}^0 = 0, \tag{D.3}$$

where $\mathbf{B}_{d_0} \in \mathbb{R}^{1\times 3}$ is the first row of the control matrix $\mathbf{B}_D$. A possible choice is given by the pseudoinverse of $\mathbf{B}_{d_0}$

$$\Delta\mathbf{V}^0 = -d_0(\mathbf{B}_{d_0}^T(\nu)\mathbf{B}_{d_0}(\nu))^{-1}\mathbf{B}_{d_0}^T(\nu). \tag{D.4}$$

Once the follower has been inserted in a relative periodic orbit by using Eq. (D.4), the state is steered towards the admissible set. In the steering process, the state is constrained to evolve in the plane $d_0 = 0$ which is achieved by designing impulses with the structure of Eq. (D.2). Note that since $d_0 = 0$, then $\Delta\mathbf{V}^0 = \mathbf{0}$. Under the previous facts, the solution of the following semi-definite linear program produces an impulse sequence stabilizing the state towards the admissible set

$$\begin{aligned}
\underset{\Delta\mathbf{V}_\ominus(\nu_j),\Delta\mathbf{V}_\oplus(\nu_j),Y_i}{\text{minimize}} \quad & \sum_{j=1}^{N}\|\Delta\mathbf{V}_\ominus(\nu_j)\|_1 + \|\Delta\mathbf{V}_\oplus(\nu_j)\|_1, \\
\text{subject to} \quad & \Delta\mathbf{V}_\ominus(\nu_j) \geq \mathbf{0}, \quad \Delta\mathbf{V}_\oplus(\nu_j) \geq \mathbf{0}, \\
& \Delta\mathbf{V}(\nu_j) = \Delta\mathbf{V}_\oplus(\nu_j) - \Delta\mathbf{V}_\ominus(\nu_j), \\
& \Delta\mathbf{V}(\nu_j) = \lambda_{xz}\mathbf{B}_{d_0}^{\perp}(\nu_j) + \Delta\mathbf{V}_y, \\
& \mathbf{d}^+(\nu_N) = \mathbf{\Phi}_D(\nu_N,\nu_1)\mathbf{d}(\nu_1) \\
& \qquad + \sum_{j=1}^{j}\mathbf{\Phi}_D(\nu_N,\nu_j)\mathbf{B}_D(\nu_j)\Delta\mathbf{V}(\nu_j), \\
& Y_i \succeq 0, \quad i = 1\ldots 6, \\
& \boldsymbol{\gamma}_i = [\mathrm{tr}(Y_iH_{2,1}),\ldots,\mathrm{tr}(Y_iH_{2,5})]^T, \\
& \boldsymbol{\gamma}_i = v_i\mathbf{t} - (h_{i,x}\mathbf{C}_x + h_{i,y}\mathbf{C}_y + h_{i,z}\mathbf{C}_z)\mathbf{d}^+(\nu_N),
\end{aligned} \tag{D.5}$$

where $\Delta\mathbf{V}_\ominus, \Delta\mathbf{V}_\oplus \in \mathbb{R}^3$ are slack variables introduced to obtain a linear form of the L1-norm. The number of impulses N and its application instants, ν_j, can be arbitrary as long as $N \geq 3$ and their spacing in time is not a multiple of the target orbital half-period. The matrices $Y_i \in \mathbb{R}^3$ are decision variables where each one corresponds to a polytopic constraint describing the hovering region. The terms $H_{2,i} \in \mathbb{R}^{3\times 3}$ are Hankel matrices with ones on the ith anti-diagonal and zeros everywhere else. The vector $\boldsymbol{\gamma}_i \in \mathbb{R}^5$ is filled with the polynomial coefficients of the admissible set polytopic constraints. The details of these coefficients can be found in [Deaconu15, Chapter 3] where the hovering region polytopic constraints were transformed to an equivalent polynomial form of degree 4th at most. As a consequence, the continuous satisfaction of polytopic constraints is equivalent to polynomial positiveness (which can be also equivalently transformed to a linear matrix inequality as shown in program (D.5)). The polynomial coefficients are constructed using the following variables

$$\mathbf{C}_x = \begin{bmatrix} 0 & 0 & 2-e & 1 & 0 & 0 \\ 0 & 4-2e & 0 & 0 & 0 & 0 \\ 0 & 0 & 2e & 2 & 0 & 0 \\ 0 & 4+2e & 0 & 0 & 0 & 0 \\ 0 & 0 & -2-e & 1 & 0 & 0 \end{bmatrix}, \quad \mathbf{C}_y = \begin{bmatrix} 0 & 0 & 0 & 0 & -1 & 0 \\ 0 & 0 & 0 & 0 & 0 & 2 \\ 0 & 0 & 0 & 0 & 0 & 0 \\ 0 & 0 & 0 & 0 & 0 & 2 \\ 0 & 0 & 0 & 0 & 1 & 0 \end{bmatrix},$$

$$\mathbf{C}_z = \begin{bmatrix} 0 & e-1 & 0 & 0 & 0 & 0 \\ 0 & 0 & 2-2e & 0 & 0 & 0 \\ 0 & -2e & 0 & 0 & 0 & 0 \\ 0 & 0 & 2+2e & 0 & 0 & 0 \\ 0 & e+1 & 0 & 0 & 0 & 0 \end{bmatrix}, \quad \mathbf{t} = [1-e,\ 0,\ 2,\ 0,\ 1+e]^T,$$

$$v_i = \{-\underline{x}, \overline{x}, -\underline{y}, \overline{y}, -\underline{z}, \overline{z}\}, \quad h_{i,x} = \begin{cases} -1 & \text{if} \quad i = 1, \\ 1 & \text{if} \quad i = 2, \\ 0 & \text{if} \quad i = 3, 4, 5, 6. \end{cases}$$

$$h_{i,y} = \begin{cases} -1 & \text{if} \quad i = 3, \\ 1 & \text{if} \quad i = 4, \\ 0 & \text{if} \quad i = 1, 2, 5, 6. \end{cases} \qquad h_{i,z} = \begin{cases} -1 & \text{if} \quad i = 5, \\ 1 & \text{if} \quad i = 6, \\ 0 & \text{if} \quad i = 1, 2, 3, 4. \end{cases}$$

Under the previous considerations, the controller commands an initial single-impulse to insert the follower into a relative periodic orbit (see Eq. (D.4)). Once the periodic relative orbit is acquired, a sequence of N impulses, computed through program (D.2) steers the state towards the admissible set. The Algorithm 7 summarizes the global stabilizing control strategy in a pseudocode form. The steps 2-10 comprises the relative periodic trajectory generation while the steps 11-21 stabilize the state to the admissible set. The impulse sequence is assumed to be placed at equidistant true anomalies such that $\nu_j = \nu_1 + (j-1)\tau_I,\ \ j = 1 \dots N,\ \ \tau_I \neq k\pi,\ \ k \in \mathbb{N}$. The possibility of impulses falling outside the feasible region (bounded by the saturation $\overline{\Delta V}$ and the minimum impulse bit $\underline{\Delta V}$) has been considered in steps 5, 15 and 7, 17 respectively. This fact was not explicitly considered in the SDP problem D.5 for the sake of feasibility. In the saturated case, the impulse is scaled with $\overline{\Delta V}$. If an impulse fall below the minimum impulse bit, it is nullified. In [Arantes-Gilz19], it was demonstrated that applying saturated impulses, along the computed direction, steers the state closer to a relative periodic orbit or the admissible set respectively. However, the controller stability in the presence of a minimum impulse bit, $\underline{\Delta V} > 0$ was not demonstrated. The parameters τ_P and τ_I are used to space the impulses in time. Intuitively, lower values of these angles will assure a faster convergence at the expense of fuel consumption and otherwise if they are higher.

The global stable controller convergence process to the admissible set is schematically shown in Fig. D.1. A subset of the in-plane space is considered

Algorithm 7: A global stable controller for spacecraft rendezvous hovering phases

```
begin
    while $d_0(\nu) \neq 0$ do
        Compute $\Delta\mathbf{V}^0(\nu)$ with Eq. (D.4);
        if $\|\Delta\mathbf{V}^0(\nu)\|_2 > \overline{\Delta V}$ then
            $\Delta\mathbf{V}^0(\nu) \leftarrow \overline{\Delta V}\Delta\mathbf{V}^0(\nu)/\|\Delta\mathbf{V}^0(\nu)\|_2$;
        else if $\|\Delta\mathbf{V}^0(\nu_j)\|_2 < \underline{\Delta V}$ then
            $\Delta\mathbf{V}^0(\nu_j) \leftarrow \mathbf{0}$;
        Apply $\Delta\mathbf{V}(\nu) \leftarrow \Delta\mathbf{V}^0(\nu)$;
        Wait $\nu \leftarrow \nu + \tau_P$;
    end
    while $\mathbf{d}(\nu) \notin \mathcal{S}_D$ do
        Obtain an impulse sequence $\Delta\mathbf{V}(\nu_j)$ by solving the SDP
          problem (D.5);
        for $j = 1 \dots N$ do
            if $\|\Delta\mathbf{V}(\nu_j)\|_2 > \overline{\Delta V}$ then
                $\Delta\mathbf{V}(\nu_j) \leftarrow \overline{\Delta V}\Delta\mathbf{V}(\nu_j)/\|\Delta\mathbf{V}(\nu_j)\|_2$;
            else if $\|\Delta\mathbf{V}(\nu_j)\|_2 < \underline{\Delta V}$ then
                $\Delta\mathbf{V}(\nu_j) \leftarrow \mathbf{0}$;
            Apply $\Delta\mathbf{V}(\nu) \leftarrow \Delta\mathbf{V}(\nu_j)$;
            Wait $\nu \leftarrow \nu + \tau_I$;
        end
    end
end
```

as $d_0 d_2 d_3$. First, a single-impulse generates a periodic trajectory ($d_0 = 0$). Subsequently a sequence of three impulses (a higher number of impulses could also have been chosen) drives the state towards the admissible set along the plane $d_0 = 0$. Let recall that the periodicity condition $d_0 = 0$ makes the state invariant over time, thus the state only changes instantaneously ($\mathbf{d}^+ = \mathbf{d} + \Delta\mathbf{d}$) when the impulses are applied at instants ν_j.

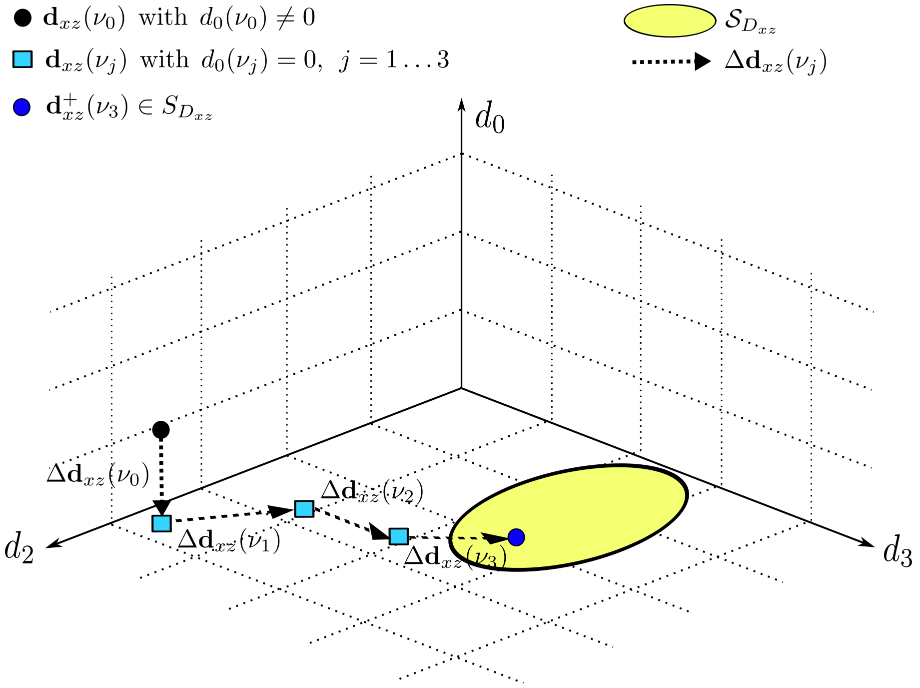

Figure D.1: Sketch of the global stable controller convergence.

This page is intentionally left blank.